Analysis of a Hybrid Propulsion Lunar Sample Return Mission

A thesis accepted by the Faculty of Aerospace Engineering and Geodesy of the University of Stuttgart in partial fulfillment of the requirements for the degree of Doctor of Engineering Sciences (Dr.-Ing.)

by

Dipl.-Ing. Christian Schmierer

born in Heilbronn

Committee Chair: Prof. Dr.-Ing. Stefan Schlechtriem

Committee Members: Prof. Dr.-Ing. Oskar Haidn

                             Prof. Dr. ir. Johan Steelant

Date of Defence: 11.03.2019

Insitute of Space Systems
University of Stuttgart
2019

Acknowledgment

Contents

Abstract

A sample return mission to the Moon brings many scientific gains to different disciplines. The Moon and its history have come back into the view of science lately. For 20 years now the interest in space missions to the Moon has constantly grown bringing new orbiters and even landing missions. The advantage of returning soil samples to Earth is widely acknowledged as the samples can be analyzed with the wide range of instruments on Earth. Advancements in analysis instruments in the future bring benefits to the investigation of the soil samples. In the past manned (Apollo, USA) and unmanned (Luna, USSR) sample return missions were conducted. These missions demonstrated great technological advancements for the nations in the 1960's and 1970's. Today space missions are also driven by economic and ecological perspectives. Low cost is a major driver in the new space era. Although economic aspects have not the highest priority for exploration missions, cost reductions are still essential. Especially the choice of propellant is important. Environmentally friendly propellants on the one hand support the low-cost processes and on the other hand make sure that no personnel or environments are exposed to hazardous materials like hydrazine. Therefore new propellants and even new propulsion systems are developed in order to reduce cost and hazards. Hybrid propulsion technology is very promising in that matter. Therefore, a hybrid propulsion lunar sample return mission is proposed and analyzed. First a survey of Moon missions and their history is conducted focusing on established propulsion systems using traditional, storable fuels and oxidizers. Then the theory of hybrid propulsion is presented. Hybrid propulsion is dominated by the effects of having a liquid and a solid propellant. This brings many advantages: an explosion hazard is impossible and the propulsion system layout becomes simpler. However, at the same time the hybrid propulsion system poses challenges: The volumetric efficiency and the thrust to weight ratio are lower as the regression rates of classical fuels are too low and the surface of the fuel grain needs to be increased. Liquefying paraffin-based fuels form a melt layer and increase the regression rate with droplet entrainment by a factor of up to six. New advances with those fuels show that hybrid propulsion can gain significant advantages from this discovery. The chamber design is simpler if liquefying fuels are used. This strengthens the low-cost approach even further. Different regression rate prediction models are presented after a literature research. New models for classical and liquefying fuels are implemented in an existing simulation model in ESPSS in order to enhance future simulation capabilities for both pre-design and test result comparison. A tool for simulation and optimization of hybrid propulsion systems in combination with the spacecraft's trajectory is developed using the ASTOS software. An interface is created for coupling both software tools, in order to simulate and optimize hybrid propulsion systems. The software tools are verified by simulating and optimizing different trajectories. The simulation of hybrid

propulsion systems in ESPSS is compared and evaluated with hybrid rocket engine tests at the DLR test bench M11. An experimental campaign was conducted in order to get data about paraffin-based fuels in combustion with gaseous oxygen. A special focus was put on longer burn durations of up to 40 s. The longer burn duration creates new problems with thermal and mechanical loads on materials, but is needed in order to make hybrid propulsion fit for a wider range of applications. Another investigated feature of hybrid rocket engines is throttleability resp. deep-throttling. Throttling is quite easy to achieve in hybrids, as only one liquid propellant needs to be actively controlled. However, due to the fact that the fuel mass flow is directly linked to the flow conditions, a shifting in mixture ratio is inevitable. This results in performance losses. With the established tools and software six variants of hybrid propulsion landers were designed and compared to each other, as well as to two liquid propulsion concepts using storable and cryogenic propellants. Cryogenic propellants are a possible choice as long as the mission duration is limited to a few days and the cryogenic temperature is held with insulation and boil-off. The six hybrid propulsion variants are using three different staging concepts and are analyzed with hydrogen peroxide and liquid oxygen as the oxidizer. The results are promising. While hybrid rocket engines have a very good ideal specific impulse, the combustion efficiency is usually lower than in liquid propulsion. Future advancements on that matter can bring hybrid propulsion nearly on an equal level with liquid propulsion. The dry mass of a hybrid propulsion system is still a bit higher than of a liquid propulsion system as the storage of fuel in a cylindrical shape is less optimal than in a spherical tank. In addition insulation material is necessary, as the chamber wall cannot be regeneratively cooled. This further increases the structural mass. But even with these restrictions the performance is comparable to liquid systems and the low-cost approach, non-toxicity and lack of explosion hazard improve the hybrid propulsion's position among the possible concepts. A hybrid propulsion lunar sample return mission is a viable option for low-cost spacecraft development and can become a future project of the European space community.

Kurzzusammenfassung

Eine Probenrückführungsmission zum Mond bietet viele Erkenntnisse für verschiedene wissenschaftliche Disziplinen. Der Mond und seine Geschichte haben sich wieder in das Blickfeld der Wissenschaft bewegt. In den letzten 20 Jahren ist das Interesse an Raumfahrtmissionen zum Mond stetig gewachsen, weswegen viele Satelliten und sogar Landefahrzeuge zum Mond geschickt wurden. Die Rückführung von Bodenproben bringt einige Vorteile, da in den Laboren auf der Erde das ganze Spektrum an Instrumenten zur Untersuchung der Proben zur Verfügung steht. Die Weiterentwicklung von Instrumenten bringt außerdem in der Zukunft die Möglichkeit, bereits untersuchte Proben noch genauer zu analysieren. In der Vergangenheit wurden bemannte (Apollo, USA) und unbemannte (Luna, UdSSR) Mondmissionen mit Probenrückführung durchgeführt. Die Missionen zeugen von den großartigen technologischen Fortschritten der Nationen in den 1960er und 1970er Jahren. Heute werden wissenschaftliche Raumfahrtmissionen auch von wirtschaftlichen und ökologischen Faktoren beeinflusst. Obwohl bei Explorationsmissionen die Ökonomie nicht im Vordergrund steht, sind Kostenreduktionen in den unterschiedlichen Bereichen einer Mission unerlässlich. Besonders die Treibstoffwahl ist in mehrerer Hinsicht entscheidend. Umweltfreundliche Treibstoffe reduzieren die Kosten bei der Handhabung und stellen andererseits sicher, dass Personal und Umwelt keinen gefahrvollen Stoffen wie Hydrazin ausgesetzt werden. Deshalb werden neue Treibstoffe und sogar neue Antriebssysteme entwickelt, um Kosten und Gefahren zu reduzieren. Die Hybridantriebstechnologie ist diesbezüglich vielversprechend. Daher wird eine Probenrückführungsmission mit Hybridraketenantrieben zum Mond vorgeschlagen und untersucht. Hierfür wird zunächst eine Übersicht über Mondmissionen und ihre Geschichte erstellt. Dabei wird der Fokus auf die etablierten Antriebssysteme mit traditionellen, lagerfähigen Brennstoffen und Oxidatoren gelegt. Anschließend werden die Grundlagen der Hybridantriebstechnologie präsentiert. Hybridraketenantriebe werden von ihrem Aufbau mit einer flüssigen und festen Treibstoffkomponente geprägt. Dies bringt einerseits viele Vorteile: es gibt keine Explosionsgefahr und der Aufbau des Antriebssystems ist einfacher. Gleichzeitig stellt das Hybridraketenantriebssystem einige neue Herausforderungen: die volumenspezifische Effizienz und das Verhältnis von Schub zu Gewicht ist niedrig, da die Abbrandrate klassischer Brennstoffe gering ist und die Oberfläche des Brennstoffkerns erhöht werden muss. Wie neue Fortschritte mit Paraffin-basierten Brennstoffen zeigen, gewinnen Hybridantriebe mit dieser Brennstoffart erhebliche Vorteile, da diese Brennstoffe eine Flüssigkeitsschicht bilden. Dies erhöht die Abbrandrate durch Tropfenbildung um einen Faktor von bis zu sechs. Wenn verflüssigende Brennstoffe genutzt werden, ist die Geometrie des Brennstoffs daher einfacher. Dies verringert die Kosten von Hybridraketenantrieben weiter. Verschiedene Modelle, um die Abbrandrate vorherzusagen, werden nach einer Literaturrecherche vorgestellt. Neue

Modelle für klassische und verflüssigende Brennstoffe werden in ein existierendes ESPSS Modell implementiert, um die zukünftige Simulationsmöglichkeiten sowohl für Vorentwurf als auch für den Vergleich mit Testergebnissen zu verbessern. Ein Programm zur Simulation und Optimierung von Hybridraketenantriebssystemen in Kombination mit der Trajektorie des Raumfahrzeugs wird mit dem Programm ASTOS entwickelt. Eine Schnittstelle wird erstellt, um beide Programme gekoppelt zu benutzen und hybride Antriebssysteme zu simulieren und zu optimieren. Die Programme werden mit Simulationen und Optimierungen verschiedener Trajektorien verifiziert. Die Simulation der hybriden Antriebssysteme in ESPSS wird mit Antriebstests am DLR Prüfstand M11 verglichen und bewertet. Eine experimentelle Testkampagne wurde durchgeführt um mehr Daten über Paraffin-basierte Brennstoffe bei der Verbrennung mit gasförmigem Sauerstoff zu bekommen. Um Hybridraketenantriebe in einem breiter gefächerten Bereich zur Anwendung zu bringen, ist eine längere Brenndauer der Triebwerke notwendig. Diese längere Brenndauer erzeugt neue Probleme durch thermische und mechanische Lasten auf Bauteile. Als weitere Eigenschaft von Hybridraketentriebwerken wird die Drosselbarkeit untersucht. Drosseln ist mit Hybridraketentriebwerken einfach möglich, da nur eine Flüssigkeit aktiv gesteuert werden muss. Dennoch ergibt sich eine Schwierigkeit: Da der Brennstoffmassenstrom direkt mit den Strömungsbedingungen verbunden ist, ist eine Veränderung des Mischungsverhältnisses unvermeidbar. Das resultiert in Leistungsverlusten. Mit den erstellten Programmen wurden sechs Varianten von Landefahrzeugen mit Hybridraketenantrieben entworfen und miteinander verglichen, so wie mit zwei Konzepten mit Flüssigantriebssystemen mit lagerfähigen und kryogenen Treibstoffen. Kryogene Treibstoffe sind nutzbar, solange die Missionsdauer auf wenige Tage begrenzt ist und die Treibstofftemperatur mit Isolation und Verdampfung gehalten wird. Die sechs Varianten mit Hybridantrieben nutzen drei verschiedene Stufungskonzepte und werden jeweils mit Wasserstoffperoxid und flüssigem Sauerstoff als Oxidator untersucht. Die Ergebnisse sind vielversprechend. Während Hybridraketenantriebe einen guten idealen spezifischen Impuls haben, ist die Verbrennungseffizienz gewöhnlich niedriger als bei Flüssigtreibstoffen. Weitere Verbesserungen in diesem Bereich können Hybridraketenantriebe auf dasselbe Leistungsniveau wie Flüssigraketentriebwerke bringen. Die Trockenmasse von Hybridantriebssystemen ist dennoch etwas höher als bei Flüssigantriebssystemen, da die Lagerung des Brennstoffs in der zylindrischen Brennkammer weniger optimal als in einem Kugeltank ist. Außerdem wird für die Brennkammer auch Isolationsmaterial benötigt, da eine regenerative Kühlung nicht möglich ist. Dies erhöht die Strukturmasse weiter. Aber selbst mit diesen Einschränkungen ist die Leistungsfähigkeit vergleichbar zu Flüssigantrieben. Die niedrigeren Kosten, die Ungiftigkeit der Treibstoffe und das Vermeiden von Explosionsgefahr verbessern die Stellung von Hybridraketenantrieben unter den verschiedenen möglichen Antriebskonzepten. Eine Probenrückführungsmission zum Mond mit Hybridraketenantriebstechnologie ist eine umsetzbare Option für die Entwicklung kostengünstiger Raumfahrzeuge und kann in der Zukunft ein Projekt der Europäischen Raumfahrtgemeinschaft werden.

List of Figures

List of Tables

Nomenclature

Formulas

H_2O_2	Hydrogen peroxide	
N_2O	Nitrous oxide	
N_2O_4	Dinitrogen tetroxide	
O_2	Oxygen	

Variables

a	Regression law parameter	
a	Semi-major axis	m
A	Flow area	m^2
A_f	Fuel surface area	m^2
B	Blowing parameter	
B_g	Evaporation blowing parameter	
C_1	Regression law coefficient	
C_{B1}, C_{B2}	Blowing correction coefficients	
C_H, C_{H0}	Stanton number with and without blowing	
c_f	Skin-friction coefficient	
c_p	Specific heat	$\frac{J}{kg\,K}$
$c^\star$	Characteristic velocity	$\frac{m}{s}$
d	Fuel grain diameter	m

D	Flow diameter	m
e_0	Entrainment coefficient	
E_a	Activation energy	$\frac{J}{mol}$
F	Thrust	N
F_r	Heat transfer correction factor for surface roughness	
G	Mass flux density	$\frac{kg}{m^2\,s}$
h_t	Melt layer thickness	mm
h	Heat transfer coefficient	$\frac{W}{m^2\,K}$
h_{ent}	Total heat of entrainment	$\frac{J}{kg}$
h_{melt}	Total heat of melting	$\frac{J}{kg}$
h_{vap}	Total effective heat of gasification	$\frac{J}{kg}$
k	Heat conductivity	$\frac{W}{m\,K}$
K_{ox}	Oxidizer concentration	
l	Length	m
L_m, L_v	Latent heat of melting and vaporization	$\frac{J}{kg}$
M	Molar weight	$\frac{kg}{mol}$
$\dot{m}$	Mass flow	$\frac{kg}{s}$
Nu_l, Nu_t	Nusselt number (laminar, turbulent)	

Symbol	Description	Unit
O/F	Mixture ratio	
p	Pressure	Pa
P_d	Dynamic pressure	Pa
Pr	Prandtl number	
$\dot{Q}_r, \dot{Q}_c$	Radiative and convective heat transfer	$\frac{J}{m^2\,s}$
$\dot{Q}_w$	Wall heat transfer	$\frac{J}{m^2\,s}$
$\dot{Q}_{vs}$	Heat transfer from the vapor of solid fuel to the gas flow	W
$\dot{Q}_{sp}$	Heat transfer from the vapor of solid fuel to the solid fuel	W
r	Distance to Earth center	m
$\dot{r}$	Regression rate	$\frac{mm}{s}$
$\dot{r}_{cl}$	Regression rate, classical	$\frac{mm}{s}$
R_{he}, R_{hv}	Ratio of effect. Heats of gasification for entrainment and vaporization	
Re, Re_x	Reynolds number (at position x)	
R_u	Universal gas constant	$\frac{J}{mol\,K}$
t_b	Burning duration	s
T	Temperature	K
T_a	Average gas temperature	K
T_{melt}	Melting temperature	K
T_{vap}	Vaporization temperature	K
T_s	Fuel grain surface temperature	K
u	Flow velocity	$\frac{m}{s}$
u_e	Velocity at the edge of the boundary layer	$\frac{m}{s}$
u_c	Velocity at the flame zone	$\frac{m}{s}$
v_1	Velocity before maneuver	$\frac{m}{s}$
v_2	Velocity after maneuver	$\frac{m}{s}$
x	Position on x-axis	m
x	Position on fuel grain	m
X_e	Entrainment parameter	$N^{0.5}$
y	Position on y-axis	m
z	Position on z-axis	m
δ	Thermal thickness	mm
Δv	Velocity change	$\frac{m}{s}$
Δh	Difference of enthalpy between the surface and flame zone	$\frac{J}{kg}$
ΔH_f^{θ}	Heat of formation	$\frac{J}{mol}$
$\Delta T_1, \Delta T_2$	Temperature differences	K

α	Inclination change	rad
β	Angle in orbit plane	rad
κ_l	Thermal diffusivity	$\frac{\text{m}^2}{\text{s}}$
λ_l	Thermal conductivity	$\frac{\text{W}}{\text{m K}}$
μ_g	Gas flow viscosity	Pa s
μ_l	Liquid layer viscosity	Pa s
μ	Gravitational parameter	$\frac{\text{m}^3}{\text{s}^2}$
ϕ_c	Relative flame position in the boundary layer	
ρ	Distance to Moon center	m
ρ_l, ρ_s	Density of liquid and solid fuel	$\frac{\text{kg}}{\text{m}^3}$
σ	Surface tension or hard-sphere diameter	$\frac{\text{m}}{\text{N}}$
ζ	Pressure loss coefficient	

Indices

0	Initial
amb	Ambience
b	Bulk
c	Combustion zone
cc	Combustion chamber
Cor	Coriolis sensor
e	Nozzle exit

e	Edge of the boundary layer
ent	Entrainment
f	Final (burn end)
fu	Fuel
g	Gas
inj	Injector (cavity)
l	Liquid
E	Earth
m	Mean
M	Moon
o, ox	Oxidizer
out	Outside
RV	Control valve
s, sp	Solid
t	Throat
vap	Vapor, vaporization

Exponents

k, l, m, n	Regression law exponents

Abbreviations

ASTOS®	Analysis, Simulation and Trajectory Optimization Software for Space Applications

CEA	Chemical Equilibrium with Applications		UTC	Coordinated Universal Time
DLR	German Aerospace Center			
ESPSS	European Space propulsion System Simulation			
FFT	Fast Fourier Transformation			
HyEnD	Hybrid Engine Development			
HTPB	Hydroxyl-terminated polybutadiene			
JPL	Jet Propulsion Laboratory			
LEO	Low Earth Orbit			
LOX	Liquid Oxygen			
M11	Test bench M11 at DLR Lampoldshausen			
MON	Mixture oxides of nitrogen			
NASA	National Aeronautics and Space Administration			
PB-5%	Paraffin based fuel with 5% addiditves			
RP	Rocket propellant			
STERN	Student Experimental Rockets Program of DLR			

1. Introduction

Planetary exploration includes a wide range of scientific disciplines, which search together for answers to basic questions of origin, genesis and evolution of planets and their moons. Next to remote exploration from Earth, for more than 50 years spacecraft have been used to explore space and our solar system's celestial bodies from a closer distance. The scientific and technological gains of these missions are enormous and in the future much more is to come. One of the most important targets of space exploration is the Moon. Since the 1960's, many missions have been conducted in Moon orbit but also on the surface, in the form of impactors, landers and even sample return missions. The first successful sample return mission from the Moon was the manned US mission Apollo 11, which brought back 22 kg of sample material from the Moon's surface. Together with the other five manned Apollo landings a total of 326 kg lunar soil material was brought back to Earth, but since Apollo 17 in 1972 no manned mission has been made and only the soviet Luna missions returned samples from the Moon to the Earth. From 1970 to 1974, the Luna program conducted three sample return missions (Luna 16, 20 & 24) and brought back a total of 325 g of regolith to Earth [1]. Yet after Luna 24, no spacecraft touched down on the lunar surface for a long time. Only in the past 25 years, the Moon received again increased attention in the scientific and space faring world. Several nations and space agencies sent spacecraft to the Moon for remote exploration: Hiten (1990, ISAS (now JAXA)), Clementine (1994, DoD/NASA), Luna Prospector (1998, NASA), SMART-1 (2004, ESA), Kaguya (2007, JAXA), Chang'e-1 (2007, CNSA), Chandrayaan-1 (2008, ISRO), Lunar Reconnaissance Orbiter, LCROSS (2009, NASA), Chang'e-2 (2010, CNSA), GRAIL (2012, NASA), LADEE (2014, NASA), Chang'e 5-T1 (2014, CNSA) and 4M (2014, OHB). Some of these missions were also impactors but the only soft landing so far in the new century was Chang'e 3 of China in 2013 with the rover Yutu. Analyses of the Moon regolith samples back at Earth are more exact and detailed than in situ analyses. Therefore, sample return missions are of high interest for science. The mission to the Moon is described in Chapter 2.

Hybrid rocket engines are using solid fuel and liquid oxidizer in their combustion chamber. This unique combination of solid and liquid state of matter has some benefits: The solid propellant is incapable of causing explosions and the range of suitable solid propellants is quite large. Hybrid rocket engines don't need chamber wall cooling and have only one liquid propellant which needs a feed system with pressurization. Therefore hybrid rocket engines can be developed at very low cost. Recent advancement in liquefying fuels using paraffin wax increase the regression rate. With this the thrust per engine volume and weight is improved. This enables hybrid rocket propulsion to be applied in spacecraft and launcher applications more easily. Therefore hybrid propulsion shall be evaluated in the application

of a lunar sample return spacecraft. In order to analyze a complete sample return mission to the Moon including hybrid rocket propulsion, both the trajectory and the propulsion system must be simulated and optimized. The trajectory optimization must include different phases for impulsive maneuvers and coasting arcs. The hybrid propulsion must be analyzed and optimized regarding diverse set-ups, starting from thrust and pressure level until the choice of propellant combinations. For trajectory simulation and optimization, "Analysis, Simulation and Trajectory Optimization Software for Space Applications" (ASTOS®) by Astos Solutions GmbH is an adequate choice. This software is highly modular, which allows modeling any kind of spacecraft trajectory from launchers over orbit maneuvers to landings on planets. In its current state, ASTOS allows different ways of implementing rocket engines. The performance of rocket engines is either modeled as constant, time depending or following a burning law (e.g. for solid rocket boosters). Yet, it cannot simulate the transient behavior of a rocket engine during start up or throttling in a detailed way. EcosimPro with its European Space Propulsion System Simulation library (ESPSS), which is developed by Empresarios Agrupados at behalf of the European Space Agency, is a system simulation tool with high flexibility. The ESPSS library allows designing and simulating many different rocket propulsion systems, like pressurized systems, turbo-pump fed cycles with a gas generator or an expander up to air-breathing hybrid rocket engines. In order to have the toolset for analyzing and optimizing a complete space mission, it is of high interest, to allow trajectory optimization in a loop with the simulation and optimization of a propulsion system. For this, an interface between the trajectory optimization software ASTOS and the propulsion cycle simulation tool ESPSS is created. A special focus hereby is put on hybrid propulsion. Firstly, hybrid propulsion offers new opportunities in the near future, while secondly understanding of processes in hybrid rockets advances at high speed. The vast amount of possible propellant combinations is very promising for the future design of high performance rocket engines, which are environmental friendly too. Hybrid rocket engines inherit a very dynamic performance from the basic architecture of their working principle: During the burning time, solid fuel burning inside the combustion chamber regresses and changes thereby the inner geometry of the engine. Hence, it is essential to have the toolset to simulate and optimize these dynamic engine processes with regard to the trajectory, in order to find not only the best design for the engine itself, but also for the entirety of vehicle and mission design. The ESPSS model of the regression rate of hybrid rocket engine fuel is improved and expanded. Existing regression rate laws are evaluated. New advanced regression rate laws for both classical and liquefying hybrid rocket fuels, which are considered state of the art in literature, are implemented in ESPSS. This further improves the possibilities to use the tool for predesign and design of hybrid rocket engines and propulsion systems. Chapter 3 elaborates on hybrid rocket engines while Chapter 4 explains the software tools created for this work and presents the verification of the software tools.

A experimental test campaign at the DLR Lampoldshausen has been conducted to support this thesis with experimental data. A new hybrid rocket engine demonstrator has been designed, constructed, built and tested at the test bench M11. The engine was specifically designed to offer a longer burn duration than previously tested engines, where the maximum burn duration

was about 20 seconds. The newly designed engine burns up to one minute or longer, depending on the throttle setting. First tests were done to analyze the regression rate behavior of the new chamber design, as well as testing the heat loads on the combustion chamber parts. It was also tested if throttling of the engine changes the combustion roughness of this experimental set-up. A comparison of simulation results with experimental results was done as well, to see if the simulation models are adequately capable of modeling test benches and propulsion systems. To compare the simulation with test results, first tests of the test campaign for this work have been used. Other publications include comparisons of other engine test results, also focusing on the tank simulation of ESPSS [2]. The experiment set-up and results are depicted in Chapter 5.

A mission to the Moon's surface is defined and evaluated. The baseline is a launch with the Ariane 5 launch vehicle. However, the created models are scalable to any launch vehicle in the same range of payload mass. The launch vehicle trajectory is optimized to bring the largest possible spacecraft in a hyperbolic Moon flyby trajectory. The mission objective is a soft lunar landing with enough payload capacity to include a small rover, instrumentation and a sample return rocket. A typical descent trajectory is defined, including a hovering phase to find a suitable landing spot. The return rocket is then supposed to be loaded with lunar soil samples that will be brought back to the Earth's surface after ascending from the Moon and returning in a reentry capsule to the Earth. Six variants of the spacecraft set-up are compared using hybrid propulsion, as well as one spacecraft using only storable liquid propulsion and one spacecraft using cryogenic propellants for the first part of the mission. The short flight duration to the Moon allows the use of cryogenic propellants, as it is possible to cool them with boil-off and the losses can be compensated by the higher specific impulse. The hybrid propulsion variants are using either hydrogen peroxide or cryogenic liquid oxygen as the oxidizer. Propellant for the use in reaction control thrusters is considered too. The returning spacecraft (referred to as "return rocket" in the following) is always modeled using storable propellants. For the spacecraft variants using hybrid propulsion, three staging concepts are evaluated: A three staged lander concept, a two staged lander and a two staged lander with jettisoning of emptied hybrid combustion chambers. The total sample return mass to Earth is taken as a measurement to compare the concepts with each other. However, the analysis is focused mainly on the performance of the spacecraft. While it is expected that liquid propulsion systems with similar or better specific impulse than hybrid propulsion systems have a higher performance, it is also necessary to take into account, that hybrid rocket propulsion systems are safer, cheaper to develop and use propellants that are not hazardous. The sample return mission analysis is presented in Chapter 6.

2. Sample Return Missions to the Moon

2.1. Orbit Mechanics of Space Flight to the Moon

With the use of chemical propulsion in impulsive maneuvers (i.e. short burning time, high thrust) the orbits of a spacecraft with destination Moon are altered quickly in a short time. In contrast, transfers to the Moon with electric propulsion have very long thrusting phases with very low accelerations. This generally increases the ΔV requirements, which is compensated by the extremely high specific impulse of electric propulsion. Transfers with chemical propulsion usually take 2.5 to 5 days whereas a transfer with electric propulsion takes up weeks or months. Up to date the landing on the Moon's surface is always requiring the high thrust of chemical propulsion. Change of orbit parameters is done with a change of velocity and/or velocity direction at a certain orbit point. The velocity change Δv is calculated by adding the velocities vectorially:

$$\Delta v = \sqrt{v_1 + v_2 + 2v_1 v_2 \cos \alpha \cos \beta}, \tag{2.1}$$

where v_1 and v_2 are the velocities before and after the maneuver. Here α is the change of inclination and β is the change of the velocity direction in the orbit plane. During a flight to the Moon both the force introduced by the Earth's and the Moon's gravity have a big impact on the spacecraft's dynamics. Therefore the transfers from the Earth to the Moon and backwards have to be calculated as a three-body problem. The dynamics are described by the following differential equations where x, y, z are the spacecraft's coordinates in a coordinate system with the Moon's orbit spanning the x-y plane [1]:

$$\ddot{x} = -\frac{\mu_E x}{r^3} + \frac{\mu_M}{\rho^3} (x_M - x) - \frac{\mu_M x_M}{a_M^3} \tag{2.2}$$

$$\ddot{y} = -\frac{\mu_E y}{r^3} + \frac{\mu_M}{\rho^3} (y_M - y) - \frac{\mu_M y_M}{a_M^3} \tag{2.3}$$

$$\ddot{z} = -\frac{\mu_E z}{r^3} - \frac{\mu_M z}{\rho^3} \tag{2.4}$$

In these equations, μ_E and μ_M are the gravitational parameters of the Earth and the Moon. r and ρ describe the distance of the spacecraft to the centers of the Earth and the Moon. x_M and y_M give the coordinates of the Moon's center. The semi-major axis of the Moon is given as a_M. As found by many missions to the Moon's orbit and surface, the gravitational field of the Moon has high local deviations, which have a crucial impact especially on low altitude orbits. Also perturbations by the Sun's gravity and solar radiation pressure can be considered for more detailed analyses. Figure A.2 shows the gravity of the Moon mapped by the GRAIL mission.

From the GRAIL data a detailed gravitational field model with spherical harmonics could be created by Konopliv et al [3]. This model can be used for more detailed analysis of Moon missions' trajectories, but for this work a simplified homogeneous gravity model is used.

2.1.1. The Moon

The Earth and the Moon form a double planet system and both orbit around the barycenter, which lies some 4700 km from the Earth's center. The rotation of the system has a length of 27.3 days. The Moon's semi-major axis is 384 748 km, it has an eccentricity of 0.055 and an inclination of 5.1° in reference to the ecliptic. The Moon's orbital plane has a precession with a periodic duration of 18.6 years, which results in an inclination in the Earth's equatorial system of 18.3° to 28.3°. A co-planar transfer without additional plane change maneuvers is always possible from a launch place below 18.3° latitude. Of course, if a transfer is done during a time when the inclination is near 18.3°, the ΔV from the Earth to the Moon is a bit smaller. The Moon has a diameter of 1737.1 km (mean) and a gravitational parameter only $1/80$ of the Earth's ($\mu_E = 3.986\mathrm{e}14\,\mathrm{m^3/s^2}$; $\mu_M = 4.904\mathrm{e}12\,\mathrm{m^3/s^2}$). The gravity acceleration on the surface of the Moon is $1.625\,\mathrm{m/s^2}$ [4].

2.1.2. Transfer Orbits to the Moon

Often a Low Earth Orbit (LEO) is chosen as a starting point for a Moon transfer, since this allows for easy corrections of mistakes of the spacecraft's orbit insertion with a launcher. Under certain circumstances a direct transfer can be favorable, e.g. if the launcher's configuration is more suited for this or if re-ignition of the upper stage is not possible. The orbit insertion into the transfer orbit can result in a hyperbolic, parabolic or elliptic transfer orbit (with reference to the Earth). Hyperbolic orbits result in a shorter transfer time (2.5 days), but in higher ΔV requirements at both orbit insertion and Moon orbit injection. A special hyperbolic transfer orbit is the free return trajectory, which guarantees a return of the spacecraft to the Earth after orbiting around the Moon without additional impulsive maneuvers (except of possible necessary course corrections). Free return trajectories are a safe choice for manned mission. Elliptical transfer orbits (Hohmann-Transfer) have the lowest ΔV budget but the longest transfer times (with chemical propulsion maneuvers) of about 5 days. The best timing for a transfer to the Moon is when the ascending node of the spacecraft and the Moon have an angle of 0° or 180°. If a spacecraft is launched directly without parking orbit in LEO, the best launch window is while the Moon is passing the equatorial plane (i.e. the ascending or descending node in the equatorial reference system). This happens every 13.7 days [5].

2.1.3. Moon Orbit Injection and Landing

In order to bring a spacecraft into a stable orbit around the Moon, an injection burn has to be done after the orbit transfer is finished. Optimally this injection burn is done at the wanted periselen at the Moon. Both elliptical and circular orbits can be chosen depending on the planned mission. By entering a polar orbit around the Moon and adjusting the periodic duration of the orbit (by optimizing eccentricity for a given periselen) almost every landing spot on the Moon can be reached within a few days. Theoretically, the periselen can be chosen between 10 and 20 km, because there is no atmospheric drag and this allows for low ΔV landings. Yet, the Moon's heterogeneous gravity field can cause high disturbances of the orbit at such low altitudes, therefore usually an orbit at 100 km to 200 km altitude will be chosen, with only small losses in ΔV for the landing. When initiating a landing the periselen is chosen to be above the landing site at low altitude. The lower the periselen, the lower is the total ΔV. However, at the same time the sensitiveness to course deviations is higher. The periselen can even be below the surface, resulting in a direct descent from the elliptic/circular orbit. Table 2.1 shows an overview of approximated ΔV requirements from low Earth orbit to the Moon and back.

2.1.4. Return Trajectory

For the return trajectory, the spacecraft can be launched from the Moon's surface either in an intermediate orbit or directly into a hyperbolic escape orbit, which has a low perigee (in or below the atmosphere of the Earth). Usually a flat reentry angle at the Earth's atmosphere is better, since it has lower maximum heat and mechanical loads. To reduce gravitational loss the launch trajectory on the Moon should be as flat as possible, turning the vehicle from a vertical into a horizontal orientation very quickly. The escape trajectory from the Moon is orientated against the Moon's velocity vector. With an optimal transfer orbit, the spacecraft needs again about five days to the Earth and reenters the atmosphere with about 11 km/s. Figure 2.1 illustrates the sequence of a possible sample return mission.

Table 2.1.: ΔV [$\frac{m}{s}$] requirements to the Moon from [1]

Maneuver	Intermediate orbit	Direct transfers
Injection into a transfer orbit to the Moon	3200	3200
Course correction	100	160
Injection into a Moon orbit	1000	0
Moon landing	2100	3000
Launch into a Moon orbit	2000	0
Injection into a transfer orbit to the Earth	1000	2900
Total	9400	9260

1. Launch at GSC
2. Possible parking orbit
3. Moon transfer injection
4. Coast to Moon
5. Trajectory course correction
6. Moon orbit insertion
7. Moon orbit
8. Phasing orbits (optional)
9. Deorbit and Landing
10. Ground operations
11. Return rocket launch
12. Return trajectory
13. Jettisoning of rocket stage and reentry of capsule
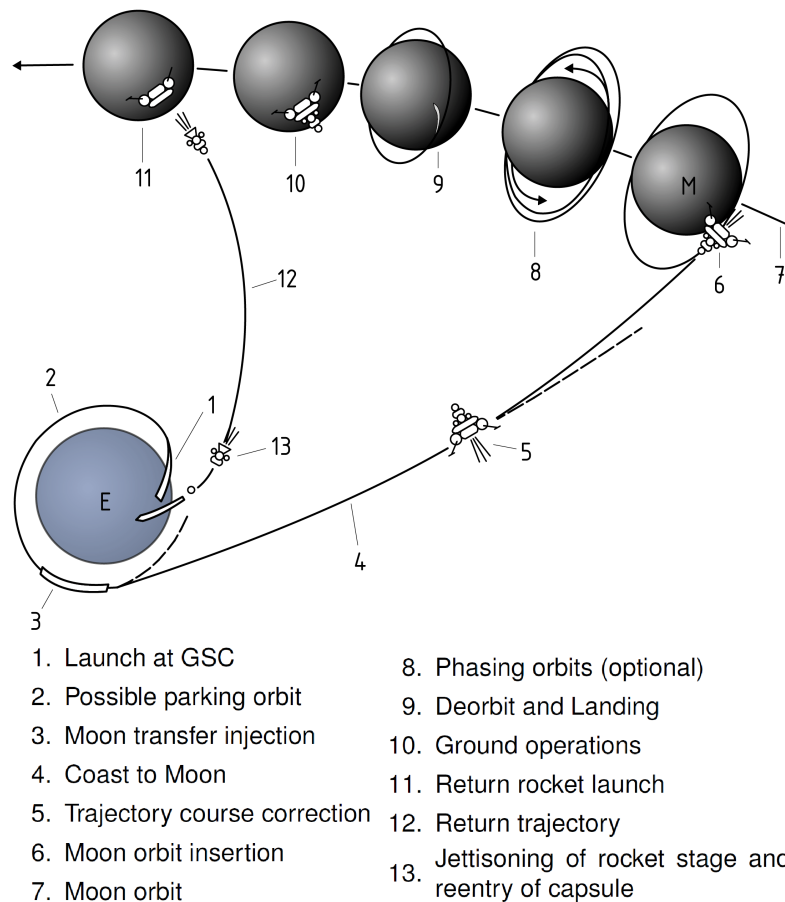
Figure 2.1.: Exemplary mission profile for a Lunar sample return, [1]

2.2. Historic Missions

The first lunar crash landing with an unmanned probe was conducted in 1959 by the Soviet Union with Luna 2, after Luna 1 had failed earlier in the same year. In the following years, several robotic landing missions to the Moon were initiated by the United States and the Soviet Union, resulting finally in the landing of the first men on the Moon on 20th July 1969. An overview of all Soviet lunar landings from Luna-2 in 1959 to Luna 24 in 1976 is given in Table A.1. The Soviet Union launched many more probes to the Moon, but only named them Luna with a number after a successful launch into Earth's orbit, in order to hide the failed launch attempts with the Semyorka launcher until 1966 and the Proton-K for later launches. Therefore the table shows only successfully launched missions. There are ten missions on Semyorka and four missions on Proton unaccounted for. A total of eight successful robotic soft landings were conducted with the Luna missions. According to the ASA online archive [6], all spacecraft since Luna 15 used resembling propulsion systems based on a very similar spacecraft design. Earlier spacecraft based on the Ye-6 series used amine-based fuel and nitric acid as oxidizer with the engine KTDU-5A. It had a turbopump-fed engine and surface tension propellant management

devices in the tank [7]. Since Luna 15 the lander series Ye-8-5 (also E-8-5) was used for the sample return missions. The engine setup of Ye-8-5 is described in section 2.2.2. The lander Ye-8 for the Lunokhod rovers was similar, using the same pump-fed engine KTDU-417.

Table A.2 lists all lunar landing missions of the US until Apollo 17. As an example, Apollo 11 is explained in more detail regarding the trajectory and propulsion system in section 2.2.2. The first Moon missions of the Ranger program had only a hydrazine (N_2H_4) monopropellant system and a solid retro rocket. The Surveyor landers had a bipropellant engine with monomethyl hydrazine monohydrate (MMH with water) and MON-10 (90 % N_2O_4 and 10 % nitric oxide), which ignites hypergolically. The engine was pressure-fed with helium pressurization and bladders in the tank for zero-g conditions. For the greater part of the ΔV requirements they also used solid retro rockets [8]. Some of the most important missions to Moon in the recent years are listed in Tables A.3 and A.4. In 1990 Hiten was the first Japanese lunar probe. It was also the first lunar probe since Luna 24, as well as the first lunar probe launched by a different nation than USA and USSR. The probe conducted several gravity assist maneuvers and aero brake maneuvers in Earth and Moon orbit. Its scientific goal was detecting and measuring micro-meteorite particles. After an orbital maneuver failed, NASA JPL helped IASA to conduct the first low energy transfer to Moon Orbit, by using very low ΔV to enter the orbit. This was done by a transfer through Moon-Earth-System Lagrange points. A controlled impact on the Moon's surface was done on 10th April 1993. Many other orbiters and impactors followed, as listed in the table. Before 2000, three more orbiter missions to the Moon were done. All of them used hydrazine as a monopropellant for their attitude and orbit control. Clementine also had a N_2O_4 & hydrazine bipropellant liquid rocket engine for orbit maneuvers. However, it failed its primary objective of meeting with asteroid Geographos.

A new approach of lunar missions was undertaken with SMART-1 in 2004 by the European Space Agency. Its main objective was the technology demonstration of an ion drive to bring the spacecraft into a Moon orbit. It used a Hall-effect thruster with a thrust of 70 mN using xenon. It had a specific impulse of 1600 s. After the launch on Ariane 5 as a secondary payload into Geostationary Transfer Orbit (GTO), the orbit was raised over 14 months to use also three lunar resonance maneuvers to minimize propellant use. During a resonance maneuver the spacecraft gets so close to the Moon that the Moon's gravity has a significant impact on the spacecraft's orbit around the Earth. SMART-1 did not leave the sphere of influence of Earth during these encounters however the orbital parameters like inclination, apogee and perigee could be drastically changed without spending propellant. When SMART-1 arrived at Moon orbit, the ion thruster was again fired for 4.5 days to lower the orbit. The ion engine went through 5000 hours of operation and 843 starts and stops. After its extended mission duration SMART-1 was used as an impactor in September 2006. In the following years many orbiter and impactors were sent to the Moon. The scientific goals were always to improve the understanding of Moon's environment by analyzing the surface, the magnet field, the gravitational field and radiation. Table 2.2 counts all landings on the Moon so far while Table A.5 sums up the planned lander missions in the coming years.

Table 2.2.: Summary of landed spacecraft on the Moon

Nation	Crash Impact	Lander	Rover	Sample Return
USSR	6	6	2	3
USA	9	6	3 (manned)	6 (manned)
Japan	2	0	0	0
ESA	1	0	0	0
China	1	1	1	0
India	1	0	0	0
Total	20	13	6	9

Beside to ESA and SMART-1, the Chinese Space Agency (CNSA) conducted several technology demonstrator missions. Chang'e 1 and Chang'e 2 were orbiters to demonstrate China's ability to send spacecraft to the Moon. These missions tested the technology for China's first lunar landing mission Chang'e 3 in 2013, which brought also a rover to the Moon's surface and was the first lunar landing since Luna 24 in 1976. The future Chang'e 5 mission is planned to be the next lunar sample return mission. It will be an unmanned landing spacecraft which is expected to land on the Moon in 2019. The Chinese launcher Long March 5 will be used as a launching vehicle which has a total lift off mass up to 810 tons (CZ-504 [9]). However, it is not clear yet which launcher setup will be used. The spacecraft itself will be composed of an orbiter module, a lander and a return rocket module. The return rocket module is planned to rendezvous and dock with the orbiter after ascent from the Moon's surface. This would be the first docking of an automated spacecraft which landed before on a celestial body. One reason for this approach is that the technology for future manned Chinese missions shall be demonstrated. Until now only two space programs included successful sample return from Moon's surface, namely the manned Apollo 11-12 & 14-17 (US) and the robotic Luna 16, 20 & 24 (USSR). Figure A.3 shows an overview over all historic and planned lunar missions (including orbiters and flyby missions). The x-axis is the launch date and the y-axis represents a logarithmic view of the launch mass ranging from 100 kg to the 30 t of Apollo. Figure A.1 shows the historical landing sites on the Moon's surface.

2.2.1. Scientific Gains of Sample Return

The interest in the Moon is reasoned with a lot of possibilities to research the past of our solar system and especially the genesis of planets. A lot of clues about Earth's development can be taken from analyzing the structure of the Moon's surface. Erosion is absent on the Moon's surface. Hence, some surface areas of the Moon are older than three billion years. By investigating these old soils, the history of the Moon's and Earth's genesis and evolution can be reconstructed. Additionally, the Moon is considered a model for all terrestrial, rocky planets. By researching the surface of the Moon it will be possible to use that knowledge to analyze other planet's surface better remotely. Beside the Moon regolith, meteorite material and cosmic

dust on the surface give insights in the development of the solar system. The Moon also offers possibilities for technology demonstration of robotic missions, sample return missions, manned missions and in-situ resource utilization (ISRU). All of those are useful later when landing on other planets like Mars. The majority of the Moon's surface regions like craters and plateaus are unexplored. More data about the surface composition needs to be gathered in order to choose the right landing spots for future manned science or ISRU missions. The age determination of the Moon's surface is done remotely by investigating the density of craters. For this, more surface samples are necessary to calibrate the methods, which will increase the precision of remote observations. Similarly this also improves the precision for observations of other celestial bodies, when the Moon's surface is taken as reference. An interesting landing area for a sample return mission is the South Pole–Aitken basin, which is an enormous impact crater on the far side of the Moon with a diameter of 2500 km. It is expected from results of impact simulations and cartography results of Clementine and Lunar Prospector that in the basin mantle rock is on the surface. Additionally, due to the high basin wall mountain range, there are areas where the sun never shines. Water ice could be located in these areas. The main advantage of sample return is that not only many more instruments can be used in laboratories on the Earth than on a lander which is limited in mass and energy, but also that the experience of researchers helps a lot to improve the gained results. The instruments that are used on a spacecraft are also less diverse and advanced than stationary instruments on the Earth. Additionally with samples on the Earth, they can be analyzed in the future, when improved instruments are available. Sample return missions are also very interesting for different celestial bodies like Mars or Jupiter's moon Europa being two of the most interesting targets in the search for evidence of extraterrestrial life. A sample return mission to the Moon is also a technology demonstration for a future mission to Mars or Europa in search for life.

2.2.2. Propulsion System

Apollo Program

The Apollo program was launched with the strongest launching system ever developed, even up to date. From 1969 to 1972, six Apollo Lander Modules landed on the Moon and returned successfully to the Earth. Figure A.4 shows an illustration of the lunar lander. The dedicated launcher Saturn V was able to launch 47 t into a Moon transfer orbit. The spacecraft consisted of a command/service module (CSM) and the Lunar Module. The CSM offered space for three astronauts. The launch vehicle Saturn V itself was built of the first stage S-IC, the second stage S-II and the third stage S-IVB. Very detailed information about all Apollo missions is found in the book "Apollo by the numbers" by Richard W. Orloff [10]. A short overview of the data for Apollo 11 spacecraft is given in Table 2.3. The sample return was realized with a docking of the LM with the CSM after launch from the Moon, which was a necessity due to the manned nature of the mission. Due to the high requirements for all systems, since Apollo was a manned program, it is not possible to compare the Apollo missions directly with small

robotic missions for sample return. Yet, the Apollo missions give a great example for what is possible within the Earth-Moon system. Some parameters like the engine data are very helpful to design future landing missions on the Moon's surface. The AJ10-137 rocket engine of the CSM used the hypergolic propellant combination of N_2O_4 and Aerozine A-50. The engine AJ10-137 was operated at relatively low pressure of 7 to 9 bar with a pressure-fed cycle [11]. Aerozine A-50 is a mixture of 50 % UDMH and hydrazine, which is chemically more stable than pure hydrazine and has a higher density and boiling point than pure UDMH [12]. It is highly toxic and carcinogenic. In addition, the oxidizer N_2O_4 is toxic and environmentally harmful, too. This is why currently a lot of effort is put in finding substitute substances for N_2O_4 and hydrazine based fuels in space propulsion. In Europe this is accelerated by REACH [13]. The Lunar Module Descent Engine (LMDE) or Descent Propulsion System (DPS) was a variable throttle hypergolic rocket engine, based on the same propellants as the AJ10-137. It could be throttled down to 10 % of the full thrust [14], which is of high advantage for a soft landing and high maneuverability near ground. The high throttle ability was realized with a pintle injector, whose flow area could be adjusted. The pressure-fed engine had a pressure of about 7.1 bar and a thrust of 4.5 to 43.8 kN. The Lunar Module Ascent Engine (LMAE) or Ascent Propulsion System (APS) was a smaller engine, similar to LMDE using the same propellants and being pressure fed.

Luna Program

The Soviet robotic Moon probes of the Luna program were launched with the three-stage launch vehicle Proton-K with a total payload into Moon transfer orbit of 5.7 t. This launcher set-up used the Blok-D as upper stage. Luna 16 was launched in 1970, Luna 20 in 1972 and Luna 24 in 1976, being the last sample return vehicle from the Moon ever since. Table 2.4

Table 2.3.: Propulsion system parameters of Apollo 11

Parameter	S-IVB	CSM	LM-Landing	LM-Ascent
Mass (total) [kg]	119119	30329	10281	4495
Dry mass [kg]	30329	11900	2033	2179
Engine	J-2	AJ10-137	LMDE[1]	LMAE[2]
Engine cycle	Gas generator	pressure-fed	pressure-fed	pressure-fed
Propellants	LOX/LH2	N_2O_4/A-50	N_2O_4/A-50	N_2O_4/A-50
Engine mass [kg]	1579	295	179	82
Vacuum thrust [kN]	1023	91.2	4.5-43.8	15.6
I_{vac} [s]	421	312	311	311
Burn duration [s]	475	585	n/a	n/a
Chamber pressure [bar]	49.9	6.7	7.1	8.3
Expansion ratio	27.5	62.5	46	45.6

[1] Lunar Module Descent Engine
[2] Lunar Module Ascent Engine

summarizes the propulsion system data of Luna 16. The KTDU main engine on the Ye-8-5 series' spacecraft was designed with two autonomous blocks. The main block was used with high-pressure combustion for orbit changes and bigger course corrections. The engine cycle was a turbo-pump fed engine setup. Due to its hypergolic propellant's combination, it could be reignited up to 11 times in nominal mission design. The low-pressure combustion chambers of KTDU/417B consisted of two combustion chambers with lower thrust for a soft landing. The engine was only throttleable in small range, which sufficed because it was of low thrust and only used for the final descent and not for bigger ΔV maneuvers. Helium was used as pressurizing gas. The sample return vehicles of the Luna program used the toxic and carcinogenic propellants N_2O_4 and UDMH, too. Similarly, the KRD-61 engine of the ascent and return vehicle used the same propellants and had a turbo-pump fed cycle, too. A photo of a mockup of Luna 24 is shown in Figure A.5.

2.2.3. Mission Phases and Trajectory

Apollo Program

The orbit maneuvers and some related information of Apollo 11 are listed in Table A.6 in the appendix. The manned Apollo mission had some particularities that are not necessarily practical for an unmanned mission. For example the spacecraft was very heavy, which won't be necessary for an unmanned mission. Apollo's third stage was ignited at least twice. The first burn inserted the spacecraft in an orbit, while the second burn brought the spacecraft into the trans-lunar trajectory. Arriving at the Moon the Control/Service module (CSM) conducted the orbit insertion with two burns (orbit insertion and circularization). Afterwards the Lunar Module (LM) undocked and did a descent burn with the Descent Propulsion System. The

Table 2.4.: Propulsion system parameters of Luna 16

Parameter	Blok-D	Ye-8-5	Landing	Ascent
Mass (total) [kg]	13360	5725	s. Ye-8-5	512
Dry mass [kg]	11273	1880	s. Ye-8-5	245
Engine	RD-58	KTDU-417	KTDU-417B	KRD-61
Engine cycle	staged comb.	open cycle [15]	pressure.-fed	open cycle[16]
Propellants	LOX/RP2	N_2O_4/UDMH	N_2O_4/UDMH	N_2O_4/UDMH
Engine mass [kg]	300	81	s. Ye-8-5	42
Vacuum thrust [kN]	83.4	7.35-18.92	2.06-3.43	19.1
I_{vac} [s]	349	308-314	252-254	313
Burn duration [s]	600	650	30	30
Chamber press. [bar]	78	82	8.9	91
Expansion ratio	189	n/a	n/a	n/a

LM descended the last kilometers with a powered descent using the deep-throttling ability of the Descent Propulsion System. The Ascent Propulsion System lifted the LM again in Moon orbit and preparing Rendezvous and Docking by several burn maneuvers. Leaving the Ascent module in the Moon orbit, the CSM started the trans-earth injection. One mid-course correction was necessary before the CM and SM could separate close to the Earth and the Astronauts returned to the ground.

Luna Program

The Luna 16 spacecraft landed on the Moon's surface by ignition of its engine KTDU-417 in the periselen. After a burning time of 263 s the engine was shut down at an altitude of 2.45 km. This was followed by a 43 s unpropelled coast. At 600 m altitude, the engine was reignited and run with throttled thrust. After the descent to 20 m, the main engine was shut off and the low-pressure combustion chambers of KTDU-417B were ignited. The 1880 kg heavy lander touched ground with 4.8 m/s. The lander was also the launch pad of the return rocket, which was a 2 m tall open structure including the capsule with a control system, three spheric propellant tanks and a non-throttleable rocket engine KRD-61. Four RCS thrusters were used to control the attitude. After a burn of 53 s the rocket reached the necessary velocity of 2700 m/s to reach the Moon escape and Earth reentry trajectory. Reentry into Earth's atmosphere was done with the 35 kg heavy reentry capsule after 84 h from lift-off at the Moon. Reentry happened with a velocity of 10 950 m/s [1].

Deep-throttling

Deep-throttling is an important feature of descent engines for a soft lunar landing. The Apollo descent engine LMDE was throttleable down to nearly 10 % of its maximum thrust. The descent engine of Luna KTDU-417 was only throttleable to about 40 %. However, it had a second engine unit KTDU-417B which was used for the final descent and had much lower thrust level than the main engine. Throttling the engine has several purposes:

- Following optimized thrust profiles during boost phases of trajectories

- Decreasing maximum loads when propellant mass is reducing

- Rendezvous in orbit

- Versatility: High ΔV and fine trajectory control burns; this saves also engine mass, since one engine fills several roles

- Descent on planets; multi-purpose use of single engine

  - Hovering for landing site selection

  - Obstacle evasion

  - Soft landing

  - Landing abort

Betts and Frederick [17] state, that for liquid rocket engines throttling to 25 % usually is easily achievable without putting a lot of effort in valve and injector design. However, at even lower pressures, so called deep-throttling, the pressure drop over the injector becomes very small. This affects propellant vaporization and mixing. These problems are mitigated by using high pressure drop injectors, actuated injectors (e.g. pintle-injector) or gaseous injection (where the oxidizer is vaporized before passing the injection). Also chamber cooling is an issue with low mass flow. Control valves need to have high precision with low mass flow rates. Turbo-pumps, gas generators, pre-burners or heat-exchangers need a wide range of performance in order to support throttling.

3. Theory of Hybrid Rocket Engines

3.1. Hybrid Rocket Engine Layout

The principle of hybrid rocket engines is to use solid fuels and liquid oxidizers. In some rare set-ups, this is inversed and the oxidizer is solid and burnt with liquid fuel, but these cases shall be neglected within this work. The liquid oxidizer is stored in a tank, while the solid fuel is stored inside the combustion chamber as illustrated in Figure 3.1. The oxidizer will be injected into the combustion chamber and the combustion will be ignited. The oxidizer flows along the solid fuel surfaces, which consequently regresses and adds fuel mass flow to the combustion process. At the end of the solid fuel, there is an optional post combustion chamber and then the combustion gases are expanded through a nozzle. The liquid oxidizer is either pressure-fed or pump-fed. The pressure feeding is either realized by a pressurization system or by using a self-pressurizing liquid (e.g. nitrous oxide). This is suitable for sounding rocket and spacecraft applications. For some high power applications like launch vehicle boosters, turbo-pumps are conceivable to feed the oxidizer into the combustion chamber. Recent studies also indicate that electric pumps might reduce the gross lift off mass of hybrid rocket propulsion systems, as no heavy pressurization tank is needed [18]. Even if the lift off mass is not reduced by an electric pump, it could also reduce the rocket length, if this is a critical design parameter. A detailed description of the history and development of hybrid rocket engines is found in [19]. Hybrid rocket engines sometimes are even seen as the fail-safe space transportation option, which could raise the safety and reliability of launchers and spacecraft up to the levels of civil aviation aircrafts [20].
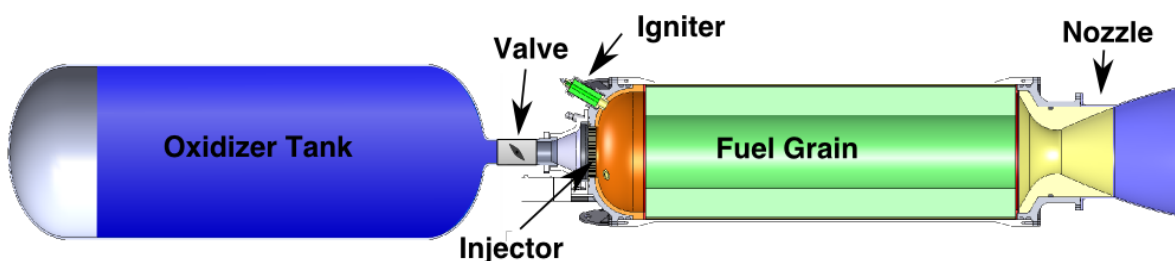
Figure 3.1.: Hybrid rocket engine layout,[21]

3.2. Hybrid Rocket Liquid Oxidizers

In principle, every liquid oxidizer is usable with hybrid rocket engines. The aim of hybrid rocket engines is to surpass the low energetic solid rocket motors. Therefore, in most cases oxidizers are chosen which offer high energetic combustion:

- Liquid, cryogenic oxygen LOX

    – gaseous oxygen GOX is also used for laboratory scale engines

- Hydrogen peroxide H_2O_2 with high concentration ("High test peroxide", HTP) from 85 % to 98 % with the rest of the liquid being water and stabilizers

- Nitrous oxide N_2O

Liquid oxygen of course offers the highest specific impulse, yet its cryogenic storability makes it less attractive for some applications (e.g. long-time storable rocket engines). Hydrogen peroxide has a lower maximum specific impulse than liquid oxygen, but it is longer storable, although it also has a slow, natural decay into water and oxygen. With stabilizers the storability can be years with only little degradation. An advantage of hydrogen peroxide is that it is ignited when passing a catalyst bed. This means that hybrid rocket engines with hydrogen peroxide do not need a pyrotechnical or electrical igniter. Hydrogen oxide is caustic and needs higher safety measurements during operations and storage as it can start a highly exothermic decomposition process. A little less problematic than H_2O_2 is nitrous oxide. Stored under high pressure (~50 bar), nitrous oxide is liquid at room temperature. Yet, it is not toxic or caustic, which makes it favorable for low cost operations. Table 3.1 lists the most used oxidizers and their characteristics. In general, also other storable oxidizers like dinitrogen tetroxide N_2O_4 are possible as oxidizers and can improve the performance of storable hybrid rocket engines. However, since hybrid rocket engines are investigated as an alternative to storable liquid propellants like hydrazine and dinitrogen tetroxide, the advantage of having "green" oxidizers is predominant. It reduces operation costs during the development of rocket engines and during ground operations on the launch site by a high amount. The impact on the environment is also reduced. However, for certain in-space applications, none of the above mentioned "green" oxidizers can be used. A recent design study by NASA JPL for a Mars ascent vehicle for a sample return vehicle suggests a hybrid rocket engine using paraffin-based fuel "SP7" and Mixed Oxides of Nitrogen (MON30) as oxidizer [18]. According to the study, the advantage of MON30 is that it has a very low melting temperature and is usable as a liquid oxidizer down to −71 °C. This simplifies the thermal management while landed on the planet Mars significantly. Also the paraffin-based fuel SP7 was specifically designed to withstand cold temperatures on Mars' surface. MON30 is a mixture of 70 % N_2O_4 and 30 % NO. Of course this oxidizer increases operations costs and test campaign costs. However, it extends the feasibility of hybrid rocket engines for a very broad area of environmental conditions of in-space applications. Some even more advanced ideas include also air-breathing hybrid (rocket) engines for the use in Earth's atmosphere [22].

Table 3.1.: Propellant options for hybrid rocket engines, [23]

Oxidizers	Advantages & disadvantages
Liquid Oxygen	+ highest possible specific impulse - cryogenic - medium density (1140 kg/m^3) - optimal mixture ratio 2.5-3 (long fuel grains)
Hydrogen Peroxide	+ storable at standard conditions + highest density (>1400 kg/m^3) + usable as monopropellant + (re-)ignition with catalyst + optimal mixture ratio 7-9 (short fuel grains) - caustic - (slow) natural decomposition - lower specific impulse
Nitrous Oxide	+ self-pressurizing + usable as monopropellant + (re-)ignition with catalyst + optimal mixture ratio 7-9 (short fuel grains) - lowest density (<900 kg/m^3) - high storing pressure (~50 bar) - lower specific impulse
MON30 (70 % N_2O_4, 30 % NO)	+ operation temperature down to −71 °C + high density (1300-1500 kg/m^3[24]) + optimal mixture ratio 4-5 - toxic, carcinogenic - lower specific impulse
Fuels	**Advantages & disadvantages**
HTPB	+ high mechanical resistance + well processable with machines + density (~930 kg/m^3) + well mixable with additives - very slow regression rate
pure paraffin wax	+ very high regression rate + density (~900 kg/m^3) - low mechanical resistance - less mixable with additives (sedimentation)
Paraffin-based fuels	+ high regression rate + density (~900-930 kg/m^3) (+) higher mechanical resistance due to polymeric additives (+) quite mixable with additives (little sedimentation)

3.3. Hybrid Rocket Fuels

The amount of propellant combinations of hybrid rockets exceeds the one of solid rocket engines. This is mainly because of the huge number of possible fuels. There are many possibilities to compose fuel grains for hybrid rocket engines. Starting with wood, which was tested in some of the first rocket engines [19], over pure polymeric fuels, to fuel blends with metallic and other energetic additives, there is a broad spectrum of fuel combinations. The most common hybrid rocket fuels are polymeric fuels, either pure or with the addition of energetic materials to improve burning rates and exhaust velocity. The most common polymeric fuels in hybrid rocket engines technology are the ones based on butadiene. The most popular one with high availability and low cost is hydroxyl-terminated polybutadiene (HTPB). A new class of solid fuels for hybrid rocket engines is liquefying fuel. This was first identified as a possible game changer by Karabeyoglu et al. [25, 26]. At the DLR Lampoldshausen liquefying fuels are studied for many years [27, 28, 29]. While the first liquefying fuels where frozen gases or liquids, in order to provide maximum exhaust velocities to hybrid rockets, the cost for cryogenic combustion chambers was much too high. By now the paraffin-based fuels found their way into hybrid rocket engines, offering a similar exhaust velocity like polymers. Due to the liquid melt layer, which they form on the burning surface, their mass flow to the combustion zone is much higher than that of polymeric fuels, which enables a more compact and versatile engine design. Especially where there is the demand for high thrust and shorter burn durations, like in boosters and sounding rockets, liquefying fuels have a high advantage over classical hybrid rocket fuels. While pure paraffin offers the highest regression rate (up to factor 6 compared to HTPB), it has a very low mechanical strength. Therefore, advanced paraffin-based fuels have been developed. Paraffin can easily be mixed with polymers up to a certain concentration. Adding more polymers increases the mechanical strength, but reduces the regression rate [30, 31]. The regression rate reduces with increasing viscosity of the melt layer. A compromise is found depending on the application. In paraffin-based fuels the mixing of additives like energetic metals is also easier than in pure paraffin, as the high viscosity prohibits the sedimentation during the casting process. Table 3.1 compares the three fuel options. The performance of several propellant combinations is given in Table 3.2, where O/F is the mixture ratio, c^* is the characteristic velocity in the combustion chamber and I_{vac} is the specific impulse in vacuum conditions. The evaluated performance is under the conditions of a chamber pressure $p_{cc} = 15\,\text{bar}$ and an expansion ratio of $\epsilon = 60$. As can be seen, the performance is very similar to liquid carbohydrate fuels like RP-1. It must be noted that the performance calculation for H_2O_2 is done with a pureness of 95 % and the oxidizer is injected as a liquid.

Table 3.3 lists the different hydrogen peroxide combinations with a paraffin-based fuel including 5 % of polymeric additives (PB-5%), taking into account liquid and gaseous injection, as well as two concentrations. The state of matter of the H_2O_2 at injection has a quite high impact. By this, injection of H_2O_2 with a catalyst for the whole oxidizer mass flow should increase the rocket engine's performance, as no energy is needed in the combustion chamber

Table 3.2.: Propellant combinations [23]

Oxidizer	Fuel	O/F_{opt}	$c^*[\frac{m}{s}]$	I_{vac} [s]	ΔI_{vac}
LOX	HTPB	2.4	1725.4	356.3	98.4 %
LOX	HTPB/Al(30 %)	1.5	1727.2	356.4	98.4 %
LOX	PB-5%	2.75	1752.2	361.7	99.9 %
LOX	PB-5%/Al(20 %)	2.05	1757.1	362.1	100.0 %
LOX	RP-1	2.75	1763.6	363.1	100.3 %
H_2O_2	HTPB	6.8	1610.6	326.3	90.1 %
H_2O_2	HTPB/Al(30 %)	5	1618.6	333	92.0 %
H_2O_2	PB-5%	7.6	1621.6	327.5	90.4 %
H_2O_2	PB-5%/Al(20 %)	6.4	1623.6	331.7	91.6 %
N_2O	HTPB	8.2	1565.7	317.1	87.6 %
N_2O	HTPB/Al(30 %)	5.6	1587.4	323.1	89.2 %
N_2O	PB-5%	9.2	1574.7	318.2	87.9 %
N_2O	PB-5%/Al(20 %)	7.4	1584.5	321.8	88.9 %
MON30	HTPB	4.1	1641.50	337.8	93.3 %
MON30	HTPB/Al(30 %)	2.6	1661.60	341.5	94.3 %
MON30	PB-5%	4.7	1652.2	340.9	94.1 %
MON30	PB-5%/Al(20 %)	3.6	1667.60	343.2	94.8 %

Calculation Settings:
$p_{cc} = 15\,\text{bar}, \epsilon = 60$, frozen equilibrium, 95 % H_2O_2 in liquid state

to vaporize the oxidizer. It has to be experimentally validated that this theoretical ideal values, calculated with NASA CEA can be actually reached with an catalyst injection system. It must be also taken into account that behind the catalyst the oxidizer is not pure H_2O_2 anymore. The oxidizer flow is a mixture of gaseous H_2O_2 steam, water steam and gaseous oxygen. This also alters the performance calculation.

Table 3.3.: Hydrogen peroxide combinations with PB-5%

Oxidizer	Conc.	State	O/F_{opt}	$c^*[\frac{m}{s}]$	I_{vac} [s]	ΔI_{vac}
H_2O_2	95 %	liquid	7.6	1621.6	327.5	90.4 %
H_2O_2	87.5 %	liquid	8.3	1579.5	315.4	87.1 %
H_2O_2	95 %	gas	7.3	1723.4	352.9	97.5 %
H_2O_2	87.5 %	gas	8.15	1692.8	344.7	95.2 %

Calculation Settings:
$p_{cc} = 15\,\text{bar}, \epsilon = 60$, frozen equilibrium, ΔI_{vac} compared to LOX PB-5%/Al(20 %)

Figure 3.2 shows the specific impulse over the mixture ratio. It is noteable, that for oxygen the gradients are much higher. This means, that $^O/_F$ shift is of higher impact with oxygen as the oxidizer than with H_2O_2 or N_2O. Several hybrid sounding rockets are currently under development, some of which already use the advantages of liquefying fuels. The student group Hybrid Engine Development (HyEnD) at the University of Stuttgart uses paraffin-based fuels (with N_2O) [2, 32, 33, 34, 35], as well as the Peregrine project at University of Stanford and NASA Ames (with LOX) [36]. The student project Stratos at TU Delft is using N_2O with sorbitol-based liquefying fuel [37]. Commercial projects until now focus on the better-known, better-understood classical hybrid fuels. One European example is Nammo and their sounding rocket project North Star with the combination HTPB and H_2O_2 [38]. Nammo plans using a modular design developed in steps to finally have a hybrid rocket engine based launcher to polar orbits for small payloads. The European Union project HYPROGEO is focused on developing a hybrid rocket engine optimized for space application [39, 40]. In order to reach long burning time, they analyze a front burning hybrid rocket engine. Another project focuses on using hybrid rocket engines for space debris removal or prevention [41]. The Spartan project was aimed to develop an advanced throttling engine for soft planetary landing [42]. NASA JPL is conducting studies for a Mars Ascent Vehicle (MAV) using hybrid rocket propulsion with paraffin-based fuel and MON30. Both the oxidizer and the fuel have been chosen to withstand the extreme temperature changes on the Mars surface [18].
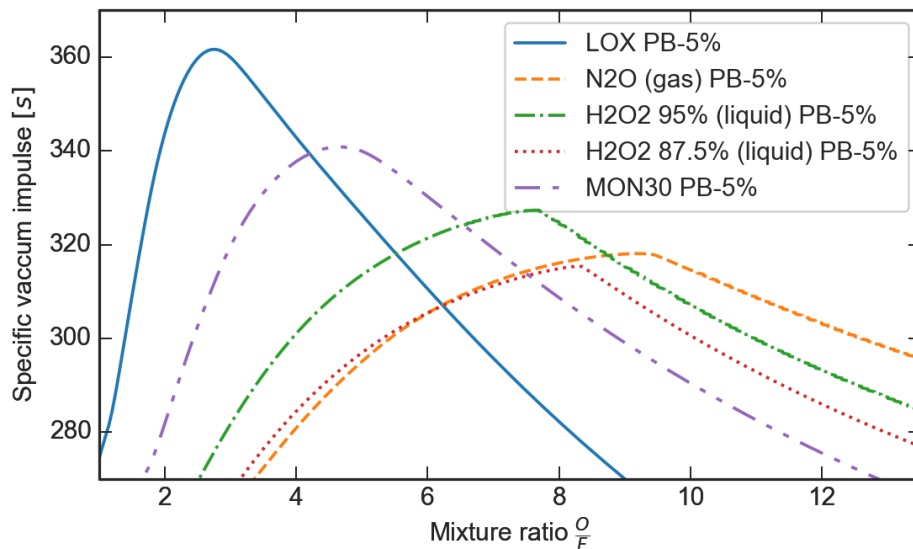
Figure 3.2.: Specific vacuum impulse with PB-5% over mixture ratio

3.4. Hybrid Rocket Engine Components

The oxidizer tank for hybrid rocket engines usually is pressurized to feed the oxidizer into the combustion chamber without pumps. This allows for simple fluid control systems. However, it adds extra mass, as the tanks need to withstand high loads. Especially when used in atmosphere and engine pressure needs to be high, oxidizer tanks become very heavy if they need to withstand high pressure loads. When nitrous oxide is used as an oxidizer, even higher working pressures of up to 60 bar need to be considered. However, with the saving of a pressurization system, nitrous oxide still stays a viable option for small hybrid rocket engines. For larger hybrid rocket engines like in boosters for heavy launch vehicles or in first stages for a hybrid small launcher, it is possible to use turbo pumps for feeding the oxidizer. The same engine cycles like in liquid rocket engines are possible, except that always only one liquid needs to be pumped, reducing the necessary power [43]. This allows compact turbo pumps. Staged combustion cycles with a pre-burner, gas generator cycles or expander cycles are possible. Pre-burners and gas generators are either hybrid rocket engines as well or catalytic monopropellant combustors of H_2O_2. A very important component for hybrid rocket engines is the injector. Since the liquid oxidizer is mixed along the chamber with fuel in the boundary layer, the injection conditions are very different compared to liquid rocket engines. The injector needs to be optimized allowing the best possible mixing of fuel and oxidizer. A fine atomization and fast vaporization of the oxidizer helps the mixing and combustion, which is increasing engine efficiency and reducing engine length. Shower head injectors with small injection holes offer a good atomization and are often used with laboratory scale engines. Bigger engines are often used with swirl injectors and impingement injectors. A very interesting topic is the injection behavior when the fuel geometry changes a lot during burning time. This is especially important with quickly regressing fuels like liquefying fuels and if the engine is designed for a long burning time. Then the difference of flow area in the beginning and end of the burning time is very high. For a similar combustion efficiency during all the burning time, the injection conditions need to be very good in the beginning and in the end of the engine's burn duration. This has to be considered when designing a long burning hybrid rocket engine. Swirl injection helps here to keep the oxidizer close to the solid fuel's surface. For throttleable engines pintle injectors like in deep-throttling liquid rocket engines are an option, given the mixing with the fuel is good. For deep-throttling it is also a possibility to heat the oxidizer before passing the injector, so that a already (partially) vaporized fluid is injected. This increases the pressure drop over the injector also for low mass flows. With N_2O this is especially easy, since it is usually at saturation pressure.

The combustion chamber of hybrid rocket engines often is thermally insulated and not using regenerative cooling. The fuel fills out most part of the combustion chamber and therefore isolates and cools the chamber ablatively. For other parts of the engine, ablative isolation materials are used like composite materials with phenolic resin. Also the nozzles are usually constructed of ablative materials. However, since a liquid oxidizer is used, it is theoretically possible for high power hybrid rocket engines to use regenerative or film cooling. Yet, this

increases system complexity, which is not desired in hybrid rocket engine applications. The standard shape for hybrid rocket fuels is a hollow cylinder. The edges can be sloped to decrease flow resistance and vortex development. More sophisticated designs include segmented fuels, where each segment has a different diameter and sometimes mixing devices are installed between segments. However, usually mixing devices are installed behind the fuel slab, at the front of a post combustion chamber, where the mixed fuel and oxidizer have residing time for the combustion reactions to complete. Longer post combustion chambers usually maximize combustion efficiency, but increase also engine weight, length and thermal loads. For slow burning fuels like HTPB it is necessary to have more sophisticated fuel designs in order to reach high thrust levels. Usually for HTPB fuels star shapes (or other shapes that increase the surface of the fuel port) are used. Also multi-port designs, where the oxidizer flows through several channels in the fuel, increase the fuel mass flow and allow for highest thrust levels with classical fuels. These multi-ports design result in a lot of residual fuel mass in the chamber after the burning time. The burn has to be stopped before the structure of the fuel collapses and large fragments of fuel damage the nozzle or block the nozzle throat.

3.5. Advantages and Disadvantages of Hybrid Rocket Engines

The characteristics of hybrid rocket engines lead to the following advantages and disadvantages in the three categories safety, performance and cost [23].

3.5.1. Safety

+ Inert fuel: The fuel grain is produced, transported and handled at high safety & low cost

+ Different state of matter: Liquid oxidizer and solid fuel cannot form an explosive mixture during any time of production, assembly, ground operation or flight of the spacecraft

+ Grain robustness: The regression rate is not depending on the chamber pressure and the boundary layer combustion prohibits combustion inside of cracks. Thus, unlike solid rocket motors, hybrid rocket engines are much less sensitive to cracks in the solid fuel.

3.5.2. Performance

+ Throttling: Hybrid rocket engines are throttleable by controlling the oxidizer mass flow into the chamber, which is a great advantage over solid rocket motors. In comparison to liquid rocket engines, only one liquid must be controlled.

+ Shut-down and re-ignition: By closing the oxidizer supply the combustion is stoppable. Depending on the oxidizer, re-ignition is very easy to achieve (catalytic decomposition of H_2O_2 or N_2O), without hypergolic reactions.

+ Propellant versatility: The range of possible propellant combinations is very high for hybrid rocket engines. This opens up a lot of possible improvements to the propulsion systems performance.

+ Storability: Derived from the previous point, storable propellants are available. The propulsion system is simple and storable for a long time without maintenance. This is mandatory for interplanetary missions.

− Low regression rate: The classical polymeric fuels of hybrid rocket engines like HTPB offer low regression rates. This results in either low thrust density or complex fuel geometries, like star-shape or multi-ports. These fuel shapes often result in high residuals at the end of the burn time, which reduces greatly the performance of the engine. Also the size of the engine is growing with these shapes. This is improved by current advancements in the field of liquefying hybrid rocket fuels, which increase the regression rate by a factor up to six.

− Regression rate prediction: Further problems with the regression rate emerge during the design of a rocket engine. The regression rate is dependent on the propellant combination, the injector design, the chamber design and the fuel geometry. It is very difficult to predict the exact regression rate without doing both lab-scale and full-scale tests.

− Limited burn duration: With long burn durations, the change of the combustion chamber internal geometry is very high. It is not proven, that the combustion conditions in a hybrid rocket engine with long burn duration is at high efficiency at all time, since the injection behavior of the liquid oxidizer, the boundary flow conditions and the mixing of the propellants will change over time. Additionally, degradation of combustion chamber inserts (like mixing devices) or ablation-cooled nozzle parts over a long burn time have a negative impact on the efficiency. Experimental investigations need to verify the behavior of hybrid rocket engines with long burn duration.

− Dynamic combustion chamber conditions: Similar to the previous point, over the burn duration, usually the mixture ratio of a hybrid rocket engine is not constant. This results in losses of specific impulse compared to the optimal mixture ratio. This is reduced by controlling the mass flow, but it cannot be avoided completely since the fuel mass flow is always coupled directly to the oxidizer mass flow.

− Combustion efficiency: The mixing of fuel and oxidizer happens in the boundary layer flow alongside the fuel grain inside the hybrid rocket engine. The mixing needs more residing time in the combustion chamber than in a liquid propellants engine. Hence, for high combustion efficiency a long post combustion chamber is needed. Additional mixing devices improve the efficiency but increase also the engine weight.

3.5.3. Cost

+ High safety: the high safety of the propellants leads to a reduced cost in all phases of development, testing, manufacturing, and operation.

+ Green propellants: the use of propellants with no or low impact on health and the environment, make it also possible to reduce the cost at all times.

+ Lower system complexity compared to liquid propulsion systems: Lower system complexity simplifies development and production.

3.6. Hybrid Rocket Propulsion Research

Figure B.1 shows a map of all European activities on hybrid propulsion to the knowledge of the author. All activities are listed in Table B.1. A short overview over the different working fields is given. This list is without any claim to completeness as the situation is changing every few months with new groups and companies emerging and others stopping their work. In summary a lot of universities work on hybrid rocket engines for education of students, for testing small to midscale rocket engines and to bring forward fundamental research in the field. Similarly institutional research centers around the world work on fundamentals, larger tests and applications for hybrid rocket engines. Some companies already try to use hybrid rocket engines for commercial applications, but the number is still small and the projects are mostly in an early stage.

3.7. Internal Ballistics of Hybrid Rocket Engines

This section is giving a short overview of the combustion processes of hybrid rocket engines and its modeling. Detailed information about classical hybrid theory (i.e. polymeric fuels) is found in "Fundamentals of Hybrid Rocket Combustion and Propulsion" [19]. Karabeyoglu et al. give a detailed description of the processes and models of liquefying fuels inside hybrid rocket engines in [25, 26]. The combustion of hybrids is defined by the boundary layer of the oxidizer flow along the surface of the fuel A_f, where the fuel mass flow $\dot{m}_f$ is increased continuously. The fuel mass flow is calculated with the surface, the fuel density ρ_s and the regression rate $\dot{r}_f$. Fuel and oxidizer react in the flame zone inside the boundary layer. Below the flame zone, the flow is very fuel rich, while above in the core of the port the flow is oxidizer rich. The most important parameter is the regression rate of the fuel, which is the velocity with which the fuel burns normal to the fuel surface. Therefore, it is the parameter, which determines together with the fuel surface area the mass flow of the fuel. The total mass flow $\dot{m}$ of the hybrid rocket engine is calculated with the sum of the oxidizer mass flow $\dot{m}_{ox}$ and the fuel mass flow $\dot{m}_f$:

$$\dot{m} = \dot{m}_{ox} + \dot{m}_f = \dot{m}_{ox} + \dot{r}_f \rho_s A_f \tag{3.1}$$

This regression rate is dependent on the propellant combination and most of the time has to be determined experimentally for each propellant combination. In addition, the combustion chamber layout with injectors, and other flow manipulating geometries, have an impact on the regression rate. Usually experiments with small-scale rocket engines yield higher regression rates than larger scale engines. With the current state of the art, it is mandatory to do experiments with a new rocket engine to measure the regression rate and iterate the design until the planned operating conditions are met. Modeling laws without relying on empirical data can only be used for preliminary designs.

3.7.1. Modeling Laws for Classical Hybrid Fuels

Marxman et al. investigated hybrid rocket's combustion processes in the 1960's [44]. By evaluating the energy conservation on the fuel surface and neglecting heat fluxes by radiation and conduction, they showed that the regression rate $\dot{r}_f$ is approximated with the following model (the equation was derived with imperial units, for SI units the constant 0.036 needs to be adjusted). It uses the instantaneous mass flux density G, which is the total mass flow at a position x along the fuel, divided by the flow section diameter. The viscosity of the gas flow μ has a small effect on the regression rate as well as the ratio of the velocity of the gas in the core stream and the flame u_e/u_c and the ratio of total enthalpy difference between flame and fuel to the effective heat of vaporization $\Delta h/h_v$ [45].

$$\dot{r}_f = 0.036 \frac{G^{0.8}}{\rho_s} \left(\frac{x}{\mu_m} \right)^{-0.2} \left(\frac{u_e}{u_c} \frac{\Delta h}{h_{vap}} \right)^{0.23} \tag{3.2}$$

Experimental data over the last decades since Marxman's publication deviate from the results gained by this equation. Experiments show that the exponent of G should be smaller and the exponent of x is not exactly -0.2. In reality the dependency of the regression rate on the position is smaller. An explanation for this is given by Zilliac and Karabeyoglu [45]. They note that Marxman derived his equations for a flat fuel slab. In a typical hybrid rocket engine, the fuel grain will be cylindrical, which changes the values of the exponents. Therefore, Zilliac and Karabeyoglu elaborated a more detailed model for regression rates of classical, non-liquefying fuels in cylindrical combustion chambers. Figure 3.3 shows all the included processes in the model. They state that the regression rate of the fuel is approximated by:

$$\dot{r}_f = \frac{A}{\rho_s} \left[1 + C_1 \left(\frac{G_{ox} D}{\mu_m} \right)^{-0.22} e^{-0.4 \frac{x}{D}} \right] G^{k+1} D^k \tag{3.3}$$

In this equation they respected the circular port shape as well as heat flows due to convection and radiation from the flame zone to the fuel grain. Additionally, the position of the flame zone in the boundary flow has been included in the derivation of the equation. In tests, the flame zone was observed to be located approximately in the middle of the boundary zone. The tube diameter D as well as a new coefficient k have an increased influence on the regression rate approximation. The parameter A, which is assumed to be a constant for a certain test setup is
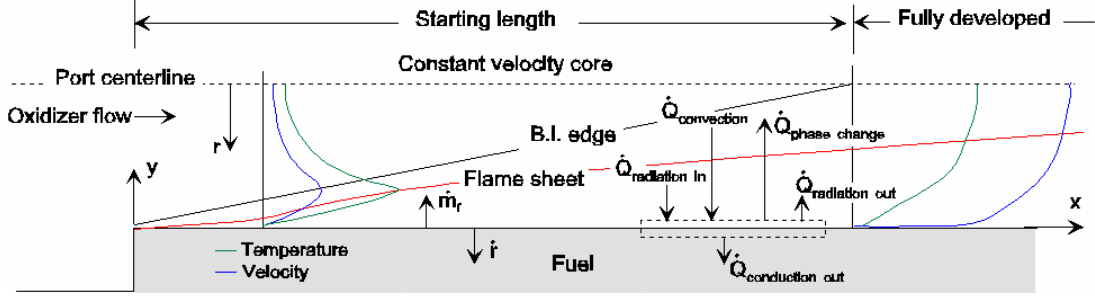
Figure 3.3.: Schematic of classical fuel's reaction process [45]

defined as:

$$A = \frac{0.022}{\mu_m^k \left(T_s/T_{melt}\right)^l} Pr^{-0.6} \left(\frac{\Delta h}{h_{vap}}\right)^{0.23} \phi_c^{0.77} \tag{3.4}$$

The temperature of the solid propellant surface T_s is either a measured value or it is close to the vaporization temperature of the fuel. The mean temperature of the gas flow T_{melt} is calculated as the equilibrium temperature of the flow. The Prandtl number Pr is either approximated by 1 or calculated by $c_p \mu/k_g$ with the mean heat capacity c_p and the mean heat conductivity of the gas flow k_g. The position of the flame sheet relative to the fuel surface ϕ_c is defined as:

$$\phi_c = \frac{1.22 \left(O/F\right) \frac{\Delta h}{h_v}}{K_{ox} + \left(O/F + K_{ox}\right) \frac{\Delta h}{h_v}} = \frac{u_c}{u_e} \tag{3.5}$$

The mixture ratio O/F is the local mixture ratio in the flame zone along the fuel's x-axis. Currently there exists no model for the calculation of this variable. However, the stoichiometric value for the fuel and oxidizer combination is used until a better model is available. The concentration of the oxidizer K_{ox} is usually close to 1, except when the oxidizer inflow is diluted by an inert medium. For some laboratory set-ups nitrogen is used to dilute the oxidizer in order to decrease combustion temperature. However, although this model is much more detailed and doesn't overestimate the influence of the fuel length on the regression rate anymore, the model is highly dependent on the viscosity μ in the flow, which is very hard to calculate precisely, and the coefficient k, which is approximated with:

$$k = -0.005 \left(\frac{E_a}{R_u T_s}\right) - 0.08 \tag{3.6}$$

The activation energy of the chemical reaction E_a is a result of the propellant combination and depends on the scale of the heat flow [45, 46]. So it is not a constant value for a given propellant combination. R_u is the universal gas constant and T_s the solid fuel surface temperature, which is also hard to determine. A first assumption, without conducting measurements in experiments, is to assume that the surface temperature is close to the vaporization temperature of the fuel. Zilliac and Karabeyoglu conclude that their model is very well suited for classical hybrid fuels. However, the model is very sensitive to the fuel surface temperature T_s. It is additionally dependent on the local O/F in the flame zone, for which there is currently no

model available. The activation energy E_a and the viscosity μ_m are also hard to obtain with high precision. Hence, comparisons with tests need to be evaluated to get a suitable model for the regression rate for the corresponding propellant combination. Zilliac and Karabeyoglu state, that their model is still not sufficient to supplant determination of regression rates in rocket engine burning tests. Therefore a simplified equation with empirically determined coefficients a, n, and m is widely used for engine design and test evaluation:

$$\dot{r}_f = aG^n x^m \tag{3.7}$$

Going along the fuel grain, more fuel will be added to the mass flow. Thus, the mass flux term G^n increases and x^m decreases. It is found that for most propellant combinations this two effects seem to even themselves out, resulting in a mostly constant regression rate over the fuel length. In addition, it requires very sophisticated instrumentation to measure the regression rate exact in time and space. This is why the regression rate data is mostly determined time- and space-averaged over a whole test and fuel (section), as well as the average oxidizer mass flux G_{ox}. Since these measured values are used to calculate and design new engines, often the regression rate law is further simplified to the following:

$$\dot{r}_f = aG_{ox}^n \tag{3.8}$$

Zilliac and Karabeyoglu note that the regression rate also has a high dependency on scale of the engine. Therefore the scale factor α is added.

$$\dot{r}_f = \alpha a G_{ox}^n \tag{3.9}$$

These simplified regression rate laws is used either to simulate existing engines, where the coefficients are known from experiments, or to design new engines. Since the scale effects are not exactly known before, all regression rate models need to be validated in experiments. Then the fuel geometry and oxidizer mass flow needs to be adjusted accordingly, in order to reach the designated thrust and mixture ratio.

3.7.2. Regression Law for Liquefying Fuels

The equations mentioned before are only valid for classical hybrid rocket fuels. They do not predict the regression rate of liquefying fuels. A great part of the fuel mass transfer with liquefying fuels is not due to vaporization at the flame zone inside the boundary layer, but due to droplet entrainment. The entrained droplets burn inside the oxidizer rich zone with the necessary heat being transferred through the boundary layer. The increased mass transfer from the boundary layer to the core flow consequently increases the regression rate. Higher regression rates from a factor 2 to 5 have been found in experiments with liquefying fuels both by experiments of Karabeyoglu et al. as well as DLR Lampoldshausen by Kobald et al. [25, 27, 28]. The droplet entrainment is currently investigated with optical measurement methods

at DLR Lampoldshausen by Kobald and Petrarolo [47] and previously the instability of the liquid film has been analyzed in order to understand the combustion in more detail [48]. The aim of many research groups around the world is to improve existing modeling theories about liquefying hybrid fuels.

An extended theory about regression rate has been formulated by Karabeyoglu, Altman and Cantwell in 2002 [25]. This theory includes also fuels that form a melt layer. First, they give an empirical equation for the critical conditions, which define the starting point for entrainment processes, from Nigmatulin et al. [50]:

$$G^{1.6}h_t^{0.6} \geq 2.5 \cdot 10^{-3} \frac{1}{c_f^{0.8}} \frac{\rho_g^{1.3}}{\rho_l^{0.3}} \frac{\mu_l^{0.6}\sigma}{\mu_g}, \tag{3.10}$$

where h_t is the thickness of the liquid melt layer, c_f is the skin-friction coefficient, ρ_g is the gas flow density, ρ_l is the liquid fuel density, μ_l is the liquid fuel viscosity and σ is the surface tension of the liquid melt layer. The skin-friction coefficient is calculated as follows [51].

$$c_f = 0.074 Re_x^{-0.2} \tag{3.11}$$

The total regression rate with droplet entrainment $\dot{r}_f$ is the sum of vaporization and entrainment regression rates $\dot{r}_v$ and $\dot{r}_{ent}$. The vaporization regression rate hereby stays the same like in Marxman's classical theory.

$$\dot{r}_f = \dot{r}_v + \dot{r}_{ent} \tag{3.12}$$

Further, Karabeyoglu et al. conducted a thermal analysis of the thickness of the melt layer. By evaluating the convective and radiative heat flux, two limits of the melt layer thickness could be stated. In the first case, the radiation heat flux is absorbed completely in the liquid layer,
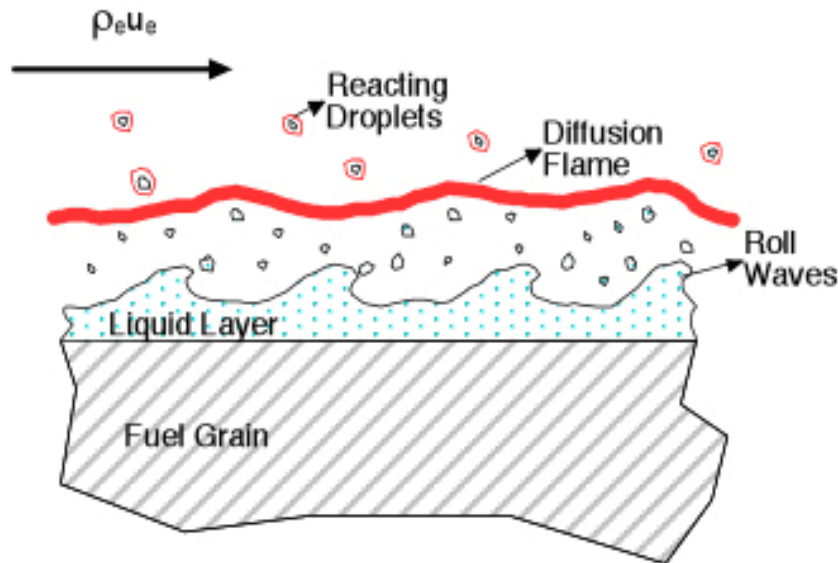
Figure 3.4.: Schematic of liquefying fuel's reaction process [49]

which equals an opaque liquid layer. In applications with liquefying hybrid rocket fuel, the paraffin is most of the time blackened with e.g. Carbon Black. This is done to reduce heating of the complete fuel block in an instant, by increasing the absorption at the fuel's surface. Therefore for most practical applications of liquefying fuels in hybrid rocket engines, this first case for the thickness of the melt layer h_t in mm is the fitting one:

$$h_t = \delta_l \ln\left(1 + \frac{c_{p,l}\Delta T_1}{h_{melt}}\right),$$ (3.13)

$$\Delta T_1 = T_{vap} - T_{melt},$$ (3.14)

$$\delta_l = \frac{\kappa_l \rho_l}{\dot{r}_f \rho_s},$$ (3.15)

where $c_{p,l}$ is the specific heat of liquid fuel and h_{melt} is the total melting heat. ΔT_1 is the temperature difference between the melting and vaporization temperatures T_{melt}, T_{vap}. δ_1 is the thermal thickness in mm. κ_l is the thermal diffusivity of the fuel.

$$\kappa_l = \frac{\lambda_l}{c_{p,l}\rho_l}$$ (3.16)

In the second case, the radiation absorption is very small, so that nearly all radiation is absorbed by the whole solid fuel. This applies for solid fuels, that are translucent. In this case the thickness of the liquid layer is

$$h_t = \delta_1 \ln\left(1 + \frac{c_{p,l}\Delta T_1}{h_{melt} - h_{vap}\dot{Q}_r/\dot{Q}_w}\right),$$ (3.17)

where h_v is the total heat of vaporization and $\dot{Q}_r/\dot{Q}_w$ is the ratio of radiative to the total heat transfer between fuel and core flow. In a next step, the analysis of Karabeyoglu and his colleagues was focused on the stability of the liquid layer and the connected entrainment of fuel droplets into the oxidizer stream. They state, that the mass flow by droplet entrainment $\dot{m}_{ent}$ is depending on the mass flow inside the liquid melt layer $\dot{m}_l$ and the flow conditions in the gaseous flow. For this they introduce the parameter X_e which is calculated with the dynamic pressure P_d, the surface tension σ and the ratio T_g/T_{vap} of the gas and vaporization temperature. An empirical relation $e_0(X_e)$ is defined. The melt layer mass flow per unit area $\dot{m}_l$ can be calculated by the shear force balance at the liquid gas interface.

$$\dot{m}_l = \frac{P_d c_f h_t^2 \rho_l}{2\mu_l}$$ (3.18)

$$\dot{m}_{ent} = 13.3 e_0(X_e) \dot{m}_l$$ (3.19)

$$X_e = \frac{(2P_d)^{0.5}}{\sigma}\left(\frac{T_g}{T_{vap}}\right)^{0.25}$$ (3.20)

$$e_0(X_e) = 1 - \exp[-1.06e{-}4(X_e - 2109)]$$ (3.21)

The formulation of X_e in [25] is inconsistent compared with the original publication of Gater and L'Ecuyer [52]. Karabeyoglu used the dynamic pressure P_d while Gater used a momentum factor $M_0 = \rho u^2$, which is $M_0 = 2 * P_d$. For this work, the factor of 2 was considered. Also the exponent of the fraction T_s/T_{vap} is unclear in Karabeyoglu's publication. Therefore it was also chosen as Gater published it. A correction of this relation has to be done for high mass transfer rates. The reason is that the entrainment mass equation does not regard the effects of reduction in the liquid mass flow rate along the axial direction. The correction was done with empirical data and resulted in the following formulation:

$$\dot{m}_{ent} = -13.3 \ln\left(1 - e_0\left(X_e\right)\right) \dot{m}_l \tag{3.22}$$

With substitution it follows

$$\dot{m}_{ent} = \rho_l \dot{r}_{ent} = 1.41\mathrm{e}{-3}\left(X_e - 2109\right) \dot{m}_l \tag{3.23}$$

$$\dot{r}_{ent} = 1.41\mathrm{e}{-3}\left(X_e - 2109\right) \frac{\dot{m}_l}{\rho_l}. \tag{3.24}$$

If $X_e < 2109$ there is no entrainment mass flow. The entrainment mass flow is proportional to the dynamic pressure P_d, the liquid film thickness h_t and the fuel properties viscosity μ_l and surface tension σ.

$$\dot{m}_{ent} \propto \frac{P_d^\alpha h_t^\beta}{\mu_l^\gamma \sigma^\pi} \tag{3.25}$$

Table 3.4 shows the parameters for this equation. The values for the four coefficients given by Gater and L'Ecuyer are the ones derived with the theory. Karabeyoglu et al adjusted the values to fit their empirical data. This means, while α can be chosen as 1.5, for the application of the theory, the coefficient β is an additional input parameter. Following the Equation 3.18 β should be 2. However Karabeyoglu et al. [25] did a fit to experimental results and found that a β of 1.0-1.5 fits better. This behaviour shows, that the equations do only approximate the real processes and are missing some parts and details. This of course makes it more difficult to apply the theory to propellant combinations, where no experimental data is available. However, the model anyway gives a good prediction for liquefying fuels, much better than the regression models for classical fuels.

Table 3.4.: Propellant options for hybrid rocket engines, [23]

Source	α	β	γ	π
Karabeyoglu [25]	1.5	1.5	$> \pi$	$< \gamma$
Gater and L'Ecuyer [52]	1.5	2	1	1
Nigmatulin [25]	1	1	-	-

3.7.3. Correction of the Classical Regression Rate Law

Karabeyoglu et al. suggest three modifications to the classical theory. Firstly, the ratio of enthalpy difference to effective heat of vaporization is altered since the effective heat of vaporization is reduced, because the evaporation energy for the same fuel mass transfer is highly reduced by the entrainment process. Secondly, the blowing factor is altered due to the two-phase flow. They assume that the droplets do not vaporize below the flame sheet. Therefore, the blowing parameter only needs to respect the vaporization mass transfer from the surface to the flame zone. A third modification is the increase in heat transfer to the surface, since waves on the liquid surface increase the surface area. Further, they extend the blowing factor curve to match the blowing parameter areas of liquefying fuel. With these modifications, they state the classical regression rate $\dot{r}_{cl}$ with the ratio of radiative to convective heat transfer $\dot{Q}_r/\dot{Q}_c$, the blowing parameter B and the blowing correction coefficient C_{B1}.

$$\dot{r}_{cl} = \frac{0.03\mu_g^{0.2}}{\rho_f}\left(1 + \frac{\dot{Q}_r}{\dot{Q}_c}\right)BC_{B1}G^{0.8}x^{-0.2} \tag{3.26}$$

The blowing correction coefficients C_{B1} and the blowing parameter B are defined as:

$$C_{B1} = \frac{2}{2 + 1.25B^{0.75}} \tag{3.27}$$

$$B = \frac{\dot{r}_f\rho_f}{\frac{c_f}{2}G} \tag{3.28}$$

Setting up the energy balance at the liquid gas interface a relation for the vaporization and entrainment regression rate can be found with the ratio of effective heats of gasification for entrainment and vaporization R_{he} and R_{hv}:

$$\dot{r}_v + \left[R_{he} + R_{hv}\left(\frac{\dot{r}_v}{\dot{r}}\right)\right]\dot{r}_{ent} = F_r\frac{0.03\mu_g^{0.2}}{\rho_f}\left(1 + \frac{\dot{Q}_r}{\dot{Q}_c}\right)B\frac{C_H}{C_{H0}}G^{0.8}x^{-0.2} \tag{3.29}$$

$$\dot{r} = \dot{r}_v + \dot{r}_{ent} \tag{3.30}$$

The blowing factor C_H/C_{H0} is calculated as

$$\frac{C_H}{C_{H0}} = \frac{2}{2 + 1.25B_g^{0.75}} = \frac{C_{B1}}{C_{B1} + C_{B2}\left(\dot{r}_v/\dot{r}_{cl}\right)^{0.75}}, \tag{3.31}$$

where the blowing correction coefficients C_{B2} nd the vaporization blowing parameter B_g are defined as:

$$C_{B2} = \frac{1.25B^{0.75}}{2 + 1.25B^{0.75}} \tag{3.32}$$

$$B_g = \frac{\dot{r}_v\rho_f}{\frac{c_f}{2}G} \tag{3.33}$$

The heat-transfer correction factor for surface roughness F_r is defined as:

$$F_r = 1 + \frac{14.1 \rho_g^{0.4}}{G^{0.8} \left(\frac{T_g}{T_{vap}} \right)^{0.2}} \tag{3.34}$$

With this set of differential equations, the regression rate of vapor for the liquefying fuel $\dot{r}_v$ can be calculated. The chemical properties are taken for the mean value between the melting and vaporization temperature for the liquid phase. The liquid surface tension is evaluated at the boiling point according to [25]. For many liquefying fuels like paraffin-based fuels, during regular combustion chamber conditions in a rocket engine, the pressure is higher than the critical pressure. This means that the regression happens under supercritical conditions where there is no defined border between liquid and gas phase. Experiments show that the regression rate of liquefying fuels is still higher, which means that even under supercritical conditions something similar to droplet entrainment is happening. "Droplets" with higher density fluid from the solid fuel surface are brought to the oxidizer mass flow by turbulent processes. Adachi and Shimada investigated supercritical behavior of fuels also by CFD simulations and could confirm this behavior [53]. Optical investigations of supercritical combustion by Chandler et al. revealed that there is not the same mechanism of droplet forming like at atmospheric pressure [54]. However, there were elongated filaments of the flame sheet along the fuels and upward burst flames, where there was a localized reaction because of a combustible oxidizer ratio. Therefore, it is assumed that also under supercritical conditions the entrainment model for liquefying fuels is applicable with the same input data, as increased regression rate could be confirmed in many experiments.

4. Software

4.1. Analysis, Simulation and Trajectory Optimization Software for Space Applications (ASTOS)

In order to design, optimize and analyze a sample return mission to the Moon, the trajectory optimization software ASTOS (version 8) is used. ASTOS includes an extensive library of aerospace vehicle differential equations with 3-DOF or 6-DOF equation of motions. With boundary constraints, path constraints and cost functions the user can design and optimize a trajectory without additional coding. The range of possible mission and trajectories that can be designed and optimized is very broad, including aerodynamically stabilized sounding rockets, orbital launchers, reentry vehicles, interplanetary missions and orbit transfers. The mission is designed by setting up a vehicle with the model library by putting together the respective components like engines, tanks, payload etc. For flight in atmosphere, the full modelling of aerodynamic configurations is included. There is the possibility to model rocket engines with predefined thrust and mass flow profiles, or engines with a given specific impulse and other possibilities to variously model rocket and air breathing engines. An interface for a completely user defined model is also integrated. The flight dynamics can be modeled with different equations of motions, best suited to the current flight phase. Controls like thrust and attitude are optimizable as well as stage sizing and trajectory phases durations. Optimization is done with the included optimizer CAMTOS [55]. It allows multiple shooting optimization for phases with high derivatives and the collocation optimization method for phases with low derivatives but long phase duration. The user can define cost functions for many parameters, e.g. maximum payload, minimum fuel consumption, heat load reduction etc. Phase constraints like orbit parameters or maximum acceleration are defined as well. Summarizing, ASTOS offers a wide palette of possibilities to model any vehicle in atmosphere and / or space and optimize its trajectory. All the equations of motions and dynamics and disturbances are already included in ASTOS. Nevertheless, in order to model and analyze a mission trajectory with ASTOS deep understanding of orbital physics and mechanics are necessary. A very good introduction to this topic is given by Curtis [56].

4.1.1. Moon Sample Return Analysis with ASTOS

With its vast possibilities, ASTOS allows to model a complete mission from launch on the Earth until landing on the Moon and return until reentry in Earth's atmosphere. Yet it is advisable to model, simulate and optimize parts of the mission that are not necessarily

hardly connected to each other separately, since this will reduce optimization time greatly. A verification that ASTOS optimizes such missions without problems has been done [57]. Some problems regarding coordinate transformations were identified and fixed by Astos Solutions GmbH preceding the start of these studies. A sample return mission with hybrid propulsion, not taking into account the dynamic behavior of hybrid rocket engines, but instead using average values for mass flow and specific impulse in ASTOS, has been analyzed by Tomilin [1].

4.1.2. User Propulsion Component for Hybrid Rocket Engines

ASTOS offers an interface in C programming language to include propulsion models, which are more sophisticated than simple fixed thrust and mass flow curves. This is used for including a hybrid rocket engine model. Different levels of detail are available for this. A first approach is to use analytical equations to simulate the time dependent behavior. Models with higher detail are possible to be implemented by creating an interface between ASTOS and ESPSS models. Hereby the connected ESPSS models can be as simple as a combustion chamber and an oxidizer inflow. They can be increased in detail with tanks, pressurization systems, and even a complete spacecraft's propulsion system with attitude control thrusters is realizable.

4.1.3. Analytical Hybrid Propulsion Component

The first step in creating a user propulsion component for hybrid rocket engines was to create a hybrid rocket engine model with analytic equations, avoiding differential equations. The oxidizer mass flow is a control value, which is set and changed with ASTOS. At the same time, also the fuel mass in the rocket engine is a state that is transferred from ASTOS to the model as well as the ambient pressure. The rocket engine geometry, the efficiency and the propellant combination are specified in an input text file. The regression rate is defined with two regression parameters a and n (sometimes a and b). The equations are used as described in Table 4.1. The combustion data and combustion pressure are iterated. The combustion data is read from a table created with NASA CEA [58]. The model was also extended with a tank model for self-pressurizing nitrous oxide using Peng-Robinson equations of state according to [59, 60]. In that case, the mass flow is not a control value of ASTOS. Instead, it is calculated with the pressure difference between the tank and the combustion chamber with

$$\dot{m}_{ox} = C_D A_{inj} \sqrt{2 \rho_{ox} \Delta p}. \tag{4.1}$$

The injector area can be an optimizable parameter in the ASTOS model.

Table 4.1.: Equations of analytical hybrid rocket engine model

Nozzle throat area A_t with the nozzle throat diameter d_t:	$A_t = \dfrac{\pi}{4} d_t^2$	(4.2)
Fuel inner diameter d_i, outer diameter d_a:	$d_i = \sqrt{d_a^2 - \dfrac{4m_f}{\pi \rho_f l_f}}$	(4.3)
Flow area A_{flow}:	$A_{flow} = \dfrac{\pi}{4} d_i^2$	(4.4)
Oxidizer mass flux G_{Ox}:	$G_{Ox} = \dfrac{\dot{m}_{Ox}}{A_{flow}}$	(4.5)
Regression rate $\dot{r}$:	$\dot{r} = a G_{ox}^n$	(4.6)
Fuel mass flow $\dot{m}_{fu}$ with fuel length l_f:	$\dot{m}_{fu} = \dot{r} \rho_f \pi d_i l_f$	(4.7)
Total mass flow $\dot{m}_{tot}$:	$\dot{m}_{tot} = \dot{m}_{fu} + \dot{m}_{ox}$	(4.8)
Mixture ratio O/F:	$O/F = \dfrac{\dot{m}_{ox}}{\dot{m}_{fu}}$	(4.9)
Combustion data[1]:	$\left[c_F, c^*, I_{sp}, I_{vac}, \gamma \right] = f\left(p_{cc}, \epsilon, O/F \right)$	(4.10)
Combustion pressure p_{cc}:	$p_{cc} = \dfrac{\dot{m}_{tot} \eta_{c^*} c^*}{A_t}$	(4.11)
Thrust for adapted conditions F_{ad}:	$F_{ad} = \dot{m}_{tot} \eta_{I_{sp}} I_{sp}$	(4.12)
Nozzle exit pressure p_e:	$p_e = p_{cc} \dfrac{p_e}{p_{cc}}$	(4.13)
Pressure ratio equation $\frac{p_e}{p_{cc}}$:	$\epsilon = \Gamma \sqrt{\dfrac{\gamma - 1}{\gamma + 1} \left(\dfrac{p_e}{p_{cc}} \right)^{-\frac{1}{\gamma}} \left[1 - \left(\dfrac{p_e}{p_{cc}} \right)^{\frac{\gamma - 1}{\gamma}} \right]^{-0.5}}$	(4.14)
Function Γ:	$\Gamma = \left(\dfrac{2}{\gamma + 1} \right)^{\frac{1}{\gamma - 1}}$	(4.15)
Thrust for ambient conditions F_{amb}:	$F_{amb} = F_{ad} + (p_e - p_{amb}) \epsilon A_t$	(4.16)
Condition for separated nozzle flow:	$p_e < 0.4 p_{amb}$	(4.17)
Thrust for separated nozzle flow:	$F_{sep} = p_{cc} A_t \left[2 \left(\dfrac{2}{\gamma + 1} \right)^{\frac{1}{\gamma - 1}} - \dfrac{p_{amb}}{p_{cc}} \right]$	(4.18)

[1] Thrust coefficient c_F, characteristic velocity c^*, specific impulse I_{sp}, vacuum impulse I_{vac} and heat capacity ratio γ from NASA CEA [58]

4.2. EcosimPro & ESPSS

EcosimPro by Empresarios Agrupados is a simulation platform for modeling 0D or 1D systems of differential-algebraic equations [61]. With different libraries, that include components for modeling complex systems, different fields of applications can be served:

- Space applications with propulsion or life-support

- Aeronautics applications (gas turbines, electric systems etc.)

- Power plants, electronics, thermos-hydraulics etc.

For modeling spacecraft and launcher propulsion systems, the European Space Propulsion System Simulation library (ESPSS) is used. It is developed at behalf of the European Space Agency (ESA) [62]. ESPSS offers a large palette of components to model rocket engine cycles with combustion chambers, nozzles, fluid management parts, turbo pumps, gas generators et cetera in different levels of detail.

4.2.1. Implementation of Hybrid Rocket Engines

In its current version, ESPSS 3.1 includes a 1D non-adiabatic component for hybrid combustors, either as a pre-burner without nozzle or with a nozzle for supersonic expansion (see ESPSS User Manual section 8.3.6) [63]. It includes the combustion chamber and an injector with a cavity volume. The chamber can be set with user-defined amount of nodes in the subsonic chamber and supersonic nozzle sections. For the combustion process, two options are available:

- All vapors of fuel and oxidizer will react instantly in the node

- Reaction time delay between the equilibrium and the actual burned gases composition

The latter is a good approach to simulate real hybrid rocket engine's combustion processes where the efficiency of the engine depends on the reaction speed and mixing of fuel and oxidizer along the length of the engine. For every node in the combustion chamber, the fuel thickness can be set. The fuel composition can be either one of a few pre-defined fuels or a user-defined fuel. The regression law can be either chosen as dependent on the coefficients a and b as in (User Manual section 8.2.5):

$$\dot{r}_f = aG^b \tag{4.19}$$

Here, G is the local instantaneous mass flux. This results in higher regression rate towards the end of the fuel. In contrast to the widely used regression laws derived from the initial model of Marxman this model has no dependency on the position along the fuel grain. As an option also the oxidizer mass flux as the injector can be chosen as G, which is preferable, when the coefficients a and b were determined by time and space averaged experiments with the measurement of only G_{ox} (see section 3.7). However this approach causes the node's fuel mass

flow to react instantly to a change in the injector's oxidizer flow, while in reality some finite time will pass until the changed mass flow density reaches the node's position. The model optionally includes also lateral regression and changes the solid fuel's geometry accordingly over time. An advanced model for regression is implemented, which assumes a thin vapor layer between the gases and the grain, and establishes the conservation equations for convective heat and enthalpy mass flows at both sides of the layer. The vaporization temperature was chosen to be the saturation temperature of the fuel and the vaporization energy is set to equal the enthalpy of formation, which is not accurate. This model is a first step in modelling the regression rate from fuel properties rather than experimental determined coefficients. However, it is not as accurate as Marxman's regression laws for classical hybrid polymeric fuels and it also has a different approach which yields regression rates with offsets of an order of magnitude in some cases. For liquefying fuels there is currently no advanced model.

4.2.2. Improved Modeling of Classical Fuels in ESPSS

The standard regression rate model, called "std_Hybrid" in ESPSS, has been enhanced by the possibility to set a regression rate coefficient separately for every node. This enables simulation of a combustion chamber setup with different, segmented fuels. The same principle has been applied to the density. For example, the first nodes could be filled with a polymeric solid fuel like HTPB while the last nodes contain a post combustion chamber with a very slow regressing insulator like a phenolic composite. It also allows the modeling of mixing devices made from e.g. graphite or ceramics, which have nearly no regression. In order to analyze hybrid rocket engines in a wide field of possible applications, the versatility of the ESPSS hybrid rocket module was improved. Mainly, it should be possible to model hybrid rocket engines without knowing the regression rate coefficients of a propellant combination. Therefore, the regression models for non-liquefying fuels introduced in section 3.7 have been included into ESPSS. This enables modeling of classical hybrid rocket fuels using chemical properties instead of empirical regression coefficients as an input for the model. Namely next to Marxman's law also Zilliac's and Karabeyoglu's model has been implemented (see section 3.7). While some variables in these models are averaged over space and time, in ESPSS these values actually are calculated with the states in the combustion chamber at the different nodes. Therefore, the following adaptions have been made to the models. The mean viscosity μ_m in both models is the mean viscosity of the flow, including the flame zone, the fuel vapor and the core flow over the complete burning time and the x-axis of the fuel. Zilliac and Karabeyoglu [45] calculated the viscosity according to the Kinetic Theory of Gases [64] as:

$$\mu_e = 26.69e{-}7 \sqrt{\frac{M T_b}{\sigma^2}} \tag{4.20}$$

The molecular weight M was defined as the average molecular weight over the x-axis. The hard-sphere diameter was chosen as $\sigma = 5$. The bulk temperature T_b was approximated as the mean temperature of the flame temperature and the surface temperature of the solid fuel. With

the ESPSS model both the viscosity and the molecular weight are determined at every node. However, the nodes have an uniform state and do not represent the reality with the highly inhomogeneous state in radial direction. In order to calculate the viscosity μ_m for a node, there are several approaches implemented.

- The same equation as in the original model can be used. The flame temperature and the surface temperature are inputs of the user, since the combustion in the boundary layer is not modeled in ESPSS. ESPSS only provides mean values for the temperature per node. This way of calculating the viscosity shows no dependency on the position on the x-axis.

- The viscosity can be represented as the node's content's viscosity. In this way the flame's and solid fuel vapor's viscosity are not included. This model showed large discrepancies to empirical regression rates. Especially at the injector side's part of the fuel, where the flow is dominated by cold oxidizer the local viscosity is highly different to the flame's and boundary layer's viscosities.

- The viscosity can be a mean value of the solid fuel's vapor viscosity with the vapor temperature T_{vap}, the local node's viscosity and the viscosity with the mean "bulk" temperature T_b as above. The molecular weight M can still be calculated for every node within the ESPSS code, instead of using a mean value.

The last option, using a mean value of the three viscosities that play a role in the model, produces the most realistic prediction of the regression rate for the compared data. However, further verifications with test results are necessary to evaluate the quality of the model's prediction. Both Marxman's and Zilliac/Karabeyoglu's model still depend heavily on assumptions and simplifications, so both are only suitable for preliminary design. However, since no regression coefficients a and n are needed, these models are usable with every possible classical, non-liquefying solid rocket fuel.

The oxidizer concentration K_{ox} is calculated from the injector inflow, by dividing the oxidizer mass flow by the total injector inflow (which is including also non-condensable gas). For both Marxman's and Zilliac/Karabeyoglu's model future improvements are possible:

- Implementation of a model for the flame mixture ratio

- Modeling the flame temperature

- Implementation of a model for actual surface temperature instead of assuming that it is a constant value roughly equal to the vaporization temperature

Even though these improvements still are possible, it is questionable how much effect and improvement it would have on the results. It is expected that also in the future the only way to get reliable regression rate models, especially for each unique combustion chamber set-up, is only via experimental tests for every combustion chamber. Table 4.2 shows the additional inputs that are necessary for the new models, as well as the chosen standard input for HTPB, according to Zilliac et al [45].

Table 4.2.: Additional input parameters for the hybrid rocket component

Parameter	Symbol	Stand. input HTPB	Unit
Activation energy	E_a	203000	$\frac{J}{mol}$[45]
Heat of formation	$H^\theta_{f,sp}$	-380000	$\frac{J}{kg}$[65]
Heat of vaporization	h_{vap}	1812000	$\frac{J}{kg}$[45]
Mixture ratio of flame zone	O/F	2.7	with O_2
Specific heat of flame gas	$c_{p,c}$	7880	$\frac{J}{kg\,K}$[45]
Specific heat of fuel vapor	$c_{p,sp}$	2386	$\frac{J}{kg\,K}$[45]
Temperature of combustion	T_c	3701	K[45]
Temperature of vaporization	T_{vap}	930	K[45]

4.2.3. Enthalpy Balance at the Solid Fuel's Surface

During development of the models it was also recognized that the current implementation of the conservation of energy equations at the solid fuel slab was not consistent (ESPSS version 3.2.0). As Figure 3.3 shows, there are several enthalpy flows between the core gas, the flame zone, the fuel vapor and the solid fuel. As a reference the layer close to the fuel's surface is evaluated. The net enthalpy which flows into this layer sublimates and decomposes the solid fuel. In case of a liquefying fuel the fuel is first melted and then vaporized. For typical hybrid rocket solid fuels like HTPB or paraffin-based fuels these processes are endothermic. Additionally a very small fraction of the reaction enthalpy in the combustion chamber is conducted into the solid fuel, similarly to the combustion chamber wall. To sum up, heat is coming by convection, radiation and conduction from the flame zone to the reference zone where the heat is splitting up in four processes:

- Heating up the solid fuel block

- Melting fuel (for liquefying fuels)

- Sublimation or vaporization of the fuel

- Pyrolising fuel (e.g C and H atoms for paraffin)

The ESPSS model was updated with a new heat and enthalpy balance at the solid fuel grain's surface. In addition the regression rate model based on vaporization has been corrected and expanded. The description of the new equations can be found in Appendix C.

4.2.4. Modeling of Liquefying Fuels in ESPSS

The implementation of the regression rate model for liquefying fuels by Karabeyoglu, Altman and Cantwell [25] is only possible by inserting equations in the "CONTINUOUS"-code of the hybrid rocket component in ESPSS. This is due to the fact that the model forms an additional nonlinear set of equations. This set of equations is based on equations 3.12, 3.19 and 3.29

including all the equations for the corresponding factors. These factors are calculated in a newly implemented function. Additionally the relation for the start of entrainment 3.10 according to [50] is implemented in the model. When the entrainment condition is not active, the regression rate is calculated by the "HybridZilliac" model. This model also replaces equation 3.26 in the liquefying model, as it has proven to be more accurate while testing the model, especially since it is considering the effects of a cylindrical fuel geometry. The liquefying regression rate model is much more sensitive to the combustion port properties. For example, if used with cryogenic oxidizer, an igniter mass flow must be set, to start the combustion. Otherwise the cold temperature in the fuel port will reduce the fuel regression rate. Once the regression rate is high enough, the produced fuel reacts with the oxidizer and produce heat, which keeps the regression right up, even after the starter mass flow is dropping.

4.2.5. Regression Rate Model Comparison

The regression rate models for classical fuels have been compared to each other with HTPB and LOX as a reference. No experimental data with HTPB/LOX were available, however literature values for the regression coefficients are. Table 4.3 lists the input parameters for the models. As HTPB is a polymer, there are many possibilities of composition regarding the average length of the polymer molecules. In literature different values are found for heat of formation. The same applies to heat of vaporization and melting. The stored value in ESPSS was calculated for a HTPB with an average chain length of 10 carbon atoms. This is rather short, hence the stored heat of formation is rather low with $-380\,\text{kJ/kg}$. Some sources even state positive values like $363\,\text{kJ/kg}$ in [65]. This means the HTPB in this configuration is chemically unstable and reacts exothermic when decomposed. An often found and cited value is $20.92\,\text{kJ/kg}$ which corresponds to 5000 calories per kg [66]. This value is also positive. This corresponds to the HTPB binder before curing. The HTPB heat of formation therefore needs careful evaluation before simulation. Khan et al. calculated the heat of formation for several HTPB configurations with different lengths of polymers [67]. They also cite $-51.9\,\text{kJ/mol}$ for $[\text{C}_{10}\text{H}_{15.4}\text{O}_{0.08}]_\text{n}$. This is the same value as used in ESPSS of $-380\,\text{kJ/kg}$.

The models for classical hybrid fuels in ESPSS were named the following:

- vapModel: The default vaporization model, which with realistic values for all input parameters produces unrealistic values.

- vapModelimproved: Improved model which respects the correct heat flow needed for vaporizing the fuel mass flow.

- stdHybrid: Model using coefficients a and b for regression rate calculation

- HybridMarxman: Marxman's law for classical hybrid fuels [44].

- HybridZilliac: Zilliac's and Karabeyoglu's improved regression rate law for classical hybrid fuels according to [45], see Equation 3.3.

Table 4.3.: Input parameters for the classical regression rate comparison

Parameter	Symbol	Input HTPB	Unit	Used by model
Activation energy	E_a	203000	$\frac{J}{mol}$ [45]	Zilliac
Heat of vaporization	h_{vap}	1812	$\frac{kJ}{kg}$ [45]	all
Mixture ratio of flame zone	O/F	2.7	with O_2	Marxman, Zilliac
Specific heat of flame gas	$c_{p,c}$	7880	$\frac{J}{kg\,K}$ [45]	Marxman & Zilliac
Specific heat of fuel vapor	$c_{p,vap}$	2386	$\frac{J}{kg\,K}$ [45]	Marxman & Zilliac
Temperature of combustion	T_c	3701	K [45]	Marxman, Zilliac, vapModelImproved
Temperature of vaporization	T_{vap}	930	K [45]	all
Heat of formation	$H_{f,sp}^{\theta}$	-380	$\frac{kJ}{kg}$ [67, 68]	all
Specific heat of solid fuel	$c_{p,s}$	2900	$\frac{J}{kg\,K}$ [65]	all
Thermal conductivity of solid fuel	k_s	0.14	$\frac{W}{m\,K}$ [65]	all
Regression rate coefficient a	a_{sp}	0.0903	[45]	stdHybrid
Regression rate coefficient b	b_{sp}	0.527	[45]	stdHybrid

To compare the regression rate a simplistic ESPSS schematic has been created. It consists only of an oxidizer inflow, a mass flow control junction, the hybrid rocket engine model and two insulations, as shown in Figure 4.1. The hybrid rocket engine has 10 subsonic nodes in the chamber, of which nodes 2 to 7 are with solid fuel (HTPB). Nodes 1, 8, 9 and 10 are used as pre- and post-combustion chamber. The solid fuel has an inner diameter of 80 mm and the chamber has an inner diameter of 120 mm. The nozzle throat diameter is 60 mm and the LOX mass flow is set to 3.5 kg/s. As the fuel is a single port design, the fuel needs to be 1.8 m long for this oxidizer mass flow. This results in a thrust of about 10 kN. Figure 4.2a and Figure 4.2b show the regression rate of the hybrid rocket engine with the "stdHybrid" model which uses the regression rate law $\dot{r} = a_{sp}G^{b_{sp}}$. In Figure 4.2a G_{ox} was used for the mass flux, which is defined with the oxidizer mass flow per flow area. This is an often used correlation in experimental investigations. For Figure 4.2b the total mass flux G_{tot} was used. As the total mass flux is increased by the transferred fuel mass flow in every node, it is visible that the regression rate is getting higher along the fuel grain. As mentioned before, the first option is more precise if the regression coefficients are determined by experimental investigations. The
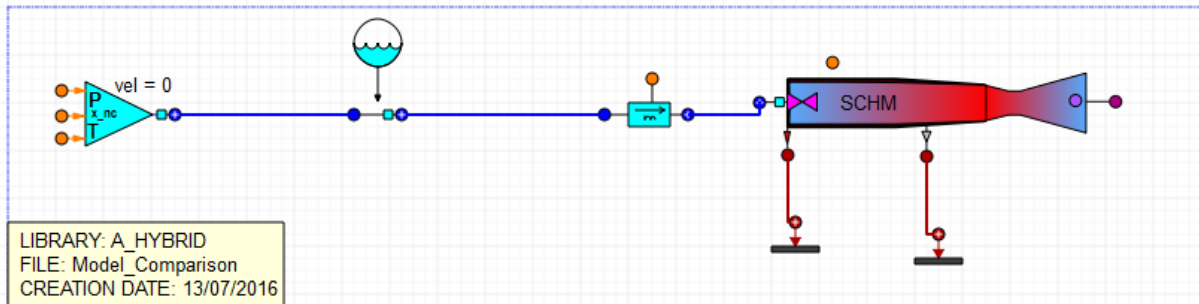

Figure 4.1.: Schematic of ESPSS model for regression rate comparison

second option is more realistic, as the regression rate in a node along the fuel grain will not react instantaneously to a change in the injected oxidizer mass flow but only after a time delay, when the mass flow actually reaches a node. For a very long fuel grain however, this model will not predict the regression rate very well, as the mass flux G_{tot} will always increase and therefore the regression rate will always increase, which is not the case in reality, where other effects will reduce the regression rate (like the blocking effect). Figure 4.2c and Figure 4.2d show the results with the regression rate models by Marxman and Zilliac. Marxman's law was developed for a flat fuel slab and has higher deviations to experimental results in cylindrical fuel shapes. In the left graph it is visible that the regression rate in the first node is quite high and then the blocking effect reduces the regression rate in the following nodes. These effects were avoided by Zilliac in his improved model. The right graph shows that the regression rate is lower in the first node and is again increasing towards the rear end. While it looks here like Zilliac's model would neglect the blocking effect, simulations with a longer fuel show that the regression rate at the rear end of the fuel grain will reach a maximum. Additionally the models using the mass flux density G as an input parameter, also are dependent on the amount of nodes in the model. More nodes make these laws more convergent and precise.

In Figures 4.3a and 4.3b the regression rate for the vaporization model based on the thermal balance near the fuel is depicted. It is easy to detect that the basic ESPSS model "vapModel" in Figure 4.3a is overestimating the regression rate by one magnitude with realistic input values. This is because it neglects the heat of formation of the decomposed gases. The improved vaporization model in Figure 4.3b predicts the regression rate much better, but still overestimates it. This is explained by the missing effects which reduce the heat transfer from the gas flow to the surface, like the blowing effect and the growing thickness of the boundary layer.

Figure 4.3c shows the regression rate and Figure 4.3d the pressure at the 4th node of the combustion chamber for the different regression rate models. These graphs give a feeling for the ability of the models to predict a combustion process in a hybrid rocket engine with classical fuels. The models by Ziliac and Marxman give the closest approximation and the deviation to the "stdHybrid" model, which is using the parameters gained by experimental data, is quite small. The advantage of these models is that they can be applied for new fuels where no experimental data were available. In these cases they give a first idea of the fuel's performance. The vaporization model is much simpler and therefore cannot give a very precise approximation. In total, the model of Zilliac and Karabeyoglu is promising to give a good prediction for a cylindrical fuel geometry. The drawback is that this model relies on the largest amount of fuel properties as an input. This is difficult if the fuel properties are not so well known yet. These models can only be applied to classical fuels that do not form a melt layer on the surface. It will also not be possible to design a hybrid rocket engine only with one of these models without basic research on the selected propellant combination's behavior, both theoretically and experimentally.
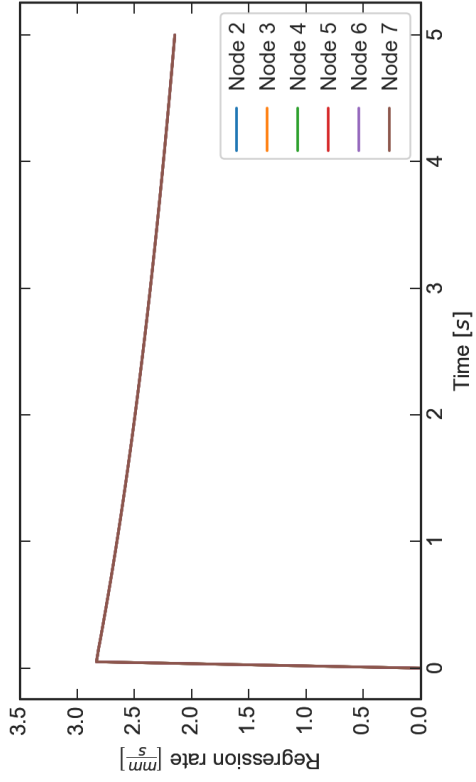
(a) $\dot{r}$ with "stdHybrid" and G_{ox} option
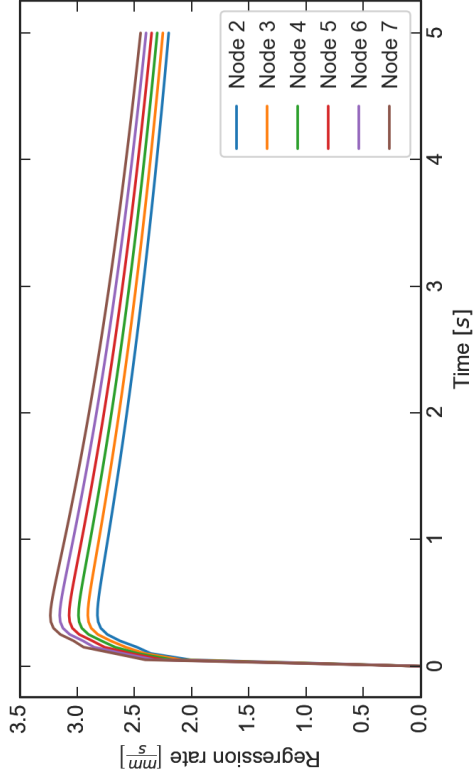
(b) $\dot{r}$ with "stdHybrid" and G_{tot} option
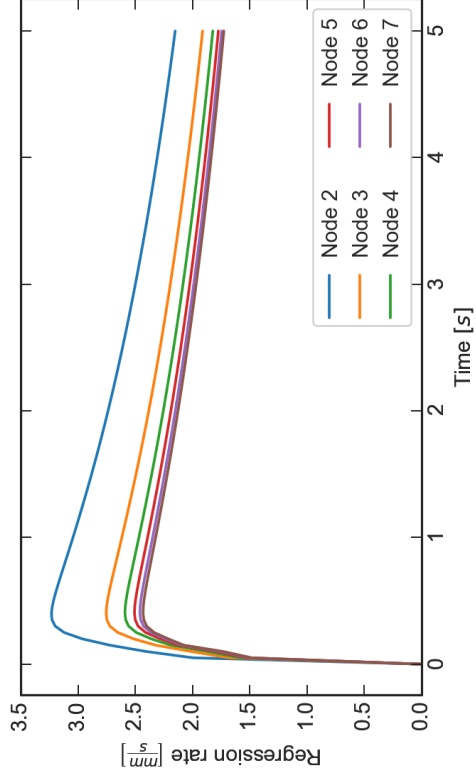
(c) $\dot{r}$ with "HybridMarxman"
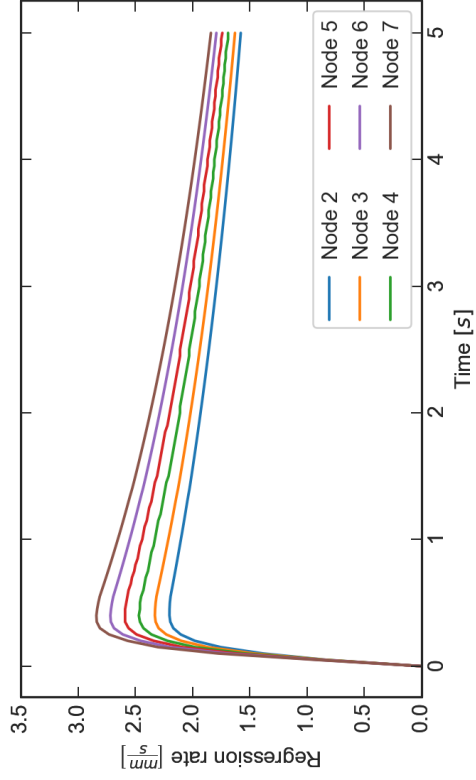
(d) $\dot{r}$ with "HybridZilliac"

Figure 4.2.: Regression rate and pressure of different models for classical fuels, part 1
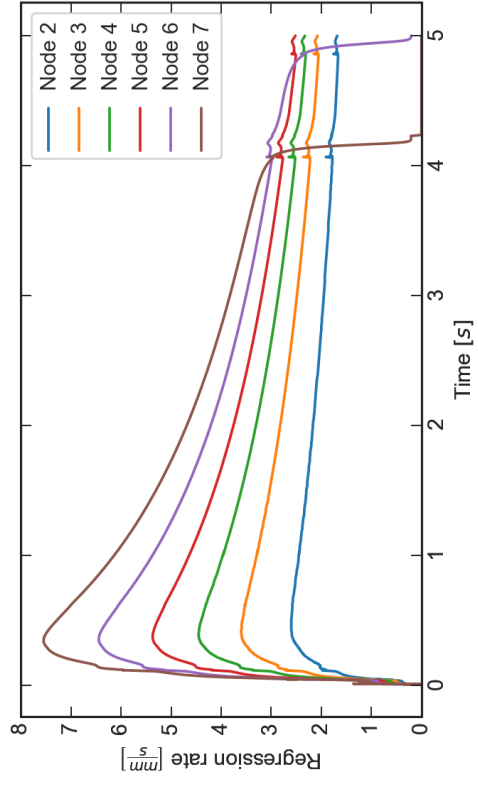
(a) $\dot{r}$ with "vapModel"
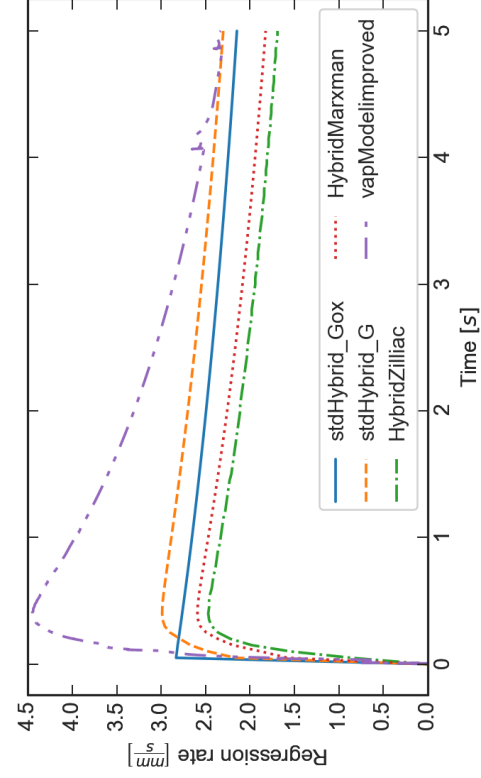
(b) $\dot{r}$ with "vapModelimproved"

(c) $\dot{r}$ at the 4th node with different models
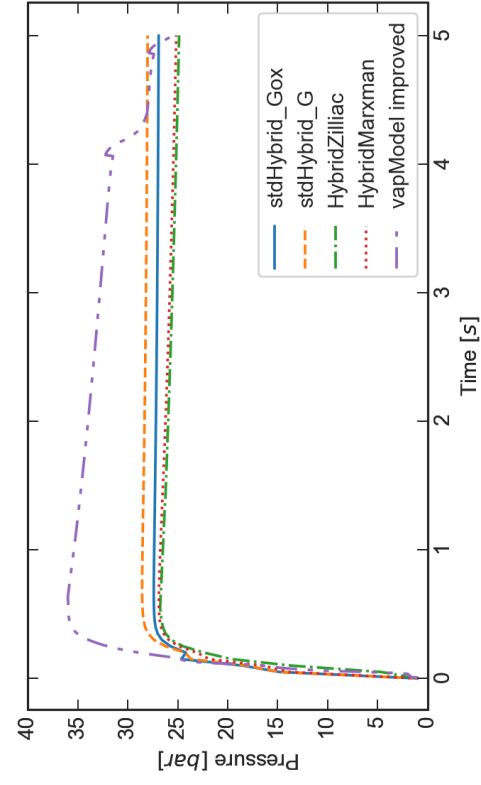
(d) pressure at the 4th node with different models

Figure 4.3.: Regression rate and pressure of different models for classical fuels, part 2

In the following the simulation of liquefying, paraffin-based fuel PB-5% is displayed. While all other hybrid rocket engine parameters stay the same compared to the chamber using classical fuel, the chamber length is reduced to only 0.5 m. The fuel thickness must be increased to 35 mm to sustain a burn time of at least five seconds. The advantage of a liquefying fuel immediately becomes clear: the fuel is much shorter for the generation of the same thrust level. However, if the diameter stays the same, the burning duration is of course much lower, because the fuel mass is also much lower. To have the same thrust for the same burn duration, a hybrid rocket engine with liquefying fuel needs a much higher diameter than with a classical fuel. If the engine dry mass is the critical factor for the application of a rocket engine, it is possible that the optimal chamber length to diameter ratio is reached for regression rates in between liquefying and classical fuels.

Figure 4.4a and Figure 4.4b illustrate the results of a simulation of a hybrid rocket engine with liquefying fuel using the model by Karabeyoglu for liquefying fuel's regression rate. The regression rate is between 1.5 and 3 times higher than with the classical fuel regression rate models. Going along the fuel with the increasing nodes from 2 to 7, the regression rate is increasing. This is due to the high dependency of the modeled regression rate on the local mass flux G. Since the optimal mixture ratio of oxygen and the paraffin-based fuel is around 2.9, the increase in the mass flux caused by the fuel mass flow has a high impact. The last fuel nodes regress faster and therefore are depleted after a shorter time. This results in this step-like depletion, which is also clearly visibly in the pressure curves. This high dependency of the regression rate on the mass flux and therefore on the position of the fuel length is not congruent with experimental results, however the trend is correct. With tuning the model's coefficients α and β, experimental results could be matched better. For this simulation $\beta = 1.85$ was chosen. One particularity of the shown regression rate curves in Figure 4.4a is, that the regression rate of a node increases in steps every time a node at the end of the fuel grain is depleting. The reason for this is found in the equations. The entrainment regression is dependent largely on the parameter X_e in the Equation 3.24. This parameter again is following the inverse of the density in the gas flow core via the dynamic pressure P_d. Obviously when a node is depleting in the simulation, the fuel mass flow drops. This causes a pressure drop in the combustion chamber. Hence, the density drops which increases the dynamic pressure, and therefore the regression rate in the remaining fuel nodes. This effect could not be observed in experiments right now. Mainly, because the depletion of fuel grain segments does not happen abruptly like in the simulation. For the future a more refined model of the fuel surface could improve this. One suggestion is to simulate the fuel not as cylindrical segments but as trapezoids. However this requires larger modifications to the ESPSS component model. For an evaluation of the influence of the node number a simulation with 50 instead of 10 subsonic chamber nodes has been done. Figure 4.4c shows that the regression rate is a bit smaller than with more nodes, however the overall trend is similar. Only 5 out of 43 regression rates for the different nodes have been plotted for clarity. Since the discretization is much finer, the pressure curves in Figure 4.4d have much more but smaller steps.

To compare the simulation's result with experimental data, a simulation with the "stdHybrid"-model using the coefficients $a = 0.117 \cdot 10^{-3}$ and $b = 0.62$ has been done, representing the empirical regression rate law. The results are displayed in Figures 4.4e and 4.4f. It must be noted that these regression coefficients were compiled from small scale hybrid rocket engine tests. The regression rate law was used with the total mass flux G, which is why there is also a dependency of the regression rate on the position along the fuel length. The magnitude of the regression rate is well comparable to the results of the simulation with Karabeyoglu's model.

4.2.6. Problems of the Regression Rate Models

The regression rate models implemented for classical and liquefying fuels all rely on a high number of fuel input parameters like viscosity, surface tension etc. Additionally the model for classical fuels by Zilliac and the liquefying fuel model by Karabeyoglu need data that could only be modeled in a 2D or 3D discretized chamber like flame sheet temperature, heat transfers between core flow, flame sheet, fuel vapor, fuel liquid layer and solid fuel. Simulation of such values that are dependent on the boundary flow and flame sheet inside the boundary flow needs a spatial discretization. With a 2D or 3D discretization however, it will be possible to simulate the flames and calculate some values, that by now are user input: Flame temperature T_c, local flame mixture ratio $O/F_{c,x}$, boundary layer viscosity μ etc. Different oxidizers are not considered in the models. The models are therefore only valid with the oxidizer which they were compared to. In the presented cases this is oxygen. To some extent the choice of oxidizer has also an impact on the models (e.g. gas flow density or viscosity, temperature) but it needs to be carefully evaluated if the models actually are predicting realistic values. The liquefying model shows a very high dependency on the mass flux density parameter G. This results in an increasing regression rate downstream of the fuel. This effect is observable in experimental investigations, but not as drastic as in the simulation results. All newly implemented regression models also show a high dependency on the number of nodes. In some cases, simulations with more nodes do not necessarily match experimental results better than with fewer nodes. Concluding, the hybrid regression rate models in literature are not at a point, where it is possible to claim that the processes in a hybrid rocket engine are completely understood and modeled. There are still a lot of simplifications and assumptions. This is why the regression rate models, which do not rely on empirical data for the regression rate coefficients a and n, are only useful as a first approach. They cannot replace experimental work for determining the regression rate of a hybrid rocket engine at this current state.
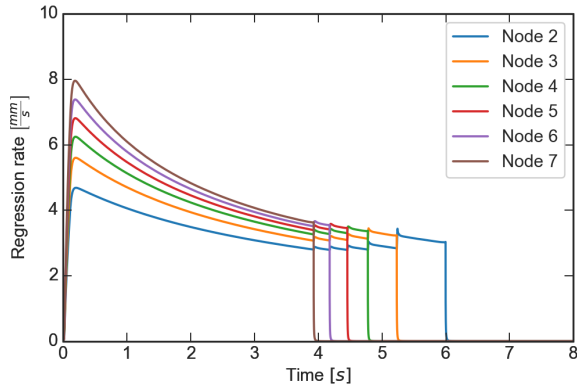
(a) Results for $\dot{r}$ with Karabeyoglu's model
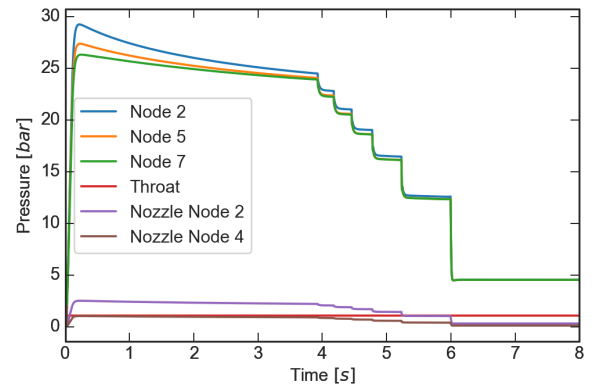
(b) Results for pressure with Karabeyoglu's model
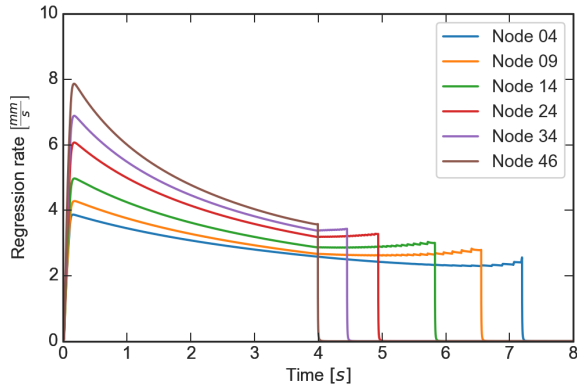
(c) Results for $\dot{r}$ with a finer mesh
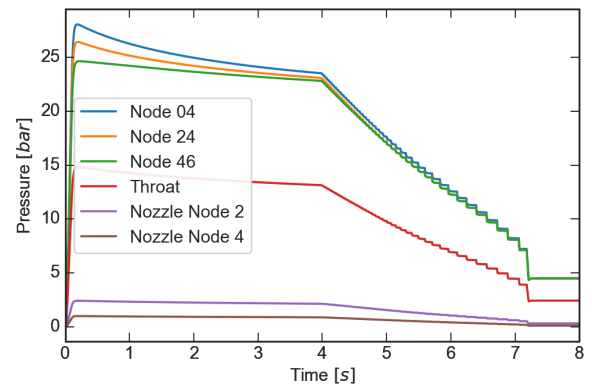
(d) Results for pressure with a finer mesh
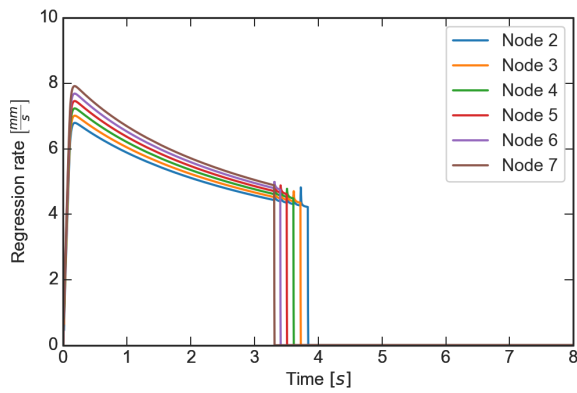
(e) Results for $\dot{r}$ with with "stdHybrid"
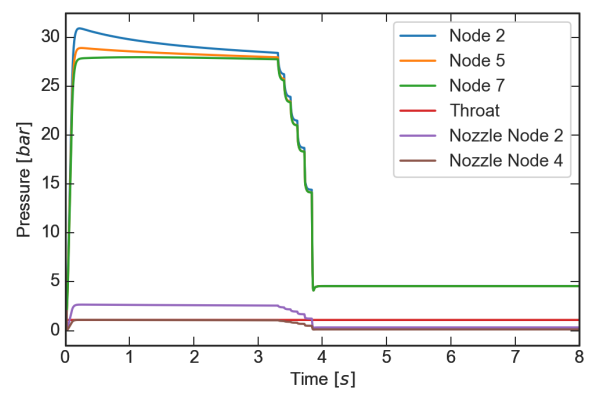
(f) Results for pressure with "stdHybrid"

Figure 4.4.: Regression rate and pressure of different models for liquefying fuels

4.3. ASTOS & ESPSS Interface

In order to link an EcosimPro/ESPSS model to the ASTOS "User Propulsion Interface", the EcosimPro "deck" function is used. The concept of the deck is, that the supplier of an EcosimPro model can create a deck and send it to his customer. The customer is only running the deck by setting input variables and evaluating the output variables. He is not changing the simulation model itself. The advantage of a deck is, that it needs no installation and license of EcosimPro. It is also possible to run a deck directly from a C++ code. This interface option is used to link the deck with ASTOS. With this it is possible to link any deck to ASTOS. Starting from basic models, which consist only out of a combustion chamber and a few lines, up to complex models, with tank pressurization or pumps, all kind of models can be used to link a deck to ASTOS.

For optimization of a trajectory with a hybrid propulsion system the direct loop with ASTOS and a ESPSS deck is not a viable. During optimization ASTOS' algorithm changes many parameters, controls and states at various points of the trajectory. This results in a very large number of propulsion system calculations for a very short time step. The disadvantage is that ESPSS is especially slow when called only for short integration intervals. In total the expected optimization time with a direct loop of trajectory optimization with ASTOS and propulsion system simulation with an ESPSS deck is extremely high. Therefore another approach is chosen: ASTOS is using the analytical model of section 4.1.3 to simulate the initial guess and afterwards optimize the trajectory. Then in a second step the thrust and mass flow of the hybrid propulsion system is simulated with the respective ESPSS deck and the propulsion system parameters and control gained by the optimization. Table 4.4 lists the inputs that are passed from ASTOS to the deck. The simulation of the ESPSS deck will result in a curve for the mass flow and the thrust that has higher precision due to the following points:

- Gradients on the thrust instead of instantaneous changes with control adaption
- Much more precise performance calculation
  - Combustion properties like c^*, c_F or T_{cc}
  - Thermal losses to the chamber wall
- 1D discretization
  - Impact on gradients: Very long chamber will act differently than a short one
  - More precise information about regression rates per node
- Lateral fuel regression possible
- Liquid oxidizer vaporization rate
- Different (initial) fuel diameters possible
- Multiple evaluation points (oxidizer dome, injector,pre- & post-combustion chamber) for temperatures, pressures, massflows, heat flows etc..

With more complex ESPSS models the decks could also simulate:

- Tanks & pressurization systems (helium or other gases)
- Pumps (electrical or with gas generator/preburner)
- Clustered combustion chambers
- Effects of reaction control thrusters on the main engines

Since the thrust and mass flow curve of the ESPSS deck simulation is in most cases not congruent another optimization process can be done afterwards. Optimization will again be conducted with the analytical model, since the ESPSS model itself is not working with the optimization of ASTOS. Therefore, correction factors for the vacuum specific impulse, oxidizer and fuel mass flow mass flow for the average values are evaluated and the analytical model's results are corrected with these factors.

4.4. Software Verification

Both ASTOS (Analysis, Simulation and Trajectory Optimization Software for Space Applications) and ESPSS (European Space Propulsion Systems Simulation) are commercially available tools. It is started from the premise that both software tools are verified for their field of application. In case of ASTOS this means that the modeling of equations of motions, coordinate system transformations and all other aspects coming with the software are not doubted in their physical and mathematical correctness. However, to test the integrity of modeling trajectories from Earth to Moon, a simulation and optimization of Apollo 11 and Luna 24 trajectories is done in order to detect possible problems. For example, in earlier versions of ASTOS problems with the coordinate system change from an Earth to a Moon centered orbit were

Table 4.4.: Input data for the ESPSS deck

Name	Symb.	Type	Name	Symb.	Type
Burning time	t_b	Param.	Injector zeta coefficient	ζ	Const.
Chamber length	L_c	Param.	Nozzle efficiency	η_{c_F}	Const.
Chamber to throat diam. ratio	D_c/D_t	Param.	Nozzle expansion ratio	ϵ	Param.
Combustion efficiency	η_{c^*}	Const.	Nozzle length	L_d	Const.
Fuel density	ρ_f	Const.	Nozzle ambient pressure	p_{amb}	Param.
Fuel initial thickness	$t_{sp,ini}$	Param.	Nozzle throat diameter	d_t	Param.
Fuel length	l_{fu}	Param.	Oxidizer inflow pressure	P_{in}	Const.
Fuel regression coefficient	a	Const.	Oxidizer inflow temperature	T_{in}	Const.
Fuel regression coefficient	n	Const.	Oxidizer mass flow	$\dot{m}_{ox}$	Control
Igniter massflow	m_{ign}	Const.	Working fluid		Oxidizer
Injector area	A_{inj}	Const.	Working fluid non-condens.		Pressurization gas
Injector volume	V_{inj}	Const.			

found. These problems were already fixed in a recent ASTOS update. For ESPSS it is assumed that all aspects of modeling and solving the systems of equations are correctly implemented. The verification for the user propulsion model that was implemented for ASTOS including an interface to an ESPSS deck was done with simulation and optimization of a hybrid micro launcher and a lunar lander module. No data was available for comparison but the main goal was to verify the functionality of combined optimization of the trajectory and the propulsion system parameters. Parts of this work were also published in [69].

4.4.1. Simulation of Moon Transfer and Landings

Apollo 11

In Chapter 2 the Apollo 11 mission was already described in some detail. Many information about the ascent, orbit, mass balance and impulsive maneuvers of the Saturn V launch vehicle as well as the Apollo 11 spacecraft are listed in "Apollo by the numbers"[10]. However not all information is available in such a high detail that the trajectories could be reconstructed without any free parameters. But even with some missing information the launch with Saturn V, the translunar orbit as well as the landing of the Lunar Module of Apollo 11 could be reconstructed with ASTOS. Table 4.5 shows some important parameters which were needed to simulate the launch of Apollo 11 on the Saturn V. The first stage S-IC was burning for about 160 s. However, after 135 s the center engine was cut off and only four engines continued burning. This is why in the simulation of the launch there are the two phases 3. and 4., which represent these two trajectory parts of the launch. In the same way the second stage S-II had a burning phase with five engines and four engines (6. and 7.) too. The reason for this is, that the acceleration needed to be reduced for the astronauts. If all five engines would have continued to burn the acceleration would have been too high at the end of the burning phase. The Saturn V rocket first launched the spacecraft into a low Earth orbit which is shown in Figure 4.5a. The simulation and optimization could reach the target orbit with a similar amount of used propellants like stated in [10]. The Saturn V launch was highly complex with ullage motors for stage separation, ejection of the escape rocket, ejection of stage adapters and others. Therefore it was not possible to reconstruct the launch in absolute detail in ASTOS since precise information about every process was not available, but the result is adequate. In the ASTOS simulations the used propellants for S-IC is ca. 2091.3 t, for S-II it is ca. 436.7 t and for S-IVB it is ca. 32.6 t. For the actual launch of Saturn V the propellant usage for the first stage was calculated as 2113.8 t, for the second stage as 436.7 t and for third stage as 31.4 t. Therefore the simulation shows a very high agreement with the real launch.

After the ascent of Saturn V into Earth orbit, the third stage S-IVB stayed attached to the spacecraft and after about 2 h 30 min the S-IVB was ignited again to inject the spacecraft onto its translunar orbit. In this phase of the simulation 71 450 kg of propellants were used, while in reality about 71 050 kg were necessary. Afterwards the spacecraft was separated from the rocket. The orbit transfer was a free-return trajectory. This means the spacecraft was aimed

Table 4.5.: Launch details for Apollo 11

Apollo 11	45 693 kg	Launch date	16th July 1969	Launch time	13:32 UTC
Launch site longitude		−80.6041°	Launch site latitude		28.447°

Ascent phases		3. Gravity turn (5 eng.)		6. 2nd stage (5 eng.)	
1. Vertical takeoff		4. Gravity turn (4 eng.)		7. 2nd stage (4 eng.)	
2. Pitch over		5. Separation		8. Separation & 3rd stage burn	

Target orbit					
Inclination	32.55°	Apogee	185.9 km	Perigee	183.2 km

Launch vehicle information					
Stage	Empty mass	Gross mass	Propellant mass	Vacuum thrust	$I_{sp,vac}$
S-IC (1st)	138 713 kg	2 261 991 kg	2 123 278 kg	39.9 MN	304 s
S-II (2nd)	39 856 kg	483 091 kg	443 235 kg	5.2 MN	421 s
S-IVB (3rd)	11 943 kg	119 038 kg	107 095 kg	916 kN	421 s

to fly around the Moon in such a way, that after passing the Moon the spacecraft was again on an Earth-centered orbit with a low perigee. This would allow a return of the crew in case of an engine failure. The free return trajectory is also faster than a more propellant efficient trajectory like a Hohmann Transfer, which takes about five days. The Apollo 11 spacecraft was underway for three days until the lunar orbit insertion. In the simulation with ASTOS the free trajectory return was reproduced. However some orbital element information was missing, therefore it cannot be analyzed how close the simulation is in reference to the real mission. The periselen at the lunar flyby is 100 km. After leaving the Moon's sphere of influence the apogee of the free return trajectory is about 550 Mm while the perigee is below 80 km, which provides an atmospheric reentry without further orbit maneuvers. Figure 4.5b shows the free return trajectory of Apollo 11 as simulated by ASTOS. The blue circle represents the Earth, while the black curve is the orbit of the Apollo 11 spacecraft. The green dotted line represents the Moon's orbit around the Earth. The view is from above the Earth's North pole. The Moon is therefore moving from the upper side to the lower side. ASTOS' ability to simulate and optimize multibody orbits proves very useful to analyze this kind of mission. A bit more than three days after lift-off the spacecraft of Apollo 11 was injected into a Moon orbit by a burn of the AJ10-137 engine of the Command & Service Module. This burn took about 358 s in the flight, while it takes 418 s in the optimized simulation. The reason for this is, that the throttle control for this engine was given to the optimizer and it reduced the throttle in the beginning. The exact throttle of the engine and amount of propellant in the real flight is not available in literature. The total propellant consumption in the simulation is 11.6 t. The orbit after insertion is defined with a periselen of 111.1 km and an aposelen of 314.3 km. However, the inclination and argument of periapsis and right ascension node is not listed in the reference. The inclination at the Moon in the simulation results in 174.3°, which is a retrograde orbit near the equatorial plane of the Moon. After 4 h of orbiting, which represents roughly two revolutions, the orbit was changed another time to circularize it further. In the simulation this

(a) Ascent trajectory of Apollo 11 on Saturn V   (b) Free return trajectory
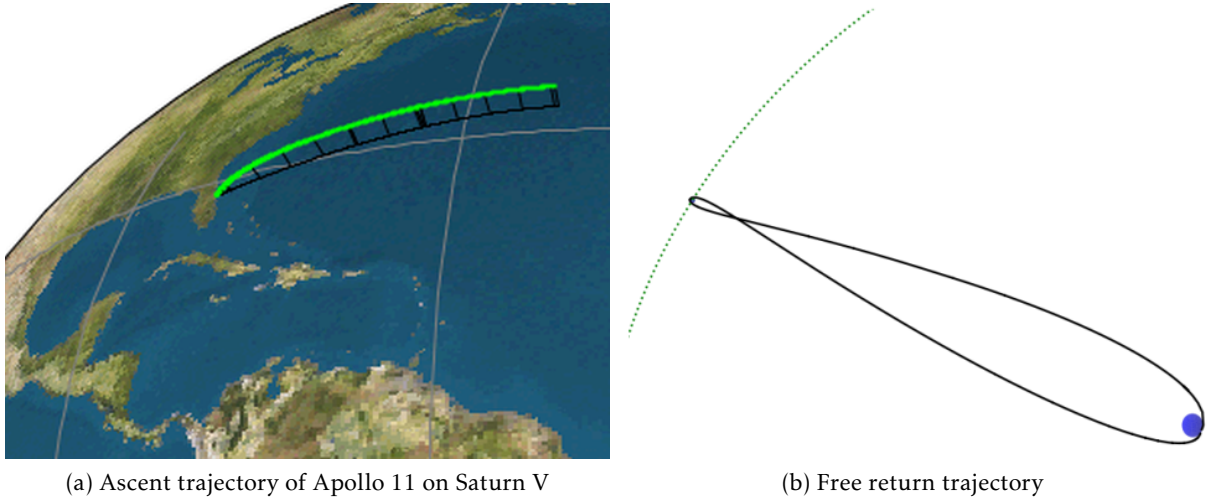
Figure 4.5.: Apollo 11 reconstruction results

burn takes 24 s, while it took 17 s in the actual mission. Again, this difference is caused by the free throttle control in the simulation. The final orbit then is 100.9 km × 122.4 km. 688 kg of propellant are used in the simulation of this circularization burn. The propellant usage of the real spacecraft is not listed in [10]. After this burn the Lunar Module is decoupled from the CSM and commences its descent to the surface.

In the description of the lunar descent it is reported, that the lander descended to about 750 m above the surface, when a horizontal flight was initiated to find a better landing spot. The exact details are not given, but the ASTOS simulation was set up in a way to represent this horizontal flight. This final descent and the horizontal flight phase is shown in Figure 4.6. Figure 4.7 illustrates the velocities during this final descent. Not enough data was available to find out in which direction the final horizontal flight happened. Therefore it was simply modeled that the spacecraft was flying to its final landing spot, which is on 0.674° North and 23.473° East. When reaching an altitude of about 750 m the radial velocity is reduced close to zero and it is kept for about a minute. Then the lander descends to the surface and lands with about 1 m/s. The propellant reserves after landing of Apollo 11 were about 350 kg, while in the ASTOS simulation 500 kg remain. An explanation is, that the ASTOS simulation does not account for reaction control thrusters. The optimization progress worked flawlessly to find this trajectory. In sum ASTOS is a very powerful tool to reconstruct, simulate and optimize translunar trajectories like the Apollo 11 mission. Even if not all details are reported for every orbital maneuver, with the use of the optimization process, the trajectory and its missing data can be found by fulfilling the boundary and path constraints.
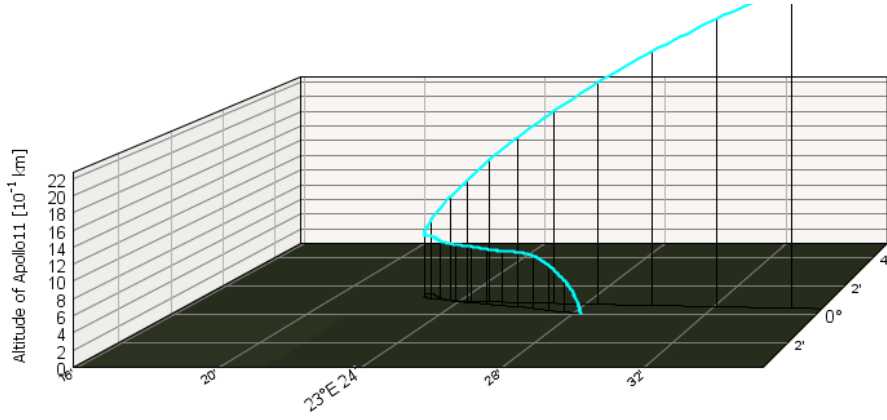
Figure 4.6.: Descent trajectory of Apollo 11 Lunar Module close to the Moon's surface in ASTOS
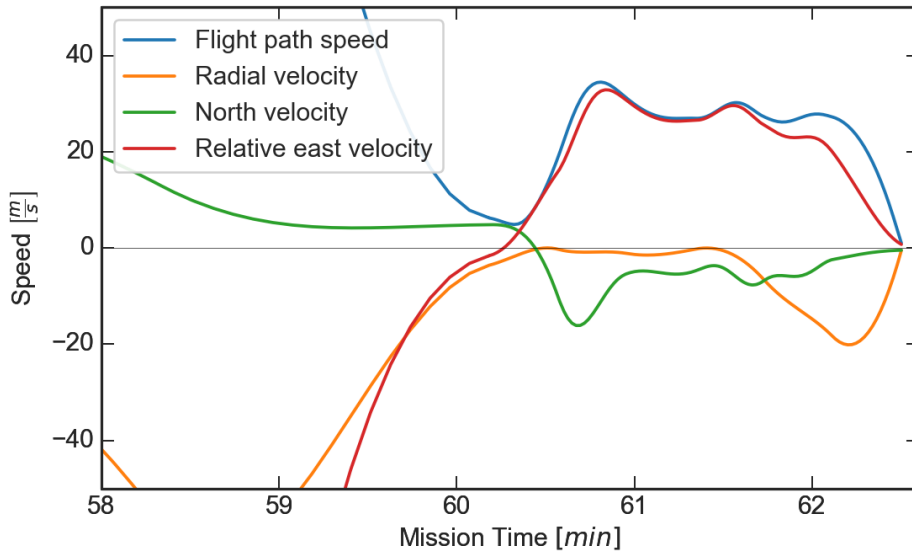
Figure 4.7.: Velocities of Apollo 11 Lunar Module during the final descent in ASTOS

Luna 24

The Luna landing and sample return missions are as well described in in Chapter 2. The trajectory of Luna 24 was reconstructed with the help of the ASTOS software. In the first ASTOS scenario the launch of Luna 24 with a Proton-K launch vehicle was simulated and optimized to reach the correct orbits. Table 4.6 lists the necessary data for the ascent trajectory optimization. All stages of the rocket used N_2O_4 and UDMH as propellants. The information has been gathered from different online sources [70, 71, 72]. The model of the launcher was set up with this information. Details about aerodynamics of the launcher were missing. Therefore a rough estimation of the drag coefficients was done. The aerodynamic losses are relatively low. This is why the impact of the aerodynamic model is small. The simulation of the launch was necessary, since detailed information about the transfer from Earth orbit to the Moon

were not available. By simulating the launch, the starting orbit for the transfer, which is the Earth centered nearly circular orbit of 243 km × 188 km, could be determined more closely. The missing orbital elements could be determined in this way.

Figure 4.8 shows the ascent trajectory on a 3D globe. The launch site Baikonur allows only launches in certain corridors, which explains the high inclination. The trajectory of Luna 24 after the launch was reconstructed. For the simulation of the transfer to the Moon, the missing orbital elements were determined and are listed in Table 4.6 too. These values do not necessarily match with the real orbital elements of Luna 24, except for the known elements inclination (51.5°), apogee (243 km), perigee (187.5 km) and the time of orbit insertion. But this set of elements allows to further simulate the trajectory from a very realistic starting point. The transfer trajectory with the burn of Blok-D upper stage as well as the course correction, orbit injection and descent to the Moon's surface was simulated in one single ASTOS scenario, which is a great proof for the usefulness of this tool for such multi-body trajectory problems. The

Table 4.6.: Launch details for Luna 24

Luna 24	5795 kg	Launch date	9th Aug. 1976	Launch time	15:04 UTC
Launch site longitude		63.34°	Launch site latitude		45.92°

Ascent phase		2. Pitch over		4. 2nd stage burn	
1. Vertical Takeoff		3. Gravity turn		5. 3rd stage burn	

Missing orbital elements					
Argument of perigee		85.0°	Ascending node		−163.2°
Mean anomaly		−1.7°	3rd stage separation		15:13:30 UTC

Target orbit					
Inclination	51.5°	Apogee	243 km	Perigee	188 km

Launch vehicle information					
Stage	Empty mass	Gross mass	Propellant mass	Vacuum thrust	$I_{sp,vac}$
1st	31 100 kg	450 510 kg	419 410 kg	10 470 kN	316 s
2st	11 715 kg	167 828 kg	156 113 kg	2399 kN	327 s
3st	4185 kg	50 747 kg	46 562 kg	613.8 kN	325 s
Blok-D	2140 kg	17 360 kg	15 220 kg	83.6 kN	363.5 s

Figure 4.8.: Trajectory of Luna 24 on the Proton-K launch vehicle in ASTOS

transfer was divided in the following phases: 1. Coast on the original Earth-centered orbit to reach the best point for the impulsive maneuver of Blok-D; 2. Burn of Blok-D and Separation; 3. Coasting Phase; 4. Course Correction; 5. Coast to the Moon's vicinity (Sphere of Influence is about 60 000 km); 6. Coast (from now on all phases are simulated Moon-centered); 7. Moon orbit injection burn; 8. Orbit lowering burn; 9. Descent coast; 10. Deceleration Burn; 11. Final vertical descent coast; 12. Soft landing phase. Because no exact information about phasing orbits around the Moon was given, the orbit injection to a 115 km circular orbit is directly followed by the orbit change to a 12 km × 120 km orbit. In the real mission there were phasing orbits for several days to reach the final landing destination. The orbit injection at the Moon was on 14$^{\text{th}}$ August 1976 while the landing was on 18$^{\text{th}}$ August. This was neglected in the simulation, but it does not affect the necessary ΔV. The landing site however is not the correct one in the simulation. The orbit and spacecraft data that was found in the before mentioned online sources are:

- Initial lunar orbit: 115 km circular with 120° inclination

- Final lunar orbit: 12 km × 120 km with 120° inclination

- Deorbit and soft touch down: 6 min duration and about 3 m/s touch down
  speed

- Luna 24 spacecraft mass: 5795 kg including 3606 kg propellant

The Luna 24 spacecraft also contains the return rocket with 515 kg.

Figure 4.9a shows the altitude of the Luna 24 spacecraft in the ASTOS simulation after optimization. The optimization was done with regard to all known orbit elements as constraints and in addition the used fuel mass was optimized, to have more reserve propellant. The vertical lines show the phase borders. After one day the course correction is simulated. The course correction is not necessary in the optimization within ASTOS, as the simulation and optimizer always reach the optimum attitude and impulse. However, to meet the propellant consumption better, a course correction phase was included, and the results showed, that with this course correction phase, the optimizer was actually able to find the optimal result faster. The change from a Earth-centered coordinate system to a Moon-centered one is visible after about 3.5 days. Figure 4.9b enlarges the altitude curve in the last 60 min after surpassing 200 km. The orbit injection burn begins already at about 180 km, due to the high radial velocity in the hyperbolical orbit. The margins for the correct burns are quite small. Start, end and total impulse of the burn need to be very precise in such a mission. After the 280 s long orbit injection burn, the impulsive maneuver to lower the perigee to 12 km requires only a short burn duration of 10 s. Then the coast phase follows over half a revolution around the moon. Afterwards the final deceleration burn lowers the velocity close to standing still. This is illustrated in Figure 4.9c. The flight path speed of the Luna 24 spacecraft when reaching the Moon's vicinity is about 2.4 km/s, which means an excess velocity of 0.9 km/s in the hyperbolic trajectory. The speed after the orbit injection is 1.6 km/s. The plotted east velocity is relative to the Moon's surface. The final soft landing is visible nearly 60 min after getting below 200 km

altitude. First, the orbital velocity of the $12\,\text{km} \times 120\,\text{km}$ is reduced to a standstill relative to the Moon's surface. The real Luna 24 mission included a similar approach, although the precise data was not available. The standstill in the optimization is at $4.7\,\text{km}$ altitude. It could be lowered, if the KTDU-417 engine would be throttled down. Then a thrust-less descent is following, until at about $1\,\text{km}$ above the surface the engine KTDU-417 is ignited again to slow down the spacecraft, since after the standstill the Moon's gravity has again accelerated the spacecraft to $110\,\text{m/s}$ vertical descent velocity. The secondary engine KTDU-417B has just enough thrust to keep the vertical velocity at a constant value. It was only ignited few meters above the surface after KTDU-417 was shut down. In this optimization this was neglected and the KTDU-417 shuts down only few meters above the ground when the velocity of the spacecraft is below $4\,\text{m/s}$. Figure 4.9d shows the last 10 minutes, when the spacecraft descends below $20\,\text{km}$. While Luna 24 back in 1976 did a full automatic landing without analysis of the landing site, which was probably the reason for the failed landing of Luna 18, today a hovering at some kilometer altitude would also allow to pick a suitable landing site in the close area. The Luna 24 mission could be reconstructed with ASTOS from lift-off in Baikonur to the landing on the Moon surface. Even if some orbital parameters and information was missing, the reconstructed trajectory seems very plausible.
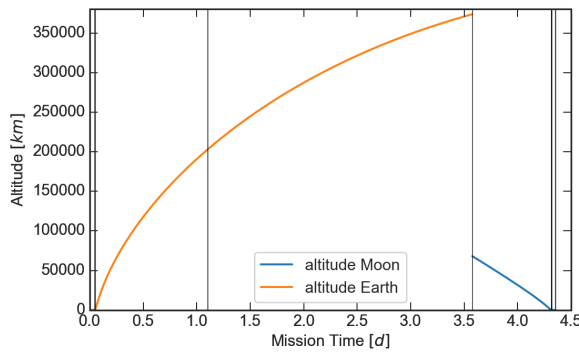
(a) Altitude
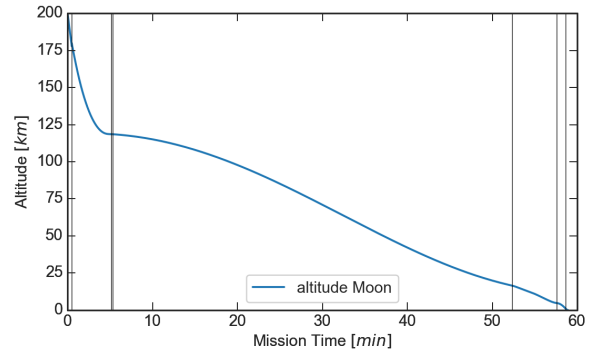
(b) Altitude close to the Moon
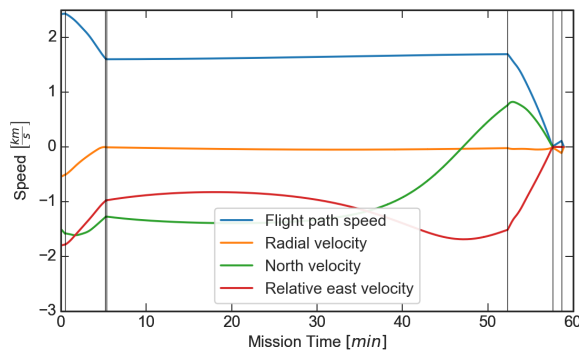
(c) Speed close to the Moon
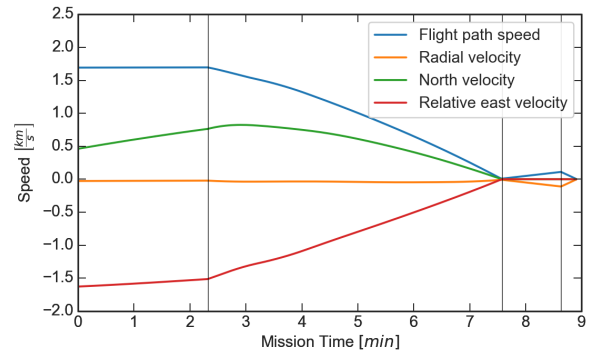
(d) Speed and altitude of the final descent

Figure 4.9.: Luna 24 spacecraft data

4.4.2. Combined Optimization of Trajectory and Propulsion

Optimization Process

The optimization of the following two test cases, a hybrid micro launcher and a lunar lander, was done in these steps[69]:

1. Creation of an initial guess: For the initial guess with ASTOS all mission phases, vehicle parameters like propellant masses or engine geometries need to be set. The initial guess for the trajectory should usually be already very close to the optimum result, in order to increase convergence of the gradient based CAMTOS optimization. Therefore it is quite time consuming to find a good initial control law for the attitude control and adapt all phase lengths to create a good initial guess. Boundaries need to be set for all optimizable parameters and controls. For the optimization in the beginning it is helpful to have rather close bounds for some parameters and controls.

2. Optimization of the trajectory: The first optimization has the goal to calculate a trajectory which meets the final constraints and requirements. The process is faster, if cost functions or constraints for optimizing the total vehicle or payload mass are inactive at first. It also is advisable to have wider path constraints in the beginning and slowly narrow them down with each optimization run.

3. Optimization of initial mass or payload mass: When the trajectory meets all constraints, the cost term for minimum initial mass or maximum payload mass is activated. Some optimization runs will be necessary to find the optimum. It is possible that some parameters or controls run against the boundaries that were initially set closer to accelerate the optimization process. Now they can be loosened.

4. Simulation with ESPSS: When the trajectory and masses are optimized, a simulation with the ESPSS interface is done in order to get the values of the correction factors.

5. Repetition: This process is iterative and is repeated until it converges and a new ESPSS simulation does not change the values of the correction factors anymore.

Hybrid Micro Launcher

Model Set-Up   In order to test the implemented ASTOS analytical tool and ESPSS interface a hybrid propulsion micro launcher was designed in a first draft. The market for small launch vehicles is potentially growing a lot in the next years. The number of launched satellites per year is growing continuously and large satellite constellations are announced like "OneWeb". These constellations pose specific challenges: the satellites are rather small (<500 kg) and have many different orbits. This means launches with multi-payload adapters could be suboptimal for satellite lifetime, as the satellite needs more propellant to reach its final orbit. Also a constellation of hundreds of satellites raises the question of replacing satellites which fail or reach end-of-life. Here is where the small launch vehicles possibly have an advantage over

heavy lift launchers. Therefore, the interest in this kind of flexible launch vehicle has grown worldwide. According to the definition for micro satellites, which have a mass of 10 to 100 kg, a micro launcher based on hybrid rocket engines, with a payload of 25 kg to a 250 km circular polar orbit was defined, simulated and optimized. In contrast to liquid propulsion rockets, hybrid rockets are always limited in their burn duration. For longer burning times, hybrid rocket engines simply get too large. Hence, a three-stage concept was initiated. Table 4.7 shows the trajectory phases of the optimized mission. The first stage burns during the first four phases, after which the stage separation is conducted. While setting up the initial guess, first simulations made clear, that a relatively large first stage causes the rocket to raise its apogee in the beginning very quickly. Therefore, the vehicle's apogee is already close to the final orbit altitude right after the burn of the first stage. Hence, after depletion of the first stage, an ascent coast is inserted. The second stage is only ignited in high altitude, to raise the perigee. Another coast phase is included between the second and third stages' burn. The third stage circularizes the orbit. The arrow symbol "→" indicates the change from the initial guess to the optimized parameter value. For a successful optimization process, several boundary constraints are set in the ASTOS model. Table 4.8 presents a list of the active constraints in this model. None of the mentioned boundary constraints are unique to a hybrid rocket. These constraints are rather the minimum set necessary to optimize a three stage launch vehicle to a circular, polar orbit.

Table 4.9 shows the initial and optimized mass parameters for the micro launcher concept. Only rough estimations were done for the structural masses. The structural mass includes also masses of GNC electronics & instruments, batteries etc. Even if the total launcher mass changed, these structural masses for all three stages were not optimized, as it is not of high importance in order to demonstrate that the hybrid propulsion tools are working as expected. Additionally, the aerodynamics of the launcher were also very rough estimations. In Table 4.10 the initial and optimized engine parameters are listed. The propulsion system is designed to use paraffin-based fuel and H_2O_2 as an oxidizer. The first stage uses seven parallel rocket engines fed from one oxidizer tank, while the second stage uses four parallel engines. The upper stage uses a single engine. The optimizer can also change the throttle of all three stages.

Table 4.7.: Trajectory phases[69]

	Name	Description	Burning	Duration		
1.	Lift-Off	Vertical take-off	1st stage	0.2 s	→	0.1 s
2.	Pitch Over	Constant pitch rate	1st stage	11.8 s	→	4.1 s
3.	Pitch Constant	Transition to gravity turn	1st stage	6 s	→	3.3 s
4.	Gravity Turn	Angle of attack is zero	1st stage	47 s	→	42.5 s
5.	Ascent	Ascent with stage & fairing separation		130 s	→	100.2 s
6.	Stage 2 burn	Orbit raising	2nd stage	35 s	→	43.8 s
7.	Coast	Coast to apogee & stage seperation		20 s	→	34.6 s
8.	Stage 3 burn	Final orbit raising	3rf stage	65 s	→	98.8 s

Table 4.8.: Optimization constraints for a micro launch vehicle[69]

Type	Constraint	Bounds	Active in Phase
Initial	Initial position	0 m, 68 °N, 21 °E	1
Initial	Initial radial, north and relative east velocity	0 m/s (landed)	1
Path	Pitch and yaw rate	±2.5 °/s	2,3,6,8
Path	Gravity turn cond.	±0.3 °	4
Final	Maximum orbital inclination	95 °	4,6,8
Final	Residual propellant in all stages	0-10 kg	4,6,8
Path	Maximum acceleration	130 m/s^2	8
Final	Apogee	250 ± 5 km	8
Final	Altitude	250 ± 5 km	8
Final	Perigee	250 ± 5 km	8
Final	Orbit inclination	94.5 ± 0.5 °	8

Table 4.9.: Initial and optimized micro launcher masses[69]

Stage	Component	Optimizable	Initial mass		Optimized
1st	Propellant	Yes	13400 kg	→	8268.3 kg
	Tank structure	Fixed ratio	7.53 % of oxidizer mass		
	Engine structure	Yes	620 kg	→	400 kg
	Additional Structures	No	310 kg		
	Total stage mass		15232 kg	→	9548.9 kg
2nd	Propellant	Yes	1525 kg	→	1538.2 kg
	Tank structure	Fixed ratio	8.77 % of oxidizer mass		
	Engine structure	Yes	130 kg	→	114 kg
	Additional Structures	No	110 kg		
	Total stage mass		1883.2 kg	→	1881.05 kg
3rd	Propellant	Yes	132 kg	→	179.1 kg
	Tank structure	Fixed ratio	9.8 % of oxidizer mass		
	Engine structure	Yes	13.5 kg	→	15.5 kg
	Additional Structures	No	35 kg		
	Total stage mass		216.9 kg	→	270.1 kg
	Payload	No	25 kg		
	Fairing	No	10 kg		
	Total lift off mass		**17332 kg**	→	**11700 kg**
	Total prop. mass		**15057 kg**	→	**9985.6 kg**

The nominal thrust, nominal mean mixture ratio and the burn time per engine are listed in the table. Table 4.11 shows the optimizable parameters that define the hybrid rocket engines of the three stages.

Optimization Results   The initial guess of the trajectory did not reach a circular orbit. The initial trajectory was a suborbital trajectory with an apogee at 420 km and a perigee at −490 km. The optimization goal was therefore to reach the defined final orbit and at the same time reduce the launcher mass. Some of the optimization results are already shown in the tables 4.7, 4.9, 4.10 and 4.11. To reach the final orbit, the burn phases of the second and third stages were prolonged, while the first stage's burn duration was reduced by 15 seconds. The maximal thrust level of the first and second stage was reduced, due to the lowered total mass. The total launcher mass was reduced by 5632 kg (32.5 %). Most of this was saved in propellant mass, where 5071.4 kg (33.7 %) was saved. This was reached by optimizing the mixture ratio O/F and optimizing the expansion ratio as well as the chamber pressure. The expansion ratios however were limited by the stage diameters. There is one limitation in the current model: The optimizer increased the chamber pressure by reducing the throat diameter in all engines, see Table 4.11. This increases the vacuum impulse and decreases engine mass, because the nozzle is getting smaller. However, this requires a higher tank pressure or a pump, which is currently

Table 4.10.: Initial and optimized micro launcher propulsion system[69]

Stage	Engine thrust			Mixture ratio			Burning time		
1st	73 kN	→	61 kN	7.6	→	9.0	65 s	→	50 s
2nd	30 kN	→	28 kN	7.6	→	7.4	35 s	→	43.8 s
3rd	5 kN	→	6 kN	7.6	→	7.6	65 s	→	98.8 s

Table 4.11.: Geometrical engine parameters[69]

Stage	Component	Initial value		Optimized value
1st	Fuel grain length	1.6 m	→	1.25 mm
	Fuel grain diameter	480 mm	→	415 mm
	Nozzle throat diameter	139 mm	→	135 mm
	Nozzle expansion ratio	6	→	4
2nd	Fuel grain length	965 mm	→	915 mm
	Fuel grain outer diameter	300 mm	→	285 mm
	Nozzle throat diameter	92 mm	→	85 mm
	Nozzle expansion ratio	50	→	51
3rd	Fuel grain length	412 mm	→	412 mm
	Fuel grain outer diameter	270 mm	→	274 mm
	Nozzle throat diameter	38 mm	→	33 mm
	Nozzle expansion ratio	60	→	170

not taken into account for the optimization's mass balance. This is a necessary step to improve the model. However, the first optimization results still are very promising. In total, the first stage was reduced most in size, while the propellant of stage two and three was increased. This is expected, as the first stage has the lowest specific impulse due to the limited expansion ratio. Additionally a larger first stage increases aerodynamic and gravitational losses. The optimization of the model was successful and it is a proof that the combined optimization of the trajectory and the engine with the analytical model works as expected. The thrust of the first stage is throttled down 20 seconds after lift-off. Figure 4.10a displays exemplarily the optimized acceleration, thrust and oxidizer mass flow of the second stage during its burn. The mass flow is for a single engine. The oxidizer mass flow, which is the controlled input of the engine model, is throttled down after optimization during the beginning and in the end of the phase. While for the throttling down at the end the cause is quite obvious, the reason for the small down throttling at the beginning is not clear. There are many possible reasons. The optimization is a multidimensional problem, and it is not always easy to understand the mechanisms that prefer one solution over another. This is also one reason for using numerical optimization, because this kind of problem cannot be solved analytically. A possible explanation for the reduced thrust in the first stage and in the beginning of the second stage's burn is that at this part of the trajectory gravitational losses are higher. At the end of the second burn the vehicle's acceleration increases as the mass is reduced every second. Therefore the acceleration reaches the limit of $130\,\mathrm{m/s^2}$ and the four engines of the second stage are throttled down. The acceleration at the phase's end is approximately $130\,\mathrm{m/s^2}$. The limit of $130\,\mathrm{m/s^2}$ was chosen to demonstrate that the path constraints work. The limit is still a bit too high for real applications. For future optimizations an applicable limit according to the payload's requirements will be used. The regression rates and mixture ratios of the three stages' engines are shown in Figure 4.10b. The regression rate of stage 1 and 2 are in a similar range, only the regression rate of the third stage is lower. This is due to the lower mass flux G in this engine, which is also necessary to sustain longer burn times. The mixture ratios of stage one and two show, that the throttling has a major effect on the mixture ratio. The mixture ratio drops by about $10\,\%$. For the propellant combination H_2O_2 and paraffin-based fuel the gradients of the function of specific impulse over mixture ratio are quite small. Therefore this oxidizer could be especially useful for throttling engines. The loss in specific impulse in this case is only $1\,\%$ from $2900\,\mathrm{m/s}$ to $2870\,\mathrm{m/s}$. Figure 4.10c displays some trajectory parameters over time to visualize the optimized ascent to the low Earth orbit. Figure 4.10d illustrates the layout of the micro launcher. It also shows the proportions of stages, engines and tanks. The base diameter is $1.5\,\mathrm{m}$ without fins and the length is $12.5\,\mathrm{m}$. Table 4.12 lists the applied correction factors determined with the ESPSS interface [69]. The pitch and yaw of the launcher is displayed in Figure 4.11a. It is visible that in the third stage's burn there is a great change from lower pitch and yaw values to higher values and then it levels out at a medium value. From experience this behavior is an indication that the density of control points in this phase is not large enough. More control points can be added to improve this. The specific impulse curves in Figure 4.11b show the increase of exit velocity with increasing expansion ratio in every stage. For the second

Table 4.12.: Optimization correction factors[69]

Stage	Oxidizer mass flow	Fuel mass flow	Specific impulse
1st	99.30 %	98.97 %	103.16 %
2nd	99.91 %	99.36 %	100.83 %
3rd	100.31 %	99.67 %	108.8 %

and third stage the specific impulse of ambient and vacuum conditions is identical, therefore the vacuum impulse for these stage is not plotted. Figure 4.11c shows the mass balance of the stages and propellants. A three-dimensional depiction of the launcher's trajectory is shown in Figure 4.11d. The line's color shows the acceleration. The blue zones are the coast phases, where only Earth's gravity is exerting influence. Due to the three stage set-up, the ascent is quite steep and only the second and third stages increase the horizontal velocity.

Lunar Lander

Similarly to the micro launcher optimization a hybrid propulsion lunar lander has been optimized. The results have always been used for the optimizations in Chapter 6. The optimization of this lunar lander is described in Appendix D.

4.4.3. Simulation of a Hybrid Rocket Test

Simulation Model

To evaluate the implemented models in the EcosimPro library ESPSS the test results from test bench M11.3 at the DLR Lampoldshausen were used to compare test and simulation data. Test No. 3 and test No. 4 which are later described in Section 5.2.1 have been used to compare to the simulations. Figure 4.12 shows the ESPSS schematic of the test bench simulation. All parts of the test bench have been modelled with measurements and data sheets of the tubing, valves, coriolis sensor and the orifices. The test bench is divided into three lines: the oxygen supply line, which includes an inflow valve (311), a release valve (313), a coriolis flow meter, which was modelled as a bended tube, a control valve (RV01), which has the smallest flow diameter in the system, and the main valve (312), which is opened at test begin. Additionally there is a nitrogen line for purging the lines and the hybrid rocket engine. Finally there is the line from the main valve to the engine, which includes several pipes, a measuring probe and the engine. The subsonic part of the combustion chamber was discretized with nine nodes, of which nodes three to five contain the cylindrical fuel. The measurement of the coriolis mass flow meter is simulated with an integration of the measured signal. The coriolis mass flow meter is averaging the mass flow measurement and therefore does not show peaks and instabilities. To compare the simulation and the measurement, a similar integration procedure is implemented in the ESPSS model and schematic. The exact formulation to reproduce the

(a) Acceleration, thrust and oxidizer mass flow during second stage burn
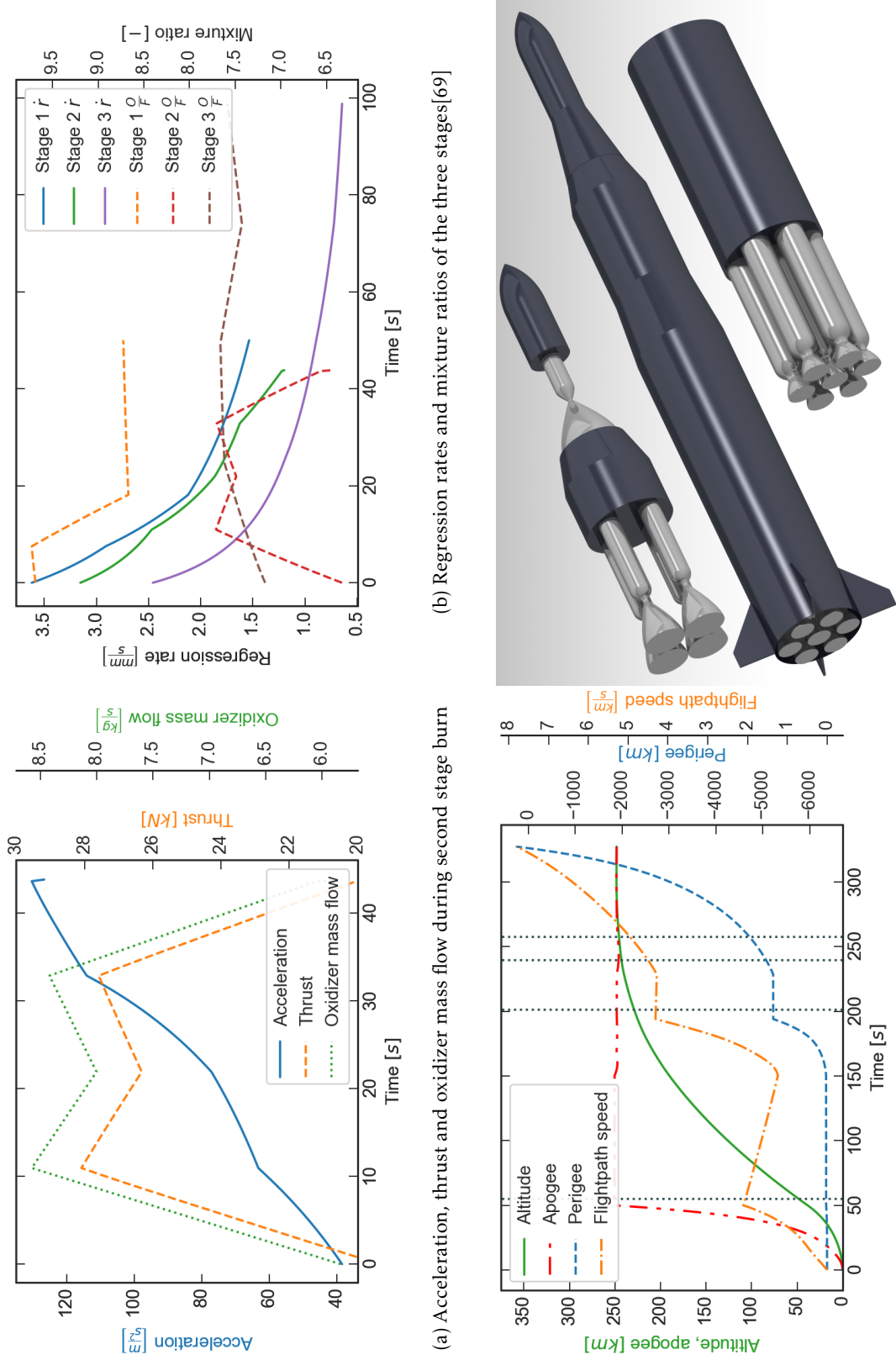
(b) Regression rates and mixture ratios of the three stages[69]

(c) Altitude, apogee, perigee and flightpath speed[69]

(d) A preliminary design of a three stage micro launcher[69]

Figure 4.10.: Hybrid micro launcher data, part 1

(a) Yaw and pitch angle over time

(b) Specific impulse of the micro launcher stages

(c) Total and propellant mass of the micro launcher over time

(d) 3D-trajectory colorized with acceleration data
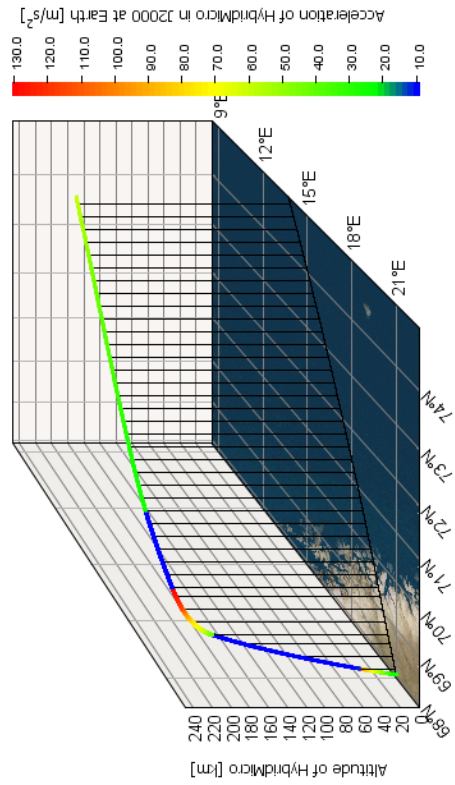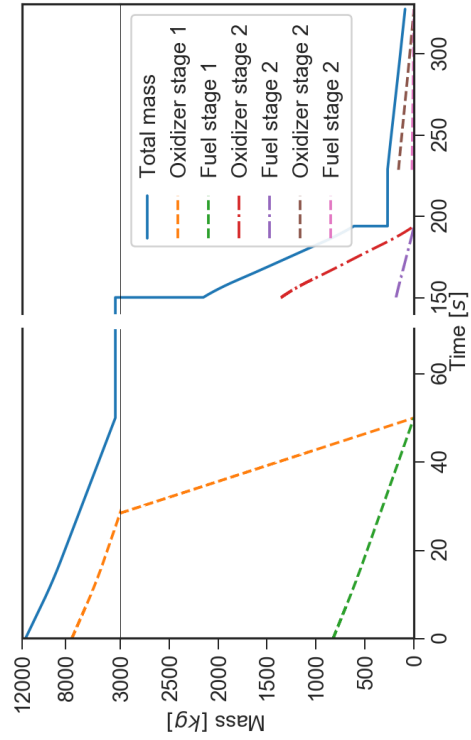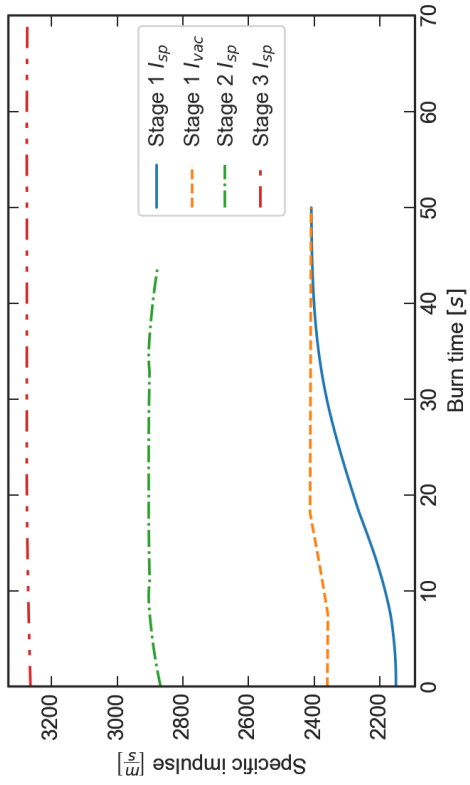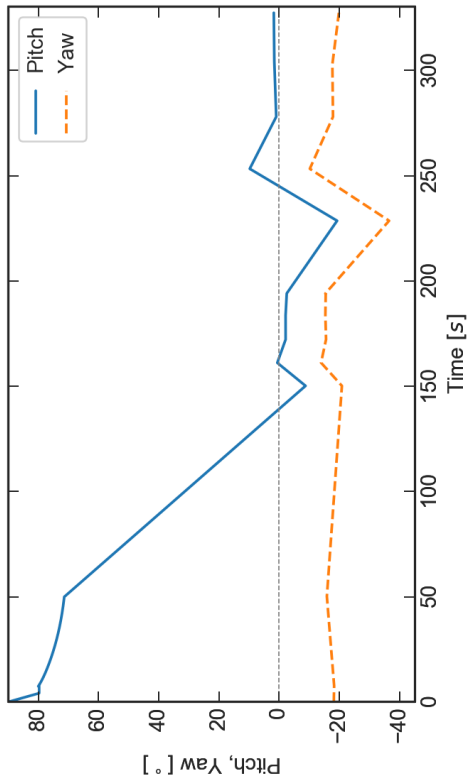
Figure 4.11.: Hybrid micro launcher data, part 2
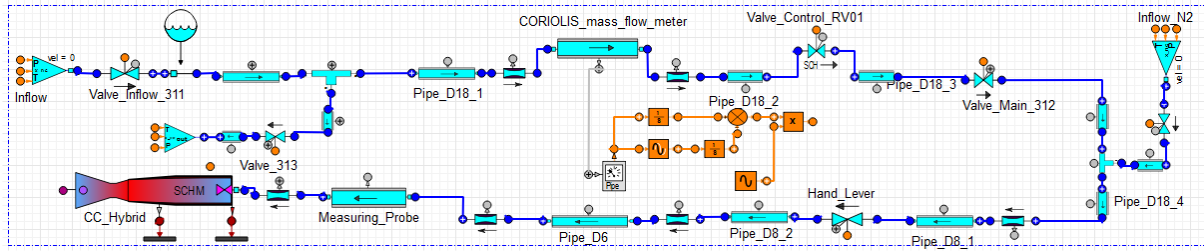
Figure 4.12.: Schematic of ESPSS model of the M11.3 test bench

coriolis measurement's signal is not known. Figure 4.13 shows a technical drawing of the combustion chamber assembly with the simulation nodes' positions. The simulation model outline is also marked with violet color. This is valid only for tests No. 1 to 4 without fuel grain protection on the lateral regression surfaces. The part numbers 1, 2, 5 and 12 mark the aluminum housing and numbers 4, 6, 7, 8 and 10 are showing insulation parts. Number 9 marks the graphite nozzle insert, while number 11 highlights the solid fuel block. For a simulation with lateral combustion turned on, the node before the fuel block and after the fuel block actually needs to be set to the fuel's outer diameter. Therefore two additional nodes without fuel have been inserted each at the front and the backside of the fuel block. If this is not done, the lateral combustion surface is not correctly calculated, as the node's diameter is always evaluated in the middle of the node. When first simulations were done with the model, the following points were identified:

- The pressure drop over the combustion chamber's injector naturally has a high impact on the simulations result. The pressure drop in ESPSS is modelled with a pressure loss coefficient ζ. This coefficient is dependent on the injector's geometry but also on pressure ratio, Reynolds number and Mach number. Therefore, for a stationary flow it is a constant
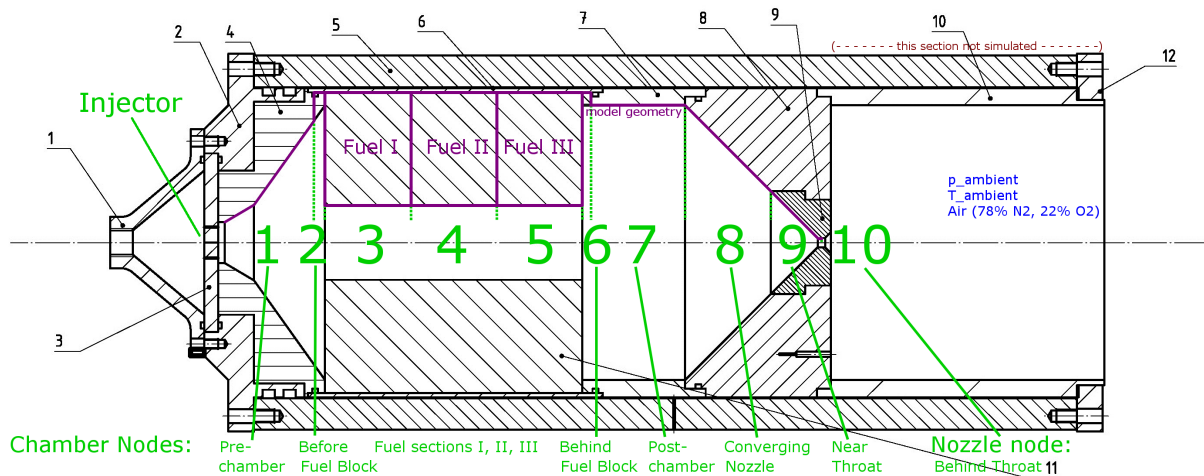
Figure 4.13.: Updated schematic of ESPSS model of the M11.3 test chamber

but needs to be adjusted for every test. In case of throttling it even needs to be adjusted for every flow condition. For future analyses a study of the pressure loss coefficient for several possible injector conditions could be done.

- The pressure in the chamber was higher in test measurements than in the first simulation runs, even though the mass flows and mixture ratio was matched. The reason was identified in the nozzle shape. The used nozzle is conic and has no ideally shaped nozzle throat but a sharp edge. Therefore the flow in the throat separates from the surface and forms a constriction of the flow. The effective nozzle diameter therefore is smaller than the geometrical measure. A nozzle discharge coefficient of roughly 95 % has been introduced to match the pressures in the combustion chamber.

Test No. 3 has been simulated with the following options: first the "stdHybrid" regression rate model was used. The regression coefficient was already determined in previous experiments as $a_{sp,0} = 0.157\,\text{mm/s}$ and $b = 0.58$. The model has been set to use lateral combustion. The front and backside of the fuel grain in this chamber configuration with a relatively large diameter to length ratio add a crucial part to the total surface area of the fuel. Since the front and backside have a slower regression rate, the lateral combustion factor was set to 70 % for test No. 3 and 40 % for test No. 4. This factor is dependent on many factors like ratio of inside and outside diameter of the fuel, mass flux density and flow conditions in the chamber. For example a recirculation zone will cause a different regression rate than if the oxidizer is directly injected onto the lateral fuel surface. Therefore this factor will be empirically determined with more tests. The oxidizer mass flux G_{ox} as a reference for the regression rate produces a constant regression rate along the x-axis. The test results quickly showed, that this is not a good approximation for the set-up, as the regression rate along the x-axis is highly increasing with distance from the injector plate. The reason for this is assumed in the injection behaviour and the large diameter to length ratio. Therefore the total mass flux G was used as a reference. After this change, the coefficient $a_{sp,0} = 0.157\,\text{mm/s}$ was too large, as it was gained from tests with a different combustion chamber size as well as using the G_{ox} and therefore needed scaling. It was multiplied with a factor of 0.86, which provided very good results for test No. 3. A second simulation has been done with the regression rate model for liquefying fuels, see Section 3.7.2. Table 4.13 shows the valve opening percentages during the test sequence. The openings are

Table 4.13.: Valve sequence for the simulation of test No. 3

Time	Inflow 311	Release 313	Control RV01	Main 312	Nitrogen
0.0 s	100 %	0 %	17.6 %	0 %	0 %
0.1 s	100 %	0 %	17.6 %	100 %	0 %
15 s	100 %	0 %	17.6 %	100 %	0 %
15.1 s	0 %	0 %	17.6 %	0 %	0 %
17.0 s	0 %	0 %	17.6 %	0 %	0 %
17.1 s	0 %	100 %	17.6 %	0 %	100 %

linearly interpolated between the table values. The most important parameters of the test bench simulation are listed in Table 4.14. The pipes between the inflow and main valve have a flow diameter of 18 mm and a summed up length of about 3.2 m. Due to the large diameter they do not add a lot of pressure losses. Behind the main valve 26 cm of 8 mm diameter pipe and 80 cm of 6 mm diameter pipe are following. Especially the 6 mm pipe adds some pressure losses. Then a 15 cm long 12 mm diameter pipe, which has the connections for the injector pressure sensor and the injector thermocouple is connecting the test bench to the rocket engine demonstrator. The pressure loss coefficient ζ for the valves and orifices that are not explicitly mentioned in Table 4.14 were automatically calculated by ESPSS. Experience shows, that this can only be used if the orifice or valve is having a relatively low pressure loss or flow diameter ratio. The simulation model of the control valve RV01 needs to have a choked flow, meaning that the orifice flow velocity is limited by the sonic velocity. This is only possible with the ESPSS option for the valve called "CV_option" being true.

Simulation Results

Figure 4.15a shows the pressure measurements of test No. 3 in comparison to the simulation results. Three positions have been compared: downstream of the control valve, upstream of the injector and inside the combustion chamber. The pressure is in very good agreement at all positions over the whole test sequence. Figure 4.15b illustrates the mass flow curves of the test measurement and simulation. The mass flow in the test set-up is only measured at the coriolis sensor. The coriolis sensor does not measure the instantaneous mass flow but an averaged resp. integrated mass flow. This can be seen in the slow rise of the measured mass flow in the beginning. The measurement needs 2.5 s for the mass flow to rise to the steady state. The simulated mass flow is plotted both for the coriolis sensor's position and the injector. The simulated mass flow at the coriolis sensor immediately rises to its maximum limited only by the sonic condition in the control valve's orifice. In the schematic of this simulation an integrator is implemented. The integrated mass flow in the simulation is also plotted and it has a much better congruence with the measured signal than the other simulated curves. However, there is still a difference in time but the curves are nearly parallel in the beginning

Table 4.14.: Important test bench simulation parameters

Parameter	Value	Parameter	Value
Inflow valve A_0	20 mm^2	Length of combustion chamber	353 mm
Control valve A_0	16 mm^2	Length of solid fuel	150 mm
Main valve A_0	20 mm^2	Thickness of solid fuel	51.6 mm
Main valve ζ	2.4	Nozzle throat diameter	5.44 mm
Hand lever A_0	18 mm^2	Injector area	3.14 mm^2
Pipe rugosity	15 μm	Injector ζ	3.3

of the test. It is undocumented why the coriolis sensor is producing such a curve. For more precise information the coriolis needs to be dismounted and tested in a separate set-up. This is currently impossible, as the test bench is also used for other test campaigns. The good agreement of the pressure curves at all three compared positions however suggests that the mass flow of the simulation is also close to the actual mass flow in the test bench set-up. The length and inner diameter of the fuel grain is depicted in Figure 4.15c. The measurement of the experiment, which were done before and after the test are plotted as points. There is a very good agreement in the length, which is due to the factor of 70 % which was imposed on the regression rate for the lateral combustion for test No. 3. The agreement of the inner fuel diameter is in good agreement as well. The diameter at the front and back side is evaluated at the node's center in the simulation, while on the real hardware it is manually measured at the outside. Therefore the measurement and simulation value have a higher discrepancy. The fuel consumption of experiment and simulation is in quite good agreement: In the experiment 455.3 g of paraffin-based fuel were used, while in the simulation 466.4 g were burned, which represents a small deviation of 2.4 %. Figure 4.15d shows the regression rates. The regression rate of the experiment is averaged in time. Therefore the points were plotted in the mid of the burn time. The average point has been calculated with the total burned mass and the assumption of a cylindrical shape of the fuel port. The regression rate at the injector's and nozzle's side was measured directly, as well as the lateral regression, which however is averaged as the lateral regression is not homogeneous on the whole fuel grain's front and back side either. The simulated regression rate matches the measured mean values quite well. The before explained difference between the node's diameter and the front and back side diameter also explains the larger differences for the injector's and nozzle's side's regression rate. Overall the regression rate of the cylindrical part is a bit too low in the simulation, which explains also that the used fuel mass is a bit lower. The regression coefficients $a_{sp,0} = 0.157 \,\mathrm{mm/s}$ and $b = 0.58$ can be improved with more test results. Figure 4.14a shows the simulated characteristic velocity c^*. The mixture ratio which is gained in the simulation is shown in Figure 4.14b. The mixture ratio is shown for all three fuel nodes. Naturally the mixture ratio is decreasing along the fuel grain. The shift in the mixture ratio is visible, but not very large. However, the mixture ratio shift, including the gradient in the startup of the engine, makes it difficult to evaluate the characteristic velocity and the combustion efficiency from the test results alone. The simulation and comparison with test results improves understanding of the effects that influence the mixture ratio, characteristic velocity and efficiency. Test No. 3 was also simulated using the regression rate model for liquefying fuels. However, the simulation results have no good agreement with the experiments. The simulated fuel mass flow is only about half of the mass flow in the experiment. The reason for this is, that the simulation with the liquefying model does not meet the conditions for entrainment according to Equation 3.10, which reveals that the equation is not valid in all operational ranges of hybrid rocket engines using paraffin-based fuel. In the experiment entrainment is increasing the fuel mass flow. Tests with this experimental combustion chamber are in a very low range of mass flux density G. Therefore the simulation with the liquefying model is out of its intended range of mass flux conditions

(a) Simulation characteristic velocity c^* (b) Simulation mixture ratio
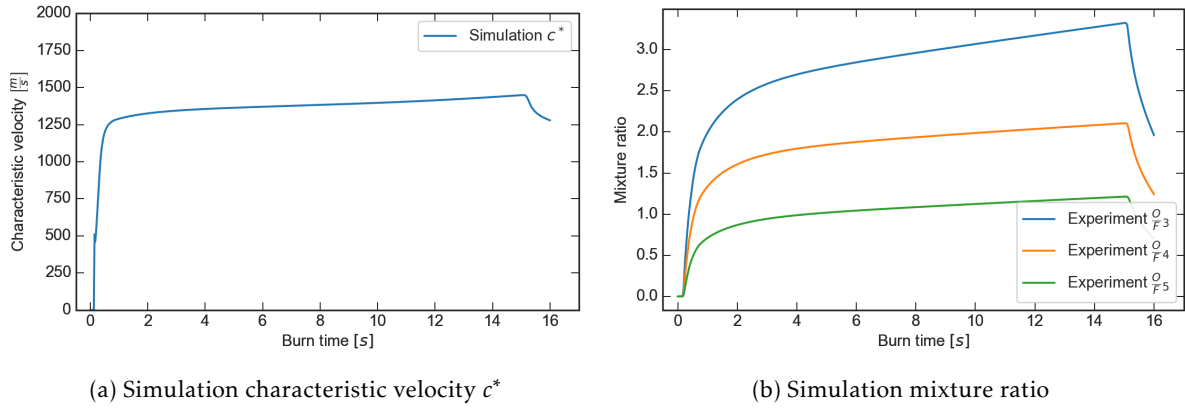
Figure 4.14.: Test No. 3 simulation results

and the results are not compared in more detail. Test No. 4 is also compared to the simulation results with the regression rate model stdHybrid. The main difference between test No. 3 and 4 is the mass flow of the oxidizer. The pressure before the control valve was set to 93 bar and this increased the oxidizer mass flow to 50 g/s. Figure 4.16a shows the pressure curves of test No. 4. The agreement between simulation and experiment was reached very quickly. Test No. 4 had a higher regression rate than expected. The reason for this can be a manufacturing problem of the paraffin fuel. Therefore the regression rate coefficient $a_{sp,0} = 0.157$ mm/s was increased by 6 % in order to match the fuel consumption of the experiment. By this, the pressure curves were automatically matching to each other. The mixture ratio is again shown in Figure 4.16b. It is very similar to test No. 3. However, this is only due to the higher regression rate. A higher mixture ratio was expected with a higher oxidizer mass flow. Figure 4.16c illustrates the fuel geometry over time. The lateral combustion factor was set to 0.4 for test No. 4. It is assumed that the lateral combustion factor is a coefficient which is very depending on fuel geometry, mass flux density and possibly other factors. Therefore for every test the lateral consumption factor needs to be adjusted. The diameter was in quite good agreement. The regression rates in 4.16d are in a less good agreement. Especially the evaluated mean regression rate of the experiment is much higher than the simulated regression rates. It is possible that this is also caused by problems with the manufactured fuel grain. The density could be inhomogeneous, which makes the evaluation of the data affected with errors. In total the simulation of hybrid rocket engines with EcosimPro & ESPSS works very well. Some coefficients like the valve's pressure loss coefficients and the parameters for regression rates of solid fuels in hybrid combustors need to be evaluated with test results. Simulations in order to predict the performance of a test set-up or new hybrid combustor are always relying on this data and only are precise if all parameters and coefficients are well known. As a conclusion the tests could be very well reconstructed in the simulation with ESPSS. In order to find the right regression rate coefficients a large amount of tests needs to be done and evaluated in the future.

(a) Pressure

(b) Mass flow

(c) Fuel geometry

(d) Regression rate
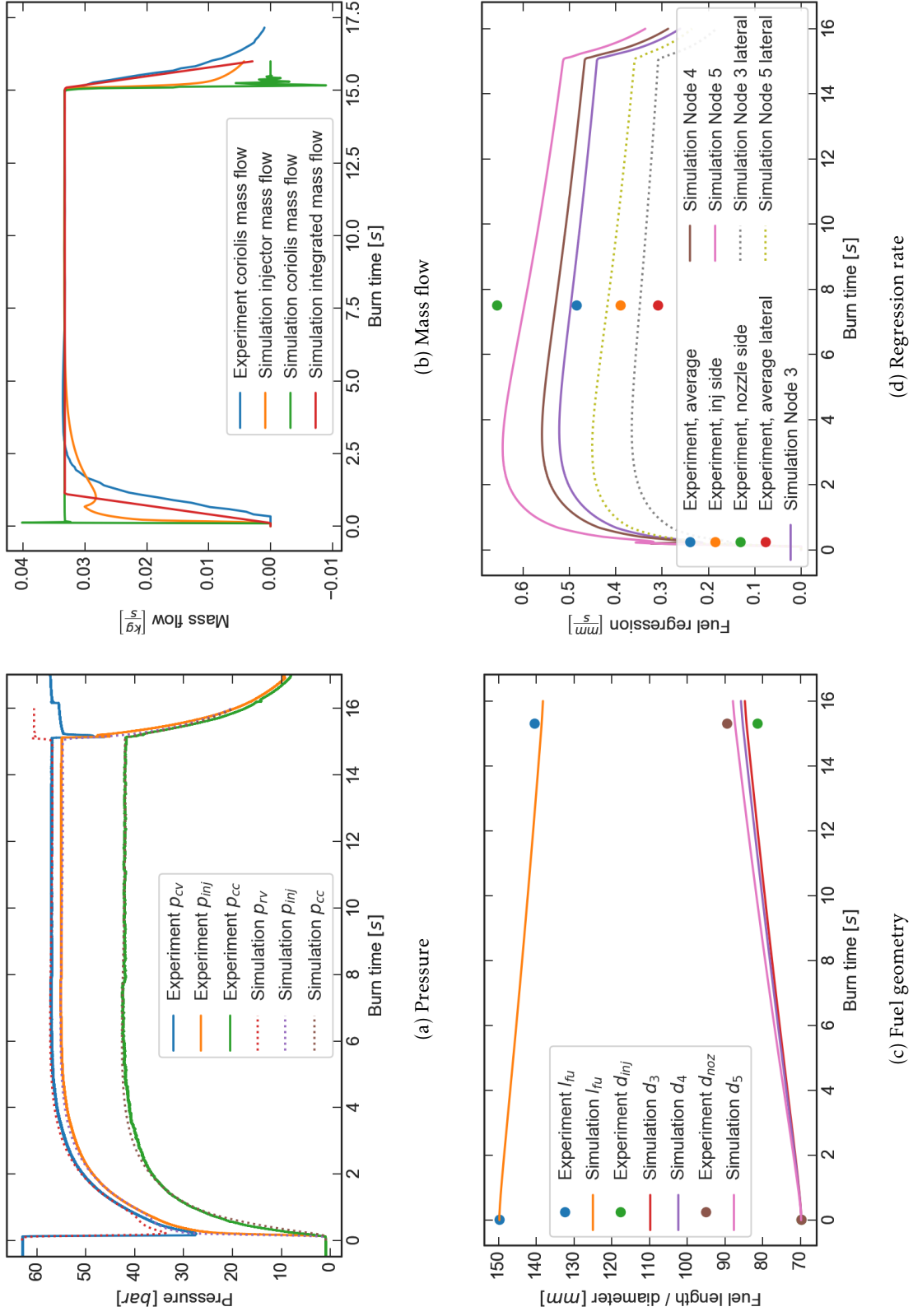
Figure 4.15.: Comparison of Experiment and Simulation: Test No. 3 simulation results

(a) Pressure

(b) Mixture ratio

(c) Fuel geometry

(d) Regression rate
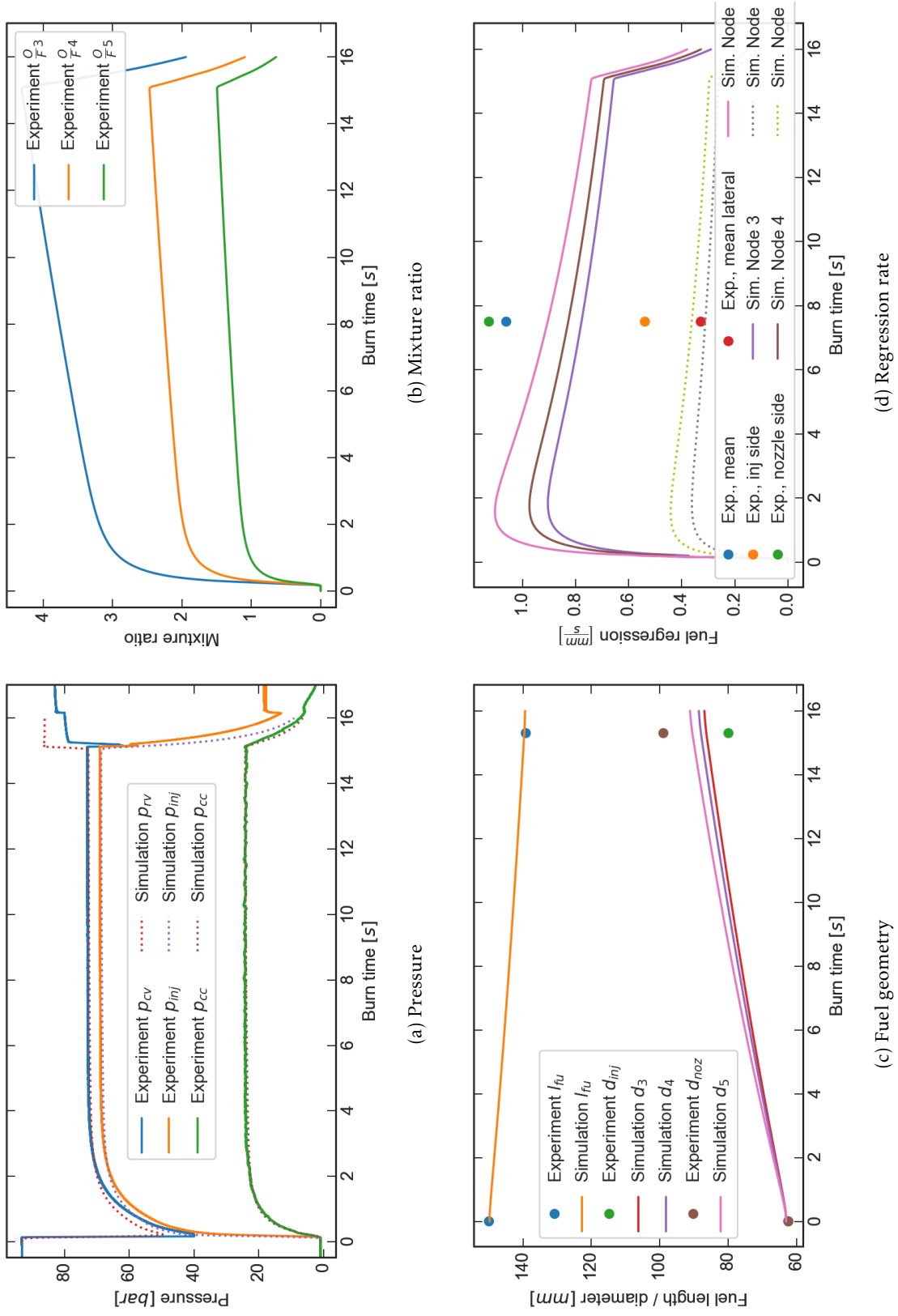
Figure 4.16.: Comparison of Experiment and Simulation: Test No. 4 simulation results

5. Experiments with a Hybrid Rocket Engine Demonstrator

5.1. Test Bench Set-up

Existing test bench infrastructure at the test complex M11 of the DLR Institute of Space Propulsion in Lampoldshausen was used for a small experimental campaign. The experiments were conducted at the test position M11.3. Previously this test bench was used for works with optical analysis of hybrid rocket engine combustion as well as for analyzing different fuel compositions with a small radial combustor [27, 30, 47]. The test bench was expanded with a new hybrid rocket engine, which sustains long burning durations at relatively low oxidizer mass flow and thrust. The flow plan of the test bench M11.3 can be seen in Figure 5.1. The oxidizer is gaseous oxygen which is supplied from a large high pressure reservoir, where the pressure is considered steady during the test duration. The oxidizer for the combustion is fed through a line with a pressure regulator PV11, the reservoir valve 0.311, a control valve RV01 and the main valve 0.312. A coriolis mass flow sensor is positioned between valve 0.311 and the control valve RV01. A second gas line is supplying nitrogen for cleaning and purging the lines with an additional valve 0.314. A further set of lines is provided for a hydrogen and oxygen torch, which is used for the ignition of the engine. The test bench is equipped with temperature and pressure sensors for each line segment between valves. A coriolis mass flowmeter is installed between valve 0.311 and the control valve RV01. Table 5.1 lists the sensor positions, which were installed to measure the pressure, mass flow and temperature at several positions along the experimental set-up. The fuel usage inside the combustor is not monitored. The fuel grain is measured before and after the test to get average regression rates and the average fuel mass flow. For the purpose of testing long burning times with a hybrid combustor a new combustion chamber was designed, constructed and built [73]. The chamber is shown in a technical drawing in Figure 5.2. The numbers represent the parts listed in Table 5.2. The combustion chamber is an engineering model design with a very thick wall. Mechanical loads therefore are no issue for the chamber wall. Since the engine was designed for long burn durations the whole chamber is protected with phenolic composite parts on the inside. The surface of the phenolic composite pyrolyzes very slowly and the heat conductivity of the material is very low, so that the temperature of the metal parts are low for several minutes of burn time. The nozzle is fixed between two tubes of phenolic composite. These two tube sections can be modified in their length and by this the length of the combustion chamber can be adjusted. This is especially useful for adapting the combustion chamber to different hybrid solid fuels. Each fuel has a unique regression rate behavior. One way to
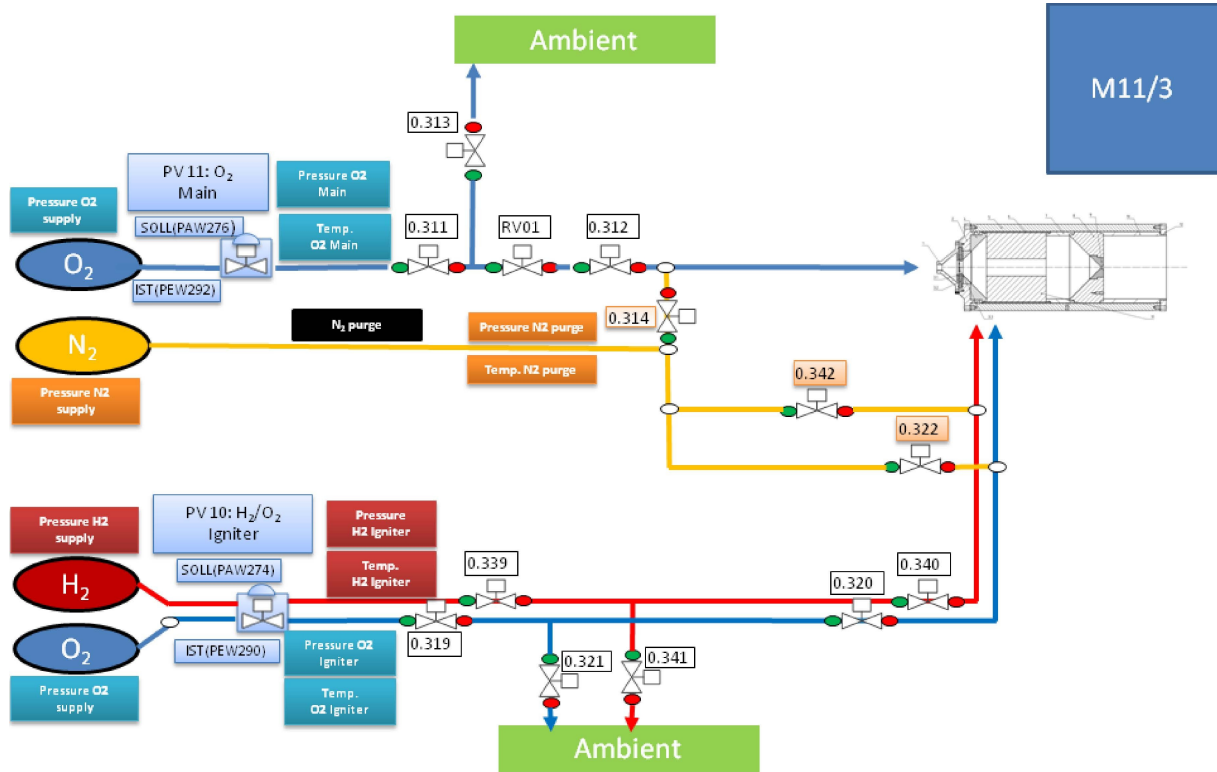
Figure 5.1.: Flow plan of the M11.3 test bench

Table 5.1.: Sensor positions

Measured value	Position	Symbol	Sample Rate
Pressure	Control valve exit	p_{RV}	20 kHz
Pressure	Injector cavity	p_{inj}	20 kHz
Pressure	Combustion chamber	p_{cc}	20 kHz
Mass flow	Before control valve inlet	$\dot{m}_{ox}$	10 Hz
Temperature	Ambience	T_{amb}	10 Hz
Temperature	Control valve exit	T_{RV01}	10 Hz
Temperature	Coriolis	T_{Cor}	10 Hz
Temperature	Oxygen inflow	$T_{Ox,in}$	10 Hz
Temperature	Chamber wall	T_{wall}	10 Hz

modify the mixture ratio inside the chamber is adjusting the length of the fuel grain, increasing or decreasing the fuel's burning surface. Hence the combustion chamber length needs to be modified as well. The nozzle throat is produced from graphite to sustain the high heat loads at the throat. The used graphite has nearly no degradation over a test, which was verified in earlier test campaigns with other combustion chambers. The injector plate is produced from brass in order to avoid melting or burning metal in case of back flows or recirculations during the transient phases in the test. Brass has a high heat capacity and high heat conductivity which reduces the risk of local hot spots. The injector has a showerhead design with only four holes. The injector plate does not need a very good spraying characteristic as the oxidizer is already gaseous. The only purpose of the injector plate is to generate a high enough pressure drop to decouple oxidizer feed line pressure from the combustion chamber pressure in case pressure oscillations occur. In hindsight the injector could have been modified to improve the distribution of oxygen on the fuel port. The engine is ignited with a hydrogen/oxygen torch which is not shown in the drawing. The hot gas flow from the torch enters the pre-combustion chamber at an angle of 45° to the oxidizer inflow. The driving design parameters of the engine are listed in Table 5.3. Thrust was not a design factor therefore the nozzle and its expansion ratio are neglectable.

5.1.1. Paraffin Fuel Production

The investigated fuel is produced at the test complex M11. The contents are industrial paraffin of the manufacturer Sasol Wax GmbH. For the first tests the paraffin wax 6805 was used. The fuel used for the tests had a long-chained polymer and color additive of 5 % by mass, hence the name in this document "PB-5%". Adding this polymer improves the mechanical properties of the fuel grain, as well as the regression behavior. One important factor for the regression behavior is the fuel's viscosity in the liquid state. The melt layer on the grain's surface increases regression rate depending on the viscosity. The lower the viscosity, the higher the droplet entrainment. Therefore, by adding high viscosity polymer to the paraffin, the regression rate
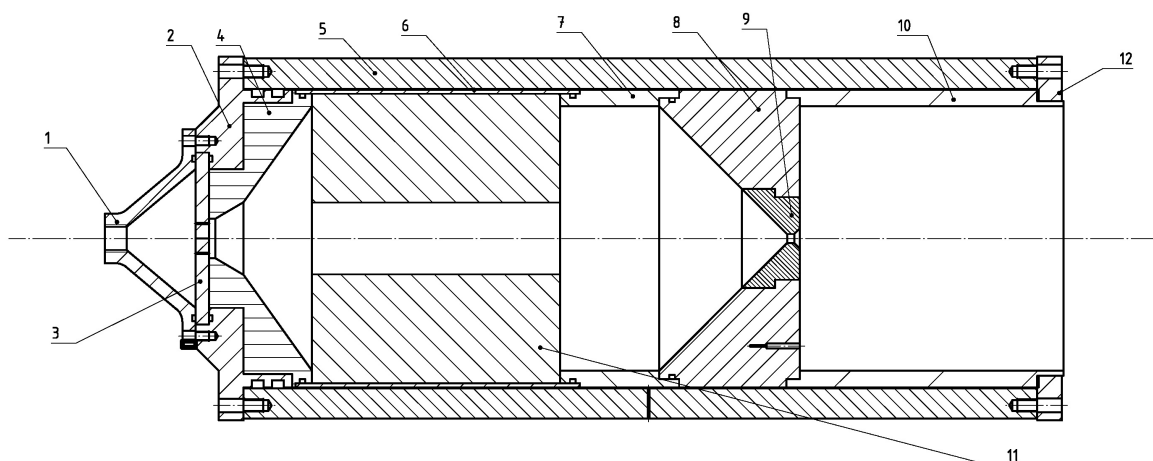
Figure 5.2.: Technical drawing of the experimental combustion chamber

Table 5.2.: Combustion chamber parts

Number	Part description	Material
1	Inflow cone	Aluminum
2	Injector cavity	Aluminum
3	Combustion chamber	Brass
4	Pre combustion chamber insulation	Phenolic composite
5	Combustion chamber wall	Aluminum
6	Paraffin fuel insulation	Phenolic composite
7	Post combustion chamber insulation	Phenolic composite
8	Nozzle insulation	Phenolic composite
9	Nozzle insert	Graphite
10	Outflow insulation	Phenolic composite
11	Fuel grain	Paraffin based
12	Flange	Aluminum

Table 5.3.: Combustion chamber design parameters

Design Parameter	Symbol	Value
Maximum burning duration	t_b	180 s
Average mixture ratio	$\overline{O/F}$	2.0-2.5
Average chamber pressure	$\overline{p_{cc}}$	30 bar
Average thrust	$\overline{F}$	100 N
Regression coefficient, estimation	a	0.117
Regression exponent, estimation	n	0.62
Fuel length	l_{fu}	150 mm
Fuel outer diameter	d_{out}	175 mm
Nozzle throat diameter	d_t	5.4 mm
Nozzle exit diameter	d_e	12.2 mm

is slowed down. Another additive is 1 % blackening additive. This is to create an opaque fuel grain in order to limit the melting process to the surface. Otherwise the radiative heat transfer into the fuel grain is too large and larger fuel parts could melt and detach. The formulation of this fuel was gained in previous works at the DLR Lampoldshausen [30]. The paraffin is melted and mixed with the polymer before the blackening additive is added. In this way it is made sure that despite the higher melting point of the polymer the fuel is homogeneously mixed. Figure 5.3 shows four images of the fuel production. The pure paraffin is melting in the first two images until the polymeric additive is added in the third image, when the paraffin is hot enough. Magnetic stirrers make sure the mixing is fast and successful. In the last picture color is added. After the melting and mixing the fuel is cast into a cylindrical shape.

5.1.2. Test Sequence

In order to control the test an automatic sequence was used. Table 5.4 shows an example sequence for the first tests. In advance of the automated test sequence, the lines are manually flushed with nitrogen for cleaning purposes. Additionally, the pressure in front of the valve 0.311 is set to the desired value. This pressure in combination with the opening of the control valve is the main influence on the oxygen mass flow. The oxidizer temperature also influences the mass flow by a small percentage. The control valve is used to precisely set the mass flow,

Figure 5.3.: Paraffin production [73]

however it is moving very slowly. Therefore the control valve cannot be used to realize quick throttling of the engine. In order to throttle the engine, the pressure at the valve 0.311 is changed, which is responding much faster.

5.1.3. Methodology

In order to analyze a test conducted at the test bench, the following information and data is analyzed and processed:

- Measurements of the fuel grain before and after the test
  - Fuel mass: The fuel mass is determined with a scale before and after the test. It is weighed together with the fuel insulation and the fuel insulation mass is deducted.
  - Length: The length of the fuel grain after the test varies depending on the measuring position. An averaged value is used for the analysis. The length is measured at positions rotated by 90°.
  - Inner diameter (at front and aft end): The diameter is also averaged by measuring in different angles.
  - Outer diameter: The outer diameter is not changing during a burning test.
- Regression of insulation parts: The regression of insulation parts is neglectable for the analysis of the combustion process. However, the inspection of the parts is necessary to replace them for future tests, if they are burned too much.
- Nozzle throat diameter: The graphite insert inside the nozzle has a very small regression. This is considered for the evaluation of the chamber performance.
- Pressure sensor data: Pressure sensor data is stored in several text files by the measurement system of the test bench M11.3.
- Temperature sensor data: Temperature sensor data is stored in several text files by the measurement system of the test bench M11.3.

Table 5.4.: Test sequence

Time in [s]	Event	Comment
-20	Start of automated sequence	Control valve opening changed to 17 %
-14	Opening 0.311, 0.319 & 0.339	Reservoir connections opened
-3	Activating spark plug	Inside the hydrogen/oxygen torch
-0.2	Opening 0.320	Oxygen flow to torch opened
0	Opening 0.312 and 0.340	Hydrogen flow to torch, oxygen flow to CC opened
0.2	Closing 0.339 and 0.340	Hydrogen flow and torch flame stopped
0.3	Closing 0.319 and 0.320	Oxygen flow to torch stopped
5	Closing 0.311 and 0.312	Oxygen flow to combustion chamber stopped

- Mass flow data from Coriolis sensor upstream of the control valve $\dot{m}_{ox}$.

The sensors' positions for pressure, temperature and mass flow are listed in Table 5.1. The manually measured data is entered in a table file. Another table was created using NASA CEA containing ideal combustion data including gas density, sonic velocity, specific impulse and the characteristic velocity for several pressure and mixture ratios. These data is specific for the combination of gaseous oxygen and the used paraffin-based fuel PB-5%. Both these table files and the data files of the sensors are read and processed by a script written in Python programming language. Figure 5.4 shows the process chain of the script and Figure 5.5 depicts the ideal temperature and characteristic velocity of the combustion with gaseous oxygen and PB-5% for different pressures in the range from 10 bar to 50 bar. In order to evaluate the connection of the regression rate $\dot{r}$ to the oxidizer mass flux density G_{ox} the regression rate needs to be reconstructed, as no device is available to measure the regression rate in real time. Therefore both regression rate and the mass flux density need to be averaged over the whole test time. The regression rate is averaged as

$$\bar{\dot{r}} = \frac{d_f - d_0}{t_b}. \tag{5.1}$$

The oxidizer mass flux density is calculated with

$$\overline{G_{ox}} = \frac{16\overline{\dot{m}_{ox}}}{\pi \left(d_f + d_0\right)^2}. \tag{5.2}$$

Therefore, a long test duration reduces the impact of measurement errors (e.g. for the dimensions of the fuel grain), but of course increases the error of the averaging technique, since during the test beginning and end the deviation from the averaged value is quite high. Shorter test duration however increases the impact of measurement errors and transient phenomena
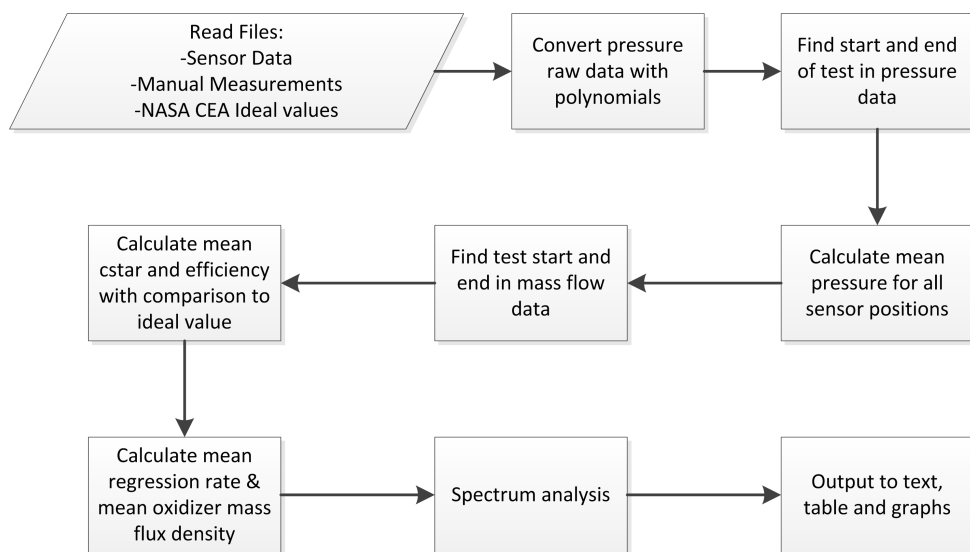
Figure 5.4.: Process flow of the script to analyze the test data
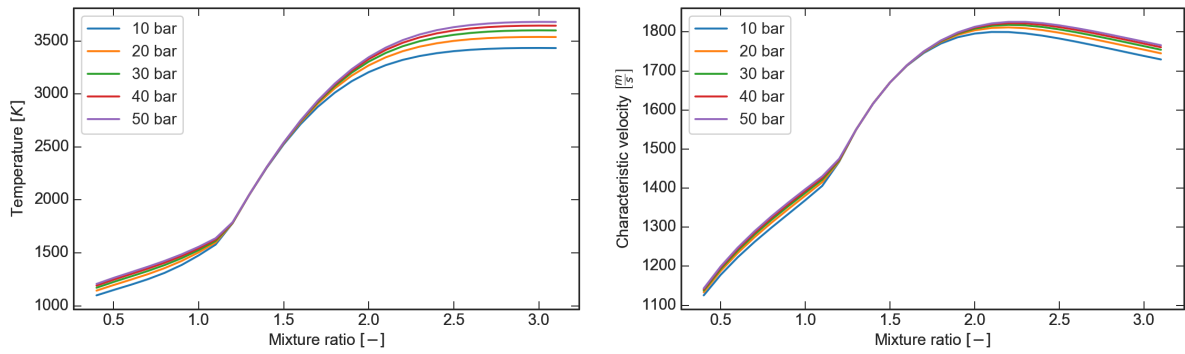
Figure 5.5.: Ideal temperature & characteristic velocity with NASA CEA

during ignition and shut-off of the engine. The frequency analysis of the combustion chamber pressure is realized with Python's own included frequency analysis functions. The Fourier transformation is done with the function "np.fft.fft" of the numpy package [74].

5.2. Test Results

5.2.1. Test Description

After the first test of the experimental combustion chamber an injector redesign was necessary. The injector was produced from two different brass parts screwed together with steel screws. The steel screws were not withstanding the high heat load and melted, which changed the injector area. The gas flow at the injector is pure oxygen. This increased the reactivity of the steel screws. Figure 5.6a shows the pressure records of the first test. After analyzing all available data, the events that lead to this strange pressure curves could be possibly explained like follows.

- Section I: When opening valve 0.312, the control valve pressure drops quickly. The pressure behind the control valve rises slowly due to the mass flow limitation that the choked flow creates. This limited mass flow needs some time to fill the large volume of the combustion chamber and all the pipes to reach a steady pressure. In all following tests it is usually taking 4 s to 5 s to reach a steady pressure level.

- Section II: Injector pressure rises in a short time, while the chamber pressure is reduced. The reason cannot be clearly identified but one explanation is that one of the five injector holes where obstructed by metal fragments from the screws. This explains why there is less mass flow with higher a pressure drop.

- Section III: The hole stays closed and the pressure rises slowly. As it is still in the first five seconds, this is expected.

- Section IV: The closed hole is most likely open again and the pressure drop is reduced to its regular value.

- Section V: The pressure is again steady for a short period of time. The chamber pressure is higher than the design point of 30 to 35 bar. Later analysis and comparison showed, that the nozzle's effective throat area is smaller than the geometrical throat area, due to a vena contracta. This was neglected during design, but has a high impact due to the chosen conical nozzle geometry.

- Section VI: The injector pressure drop is getting smaller and approaches zero. This is when the steel screw in the injector finally melts and burns away and a large hole is inside the injector plate.

- Section VII: The main valve 0.312 is closed and the pressure drops. The residual oxidizer in the line and the injector dome keep the combustion going for nearly a second until the nitrogen flushing starts.

One interesting observation of the first test was that even when the steel screws melted and burned, the brass plate did not melt, although the brass' melting point is lower than that of steel. The reason for this is that the heat conductivity of brass is much higher and the injector plate never reached the melting point temperature. This led to further improvements of the combustion chamber design, where steel is exposed to the hot gas. The injector and the preburner inlet were redesigned to include only brass parts where contact to the hot gas is imminent. Also the torch flame inlet was reconstructed with brass and phenolic composite protective covering. For the evaluation of the following tests a nozzle throat area coefficient of 0.95 was added in order to include the effects of the vena contracta. It must be kept in mind, that this is simply an estimation and cannot be determined in more precision. However, if the value is kept constant, a comparison between the different tests is possible. Figure 5.6b shows a Fourier analysis of the combustion chamber pressure signal. It shows that the magnitudes of the frequencies are very small. There are some peaks up to about $-50\,\mathrm{dB}$. Opposing the problems in the combustion chamber during the first test, the combustion itself was still very smooth and no high combustion chamber instabilities were occurring. For comparison in Figure 5.6c and 5.6d the Fast Fourier Transform (FFT) analysis for test No. 3 and test No. 4 are shown. It is visible that the oscillations in these two tests are even lower in magnitude. All other tests have a very similar FFT graph like these two tests. During test No. 2 some leakage in the oxidizer line reduced the mass flow inside the chamber and the test procedure was changed accordingly to double check all connections in advance of the test. Starting with test No. 3 the results were in good agreement with the expectations. However, in contrast to most hybrid rocket engines tests conducted at the DLR Lampoldshausen before this test campaign, the fuel block has a very high diameter to length ratio. This is the reason, why the lateral combustion at the front and end side of the fuel grain has a major impact on the combustion behavior. While in earlier tests with very long but thin fuel grains the lateral combustion could be neglected during the design of the engine, with the new combustion chamber layout the fuel regression on the lateral sides added a larger fuel mass flow to the combustion. Additionally the fuel regression rate is a bit higher than expected, since the regression rate behavior was not known for the region of low G_{ox}. These two factors changed the mixture ratio of oxidizer to fuel mass

flow in the combustion chamber compared to the design point to a much lower value of about 1 to 1.1 in the first tests. The design point was at about 2 for the mixture ratio. As can be seen in Figure 5.5 the optimum for the characteristic velocity c^* is between 2 and 2.5. In order to reach a higher mixture ratio and a high mass flux density G_{ox} the combustion chamber was modified after test No. 3. The only change was the nozzle throat diameter to 9 mm and the pressure before the control valve was adjusted to 90 bar from 60 bar in order to enlarge the oxidizer mass flow without increasing the chamber pressure to much. However, even a higher oxidizer mass flow could not increase the mixture ratio, as the regression rate climbed nearly at the same rate. Figure 5.7a, 5.7b, 5.7c and 5.7d show the measured pressure and mass flow signals of test No. 3 and 4. It is again visible that the pressure graph has a slow rise to a constant value during the first five seconds of the test. This is due to the fact, that the mass flow is limited by the choked conditions in the control valve. As the mass flow is limited, the initial "filling" of volumes of the combustion chamber and pipes with high pressure gas takes some seconds. The mass flow in test No. 4 after the changes in the operating point pressure and nozzle throat diameter rose to roughly $50 \frac{g}{s}$ in comparison to $30 \frac{g}{s}$ during test No. 1 to No. 3. In both mass flow graphs a transient phase at the beginning of the test after the main valve opening is visible. The duration of the transient phase is roughly 3 s. This transient behavior related to the integration of the coriolis sensor's internal signal. The coriolis sensor was pre-installed. This coriolis sensor type is rather meant to measure constant mass flows over a long time. It is not very suitable for measuring quickly changing mass flows. The chamber pressure in test No. 4 was only 20 bar compared to 40 bar as before. The reason for this is, that the mass flow was increased, but the oxidizer ratio was not. With a higher oxidizer ratio the pressure would have been higher. In Test 5 a protection was mounted on the front side of the fuel, to reduce the lateral regression and increase the mixture ratio. Test No. 1 to 5 used the same nozzle and insulation parts, which corresponds to a total testing time of 45 s until the beginning of test No. 5, which was initally set for a burn duration of 25 s. However, a material defect in the nozzle insulation part (part No. 8 in Figure 5.2) caused the creation of a hole in the material at the contact side between graphite and insulation material. This hole finally burned through during test No. 5 quite at the beginning of the test sequence. The hole slowly increased until the test was aborted after 24 s. The pressure inside the combustion chamber accordingly was not stable but decreased continuously during the test duration. An evaluation of combustion efficiency and other characteristic numbers is hence not possible. The values for regression rate however are useful. For test No. 6 on 21st January 2018 a test duration of 30 s at 54 g/s was realized which was the longest test duration with full mass flow for a hybrid rocket engine at the DLR Lampoldshausen up to this date. Inspection of the fuel grain showed, that the front side protection, which was introduced in test No. 5 was very useful. On the rear side of the grain however, the regression was still too large. During long test duration the heat loads on the post combustion chamber insulation are very high and also the nozzle becomes white glowing. This increases the heat flux into the back side of the grain. Therefore it was decided to introduce the fuel grain protection also on the back side. Test No. 7 was the first test which had a changing supply pressure in order to simulate throttling of the engine. At the same time the

(a) Test 1 Pressure

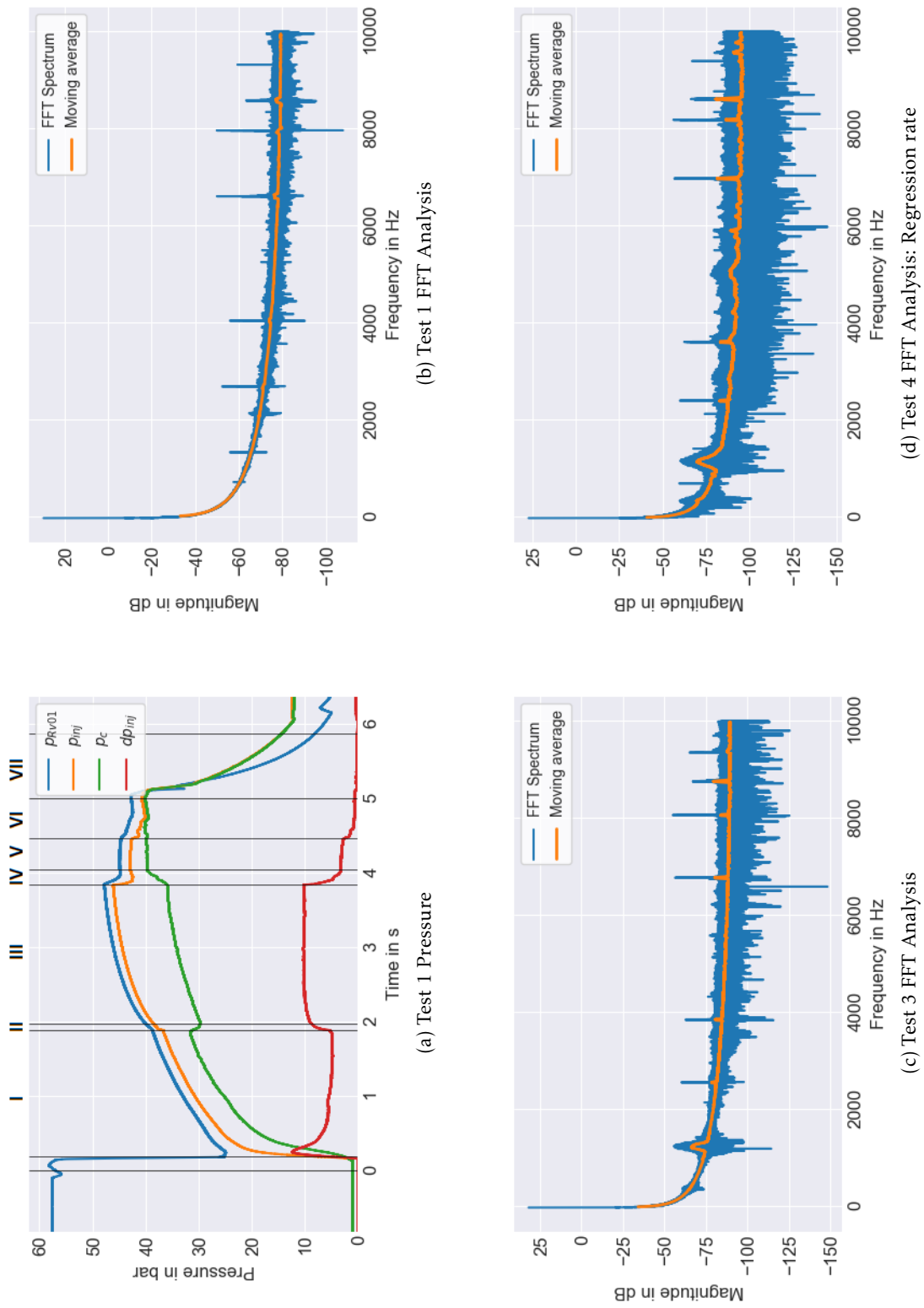(b) Test 1 FFT Analysis

(c) Test 3 FFT Analysis

(d) Test 4 FFT Analysis: Regression rate

Figure 5.6.: Test 1, 3 and 4 measurements

(a) Test 3 Pressure

(b) Test 3 Oxidizer Mass Flow

(c) Test 4 Pressure

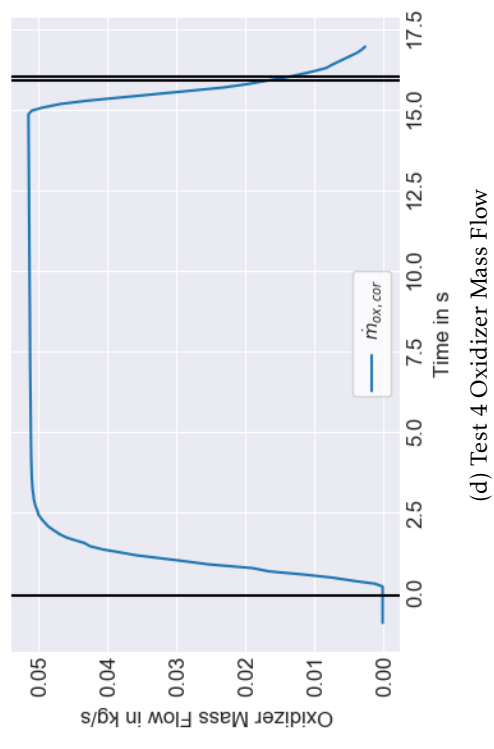(d) Test 4 Oxidizer Mass Flow
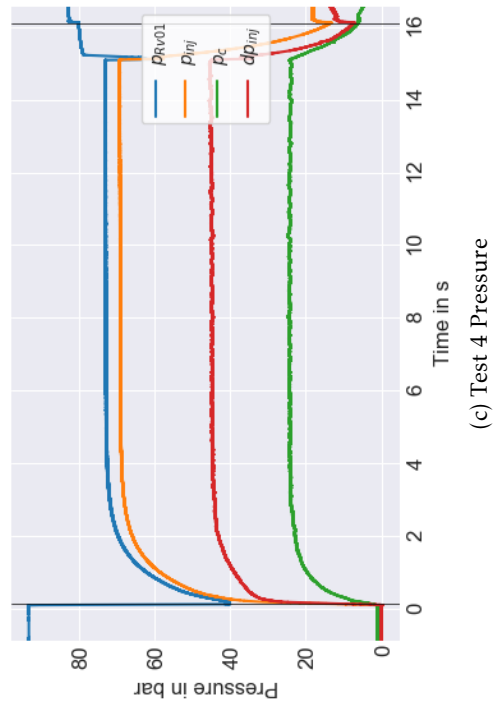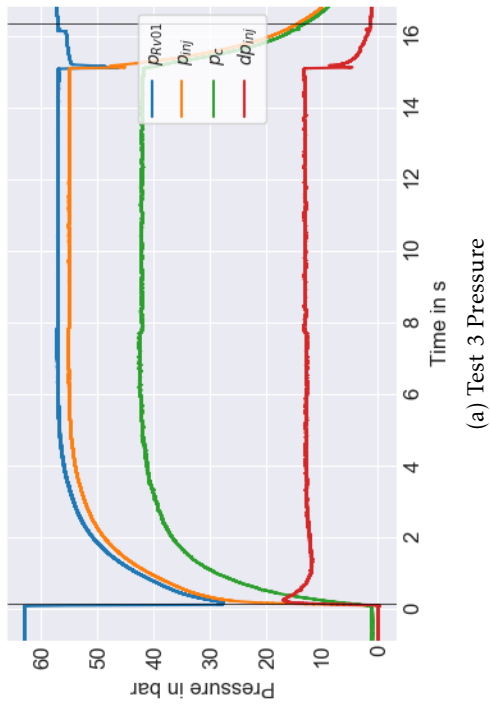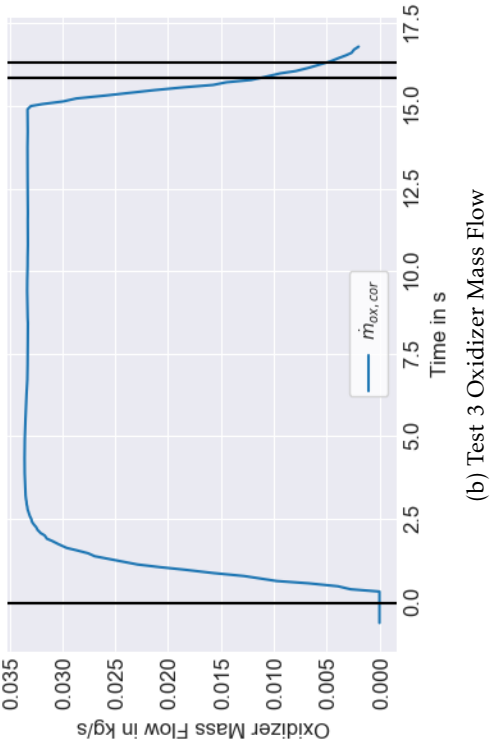
Figure 5.7.: Test 3 and 4 measurements

burn duration was prolonged to a planned 40 sec. Unfortunately the nozzle which was used in several earlier tests did not withstand the accumulated heat and mechanical loads and broke and the test sequence was stopped after 14 sec. The test campaign for this work was concluded after test No. 7. All test parameters are summarized in Table 5.5. Additional plots of test No. 2, 5 and 6 have been added to the appendix E.

5.2.2. Regression Rate Tests

One important part of the test campaign for this work was to further identify the regression rate law for the used propellant combination at the DLR Lampoldshausen. The fuel production is described in section 5.1.1. The propellant combination has been previously used in a small chamber test campaign. The data points won by this campaign are also included as a reference. The tests were conducted with a very small combustion chamber (100 mm long and 30 mm in diameter), which is abbreviated "MiniCC" in the following. The most important numbers to predict the behavior of a propellant combination in hybrid rocket engines from an experimental point of view are the regression coefficients a and n. The averaged regression rates of every test is plotted against the average oxidizer mass flux in order to do a curve fit according to the equation

$$\dot{r} = a G_{ox}^n.$$ (5.3)

Figure 5.9a shows the regression rate of the tests conducted for this work. The Figure 5.9b diagram compares the actually measured regression rates with the ones being corrected for the mixture ratio. The mixture ratio correction is suggested by Karabeyoglu [75] as

$$f_c(O/F) = \frac{1-n}{\left(\left(1 + \frac{1}{O/F}\right)^{1-n} - 1\right) O/F}.$$ (5.4)

It must be noted that this correction always yields a factor larger than one. Therefore the equation given in the paper by Karabeyoglu is not complete. It must be normalized by a factor evaluated at a reference mixture ratio. From the paper it is extracted that $O/F = 2.05$ has been chosen as the reference point. The completed equation is then

$$\dot{r} = a G_{ox}^n \frac{f_c(O/F)}{f_c(2.05)}.$$ (5.5)

As all test conducted within this work had a lower mixture ratio than 2.05 the regression rate is always higher than it would be predicted by the regression rate law. Therefore in the diagram all data points of the corrected regression rate are lower than the actually measured ones. The scatter of the data points is quite high, which is only natural since most tests had caused a change to the chamber set-up for the following tests like changing the nozzle diameter, adding the fuel protection on the front and back side and changing the combustion duration every test. Figure 5.8 depicts the regression rate data of both the miniCC and the current tests in one diagram. Both data sets are printed with and without correction. Additionally the

<div align="center">Table 5.5.: Test parameters</div>

Test No.	1	2	3	4	5	6	7
Test Date	18.01.2017	21.02.2017	08.03.2017	16.05.2017	25.10.2017	23.01.2018	15.02.2018
Fuel parameters at t_0							
Inner diameter d_i	65 mm	69.3 mm	69.8 mm	62.5 mm	100 mm	100 mm	62 mm
Outer diameter d_o	172 mm	172 mm	173 mm	174 mm	173.6 mm	173 mm	173.5 mm
Fuel length l_f	149.8 mm	148 mm	149.8 mm	150 mm	141 mm	141 mm	132 mm
Initial mass m_f	2.797 kg	2.657 kg	2.732 kg	2.851 kg	2.047 kg	2.037 kg	2.529 kg
Fuel density ρ_f	937 $\frac{kg}{m^3}$	922 $\frac{kg}{m^3}$	927 $\frac{kg}{m^3}$	924 $\frac{kg}{m^3}$	918 $\frac{kg}{m^3}$	923 $\frac{kg}{m^3}$	929 $\frac{kg}{m^3}$
Fuel parameters at t_b							
Fuel length l_f	148 mm	146.8 mm	140.5 mm	139.3 mm	118.3 mm	97 mm	132 mm
d_i injector side	68.1 mm	74.2 mm	81.5 mm	80 mm	109 mm	124 mm	82 mm
d_i nozzle side	70.5 mm	74.8 mm	89.5 mm	99 mm	136 mm	168 mm	108 mm
d_i averaged	69.3 mm	74.5 mm	85.5 mm	89.5 mm	122.5 mm	146 mm	95 mm
d_i calculated	69.9 mm	76.1 mm	87.6 mm	96.3 mm	124.6 mm	140.4 mm	98.6 mm
Final mass m_f	2.691 kg	2.53 kg	2.277 kg	2.105 kg	1.247 kg	0.719 kg	1.964 kg
Nozzle throat d_t	5.4 mm	5.4 mm	5.4 mm	9 mm	9.1 mm	8.6 mm	8.7 mm
Burn time t_b	5 s	5 s	15 s	15 s	25 s	30 s	14 s
Used oxygen m_{ox}	0.129 kg	0.145 kg	0.488 kg	0.753 kg	1.314 kg	1.677 kg	0.666 kg
Ox. mass flow $\dot{m}_{ox}$	22.7 $\frac{g}{s}$	25.9 $\frac{g}{s}$	30.2 $\frac{g}{s}$	47.3 $\frac{g}{s}$	53.7 $\frac{g}{s}$	54.3 $\frac{g}{s}$	44.9 $\frac{g}{s}$
Ox. temp. $T_{ox,inj}$	8.1 °C	16.1 °C	11.6 °C	14.92 °C	11.9 °C	12.8 °C	15.0 °C
Time averaged pressures							
Aft. contr. valve p_{rv}	37.6 bar	38.0 bar	54.7 bar	71.5 bar	81.8 bar	84.5 bar	71.1 bar
At injector p_{inj}	36.2 bar	35.9 bar	50.7 bar	65.1 bar	73.1 bar	75.6 bar	62.3 bar
In combustor p_{cc}	30.5 bar	26.9 bar	38.6 bar	22.8 bar	16.5 bar	27.6 bar	21.1 bar
Performance data							
Mean mixt. ratio o/f	1.23	1.15	1.07	1.01	1.64	1.27	1.18
Charact. vel. c^*	1511 $\frac{m}{s}$	1134 $\frac{m}{s}$	1355 $\frac{m}{s}$	1376 $\frac{m}{s}$	1109 $\frac{m}{s}$	1476 $\frac{m}{s}$	1350 $\frac{m}{s}$
Efficiency η_{c^*}	101.3 %	78.5 %	95.6 %	99.3 %	64.2 %	96.7 %	92.6 %
Mass flux G_{ox}	6.4 $\frac{kg}{m^2 s}$	6.2 $\frac{kg}{m^2 s}$	6.2 $\frac{kg}{m^2 s}$	9.5 $\frac{kg}{m^2 s}$	5.4 $\frac{kg}{m^2 s}$	4.8 $\frac{kg}{m^2 s}$	8.9 $\frac{kg}{m^2 s}$
Regression rate $\dot{r}_f$	0.43 $\frac{mm}{s}$	0.61 $\frac{mm}{s}$	0.55 $\frac{mm}{s}$	1.06 $\frac{mm}{s}$	0.50 $\frac{mm}{s}$	0.65 $\frac{mm}{s}$	1.23 $\frac{mm}{s}$

literature regression rate law of the paraffin-based fuel SP-1 [75] is shown. The regression rates of the used fuel with 5 % polymer are only slightly higher than the SP1a regression rate would predict. This suggests that a similar mixture has been found. The current data set does not allow yet to create a reliable curve fit to get the a and n coefficients for the used paraffin-based mixture. More data points with much higher G_{ox} need to be gathered for the curve fit to work properly. However, in Figure 5.8 the curves for an exponential fit for the gathered data points are shown. The best curve fit with the highest coefficient of determination of 0.89 is $\dot{r} = 0.3G^{0.42}$ which is probably predicting too slow regression rates for high mass flux density $G_{ox} > 100\,\mathrm{kg/m^2\,s}$. If a regression is conducted with a fixed exponent equal to the literature value of SP-1a, the equation is $\dot{r} = 0.13G_{ox}^{0.62}$. The coefficient of determination is only 0.8. Tests with higher oxidizer mass flux density are necessary to improve this prediction. The effect of using LOX instead of gaseous oxygen needs to be investigated as well.

5.2.3. Throttling Tests

Test No. 7 on the 15$^{\mathrm{th}}$ February 2018 was the first test with a sequence including throttling of the engine. The throttling was realized with changing the supply pressure of the oxidizer inflow at the valve PV11. The reasoning for this approach is that the control valve's motor is too slow and therefore not an option in order to regulate the mass flow in short time frames. As mentioned before the graphite nozzle broke in this test and therefore the planned sequence of 40 s was manually stopped at 14 s. The planned sequence was including four different supply pressures for 10 s each: 80 bar to 100 bar to 60 bar and finally again 80 bar. As the test was stopped prematurely only the first two levels were executed. Figure 5.9c shows the pressure diagram of test No. 7. The diagram shows the already familiar slow ramp up of the pressure which takes about 4 s to get to a stationary operation of the rocket engine. The pressure at

Figure 5.8.: Regression rate results and exponential fit
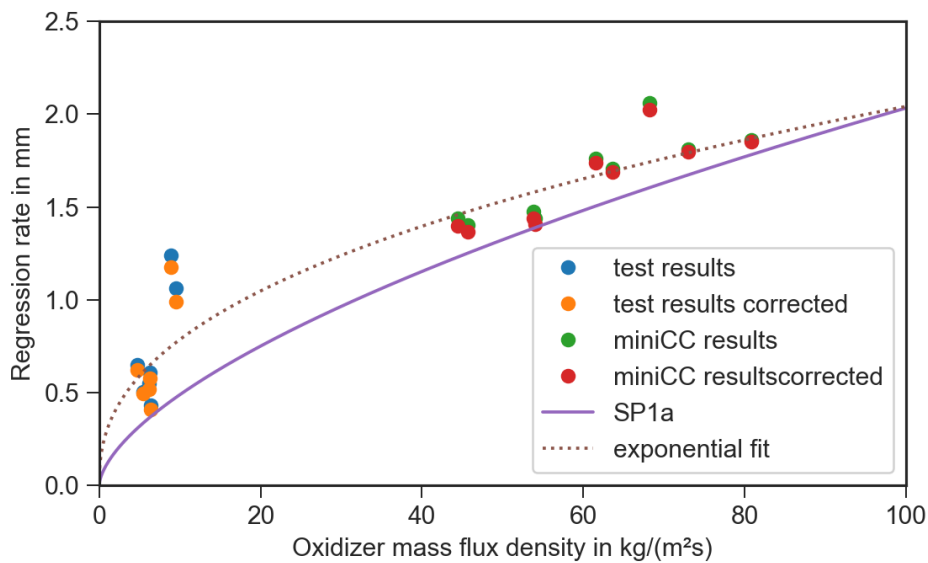
the control valve sets up at 68 bar and the chamber pressure at around 23 bar. At 10 s the feed pressure is changed to 100 bar and the control valve pressure starts increasing to 86 bar while the chamber pressure rises to 29 bar. The pressure rise again takes nearly 4 s to 5 s. At 13.6 s the nozzle breaks open which is clearly identified in the chamber pressure drop and the rise in the injector pressure. It can also be seen that the engine pressure drop has nearly no influence on the injector pressure and no effect at all on the pressure at the control valve. This confirms that the valve is working at choked flow conditions as it is supposed to. The throttling process itself did not impose any problems or instabilities on the chamber, however, the change of pressure is quite slow as the whole piping and chamber volumes are quite large compared to the oxidizer volume flow. Figure 5.9d illustrates the mass flow of the gaseous oxygen in test No. 7. The oxygen mass flow increases as expected with the higher feed pressure. The stationary level in the first 10 s was 45 g/s and after the rise to the higher supply pressure it was 58 g/s. In order to realize more realistic throttling tests, a new engine design with a larger oxidizer gas volume flow compared to the piping and engine volume is necessary, in order to decrease the duration of the transient phases. Alternatively the engine could be tested with LOX as oxidizer on a different test bench. The nozzle throat graphite part was redesigned after test No. 7. The part had a quite sharp edge close to the point of the highest heat load. This was replaced with a conical shape. More tests in the future to include throttling at the test bench M11.3 are planned.

(a) Regression rates

(b) Corrected regression rates

(c) Test 7 Pressure

(d) Test 7 Mass flow
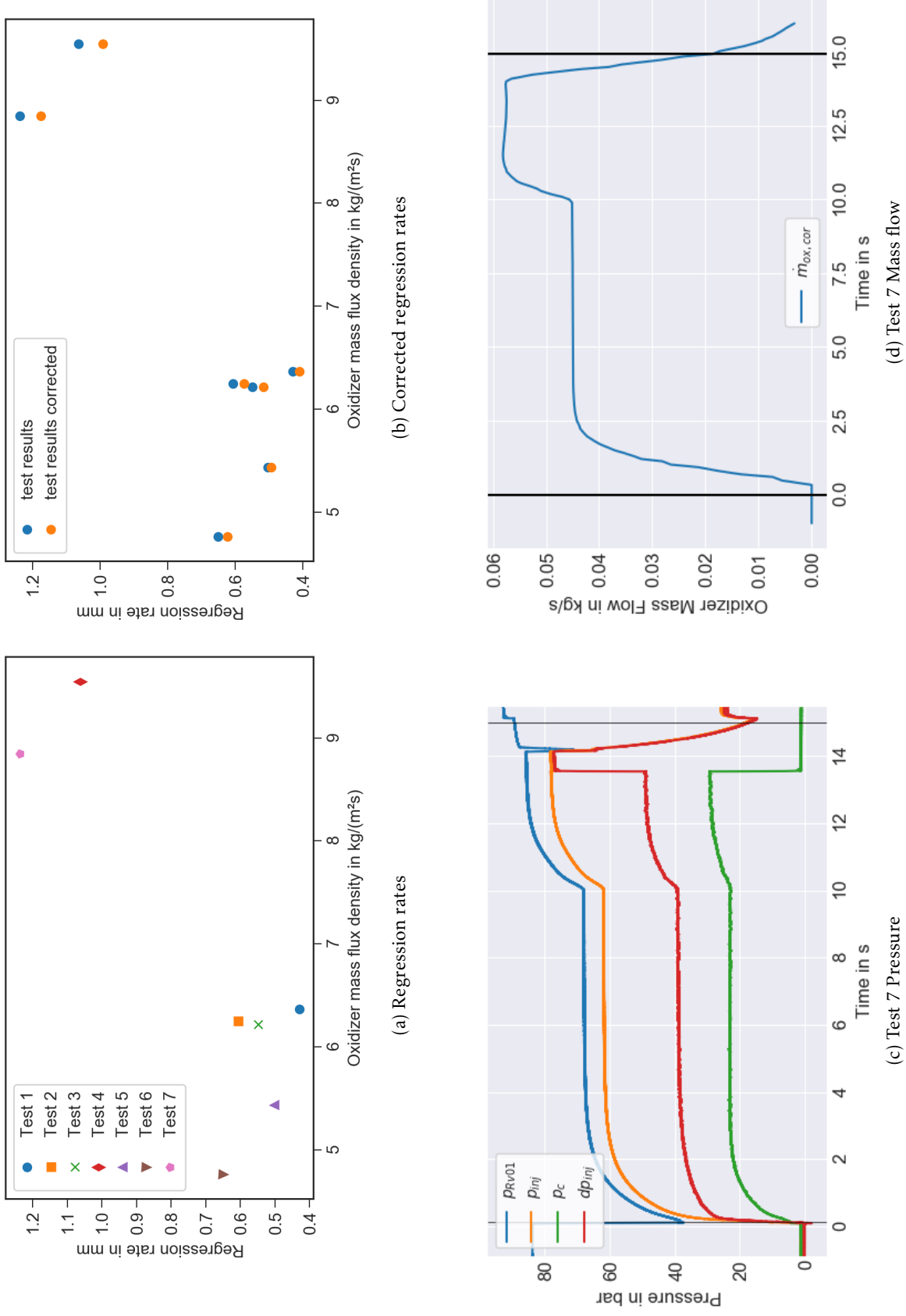
Figure 5.9.: Regression rate data and test No. 7 measurements

6. Hybrid Propulsion Lunar Mission Analysis

6.1. Reference Mission

6.1.1. Launch with Ariane 5

The concept being investigated is a Moon spacecraft launched by the Ariane 5 launcher. There are several options possible to consider when launching a spacecraft to the Moon with a heavy launcher like Ariane 5.

1. Launch to LEO and from there the spacecraft conducts its own maneuvers to reach the Moon

   - highest spacecraft mass
   - high payload
   - high spacecraft complexity, larger ΔV budget
   - short transfer time
   - launch window flexibility

2. Direct launch into a Moon transfer trajectory

   - lower spacecraft and payload mass
   - less spacecraft complexity and less ΔV budget

3. Low-thrust transfer using electrical engines from LEO to Moon orbit

   - very long transfer time
   - high payload
   - electric propulsion system and high power demand necessary

For the mission analysis the direct launch into a Moon transfer trajectory was chosen as a reference. The spacecraft is launched at Guiana Space Center. At the apogee of the Hohmann-transfer ellipse, the spacecraft is then caught up by the Moon. This is comparable to the Luna 24 mission. The aim is to enable a lower cost Moon mission. This is reached by reducing the spacecraft's complexity and cost. A direct transfer orbit injection lower's the ΔV requirements and allows for a simpler spacecraft design. The Ariane 5 launch capability to the Moon has been analyzed. An exemplary launch date has been chosen to be the 31$^{\text{st}}$ December 2024 at about 4:30 am. This launch window is optimal to reach a maximum payload as the Moon crosses the orbital plane when the launched spacecraft crosses the Moon's

path. However, this is only an exemplary date. A similar launch window is opening every two weeks, when the Moon is close to its ascending or descending node. The possible payload was determined to be 8800 kg with the current Ariane 5 launcher data. The Moon orbit of the spacecraft would have a periselen of 100 km altitude and an excess velocity of 860 m/s. A polar inclination of 90° was chosen for this reference mission as every landing site could be reached from this orbit if phasing orbits are done (but only if all propellants are storable for up to one month). Different inclinations around the Moon could be easily reached as only a slight change in the transfer orbit will increase or decrease the inclination around the Moon by a lot. This reference trajectory for the Moon transfer is shown in Figure 6.1. The 3D visualization shows the highly elliptical transfer from the Earth's surface to the vicinity of the Moon. At a distance of roughly 60 000 km to the Moon the reference coordinate system is changed as this represents roughly the borderline of the sphere of influence of the Moon. This is marked with the red line. At this point the reference center of the trajectory is the Moon. The Moon is highlighted with a white circle. Figure 6.2 displays the hyperbolic trajectory that the spacecraft will have when arriving at the Moon's sphere of influence after being injected into a transfer orbit with Ariane 5. The trajectory has been optimized, so that the excess velocity is at a minimum at 860 $\frac{m}{s}$ and the periselen of the spacecraft is at about 100 km. The orbit inclination to the Moon's equatorial plane is close to 90°. With this inclination phasing orbits could be conducted to reach any landing spot on the surface. Therefore for the future landing analysis no specific landing spot had been chosen, as this is totally open from a spacecraft propulsion system point of view. The inclination of the spacecraft at the Moon is easily adapted with very small changes in the transfer orbit. The trajectory optimization resulted in a maximum payload of 8800 kg. This payload includes the whole spacecraft mass that is sent to the hyperbolic flyby at the Moon. The spacecraft itself must conduct course corrections while on its transfer orbit, as well as the orbit injection at the Moon. This is described in the next section. The transfer orbit
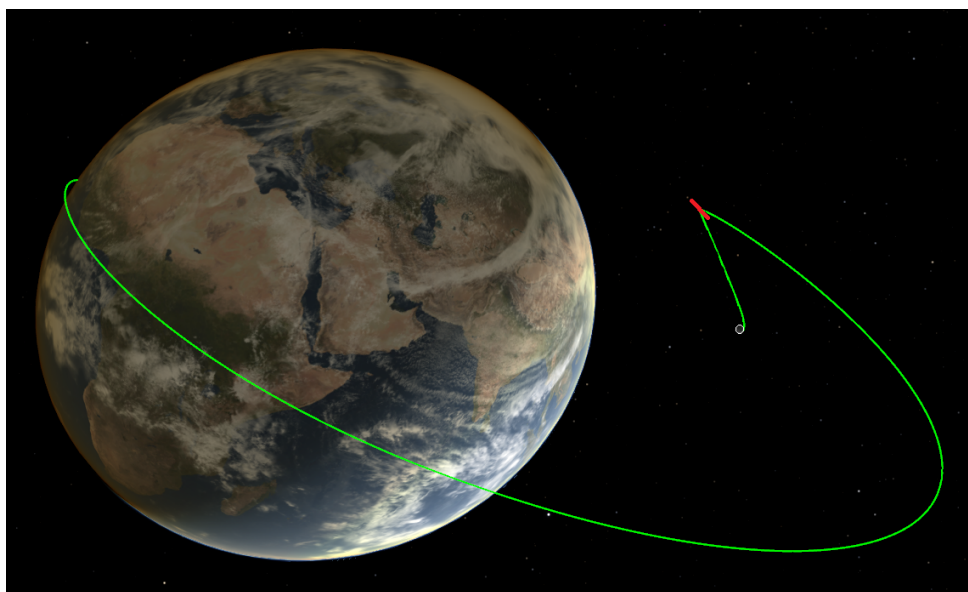
Figure 6.1.: Moon transfer trajectory of a Ariane 5 launched spacecraft
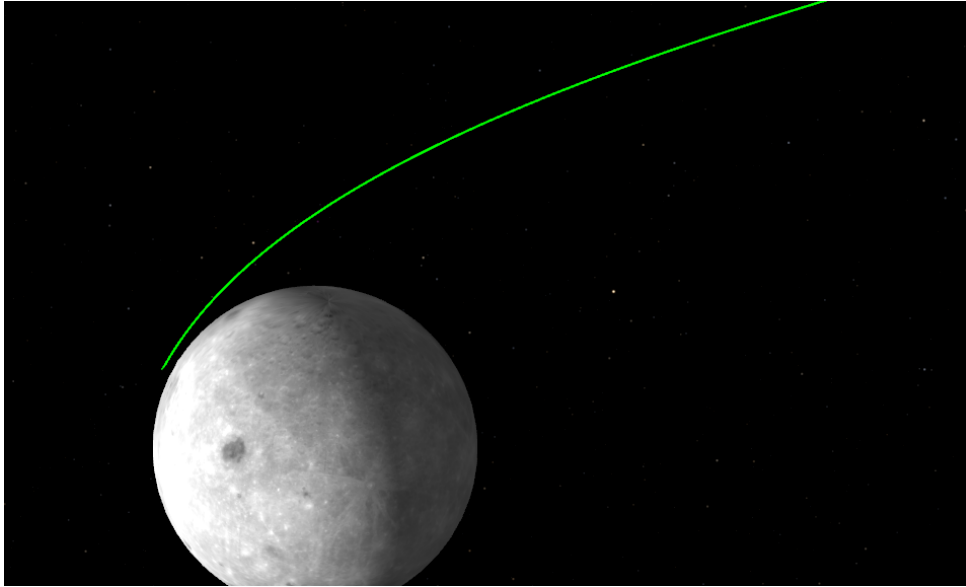
Figure 6.2.: Hyperbolic Moon trajectory after launch with Ariane 5

parameters after separation from the Ariane 5 Upper Stage are listed in Table 6.1, as well as all the orbital elements when arriving at the Moon's orbit periapsis. The complete duration of the orbit transfer is about 5 days. As a note, the Ariane 5 Upper Stage is not reignitable. If it was, the payload could possibly be increased by choosing different orbit maneuvers. A future update of the mission profile could be done with the performance values of Ariane 6, when they are released.

6.1.2. Moon Orbit Injection And Landing

When the spacecraft reaches the periselen at about 100 km, several maneuvers are performed to land on the Moon's surface. The first impulsive maneuver is conducted to stabilize the spacecraft in an orbit around the Moon. For this the rocket simply fires backwards and slows down. The resulting orbit is either highly elliptical or circular. Another possibility is a direct landing trajectory after the first burn. In all other cases the spacecraft can conduct phasing

Table 6.1.: Orbital elements after launch with the Ariane 5 ECA

Parameter	Value	Unit	Parameter	Value	Unit
Reference center	Earth center	-	Reference center	Moon center	
Apoapsis altitude	366539	km	Apoapsis altitude	-16738	km
Periapsis altitude	460	km	Periapsis altitude	100	km
Periapsis argument	72.9	°	Periapsis argument	175.4	°
Ascending node	96.5	°	Ascending node	76.2	°
Inclination	4.9	°	Inclination	90	°

orbits to reach nearly every spot on the Moon's surface. Then another burn is performed to lower the periselen to a very low altitude above the surface. A coast arc follows and the spacecraft travels half way around the Moon to reach the periselen. Close to the lowest altitude the engines are fired again and the spacecraft is slowed down. This burn can be separated into two phases with a coast arc in between, if the mission makes it necessary (e.g. if the spacecraft needs to descend closer to the surface). In order to be able to choose the right landing spot with suitable surface conditions, a hovering phase at 1 km to 0.85 km altitude is added. During this phase the lander roughly stays at the same position in the reference trajectory. In the real mission, this phase can be used to adapt the position to the surface conditions. After the hovering phase a coasting phase is added, during which the lander is pulled down by Moon's gravity and in a final engine burn the spacecraft will land softly on the surface. For the analysis of a lander spacecraft using hybrid propulsion, a three stage concept is the baseline. The reason for this lies in the limited burning duration of hybrid rocket engines. The hybrid rocket engine imposes low-cost combustion chamber technology but introduces higher staging complexity. The three stages are used as follows: The first stage is used to conduct the orbit insertion and lower the periselen to below 30 km. The exact value is left to the optimizer to find. The second stage is used to slow down and initiate the final landing. The third stage is the actual lander. It needs very little propulsion power. However, it needs to be maneuverable and to touch down in a soft and controlled way. Eight spacecraft concepts have been established and are compared in the next section. The altitude over time of this landing maneuver is shown in Figure 6.3. On the left the whole landing trajectory is shown, on the right side a detail of the final 4 km of the descent is shown. The different phases, which are defined in ASTOS, are highlighted with color. The plots refer to the optimized trajectory of a three staged spacecraft. For other variants the trajectory looks similar, even if the phases' duration might differ. In the detailed view of the altitude in the last 3 min during the landing, it is visible, that at 1 km altitude the spacecraft's sinking speed is reduced and for 1 min the spacecraft is nearly staying at the same altitude. Figure 6.4 illustrates the corresponding velocities and speed. The flight path speed is shown together with the three velocity components in northern, eastern and radial direction. The east velocity is relative to the surface, taking into account the rotation of the Moon. It can be seen that the larger amount of ΔV is done at the second stage burns. The
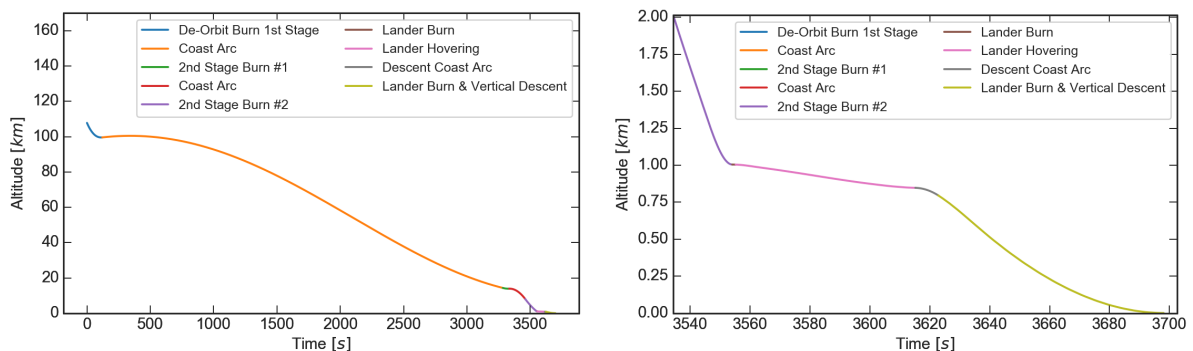
Figure 6.3.: Altitude over time of the Moon lander (total and detail)

first stage is performing a smaller ΔV. The first stage burn is capturing the spacecraft into a circular Moon orbit and afterwards lowers the periselen even more. The first burn of the second stage is reducing the velocity, to lower the periselen farther and leave the elliptical orbit around Moon. The second burn of the second stage is then reducing the vertical velocity during the descent. The east velocity rises to a maximum during the first coast arc while the north velocity passes through zero. This is when the spacecraft flies very closely to the south pole of the Moon and the negative north velocity (i.e. heading south) is flipping into a positive north velocity. The detailed view shows the final landing, where from 3550 s roughly a vertical descent is conducted. This is identified as the relative east and north velocities are zero. This was a constraint given to the optimizer. The optimization in ASTOS does not only optimize the spacecraft's components, but also the controls like attitude and thrust level. Figure 6.5 shows exemplarily the pitch and yaw controls of this trajectory. A smooth control is usually a sign for an optimal solution. If there are spikes and jumps it is an indicator that the trajectory is not fully optimized yet. The curves in Figure 6.5 are considered very well optimized. The x-axis value is the independent variable. This variable is the "optimization time". It starts at zero and every phase is exactly one unit long. Figure 6.6 depicts the oxidizer mass flow of a single lander stage engine during the last phases of the descent.
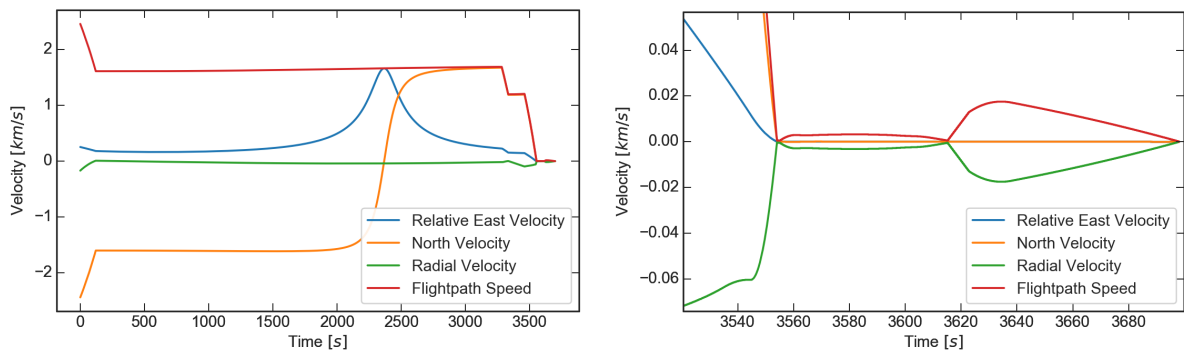
Figure 6.4.: Speed over time of the Moon lander (total and detail)
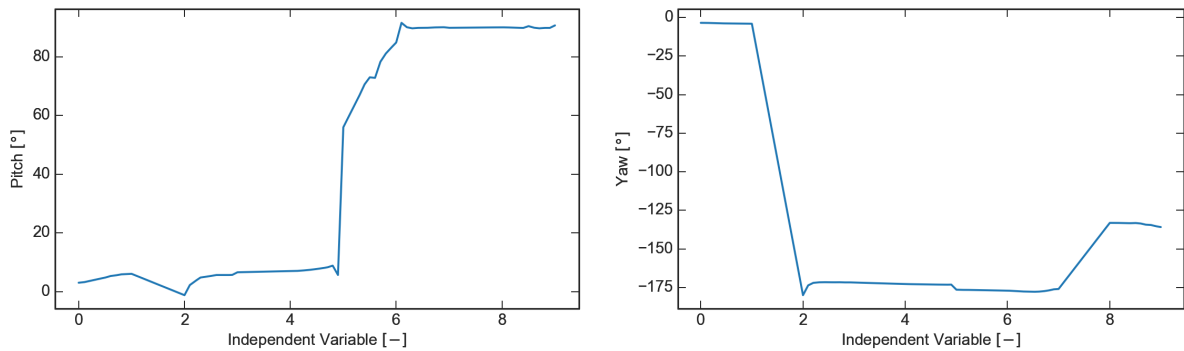
Figure 6.5.: Attitude over independent phase variable
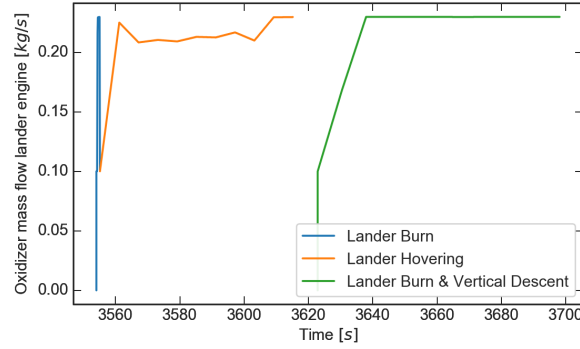
Figure 6.6.: Oxidizer mass flow of a single lander engine

ASTOS Model Set-Up

The ASTOS model for this reference landing mission has the constraints for the different phases listed in Table 6.2, where the abbreviations IBC is an initial boundary constraint. FBC is a final boundary constraint respectively and PC marks path constraints. The phases are named as follows:

A Orbit Capture Burn 1st Stage   D Coast Arc #2   G Lander Hovering

B Coast Arc   E 2nd Stage Burn #2   H Descent Coast Arc

C 2nd Stage Burn #1   F Lander Burn   I Lander Burn & Vertical Descent

Phase B is initialized with 29 major grid nodes in addition to the first and last one. Accordingly, phase B is optimized with the "Collocation Hermite" method (see [55]). All other phases are initialized with only one major grid node and hence optimized with the "Runge Kutta 4/5" multiple shooting method. This proved to be the fastest way of optimizing this type of trajectory. For very long coast phases with low gradients in the acceleration the collocation method works best as it replaces the integration of the real trajectory with a polynomial curve with much less integration work. In this case the Moon's gravitational acceleration changes only by about 9 % during the nearly one hour long coast. The trajectory was not optimized with all constraints active initially. The first optimization was done with wider ranges of the constraints, as well as attitude controls as parameters instead of control parameters. This made the first optimization to reach the rough trajectory very quick. Afterwards it was reinitialized with the parameters from this first result to introduce more precise constraints and the attitude control parameters. The control is refined with 9 nodes in every phase.

Table 6.2.: Moon landing optimization constraints

Constr.	A De-orbit burn	F	G	I
Mass IBC[1]	8500 kg			
Altitude FBC	99.5 km to 100.5 km	0.85 km to 1.0 km	0.85 km to 1.0 km	0.0 m to 1.0 m
PC			0.85 km to 1.0 km	
Aposelen FBC	99.5 km to 100.5 km			
Periselen FBC	10 km to 30 km			
Radial vel. FBC		$-0.5\,\frac{m}{s}$ to $0.5\,\frac{m}{s}$	$-0.5\,\frac{m}{s}$ to $0.5\,\frac{m}{s}$	
PC			$-5\,\frac{m}{s}$ to $0\,\frac{m}{s}$	
North vel. PC			$-0.1\,\frac{m}{s}$ to $0.1\,\frac{m}{s}$;	$-0.1\,\frac{m}{s}$ to $0.1\,\frac{m}{s}$
East vel. PC			$-0.1\,\frac{m}{s}$ to $0.1\,\frac{m}{s}$	$-0.1\,\frac{m}{s}$ to $0.1\,\frac{m}{s}$
Flightp. sp. FBC				$0\,\frac{m}{s}$ to $0.5\,\frac{m}{s}$

[1] For the cryogenic variants the vaporized propellant needs to be substracted, 300 kg are substracted for the orbit correction maneuvers
Note: IBC: Initial Boundary Constraint; FBC: Final Boundary Constraint; PC: Path Constraint

6.2. Lunar Lander Spacecraft Design

6.2.1. Mass Estimations

In order to validate the spacecraft's design and trajectory, some spacecraft subsystem masses were approximated with simple estimations. Table 6.3 shows the assumptions which were used in the calculation of the spacecraft masses. For the subsystems not related to the propulsion system, the mass estimation is very preliminary. The estimations are based on comparisons of existing missions and experience values.

Propulsion System Model

In order to correctly predict the hybrid propulsion system performance for the trajectories the hybrid analysis tool for ASTOS has been used and the results and mass estimations have been validated with ESPSS simulations. Especially the pressurization gas mass, hybrid engine specific impulse and thrust have been confirmed with the EcosimPro/ESPSS model. The simulation model schematic is shown in Figure 6.7. The simulation model includes a pressurization tank, valve and pressure regulator, an oxidizer tank and the piping connecting the tank to the engine. As the stage has multiple engines, only one engine was modeled while the respective mass flows to the remaining engines were simply mirrored with a fixed mass flow component. The pressurization gas is stored in a 300 bar tank. The oxidizer tank is pressurized to 30 bar after the start of the simulation sequence. The initial filling level with oxidizer is 90 % of the total tank volume. The valves and orifices cross sections have been modeled in order to reach a 10 bar pressure drop over the injector and an engine pressure of about 15 bar. The

Table 6.3.: Mass estimation for spacecraft design

Hybrid rocket engine			
Chamber wall	Cylinder shaped carbon reinforced plastic wall, scaled with pressure loads		
Injector dome	Mass estimation based on CAD models with aluminum casing and brass injector plates		
Chamber insulation	Mass estimation based on CAD models for insulation parts (phenolic composite, graphite)		
Nozzle	Simple mass estimation of a simple laval nozzle		
Oxidizer supply			
Oxidizer tank	Spheric composite tank, safety factor 2, metallic liner, 25 bar pressure		
Oxidizer feed system	15 kg for the kick stage, 5 kg for the lander and return rocket		
Oxidizer pressurization	Helium for pressurization and corresponding high pressure tank		
Structural parts			
Staging adapter	1.5 % of the stage mass		
General structure	7.5 % of the stage mass		
Landing legs	130 kg		
Other subsystems			
Power supply	35 kg	Others	25 kg
Flight computer unit	8 kg	Driller	70 kg
Thermal control	100 kg	Manipulator arm	70 kg
Telemetry & communication	35 kg	Scientific instruments	150 kg
GNC	11 kg	Rover	100 kg

oxidizer mass flow is actively controlled by a proportional-integral-derivative (PID) controller. The PID controller uses proportional, integral and derivative terms to calculate the control value. In this way the controller is reducing the risk of an overshoot when the set point of the controller's input changes. The controller's output is then connected to the valve's opening position input. For the simulation of the regression rate in the hybrid rocket engine the standard regression law with experimental coefficients a and n has been used. The exemplary simulation results are shown in the Appendix F. Due to the long burning time the ratio of final to initial inner diameter of the fuel grain is about 1.73. This means the port cross area at the end of the burn is about three times higher than in the beginning. If the initial diameter is reduced further the size of the engine can be shrinked but it will increase the diameter ratio even more, which might influence the combustion behaviour negatively as the flow changes drastically during the burn duration. This can cause areas of combustion instability during the burn and needs to be verified with large scale engine tests. A similar EcosimPro/ESPSS model was created for a liquid bipropellant kick stage using nitrogen tetroxide and hydrazine as well as cryogenic oxygen and methane. The results won with the simulations of this model
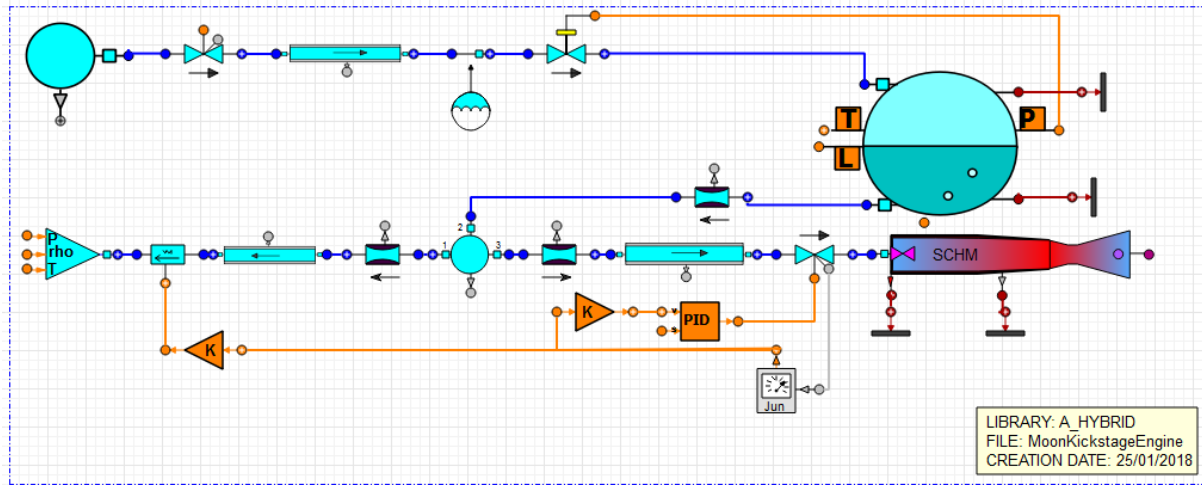
Figure 6.7.: ESPSS schematic for a Moon lander kick stage

were used to do an optimized trajectory with ASTOS in order to compare the performance of the used hybrid propellants with classical storable liquid propellants and also cryogenic propellants with higher performance but the need to cool the propellants. Table 6.4 compares some data between hybrid and liquid combustion. For the spacecraft performance another major difference lies in the propulsion systems' dry mass which is usually smaller for a pressure fed liquid bipropellant engine, even if it's complexity is higher. The engine efficiency has been chosen as 95 % for the N_2H_4/N_2O_4 engine and the LOX/Methane engine, as this is an usually achieved efficiency in liquid rocket engines. For the hybrid rocket engines it is more difficult to reach a higher efficiency. This is why only 90 % engine efficiency has been considered. However, this is conservative, and further advances in hybrid rocket engines might push the efficiency to higher values as well. The optimal mixture ratio for N_2H_4 and N_2O_4 with an expansion ratio of 100 is at about 1.4 and for LOX and Methane it is at 3.4 . For the hybrid rocket engines the mixture ratio is not fixed, as it is a function of the combustion time. However, the stage's propellant ratio is fixed and is between 7.5 to 7.6 for H_2O_2 and 2.8 to 2.9 for LOX. The concentration of the hydrogen peroxide is chosen as 95 %.

Table 6.4.: Propellant comparison in the chosen kick stage design

Parameter	NTO & N_2H_4 storable bi-liquid	LOX & LCH_4 cryogenic bi-liquid	H_2O_2 & PB-5% storable hybrid	LOX & PB-5% cryogenic hybrid
$\overline{I_{vac}}$	3300 $\frac{m}{s}$	3553 $\frac{m}{s}$	2950 $\frac{m}{s}$	3280 $\frac{m}{s}$
η_{eng}	95 %	95 %	90 %	90 %
$O/_F$	1.4	3.4	7.5 to 7.6	2.8 to 2.9
ϵ	100	100	100	100

6.2.2. Hybrid Propulsion Spacecraft Variants

Variant Hybrid 1: Three staged Lander

A first concept design for a lunar lander vehicle with hybrid propulsion had been introduced in [23]. This design still serves as the first reference in this work even if it has been updated. Figure 6.8 shows the design sketch of the vehicle. The left upper half of the figure shows the return rocket module with four hybrid rocket engines, a RCS thruster system, an oxidizer tank with storable H_2O_2 (95 % concentration) and the return capsule on top. Below the return rocket the lander with extended legs is shown. At the bottom left the kick stage design is shown. There is a LOX and H_2O_2 oxidizer version for the kick stages and the lander module. The return rocket always is in all cases using H_2O_2 as the oxidizer, as the return rocket is stored for several days or weeks before being launched back towards the Earth. For the other stages LOX could be used, when it is cooled by boil-off. On the right side of the figure, the assembled spacecraft is illustrated. It is already visible, that a LOX version of the spacecraft would be longer, as the hybrid rocket engines are longer due to the lower mixture ratio and the resulting long fuel grains. In comparison to the already published preliminary data, the mass estimations have been updated. Table 6.5 shows the overview of the mass distribution of the spacecraft. The initial mass of 8800 kg for the H_2O_2 version accounts also 300 kg of H_2O_2 for
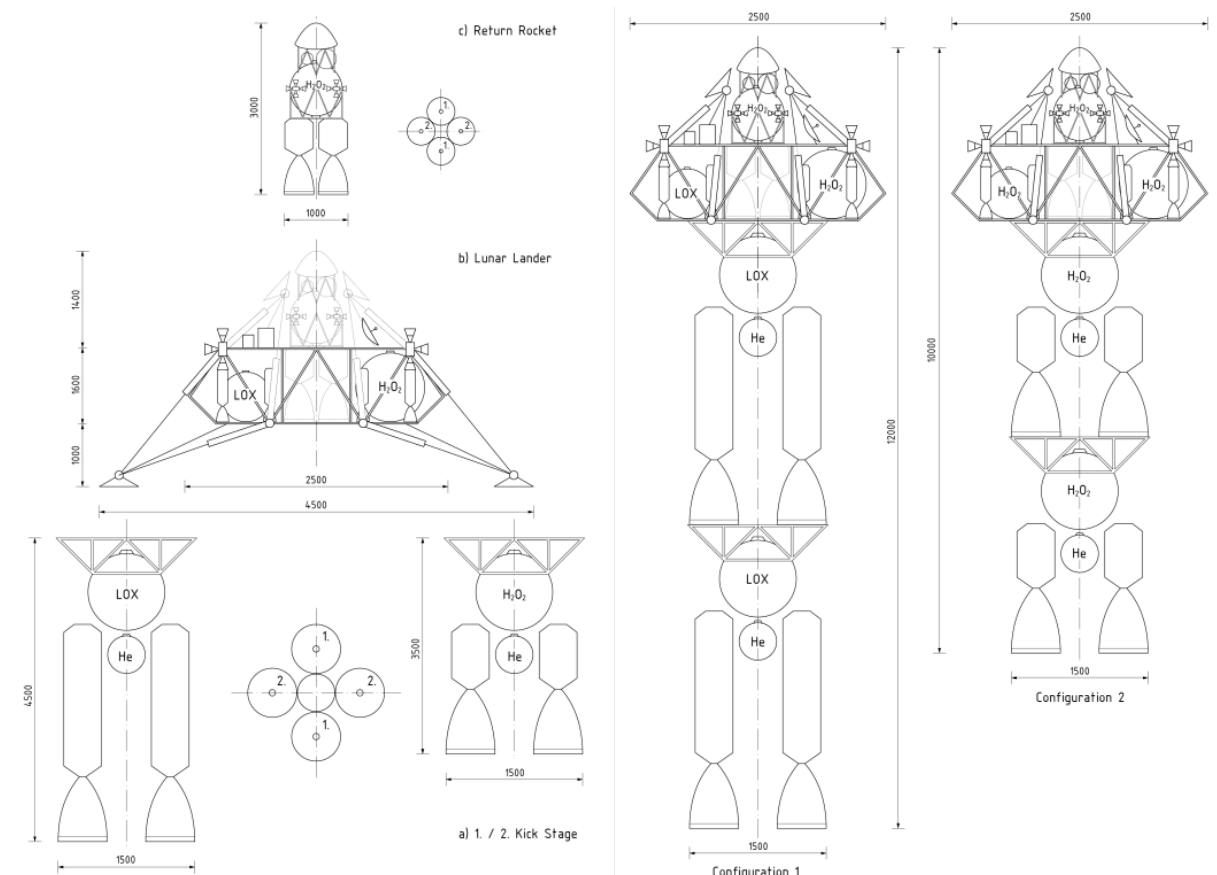

Figure 6.8.: Lunar lander spacecraft design sketch, [23]

course correction maneuvers with monopropellant thrusters prior to reaching the Moon flyby position. The additional mass for the lander is a sum of all structural and subsystem mass, according to the Table 6.3. The H_2O_2 for course corrections and steering of the spacecraft in all phases is used from the current active stage, if the oxidizer of the hybrid rocket engines is H_2O_2 as well. This is an advantage in mass, as the spacecraft doesn't need an additional H_2O_2 tank on the lander stage. In the LOX version the H_2O_2 is always drained from a tank on the lander module, which weighs additional 22 kg. The LOX version also includes an estimated LOX boil-off mass which is about 7.5 % of the total tank contents (for 5 days of flight to the Moon, roughly 1.5 % per day). Studies show, that with multi layer insulations the boil-off is reduced to 1 % to 3 % per month for liquid oxygen [76]. Usually the vaporization rate for LOX in a tank varies from 1 % to 10 % in 5 days depending on the tank design, the environment and the total tank volume. The masses in the table are valid for the lift-off. The H_2O_2 for course correction and RCS, as well as the vaporizing LOX are drained over time while transferring from LEO to the Moon. Therefore the stages have a smaller mass, when they are entering the Moon's orbit. In summary the spacecraft with LOX as the main engine's oxidizer has a higher performance and hence a greater return rocket mass. However, the mission conducted with LOX has more restrictions on the time windows: Phasing orbits in Low Earth or Low Moon Orbit would not be easily realizable. Also the filling of the tanks on the launch pad would be more difficult as it has to be done very late during launch preparations. Another issue with LOX is the ignition. A reignitable engine with H_2O_2 is realized quite easily and reliably with a catalyst bed. For a LOX based hybrid rocket engine an additional ignition system must be installed (i.e. laser ignition). The thrust of the four engines was first estimated to 13 kN each and the optimizer kept close to this value.

Variant Hybrid 2: Two staged Lander

Another variant is using a two staged spacecraft. This version is expected to have a smaller return rocket mass, as it is less effective, because more dry mass needs to be slowed down. However, it could be more optimal from a financial point of view, as a two staged spacecraft might be essentially cheaper than a three staged spacecraft. The optimization was conducted to investigate if the kick stage is still optimal when it provides the ΔV for both the orbital change and the landing velocity reduction, or if the optimizer scales up the lander vehicle, which in return could then do the latest ΔV maneuvers on its own. Having a single stage has some advantages: Due to the spherical shape the oxidizer tank has a higher volume to mass ratio than two single tanks. Also there is only one feed system, one pressurization system, and only one staging adapter to the lander, which in total is saving some dry mass. However, as mentioned, the mass is never jettisoned and therefore the total ΔV of the kick stage is less than two kick stages in the three staged Variant 1. This also implies that the lander itself has to provide more ΔV. This is confirmed with the ASTOS simulations and can be seen in Figure 6.9. This Figure compares the descent of Variant 1 and Variant 2 by showing the altitude over time. The x-axis zero point is the touch down event. Table 6.6 lists the defining masses for the two

Table 6.5.: Lunar lander Variant 1 mass overview

Vehicle system	Component	Mass H_2O_2 version	Mass LOX version
Total spacecraft mass		8800 kg	8800 kg
First kick stage		2986 kg	2512 kg
	H_2O_2 for course correction	300 kg	
	H_2O_2 for RCS	50 kg	
	Boil-off LOX for cooling		106 kg
	Main engine oxidizer	1883 kg	1410 kg
	Main engine fuel	247 kg	481 kg
	Propellant reserve	20 kg	20 kg
	Structure engines	90 kg	131 kg
	Structure oxidizer	64 kg	55 kg
	Additional structural mass	332 kg	309 kg
Second kick stage		3154 kg	3019 kg
	H_2O_2 for RCS	100 kg	
	Boil-off LOX for cooling		131 kg
	Main engine oxidizer	2249 kg	1750 kg
	Main engine fuel	296 kg	600 kg
	Propellant reserve	20 kg	20 kg
	Structure engines	90 kg	131 kg
	Structure oxidizer	65 kg	68 kg
	Additional structural mass	334 kg	319 kg
Lander stage		1337	1829 kg
	H_2O_2 for course correction		300 kg
	H_2O_2 for RCS	150 kg	300 kg
	Boil-off LOX for cooling		11 kg
	Main engine oxidizer	168 kg	144 kg
	Main engine fuel	23 kg	59 kg
	Propellant reserve	2 kg	2 kg
	Structure engines	19 kg	24 kg
	Structure oxidizer	9 kg	6 kg
	Structure H_2O_2 tank		20 kg
	Additional mass	966 kg	963 kg
Return rocket		1323 kg	1440 kg

staged Variant 2. The altitude is drawn from the beginning of the lander burning phase. The first phase in Variant 1 is less than 2 s, while for Variant 2, where the lander has to deliver higher ΔV, the first lander phase before the hovering phase is about 30 s long. The two-staged Variant 2 has eight engines with 13 kN each on its kick stage in order to deliver the same ΔV and having the same burning time per engine as before. The engines can be fired in groups of four to reduce the acceleration.

Variant Hybrid 3: Engine Jettisoning

The hybrid propulsion system with the fuel being stored in the rocket engine allows for a simple modification of the two staged model: the engines are ignited and burnt sequential and jettisoned when emptied. This could be realized by having a similar layout of the spacecraft like in Figure 6.8, except that the first kick stage has no tank of its own. This variant offers

Table 6.6.: Lunar lander Variant 2 mass overview

Vehicle system	Component	Mass H_2O_2 version	Mass LOX version
Total spacecraft mass		8800 kg	8800 kg
Kick stage		6292 kg	5641 kg
	H_2O_2 for course correction	300 kg	
	H_2O_2 for RCS	150 kg	
	Boil-off LOX for cooling		246 kg
	Main engine oxidizer	4278 kg	3284 kg
	Main engine fuel	561 kg	1122 kg
	Propellant reserve	40 kg	40 kg
	Structure engines	181 kg	245 kg
	Structure oxidizer	132 kg	125 kg
	Additional structural mass	650 kg	579 kg
Lander stage		1341 kg	1804 kg
	H_2O_2 for course correction		300 kg
	H_2O_2 for RCS	150 kg	300 kg
	Boil-off LOX for cooling		10 kg
	Main engine oxidizer	182 kg	133 kg
	Main engine fuel	25 kg	58 kg
	Propellant reserve	2 kg	2 kg
	Structure engines	22 kg	22 kg
	Structure oxidizer	9 kg	5 kg
	Structure H_2O_2 tank		20 kg
	Additional mass	951 kg	954 kg
Return rocket		1167 kg	1355 kg
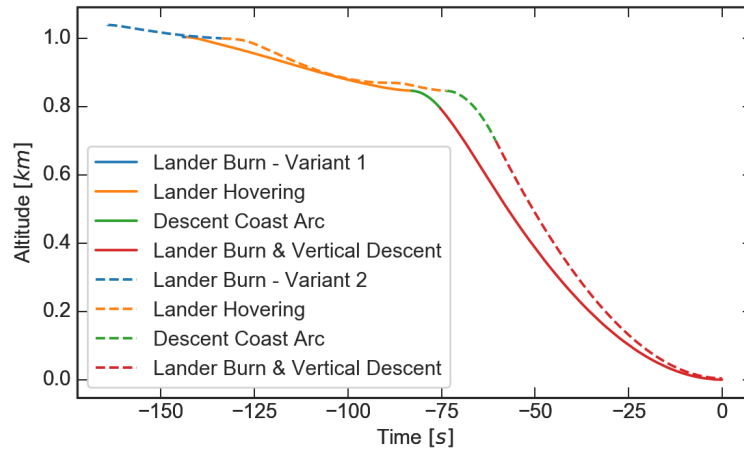
Figure 6.9.: Altitude comparison between Variant 1 and 2

only one oxidizer tank for the kick stage but still allows jettisoning empty dry mass of the first four engines. To realize this in the ASTOS model, first the total dry mass of the kick stage was increased, as additional staging and structural parts are necessary. Then a certain fraction of the first stage's dry mass representing half the engine and part of the structural mass was ejected after the first burn of the kick stage. Even when the total dry mass of the kick stage is higher in this variant, the total return rocket mass is still higher than in the Variant 2. This and all the other respective masses are listed in Table 6.7.

6.2.3. Hybrid Propulsion System Performance

A comparison between an EcosimPro/ESPSS simulation and the ASTOS hybrid tool calculations has been conducted with the simulation model detailed in Section 6.2.1. The second stage of Variant 1 with three stages using H_2O_2 as an oxidizer has been used. The values in the following Figures have been changed in the time stamp: The first burn starts $10\,s$ after the simulation starts. It takes $57\,s$ like in the trajectory simulation. Then the second ignition takes place at $100\,s$ and the second burn takes $95.5\,s$. In Figure 6.10 the mass flow of both ASTOS and ESPSS model is compared. It is visible that at this zoom level, no discrepancy is seen. The oxygen mass flow at the injector is a control value in the ASTOS model and an actively controlled value as well in the ESPSS model. However, it depends on the pressure in the tank as well and it can be seen that in the last few seconds of the second burn, that the pressurization pressure is too low to keep up the mass flow. However, the difference is only very small. Another difference is the gradient at start-up and shut-down of the engine. For long burn duration the effect is very small, but for a different engine burn duration the effect can have an impact on the trajectory. The fuel mass flow model is the same in both simulations. This means as long as the oxygen mass flow and the fuel diameter and length is the same, the simulation result is also congruent. This could be changed, if EcosimPro/ESPSS uses a different regression model. However, the current state of the art is, that regression is best modelled with

Table 6.7.: Lunar lander Variant 3 mass overview

Vehicle dystem	Component	Mass H_2O_2 version	Mass LOX version
Total spacecraft mass		8800 kg	8800 kg
Kick stage		6237 kg	5569 kg
	H_2O_2 for course correction	300 kg	
	H_2O_2 for RCS	150 kg	
	Boil-off LOX for cooling		239 kg
	Main engine oxidizer	4217 kg	3188 kg
	Main engine fuel	559 kg	1138 kg
	Propellant reserve	40 kg	40 kg
	Structure engines	181 kg	254 kg
	Structure oxidizer	131 kg	121 kg
	Additional structural mass	659 kg	589 kg
Lander stage		1356 kg	1815 kg
	H_2O_2 for course correction		300 kg
	H_2O_2 for RCS	150 kg	300 kg
	Boil-off LOX for cooling		10 kg
	Main engine oxidizer	189 kg	137 kg
	Main engine fuel	26 kg	58 kg
	Propellant reserve	2 kg	2 kg
	Structure engines	22 kg	22 kg
	Structure oxidizer	9 kg	6 kg
	Structure H_2O_2 tank		20 kg
	Additional mass	958 kg	960 kg
Return rocket		1207 kg	1416 kg

empirical regression rate coefficients according to $\dot{r} = aG_{ox}^n$. Figure 6.11 depicts the thrust curve of ASTOS and ESPSS in comparison. Here a difference can be seen in the according zoom level of the diagram. This is caused by three things: the before mentioned gradients at start-up and shut-down, the mass flow drop at the end due to missing high pressure in the pressurization system and lastly a slightly different calculation of the thrust in ESPSS. ASTOS uses an ideal thrust calculation with an efficiency coefficient. ESPSS also uses the same procedure. However, small differences in the exit velocity of the exhaust gases have been recognized in comparisons between ESPSS and NASA CEA results. The corresponding specific impulse is shown in the next Figure 6.12. While ASTOS' specific impulse is merely a function of expansion ratio, chamber pressure and mixture ratio, the specific impulse in ESPSS considers also gradients and losses. This is why there is a small difference in the specific impulse similar to the thrust.
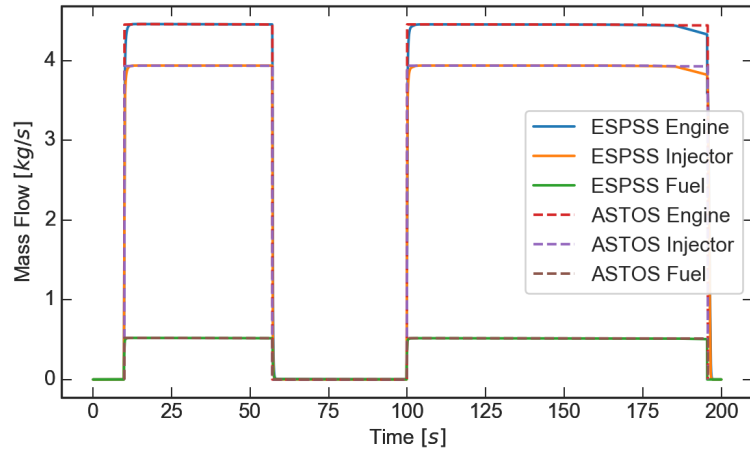
Figure 6.10.: Mass flow computation comparison between ESPSS and ASTOS model
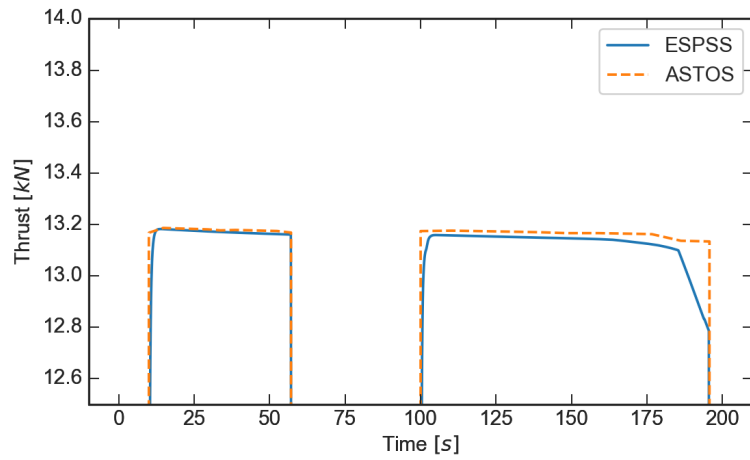

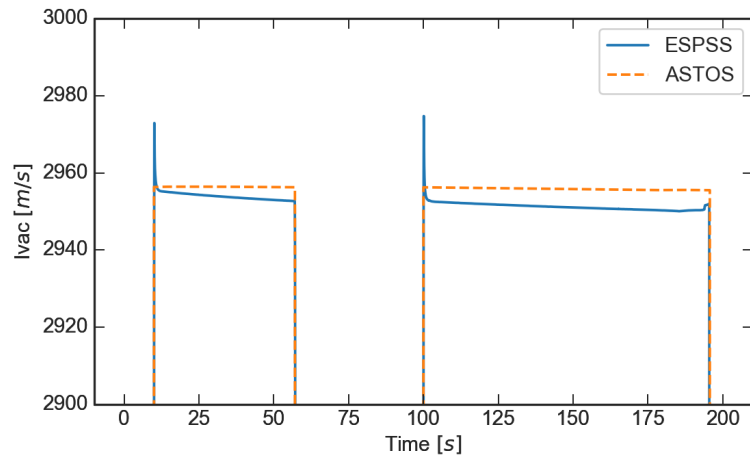Figure 6.11.: Thrust computation comparison between ESPSS and ASTOS model

Figure 6.12.: Specific impulse computation comparison between ESPSS and ASTOS model

6.2.4. Liquid Propulsion Spacecraft Variants

Variant Storable Propellants

To compare the hybrid propulsion system with conventional storable liquid propellant systems using nitrogen tetroxide (N_2O_4) and hydrazine (N_2H_4) a comparable two-staged spacecraft with storable propellants was optimized and simulated. The mass assumptions were similar except that a fixed engine mass was estimated. For the kick stage an engine mass of 130 kg was estimated. This is comparable to the Aestus engine. For the lander spacecraft the mass was estimated to be 20 kg, which is roughly similar to the Luna 24 engine. The storable propellants propulsion system has a lower structural mass and a higher specific impulse (mainly due to efficiency) and therefore the spacecraft has an increased return rocket mass of up to 1545 kg. This is completely explained with the more lightweight engine structure and the higher specific impulse. From a narrow performance point of view, storable propellants are preferable to the LOX/paraffin combination due to storability and performance, and also preferable to the H_2O_2/paraffin combination due to much higher performance. However, with environmental effects, health threats, ground operation difficulties, cost of transport, storing and cost of engine development, the hybrid rocket engines seem to be a viable alternative, if the loss in payload is considered acceptable.

Variant Cryogenic Propellants

In addition to classical storable liquid propellants, which have a long history of application on spacecraft flying to the Moon, a cryogenic liquid propellant combination was analyzed as well. The cryogenic propellants liquid oxygen and liquid methane were used for an optimization of the landing trajectory. The mass estimations were similar to the storable variant, however, the tanks mass was increased to consider insulation and a 7.5 % boil-off was considered for all propellants. As the specific impulse is higher and the boil-off mass is comparably low, the total return rocket mass was 1566 kg. Possibly the mass estimation for the boil-off and tank insulation mass is underestimated. However, it seems that cryogenic liquid bi-propellant systems might be a viable alternative to storable systems, if the mission duration is limited to a few days. The return rocket itself in this variant is again using storable liquid propellant N_2H_4 and N_2O_4 as the return rocket might reside for many days or even weeks on the lunar surface before flying back to Earth.

6.2.5. Spacecraft Variants Summary

Three spacecraft staging variants using hybrid propulsion have been compared on a landing trajectory starting from a hyperbolic flyby trajectory around the Moon. The most complex spacecraft with three stages, namely two kick stages and a lander, provide the highest payload mass with a fixed initial launch mass from Earth of 8800 kg. Figure 6.13 shows the different masses of the variants in direct comparison. The differences are comparably small, the only

large one is the oxidizer to fuel ratio between the H_2O_2 and LOX variants. It is also visible, that the structural mass of the LOX variants is slightly higher even though the propellants mass is smaller. The reason for this is that the larger fuel proportion means that the combustion chambers are larger. The combustion chamber have more structural mass per propellant mass, as the design is including thermal insulation materials and the long, slender cylinders of the combustion chamber is less weight optimal than spherical tanks. The ASTOS simulations and optimizations were done with the hybrid optimization tool. The fuel grain sizes as well as the resulting mixture ratios were optimizable. Table 6.8 lists the data for the fuel grains in the different variants. The kick stage fuel grains are taken as a reference. For the three staged variant, the second kick stage has been chosen. One fundamental advantage of the H_2O_2 engines is the high mixture ratio, which leads to a short combustion chamber. This is often an advantage in order to keep structural mass low, shorten the spacecraft if the length is limited e.g. by a payload fairing and for cheaper and easier fuel production. Figure 6.14
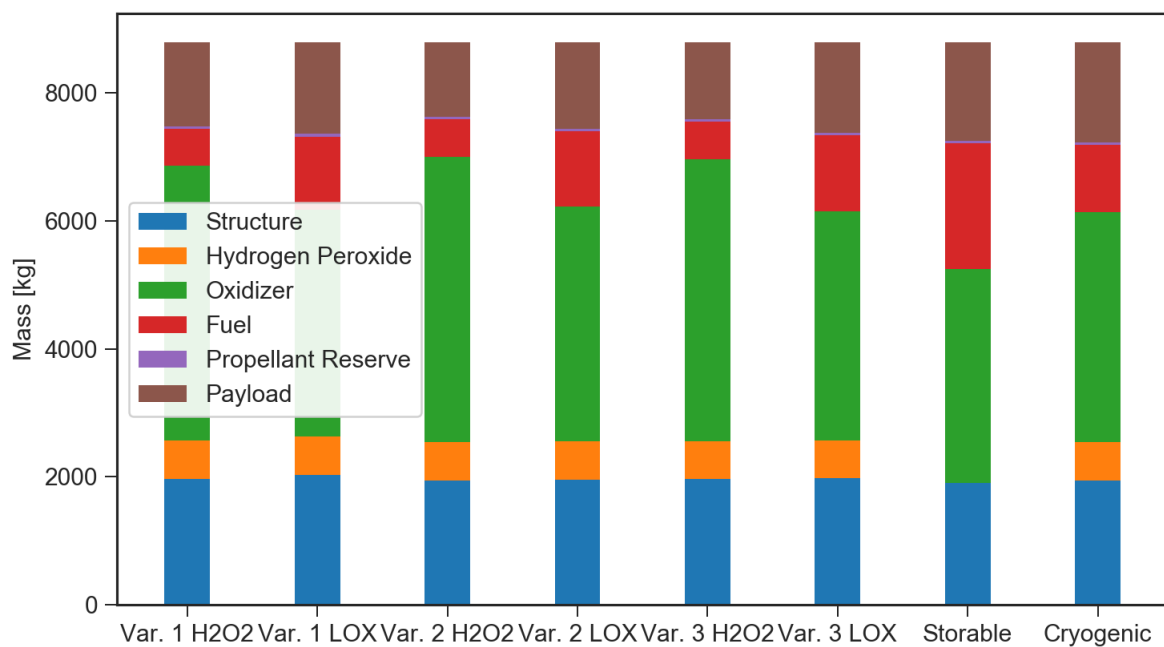
Figure 6.13.: Mass comparison of different variants

Table 6.8.: Fuel grain data kick stage

Phase	Var. 1		Var. 2		Var. 3	
	H_2O_2	LOX	H_2O_2	LOX	H_2O_2	LOX
Mass per grain	74 kg	150 kg	70.1 kg	140.3 kg	69.9 kg	142.3 kg
Length	0.64 m	1.51 m	0.64 m	1.52 m	0.65 m	1.58 m
Outer diameter	451 mm	450 mm	450 mm	450 mm	450 mm	450 mm
Inner diameter	210 mm	257 mm	227 mm	272 mm	232 mm	279 mm

illustrates an early design sketch of the propulsion system of the second stage in the three staged variant using H_2O_2. The engines with the nozzle and injector inflow connections have a total length of about 2 m long. The length of the whole propulsion system is about 3.5 m, if the pressurization tank is located between the engines. The largest diameter is at the nozzle exit with 2.1 m. With the LOX version, the tanks' sizes stay nearly the same. Much less oxidizer mass is needed. However, the density of LOX is lower. The major difference is the fuel length, which is 0.9 m longer. This is also the difference in the total length of the propulsion system and results in 4.4 m for the LOX propulsion system. A cross section of a 13 kN hybrid rocket engine using H_2O_2 and PB-5% as propellants is shown in Figure 6.15. The only difference in a LOX version is the length and inner diameter of the paraffin. The injector inflow is connected to the supply pipe for the oxidizer. An injector cavity is following downstream. For the H_2O_2 engines the catalytic material is stored in this cavity as a mesh in order to decompose the oxidizer. If the oxidizer is LOX this cavity is not necessary. Behind the injector cavity the injector head with an injector plate is following. There are different options for the injector plate. With hybrid rocket engines, all kinds of injectors have been tested in the past, from simple showerhead via impinging and swirling injectors to pintle injectors. It depends on the chamber design and the oxidizer inflow conditions to choose the right injector type. The rocket chamber itself is made from the fuel grain and insulation material, which is not burning and carbonizing and therefore withstanding the high heat loads. It also needs very low heat conductivity. In front of the fuel grain, a pre-chamber is typically found, where the oxidizer vaporizes and spread evenly over the fuel port. At the end of the fuel grain another section is found, which is used to give the combustion gases longer residing time inside the chamber
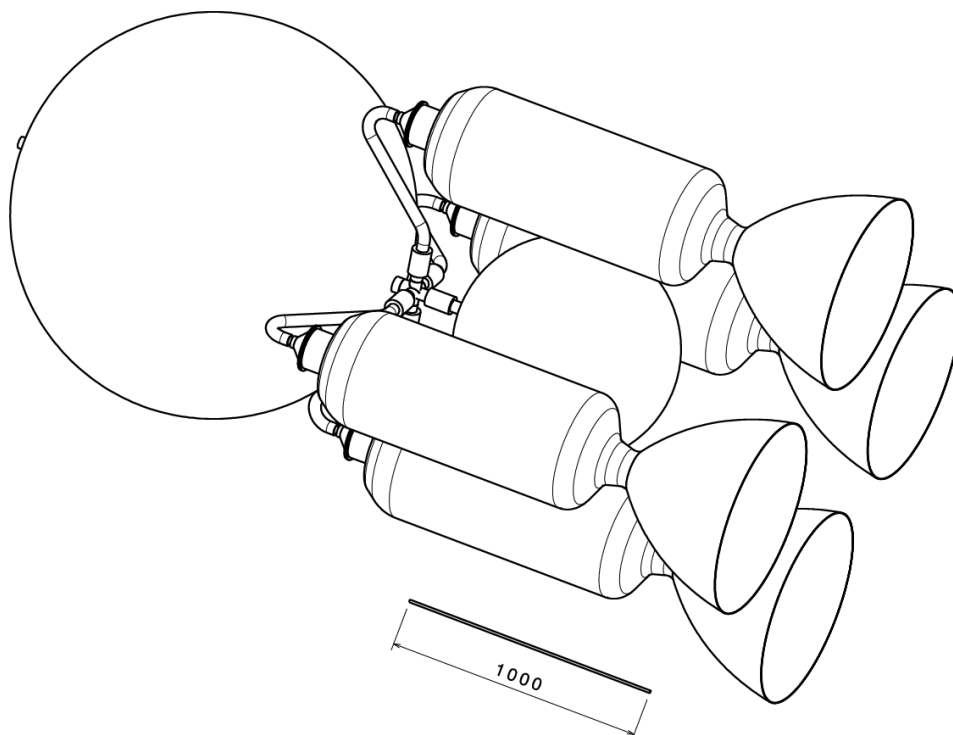
Figure 6.14.: Early design of the kick stage's propulsion system

in order to mix and burn completely. Then a Laval nozzle is ending the chamber. The nozzle throat is protected by a graphite insert, which withstands the high temperature and heat load and still has a very slow regression rate. The outside of the chamber is wrapped in carbon fiber reinforced plastic to complete the light weight design. Table 6.9 lists the ΔV per phase and spacecraft variant. It shows that the total required ΔV is about $2800\,\frac{m}{s}$ for this kind of landing on the Moon. The differences between the variants are caused by the spacecraft set-up but also by thrust to weight ratio in different trajectory sections. One remaining issue with a three staged spacecraft is the remaining of the stages. Currently there is no regulation about space debris in Moon orbit. Space debris in orbit poses a threat to future missions to the Moon as the Moon's gravitational field is very inhomogeneous [77]. Therefore orbits are not stable for a long time. It is possible for all debris parts like empty stages or inactive satellites to hit the Moon's surface after some months or years. This is threatening future surface based missions, both manned and unmanned. Therefore it is preferred by mission planners to have all empty
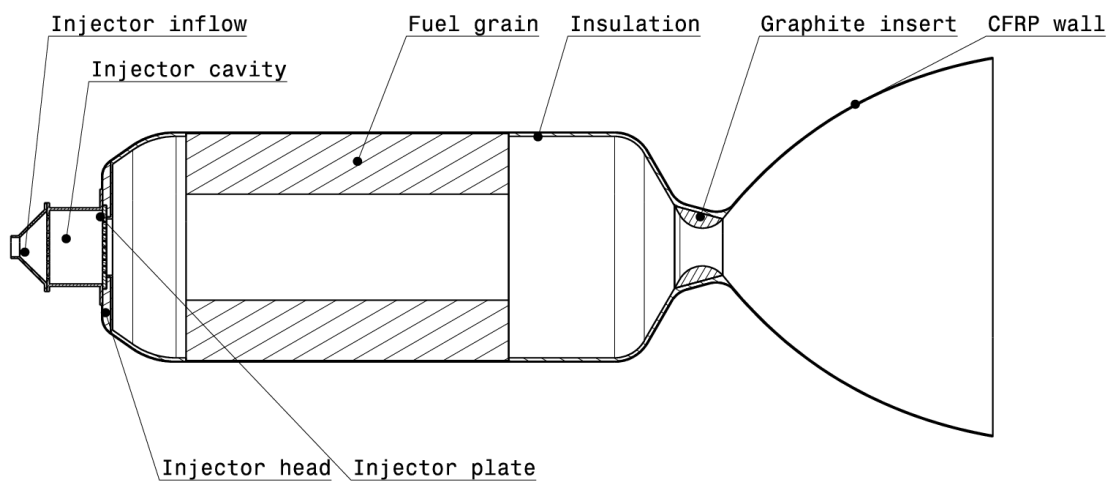
Figure 6.15.: Cross section of a H_2O_2/PB-5% engine with 13 kN thrust

Table 6.9.: $\Delta V\ [\frac{m}{s}]$ per trajectory phase

| Phase | Var. 1 | | Var. 2 | | Var. 3 | |
	H_2O_2	LOX	H_2O_2	LOX	H_2O_2	LOX
A	856	856	853	854	854	853
C	462	572	216	248	222	245
E	1265	1158	1468	1449	1464	1451
F	2	1	54	53	52	55
G	97	97	98	97	98	97
I	129	151	110	88	116	87
Total	2811	2835	2799	2789	2806	2788
	0 %	0.85 %	−0.43 %	−0.78 %	−0.18 %	−0.82 %

stages either leave the Moon orbit (and possibly Earth orbit) or to put them down on the Moon's surface in a controlled crash. In the trajectory of Variant 2 no debris remains in orbit. The first stage is separated in one piece, when the periselen is already below the surface. Hence, the first stage will splash down closely to the landing site of the lander. By further optimizing the horizontal velocity before separation the distance between splash down and landing site is manipulated. Variant 1 and 3 have a separation after the first burn, where the periselen is still above 10 km. Only a very small impulsive maneuver is enough to bring the first stage or drop off mass to a impact on the Moon's surface. This could be realized by a small cold gas thruster system, a very small solid rocket motor or a further short ignition of the hybrid rocket engines.

6.2.6. Return Rocket

The return rocket vehicle has the same design in all six before aforementioned hybrid rocket variants. As seen in Figure 6.8 it has four hybrid rocket engines with about 4 kN thrust each, a single oxidizer tank with H_2O_2 and a reentry capsule for the Moon soil samples. In the liquid bipropellant rocket engine set-up the return rocket has a rocket engine using N_2H_4 and N_2O_4. Its lift-off mass from Moon is determined by the lander variant, because it is equivalent to the payload of the lander. Tables 6.10 and 6.11 list the masses of the return rocket in the different variants. The names of the mission variants are not to be confused with the actual propellant choice for the return rocket. The return rocket always uses storable H_2O_2 as the oxidizer in the hybrid configuration and storable N_2H_4 and N_2O_4 for the liquid propulsion versions. For the hybrids, the total mass is at its maximum with the three staged LOX spacecraft variant, as the specific impulse with LOX is higher. The average specific impulse with the LOX spacecraft is about 11 % higher with LOX than with H_2O_2. Considering the whole spacecraft design, the payload is also 10 % to 20 % higher for the different variants with LOX. The liquid bipropellant spacecraft have a much higher return rocket mass. This higher return rocket mass supported by the lower structural mass for the propulsion system nearly doubles the capsule mass of the return rocket compared to the hybrid rocket engine variants. The structural mass of the hybrid rocket engines is very high, as the long cylinder is not an optimal shape for a pressure vessel. Additionally the whole chamber needs to be insulated. An additional fact is the lower efficiency, which is a possible improvement point for the calculated trajectories. If it is proven that hybrid rocket engines reach a very high efficiency like liquids without adding a lot of structural mass for better injection, preheating liquid oxidizers or mixing devices in the chamber, the performance of the hybrid rocket engine might be improved a lot and could compare more easily with a storable liquid propellant spacecraft. For the return rocket, the same holds true like for the descend vehicle: If a mission is targeted at maximum performance in terms of payload mass, sample return mass and therefore lowest structural mass and highest specific impulse, the best variant is to use cryogenic liquid propellants with boil-off on the landing vehicle and storable liquid propellants on the return vehicle. However, if low-cost and low hazards during development, ground operations and rocket launch have a high priority

as well, the hybrid propellants offer a good alternative to the storable liquid propellants.

Table 6.10.: Return rocket mass overview: part 1

Variant	Var. 1		Var. 2	
Name	H_2O_2	LOX	H_2O_2	LOX
Oxidizer	H_2O_2	H_2O_2	H_2O_2	H_2O_2
Fuel	PB-5%	PB-5%	PB-5%	PB-5%
Total mass	1323 kg	1440 kg	1167 kg	1355 kg
Relative	100 %	108.8 %	88.2 %	102.4 %
Oxidizer mass	654 kg	715 kg	572 kg	670 kg
Fuel mass	87 kg	95 kg	76 kg	89 kg
RCS propellant mass	100 kg	100 kg	100 kg	100 kg
Propellant reserve	40 kg	40 kg	40 kg	40 kg
Tank mass	19 kg	20 kg	17 kg	19 kg
Engine mass	34 kg	37 kg	29 kg	34 kg
Feed system mass	30 kg	30 kg	29 kg	30 kg
Power supply	24 kg	24 kg	24 kg	24 kg
Thermal control	8 kg	8 kg	8 kg	8 kg
Electronics	8 kg	8 kg	8 kg	8 kg
Staging	15 kg	15 kg	15 kg	15 kg
Structure	99 kg	108 kg	88 kg	102 kg
Reentry capsule	205 kg	240 kg	161 kg	216 kg
Structure	51 kg	60 kg	40 kg	54 kg
Electronics	6 kg	6 kg	6 kg	6 kg
Parachute	41 kg	48 kg	32 kg	43 kg
Heat protectection	62 kg	72 kg	49 kg	65 kg
Soil sample	45 kg	54 kg	34 kg	48 kg

The trajectory of the returning rocket vehicle is shown in Figure 6.16. The depicted snap-shot shows the position of the spacecraft just at the change of the sphere of influence. Hence the blue line representing the trajectory is switching the coordinate frame as well at that position. The rocket is ascending from the lunar surface with a sharp gravity turn into a Moon escape orbit with a periselen of about 10 km. The ΔV of this ascent from this launch position is 2600 m/s. The escape trajectory points in the contrary direction of the Moon's velocity vector in the Earth fixed coordinate system. The vehicles orbit when leaving the Moon's sphere of influence is a highly elliptical orbit with −2000 km perigee and 415 000 km apogee. The orbit is still in prograde direction. The perturbation forces after leaving the sphere of influence of the Moon are still high and hence when the spacecraft reaches an altitude of 10 000 km above the Earth's surface, the perigee has increased to 100 km (which was the optimization's boundary constraint) while the apogee has decreased slightly to 409 000 km. With a perigee at such low altitudes a reentry is certain (even if more than revolution might be necessary, depending on

Table 6.11.: Return rocket mass overview: part 2

| Variant | Var. 3 | | Bi-liquid 1 | Bi-liquid 2 |
Name	H_2O_2	LOX	Storable	Cryo
Oxidizer	H_2O_2	H_2O_2	N_2O_4	N_2O_4
Fuel	PB-5%	PB-5%	N_2H_4	N_2H_4
Total mass	1207 kg	1416 kg	1545 kg	1566 kg
Relative	91.3 %	107.0 %	116.8 %	118.4 %
Oxidizer mass	593 kg	703 kg	464 kg	469 kg
Fuel mass	79 kg	93 kg	332 kg	335 kg
RCS propellant mass	100 kg	100 kg	100 kg	100 kg
Propellant reserve	40 kg	40 kg	40 kg	40 kg
Tank mass	17 kg	20 kg	26 kg	26 kg
Engine mass	30 kg	36 kg	20 kg	20 kg
Feed system mass	30 kg	30 kg	31 kg	31 kg
Power supply	24 kg	24 kg	24 kg	24 kg
Thermal control	8 kg	8 kg	8 kg	8 kg
Electronics	8 kg	8 kg	8 kg	8 kg
Staging	15 kg	15 kg	15 kg	15 kg
Structure	91 kg	106 kg	116 kg	117 kg
Reentry capsule	172 kg	233 kg	361 kg	373 kg
Structure	43 kg	58 kg	90 kg	93 kg
Electronics	6 kg	6 kg	6 kg	6 kg
Parachute	34 kg	47 kg	72 kg	75 kg
Heat protection	52 kg	70 kg	109 kg	112 kg
Soil sample	37 kg	52 kg	84 kg	87 kg

the ballistic coefficient of the capsule). The capsule has heat protection to endure the high heat loads and will descend on a parachute safely to ground. The rest of the return rocket structure will burn up in the atmosphere.

6.2.7. Impact of Engine Efficiency

The engine efficiency has a direct impact on the specific impulse and therefore on the ΔV-budget of each rocket stage. As shown in Table 6.4 a lower efficiency has been chosen for the hybrid rocket engine variants, as it is harder to increase the efficiency of a hybrid rocket engine compared to a liquid propellant engine, as the boundary layer combustion along the fuel grain makes effective mixing of the propellants more difficult. However, in order to estimate the effect of this lower efficiency on the hybrid rocket variants performance, the three staged variant with LOX as the oxidizer has also been simulated and optimized with an combustion efficiency of 95 %. Some parameters are compared for the three staged LOX using variant in
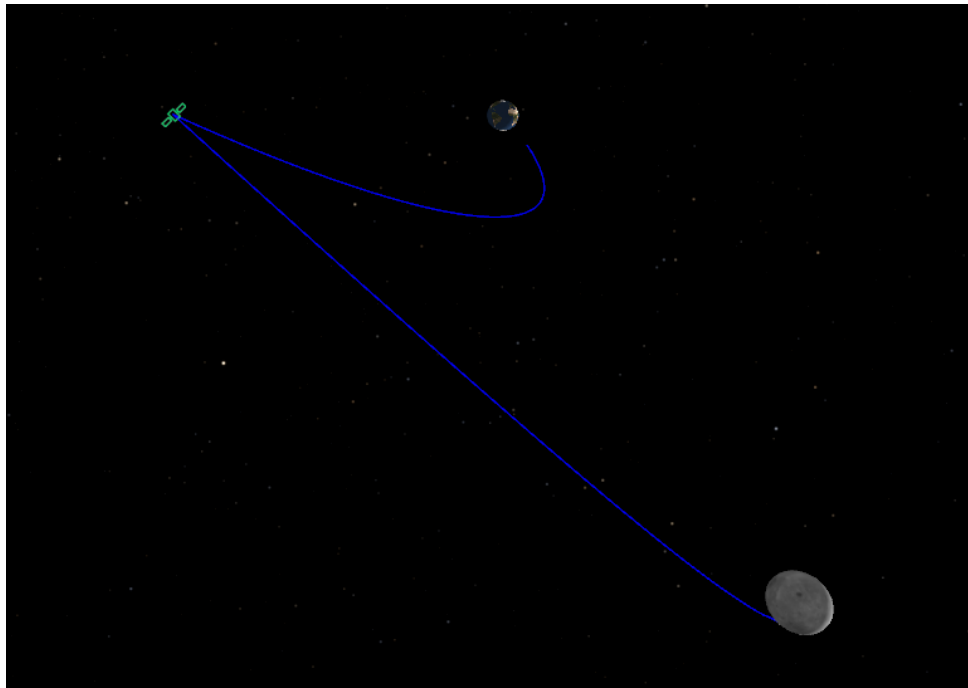
Figure 6.16.: Return rocket trajectory

Table 6.12. It is easily visible that the efficiency has a high impact. In comparison the return rocket's mass gains 10.4 % and the soil sample mass even 38.9 %. If a comparison to Tables 6.10 and 6.11 is done it is visible that the higher efficiency hybrid rocket variant even reach similar values like the liquid biproppelant variants for the return rocket and the sample return mass. However, the liquid variants are only two-staged. A three staged liquid propulsion system will have an even higher payload capability at higher spacecraft costs.

Table 6.12.: Comparison of 90 % and 95 % combustion efficiency 3-staged variant using LOX

Efficiency	Lander propellant	Return rocket	Soil sample	Specific impulse (LOX)
90 %	4734 kg	1440 kg	54 kg	3280 $\frac{m}{s}$
95 %	4597 kg	1590 kg	75 kg	3460 $\frac{m}{s}$

7. Conclusion

In the 60's and 70's, the space race led to several missions to the Moon, including impactors, autonomous and manned landings. The Apollo program brought back many samples of lunar soil. The Luna program included three successful sample return missions. Analytical results on lunar soil back on the Earth are much better than in-situ analyzes. The variety and exactness of instruments is much higher in laboratories than on a spacecraft. Acquisition of scientific insights about the Moon's surface improves the understanding of genesis, development and evolution of the Moon, the Earth, other terrestrial planets and the inner solar system. The Moon is seen as a technology testing ground for interplanetary space applications like manned missions or in-situ ressource utilization. Soft landings on a celestial body require safe, reliable and high-performance propulsion systems. For example, deep-throttling is needed to land softly with the options of hovering over landing sites or evading obstacles. In the past, only hazardous propellants were used on the spacecraft, taking advantage of storability, monopropellant use and hypergolic ignition. In the last twenty-five years many missions to the Moon showed, that the interest of science and space-faring organizations is very high to conduct further missions. Several robotic, soft landing missions on the Moon are planned in the near future by many different organizations or nations.

Hybrid rocket engines are a good choice for replacing hazardous, toxic liquid propellant propulsion systems. Several fuel and oxidizer combinations provide similar specific impulse like storable liquid propellants. Hybrid rocket engines share also the ability to stop, reignite and throttle, which is very important for landing applications. The simple design of hybrid rocket engines as well as the safe operations with its fuels and oxidizers make them an attractive choice for in-space propulsion as they increase safety at ground testing and in space. They also reduce costs of development and operation. The modeling of regression rates in design tools and simulation programs is one of the key aspects in developing propulsion systems with hybrid rocket engines. Regression models for classical and liquefying fuels have been established in the past. The implementation of these models in ESPSS creates a good tool to simulate hybrid rocket propulsion systems in different levels of details with more detailed regression rates. The simplified model that relies solely on regression rate coefficients always needs experiments to determine these coefficients beforehand. Models to predict the performance of hybrid rocket engines with high precision are necessary to develop hybrid propulsion systems for certain applications before experiments with that engine and propellants are conducted. However, this does not come without a drawback: These regression models based directly on the theory of a boundary layer flame need many input parameters. In case of liquefying fuels, the models have to consider droplet entrainment as well and

need additional input parameters. These input parameters are mainly fuel properties like viscosity or heat of gasification, but there are also obscure inputs like flame temperature or flame mixture ratio. In general the regression rate models are very flexible and applicable for predesign. To simulate a real rocket engine or propulsion system and compare measurements with the simulation, the regression rate coefficients need to be determined by experiments. Then the coefficients are used as an input for the simulation. The coupling of trajectory simulation and optimization with rocket cycle analysis in ESPSS allows optimizing hybrid rocket engines and spacecraft trajectories in a direct loop. This enables engineers to maximize the performance not only of the hybrid rocket engine itself, but of all the propulsion system and rocket stages depending on propellant combinations and trajectory requirements.

In order to verify if the used software is suitable to simulate, optimize and analyze a hybrid propulsion sample return mission to the Moon, different software tools were tested. First, ASTOS was used to reproduce the trajectories of Apollo 11 and Luna 24, two of the most important missions to the Moon in the last century. Apollo 11 was the first manned mission to land on another celestial body and Luna 24 was one of the first conducted robotic sample return missions ever. For both missions detailed trajectory data is available. However, still not all the necessary information to reconstruct the trajectories with full precision is attainable. With the given information it is well possible to simulate, optimize and analyze the trajectories within ASTOS. The optimization process helps out, where data is missing, because by fulfilling the known boundary and path constraints, missing parameters are found by the optimizer. ASTOS has proven to be a very powerful trajectory analysis tool to simulate translunar missions. The second step was to test the newly developed interface for ASTOS to simulate and optimize hybrid rocket engines. For verifying this interface's functionality no reference mission was available. Instead, an example was produced to evaluate the optimization result based on experience. The first example is a hybrid propulsion micro launcher. Small launch vehicles are a promising application for hybrid propulsion, as they offer low cost and high safety. A hybrid micro launcher concept was set up with ASTOS and the tool for hybrid propulsion simulation and optimization. The trajectory and the vehicle could be optimized reliably. While the trajectory boundary constraints were reached, the hybrid rocket engines were optimized as well as the staging of the launcher. By this the total vehicle mass for a payload of 25 kg could be optimized from 17.3 t to 11.7 t. Although some parameters like the structure mass ratio are just educated guesses, the trend was correct and the optimization tool for hybrid rocket engines worked very well. Ultimately, a lunar lander was simulated and optimized with the hybrid propulsion tool as well. In this case the final descent from a $100\,\mathrm{km} \times 100\,\mathrm{km}$ orbit around the Moon to the surface touchdown was considered. The tool worked as intended, the hybrid propulsion system was optimized, as well as the control and the sizing of the lander. In summary, the tools for simulating, optimizing and analyzing a hybrid propulsion lunar sample return mission, namely ASTOS and the hybrid propulsion tool, were tested and verified to work as intended.

An experimental campaign using a test chamber for long burn durations has been conducted at the test bench M11.3 in Lampoldshausen. The test chamber uses gaseous oxygen in combination with the paraffin-based fuel PB-5%. The mass flow is set to a reproducible operation point with a control valve and the supply pressure. Several pressure sensors were recording test data and the mass flow of the oxidizer was measured with a coriolis sensor. The fuel usage was determined by weighing the paraffin fuel grain before and after each test. Frequency analysis has been done for the different tests but no instabilities with high amplitude were recorded. The regression rate depending on the propellant combination and the chamber design were evaluated. A mixture ratio correction was necessary, since the mixture ratio was too fuel rich for most of the tests. The chamber geometry was adjusted in order to decrease the fuel surface and hence fuel mass flow. The reason for this was that the regression rate was a bit higher than predicted and that the fuel's front and back side added a fuel mass flow portion that in earlier tests was always negligible. In this campaign however, the chamber design included a fuel grain with a larger diameter compared to the fuel length and therefore the fuel front and back side added a larger area relatively to the total solid fuel burning surface area. A throttling test was conducted as well. However, the planned test duration of 40 s was not reached due to a failure of the nozzle graphite insert. Finally two out of four pressure levels were demonstrated in the test. Throttling itself did not inflict any problems on the test chamber. Changing the pressure did not increase oscillations. However, the throttling with a gaseous oxidizer is expected to be less prone to oscillations. Also the gas volume flow is low compared to the pipe and engine volumes, which causes the pressure in the chamber to always change in slow gradients. In order to test throttling under more realistic conditions a higher oxygen flow or a change to liquid oxygen is necessary , which is currently not possible at the test bench M11.3. The experimental results have also been compared to simulations done with a corresponding EcosimPro/ESPSS model in order to validate the ESPSS models. The experiments at the DLR test complex M11 showed that longer burn durations are possible but also bring new challenges like material life cycles and insulation problems. In order to obtain more data in the future, different engines should be tested with both GOX and LOX in order to characterize regression rates in a wider range and also investigate deep-throttling further.

Eight different Moon sample return mission variants have been analyzed with ASTOS, the analytical tool for hybrid rocket engines, and ESPSS models. The baseline for the launch of the spacecraft is an Ariane 5 ECA launch into a direct Moon transfer with about 8.8 t payload in a hyperbolical Moon flyby trajectory. The transfer time is about five days, which allows the spacecraft to carry either storable or cryogenic propellants, where the cryogenic propellants need to be cooled with boil-off. The landing trajectories of all compared spacecraft variants are quite similar: At 100 km altitude the rocket engines are ignited to decelerate the spacecraft into an elliptical orbit with a low periselen of about 10 km to 20 km. Close to the periselen, the spacecraft is further decelerated and begins its descent onto the surface. At 1 km altitude, the spacecraft initiates a hovering phase of one minute, which allows to choose the correct landing spot. After the soft landing, ground operations with a rover, driller and manipulator arm are conducted. When soil samples are filled into the return capsule, a return rocket is

launched towards the Earth and enters the Earth's atmosphere. Six variants of the hybrid propulsion spacecraft have been compared of which three use hydrogen peroxide and three use liquid oxygen as the oxidizer. Additionally the staging was divided in three options: three-staged, two-staged and two-staged with jettisoning of depleted hybrid combustion chambers. The return rocket is always using hydrogen peroxide in the hybrid propulsion concepts and is always a single stage rocket. In addition to the hybrid propulsion concepts, two liquid bipropellant propulsion concepts have been analyzed. The first one is using storable hydrazine and dinitrogen tetroxide in all stages whereas the second one is using cryogenic oxygen and methane on the landing stages. Both concepts use hydrazine and dinitrogen tetroxide in the return rocket. The soil sample mass is used as an indicator to compare the performance of the concepts. The sample mass of the liquid bipropellant concepts are the highest. This is due to the higher combustion efficiency and specific impulse as well as the smaller structural mass of the propulsion system. With the cryogenic liquid bipropellant concept a soil sample mass of 87 kg is reached while the storable liquid bipropellant concept reaches a sample mass of 84 kg. The difference is quite small. The cryogenic concept has a more complex thermal set-up and will probably require insulated tanks, pipes and valves but offers less hazardous propellants compared with the toxic and carcinogenic hydrazine in the storable concept. The largest soil sample mass with hybrid propulsion is reached with the three-staged concept using liquid oxygen. The sample mass is 54 kg and therefore 62 % of the two-staged cryogenic liquid bipropellant concept. The two-staged hybrid concept using LOX and jettisoning of empty combustion chambers reaches a similar value of 52 kg. The lowest sample mass is reached with the two-staged concept using hydrogen peroxide as an oxidizer with 34 kg soil. From a narrowed perspective regarding performance, the hybrid propulsion concepts are useful, but not competitive with an all liquid propellant concept. They could be improved by raising the efficiency of combustion which was still conservatively low in these calculations. A simulation with a three staged lander spacecraft using LOX and an increased efficiency of 95 % showed that the sample return mass is 75 kg, which is competitive to the liquid concepts. This shows that if development of hybrid rocket engines in the near futures brings them to a level, where high combustion efficiency is the standard, hybrid rocket engines become a real alternative to liquid rocket engines. If the perspective is widened and other factors next to performance are considered, hybrid propulsion might be a good choice even at the cost of lower performance. Storable liquid propellants like dinitrogen tetroxide and hydrazine are very toxic and carcinogenic. The advantage of the hybrid propellant combination with hydrogen peroxide as an oxidizer is the much lower toxicity. This reduces cost drastically during storage, transport, engine development and launch operations. The hybrid rocket engine still has the advantage of needing only one fluid management system, which also reduces the cost and complexity of the system. There will always be advantages and disadvantages to every options of hybrid and liquid rocket engines and for every application all suitable solutions need to be considered and compared.

Bibliography

[1] K. Tomilin. "Vorentwurf eines Mondlandefahrzeugs mit hybrid Raketenantriebssystem für eine Probenrückführungsmission". MA thesis. University of Stuttgart and DLR Lampoldshausen, 2016.

[2] Mario Kobald, Christian Schmier, Ulrich Fischer, Konstantin Tomilin, and Anna Petrarolo. "A Record Flight of the Hybrid Sounding Rocket HEROS 3". In: *31st ISTS Japan*. 2017.

[3] A. Konopliv, R. Park, D. Yuan, S. Asmar, M. Watkins, and et al. "The JPL lunar gravity field to spherical harmonic degree 660 from the GRAIL Primary Mission". In: *Journal of Geophysical Research: Planets* 118 (2013), pp. 1415–1434.

[4] NASA. *Moon Fact Sheet*. Website. Mar. 2016. URL: nssdc . gsfc . nasa . gov / planetary/factsheet/moonfact.html.

[5] ESA Concurrent Design Facility. *Lunar Exploration Study - Cargo Transportation System*. Tech. rep. 2005.

[6] *NASA Space Science Data Coordinated Archive*. Website. 2016. URL: nssdc . gsfc.nasa.gov/nmc/.

[7] *KTDU-5A, encyclopedia astronautica*. Website. 2016. URL: www.astronautix. com/engines/ktdu5a.htm.

[8] *TD-339 (SURVEYOR VERNIER) ROCKET ENGINE*. Website. 2016. URL: heroicrelics . org / info / surveyor / surveyor-vernier.html.

[9] *Space Launch Report CZ-5-5-7 Data sheet*. Website. 2016. URL: www . spacelaunchreport.com/cz5.html.

[10] R. Orloff. *Apollo By The Numbers*. 2016.

[11] *AJ10 Wikipedia*. website. Mar. 2016. URL: en.wikipedia.org/wiki/AJ10.

[12] *Aerozine 50 Wikipedia*. website. Mar. 2016. URL: en . wikipedia . org / wiki / Aerozine_50.

[13] European Commission. *REACH*. Website. Mar. 2016. URL: ec . europa . eu / environment / chemicals / reach / reach_en.htm.

[14] *Descent Propulsion System Wikipedia*. website. Mar. 2016. URL: en.wikipedia. org/wiki/Descent_Propulsion_System.

[15] *KTDU-417*. Website. 2017. URL: www.space-ru.com/russian-rocket-engines/rocket-engine-ktdu-417.

[16] *KRD-61*. Website. 2017. URL: www . space - ru . com / russian - rocket - engines/rocket-engine-krd-61.

[17] E. Betts and R. Frederick. "A Historical Systems Study of Liquid Rocket Engine Throttling Capabilities". In: *AIAA Joint Propulsion Conference*. 2010.

[18] A. Chandler Karp, B. Nakazono, J. Benito, R. Shotwell, D. Vaughan, and G. Story. "A Hybrid Mars Ascent Vehicle Concept for Low Temperature Storage and Operation". In: *52nd AIAA/SAE/ASEE Joint Propulsion Conference*. 2016.

[19] M. J. Chiaverini. "Fundamentals of Hybrid Rocket Combustion and Propulsion". In: ed. by M. J. Chiaverini and K. K. Kuo. Progress in Astronautics and Aeronautics. American Institute of Aeronautics and Astronautics, 2007.

[20] A. Takahashi and T. Shimada. "Essentially Non-explosive Propulsion Paving a Way for Fail-Safe Space Transportation". In: *31st ISTS Japan*. 2017.

[21] *Hybrid Rocket*. Website. Apr. 2015. URL: en.wikipedia.org/wiki/Hybrid%5C_rocket.

[22] Yen-Sen Chen, J. Lin, and S. Wei. "Development of an Airbreathing Hybrid Rocket Booster". In: *31st ISTS Japan*. 2017.

[23] C. Schmierer, K. Tomilin, J. Steelant, and S. Schlechtriem. "Analysis and Preliminary Design of a Hybrid Propulsion Lunar Lander". In: *Space Propulsion Conference*. 2016.

[24] Alfred Wright. *Nitric Acid/Nitrogen Tetroxide Oxidizers*. Martin Marietta Corporation, 1977.

[25] M. A. Karabeyoglu, D. Altman, and B. J. Cantwell. "Combustion of liquefying hybrid propellants: Part 1, general theory". In: *Journal of Propulsion and Power* 18.3 (2002), pp. 610–620.

[26] M. A. Karabeyoglu and B. J. Cantwell. "Combustion of liquefying hybrid propellants: Part 2, Stability of liquid films". In: *Journal of Propulsion and Power* 18.3 (2002), pp. 621–630.

[27] M. Kobald. "Combustion phenomena of advanced hybrid rocket fuels". PhD thesis. University of Stuttgart, 2015.

[28] M. Kobald, C. Schmierer, H. Ciezki, S. Schlechtriem, E. Toson, and L. De Luca. "Evaluation of Paraffin-based Fuels for Hybrid Rocket Engines". In: *50th AIAA/ASME/SAE/ASEE Joint Propulsion Conference*. 2014.

[29] A. Petrarolo, M. Kobald, and C. Schmierer. "Characterization of Advanced Hybrid Rocket Engines". In: *6th European Conference for Aeronautics and Space Sciences*. Krakow, Poland, 2015.

[30] Mario Kobald, Christian Schmierer, Helmut Ciezki, Stefan Schlechtriem, Elena Toson, and Luigi De Luca. "Viscosity and Regression Rate of Liquefying Hybrid Rocket Fuels". In: *Journal of Propulsion and Power* 33.5 (2017), pp. 1245–1251.

[31] Y. Tang, S. Chen, and L. T. DeLuca. "Mechanical Modifications of Paraffin-based Fuels and the Effects on Combustion Performance". In: *Propellants, Explosives, Pyrotechnics* (2017).

[32] C. Schmierer, M. Kobald, K. Tomilin, U. Fischer, M. Rehberger, and S. Schlechtriem. "HEROS - Sounding Rocket Development by the HyEnD Project". In: *6th European Conference for Aeronautics and Space Sciences*. 2015.

[33] M. Kobald, C. Schmierer, and A. Petrarolo. "Test campaign of a 10000 N Hybrid Rocket Engine". In: *6th European Conference for Aeronautics and Space Sciences*. Krakow, Poland, 2015.

[34] M. Kobald, U. Fischer, K. Tomilin, A. Petrarolo, and C. Schmierer. "Hybrid Experimental Rocket Stuttgart: A

Low-Cost Technology Demonstrator". In: *Journal of Spacecraft and Rockets* 55.2 (2018), pp. 484–500.

[35] M. Kobald et al. "Sounding Rocket "HEROS" - A Low-Cost Hybrid Rocket Technology Demonstrator". In: *53rd AIAA/ASME/SAE/ASEE Joint Propulsion Conference*. 2017.

[36] J. Dyer et al. "Status Update Report for the Peregrine 100km Sounding Rocket Project". In: *44th Joint Propulsion Conference and Exhibit*. AIAA 2008-4892. Hartford, CT, 2008.

[37] T. Knop, J. Wink, and et al. "Failure Mode Investigation of a Sorbitol-based Hybrid Rocket Flight Motor for the Stratos II Sounding Rocket". In: *51st AIAA Joint Propulsion Conference*. 2015.

[38] O. Verberne, A. Boiron, M. Faenza, and B. Haemmerli. "Development of the North Star Sounding Rocket: Getting ready for the first demonstration Launch". In: *51st AIAA Joint Propulsion Conference*. 2015.

[39] *Hyprogeo*. Website. Dec. 2015. URL: www.hyprogeo.eu.

[40] Karine Odic et al. "HYPROGEO Hybrid Propulsion: Project Objectives & Coordination". In: *Space Propulsion Rome*. 2016.

[41] M. Faenza, O. Verberne, S. Tonetti, S. Cornara, and T. Langener. "Hybrid Propulsion Solutions for Space Debris Remediation Applications". In: *Industrial Days ESA ESTEC*. 2016.

[42] G. Parissenti, M. Pessana, E. Gaia, and et al. "Throttleable hybrid engine for planetary soft landing". In: *4th European Conference for aerospace sciences*. 2011.

[43] R. Hahn, G. Waxenegger-Wilfing, C. Schmierer, and J. Deeken. "Cycle Analysis and Feasibility Evaluation of Pump Fed Hybrid Propulsion System". In: *SpacePropulsion Conference*. 2018.

[44] G. Marxman and et al. "Fundamentals of hybrid boundary combustion". In: Progress in Astronautics and Aeronautics, 1964.

[45] G. Zilliac and M. A. Karabeyoglu. "Hybrid Rocket Fuel Regression Rate Data and Modeling". In: *42nd AIAA/ASME/SAE/ASEE Joint Propulsion Conference and Exhibit*. AIAA-2006-4504. Sacramento, CA, 2006.

[46] M. J. Chiaverini, N. Serin, D. Johnson, Y. Lu, K. Kuo, and G. Risha. "Regression Rate Behavior of Hybrid Rocket Solid Fuels". In: *Journal of Propulsion and Power* 16.1 (Jan. 2000).

[47] A. Petrarolo. "Optical Analysis of Hybrid Rocket Combustino with Decomposition Methdos". In: *Space Propulsion*. 2016.

[48] M. Kobald, I. Verri, and S. Schlechtriem. "Theoretical and Experimental Analysis of Liquid Layer Instabilities in Hybrid Rocket Engines". In: *CEAS Space Journal* 7.1 (Mar. 2015), pp. 11–22.

[49] M. A. Karabeyoglu, B. J. Cantwell, and J. Stevens. "Evaluation of Homologous Series of Normal-Alkanes as Hybrid Rocket Fuels".

In: *41st AIAA/ASME/SAE/ASEE Joint Propulsion Conference and Exhibit*. AIAA-2005-3908. Tucson, AZ, 2005.

[50] R. Nigmatulin, B. Nigmatulin, Y. A. Khodzaev, and V. Kroshilin. "Entrainment and Deposition Rates in a Dispersed-Film Flow". In: *International Journal of Multiphase Flow* 22.1 (1996), pp. 19–30.

[51] J. Anderson. *Introduction to Flight*. 1979. Chap. 4.17, p. 210.

[52] R. A. Gater and M. R. L. L'Ecuyer. "A Fundamental Investigation of the Phenomena that Characterize Liquid Film Cooling". In: *International Journal of Heat and Mass Transfer* 13.3 (1970), pp. 1925–1939.

[53] M. Adachi and T. Shimada. "Liquid FFilm Instability Analysis of Liquiefying Hybrid Rocket Fuels Under Supercritical Conditions". In: *AIAA Journal*. 2015.

[54] A. A. Chandler, E. T. Jens, B. J. Cantwell, and G. S. Hubbard. "Visualization of the Liquid Layer Combustion of Paraffin Fuel at Elevated Pressures". In: *63rd International Astronautical Congress*. Naples, Italy, 2012.

[55] P. Gath. "CAMTOS - A Software Suite Combining Direct and Indirect Trajectory Optimization Methods". PhD thesis. University of Stuttgart, 2002.

[56] H. Curtis. *Orbital Mechanics for Engineering Students*. Elsevier, 2010.

[57] C. Schmierer. *Modellierung einer Mondmission mit Hybridantrieben*. Tech. rep. DLR Lampoldshausen and University of Stuttgart, 2015.

[58] *Chemical Equilibrium with Applications*. Website. 2015. URL: www.grc.nasa.gov/WWW/CEAWeb/.

[59] M. M. Fernandez. "Propellant Tank Pressurization Modeling for a Hybrid Rocket". MA thesis. Rochester, NY: Rochester Institute of Technology, 2009.

[60] J. E. Zimmerman, B. S. Waxman, B. J. Cantwell, and G. Zilliac. "Review and Evaluation of Models for Self-Pressurizing Propellant Tank Dynamics". In: *49th AIAA/ASME/SAE/ASEE Joint Propulsion Conference and Exhibit*. AIAA 2013-4045. San Jose, CA, 2013.

[61] *EcosimPro*. Website. 2016. URL: www.ecosimpro.com/products/ecosimpro.

[62] *European Space Propulsion System Simulation*, *ESPSS*. Website. 2016. URL: www.ecosimpro.com/products/espss.

[63] *ESPSS User Manual*, *Volume 1*. Empresarios Agrupados. 2016.

[64] R.C. Reid, J.M. Prausnitz, and T.K. Sherwood. *The Properties of Gases and Liquids*. McGraw-Hill, 1977.

[65] P.A. Ramakrishna, P.J. Paul, and H.S. Mukunda. *Sandwich Propellant Combustion: Modeling and Experimental Comparison*. Vol. 29. Proceedings of the Combustion Institute. 2002.

[66] Nicholas P. Cheremisinoff. *Handbook of Engineering Polymeric Materials*. Marcel Dekker, Inc., 1997.

[67] Abdul Khan, Abhijit Dey, Javaid Athar, and Arun Kanti Sikder. "Calculation of enthalpies of formation and band gaps of polymeric binders". In: *RSC Advances* (2014).

[68] H.G. Ang and S. Pisharath. *Energetic Polymers: Binders and Plasticizers for Enhancing Performance*. WILEY-VCH, 2012.

[69] Christian Schmierer, Mario Kobald, Johan Steelant, and Stefan Schlechtriem. "Combined Trajectory Simulation and Optimization for Hybrid Rockets using ASTOS and ESPSS". In: *31st ISTS Japan*. 2017.

[70] *Proton-K Wikipedia entry*. Website. May 2017. URL: https://en.wikipedia.org/wiki/Proton-K.

[71] *Blok-D Wikipedia entry*. Website. May 2017. URL: https://en.wikipedia.org/wiki/Blok_D.

[72] *Luna 24 information page*. Website. May 2017. URL: http://www.russianspaceweb.com/luna24.html.

[73] Jonas Breitinger. "Development and Test of an Experimental Hybrid Rocket Engine for Orbital Application". 2017.

[74] *Discrete Fourier Transform in Python with Fast Fourier Transform algorithm*. SciPy. URL: https://docs.scipy.org/doc/numpy-1.13.0/reference/generated/numpy.fft.fft.html.

[75] M. A. Karabeyoglu, G. Zilliac, B. J. Cantwell, S. DeZilwa, and P. Castellucci. "Scale-up tests of high regression rate paraffin-based hybrid rocket fuels". In: *Journal of Propulsion and Power* 20.6 (2004), pp. 1037–1045.

[76] Patrick Chai and Alan Wilhite. "Cryogenic thermal system analysis for orbital propellant depot". In: *Acta Astronautica 102* (2014).

[77] *NASA Aims to Keep Moon's Skies Junk-Free*. Website article. Oct. 2008. URL: https://www.space.com/6031-nasa-aims-moon-skies-junk-free.html.

[78] NASA. *Human Artifacts*. Website. Mar. 2016. URL: history.nasa.gov/humanartifacts.html.

[79] NASA. *NASA's GRAIL Creates Most Accurate Moon Gravity Map*. Website. 2016. URL: www.nasa.gov/mission_pages/grail/multimedia/pia16587.html.

[80] *Moon Landing, Wikipedia*. Website. 2016. URL: en.wikipedia.org/wiki/Moon_landing.

[81] *LADEE Spacecraft Overview*. Website. 2016. URL: spaceflight101.com/ladee/spacecraft-overview/.

[82] *Chang'e 3*. Website. 2016. URL: spaceflight101.com/change/change-3/.

[83] NASA. *Apollo Images*. Website. Mar. 2016. URL: history.nasa.gov/ap11ann/kippsphotos/apollo.html.

[84] Capcomespace. *Lunar probe images*. Website. Mar. 2016. URL: www.capcomespace.net/dossiers/espace_US/apollo/annexes/15_les_sondes_lunaire_2.htm.

[85] Skyatnight Magazine. *Gallery of Luna 24*. Website. Mar. 2016. URL: www.skyatnightmagazine.com/gallery/cosmonauts-exhibition-opens-science-museum.
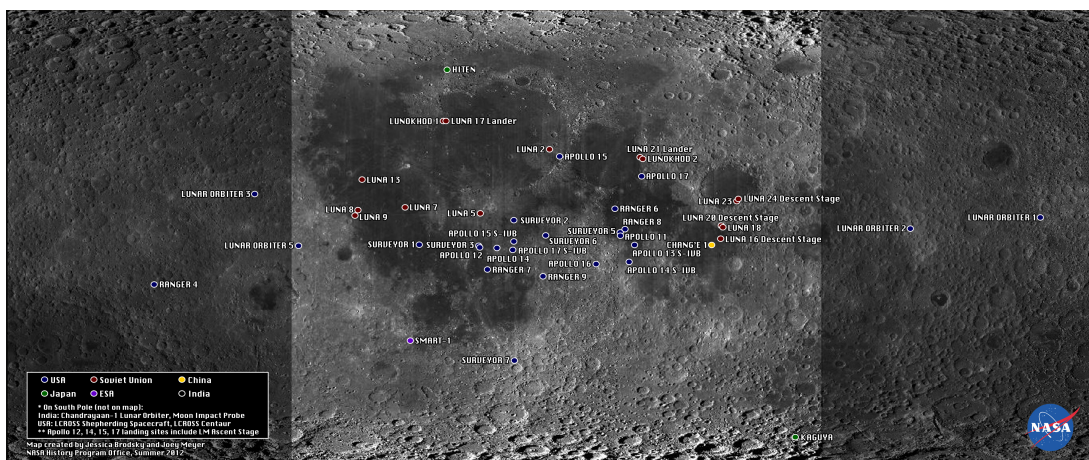
A. Moon Missions

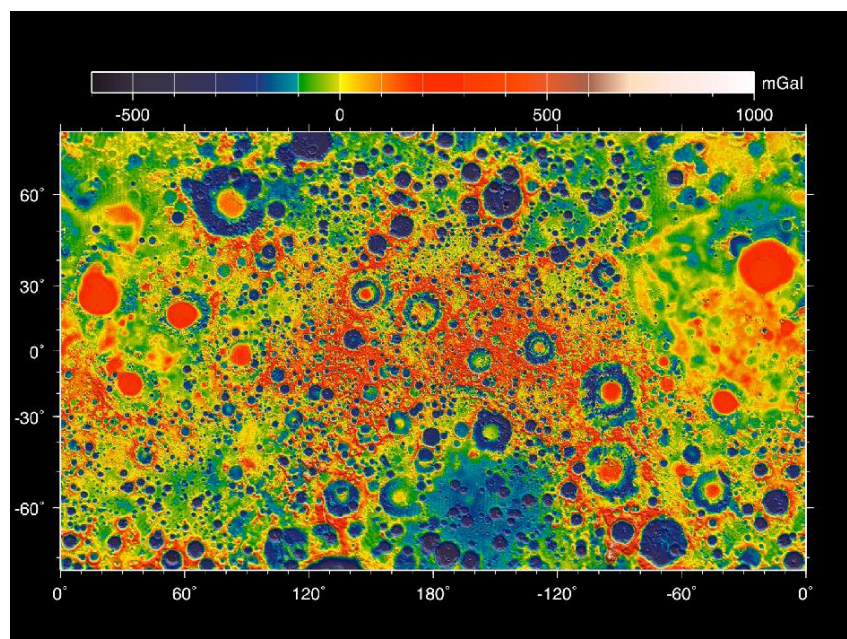Figure A.1.: Historical landing sites on the Moon's surface, [78]

Figure A.2.: Moon's gravity map by GRAIL, [79]

Table A.1.: Soviet lunar landing missions from 1959 to 1976 [6, 80]

Mission	Launch date	Mass	Spacecraft	Objective	Result
Luna 1	02.01.1959	361 kg	Ye-1	Impact	Flyby
Luna 2	12.09.1959	390 kg	Ye-1A	Impact	Success
Luna 3	04.10.1959	270 kg	Ye-2A	Flyby	Success
Sputnik 25	04.01.1963	1500 kg	n/a	Landing	LEO
Luna 4	02.04.1963	1422 kg	Ye-6	Landing	Flyby
Cosmos 60	12.03.1965	6530 kg	n/a	Landing	LEO
Luna 5	09.05.1965	1475 kg	Ye-6	Landing	Impact
Luna 6	08.06.1965	1440 kg	Ye-6	Landing	Flyby
Luna 7	04.10.1965	1504 kg	Ye-6	Landing	Impact
Luna 8	03.12.1965	1550 kg	Ye-6	Landing	Impact
Luna 9	31.01.1966	1580 kg	Ye-6	Landing	Success
Luna 13	21.12.1966	1580 kg	Ye-6M	Landing	Success
Luna 15	13.07.1969	5700 kg	Ye-8-5	Sample Return	Impact
Cosmos 300	23.09.1969	5600 kg	Ye-8-5	Sample Return	LEO
Cosmos 305	22.10.1969	5600 kg	Ye-8-5	Sample Return	LEO
Luna 16	12.09.1970	5600 kg	Ye-8-5	Sample Return	Success
Luna 17	10.11.1970	5700 kg	Ye-8	Lunar Rover	Success
Luna 18	02.09.1971	5750 kg	Ye-8-5	Sample Return	Impact
Luna 20	14.02.1972	5727 kg	Ye-8-5	Sample Return	Success
Luna 21	08.01.1973	5950 kg	Ye-8	Lunar Rover	Success
Luna 23	28.10.1974	5800 kg	Ye-8-5 M	Sample Return	Landing
Luna 24	09.08.1776	5800 kg	Ye-8-5 M	Sample Return	Success

Table A.2.: US lunar landing missions from 1962 to 1972 [6, 80]

Mission	Launch date	Mass	Propulsion	Objective	Result
Unmanned					
Ranger 4	23.04.1962	331 kg	solid rocket	Landing	Impact
Ranger 7	28.07.1964	367 kg	N_2H_4 mono-prop	Impact	Success
Ranger 8	17.02.1965	367 kg		Impact	Success
Ranger 9	21.03.1965	367 kg		Impact	Success
Surveyor 1	30.05.1966	995 kg		Landing	Success
Surveyor 2	20.04.1967	~1000 kg		Landing	Impact
Surveyor 3	20.04.1967	~1000 kg	solid rocket and MMH	Landing	Success
Surveyor 4	14.07.1967	~1000 kg	& MON-10 vernier	Landing	Signal lost
Surveyor 5	08.09.1967	~1000 kg		Landing	Success
Surveyor 6	07.11.1967	~1000 kg		Landing	Success
Surveyor 7	07.01.1968	~1000 kg		Landing	Success
Manned					
Apollo 11	16.07.1969	45 702 kg		Sample Ret.	Success
Apollo 12	24.11.1969	45 870 kg		Sample Ret.	Success
Apollo 14	31.01.1971	46 305 kg	see section 2.2.2	Sample Ret.	Success
Apollo 15	26.07.1971	48 599 kg		Sample Ret.	Success
Apollo 16	27.04.1972	48 637 kg		Sample Ret.	Success
Apollo 17	07.12.1972	48 607 kg		Sample Ret.	Success

Table A.3.: Missions to Moon from 1990 to 2010, data from [6]

Mission, Organisation	Function	Propulsion system	Launcher Payload
Hiten, 1990, ISAS (now JAXA)	Orbiter, impactor: Gravity assist and aero braking	N_2H_4 monoprop.: 8x23 N, 4x3 N	M-3SII 197 kg
Clementine, 1994, BMDO, NASA	Orbiter: Imaging, gravimetry, mineralogy	489 N N_2O_4 & N_2H_4, RCS: 12 mono-N_2H_4	Titan II-G 227 kg
Luna Prospector, 1998 NASA	Orbiter, impactor: Surface mapping, gravimetry, etc.	N_2H_4 monoprop.: 6x22 N	Athena 2 296 kg
SMART-1[1], 2003, ESA	Orbiter, impactor: Ion drive demonstrator	Hall-effect 70 mN Xenon RCS: 8 mono-N_2H_4	Ariane 5 366.5 kg
Kaguya, 2007, JAXA	Orbiter, impactor: Global survey of the Moon	500 N N_2O_4 & N_2H_4 RCS: 12x20 N biprop.	H2-A 2885 kg
Chang'e 1, 2007, CNSA	Orbiter, impactor: Technology demonstrator, imaging	n/a	LM 3A 2350 kg
Chandrayaan-1, 2008, ISRO	Orbiter, impactor: Surface topograhpy etc.	Bipropellant propulsion system	PSLV-XL 1380 kg
LRO[2], LCROSS[3] 2009, NASA	Orbiter, impactor[4]: Surface mapping, resource detection	N_2H_4 monoprop.	Atlas V 1846 kg / 621 kg
Chang'e 2, 2010, CNSA	Orbiter: High resolution images	n/a	LM 3C 2480 kg

[1] Small Missions for Advanced Research in Technology-1
[2] Lunar Reconnaissance Orbiter
[3] Lunar Crater Observation and Sensing Satellite
[4] The Centaur upper stage crashed on Moon too

Table A.4.: Missions to Moon from 2010, data from [6]

Mission, Organisation	Function	Propulsion system	Launcher Payload
ARTEMIS[1] 1&2, 2011, NASA	Orbiter: Analysis of magnetic phenomena	Monoprop.	Delta II, 5 satellites, 126 kg each
GRAIL A & GRAIL B, 2011, NASA	Orbiter, Impactor: High quality gravitational field mapping	22 N thruster, N_2H_4 monoprop., low energy transfer	Delta II, 202.4 kg each
LADEE[2] , 2013, NASA	Orbiter, Impactor: Analysis of atmoshpere and dust around Moon	Bipropellant MON-3 & MMH [81]	Minotaur-V, 383 kg
Chang'e 3, 2013, CNSA	Lander, Rover: Technology demonstrator, optical investigations	throttleable engine, bipropellant UDMH & N_2O_4 [82]	Long March 3B, ~3800 kg
Chang'e 5-T1 [3], 2013, CNSA	Flyby, Earth Reentry Capsule, Orbiter: Technology demonstrator	n/a	Long March 3C

[1] Acceleration, Reconnection, Turbulence and Electrodynamics of the Moon's Interaction with the Sun
[2] Lunar Atmosphere and Dust Environment Explorer
[3] Piggyback mission 4M by OHB with radio experiment

Table A.5.: Planned lander missions to Moon [80]

Mission	Organisation	Function	Intended launch[1]
Chang'e 5	CNSA	Sample Return	2017
Google Lunar X Prize	Several teams	Landers & Rovers	Planned for 2017[2]
Chandrayaan-2	ISRO	Lander, Rover	2018
SELENE-2	JAXA	Lander, Rover	2018
Chang'e 4	CNSA	Lander, Rover	Before 2020
Chang'e 6	CNSA	Sample Return	2020
Exploration Mission-2	NASA	Manned Landing	2023
Lunar Mission One	UK	Lander	2024
Luna-Glob 1	Roscosmos	Lander	Late 2020's
Internat. Lunar Network	NASA & others	Landed stations	n/a
Moon village	ESA & others	Manned base	n/a

[1] No launch date is officially confirmed and fixed
[2] Two teams have launch contracts for 2017: Team Moon Express plans to launch on Electron and SpaceIL plans a Falcon 9 launch
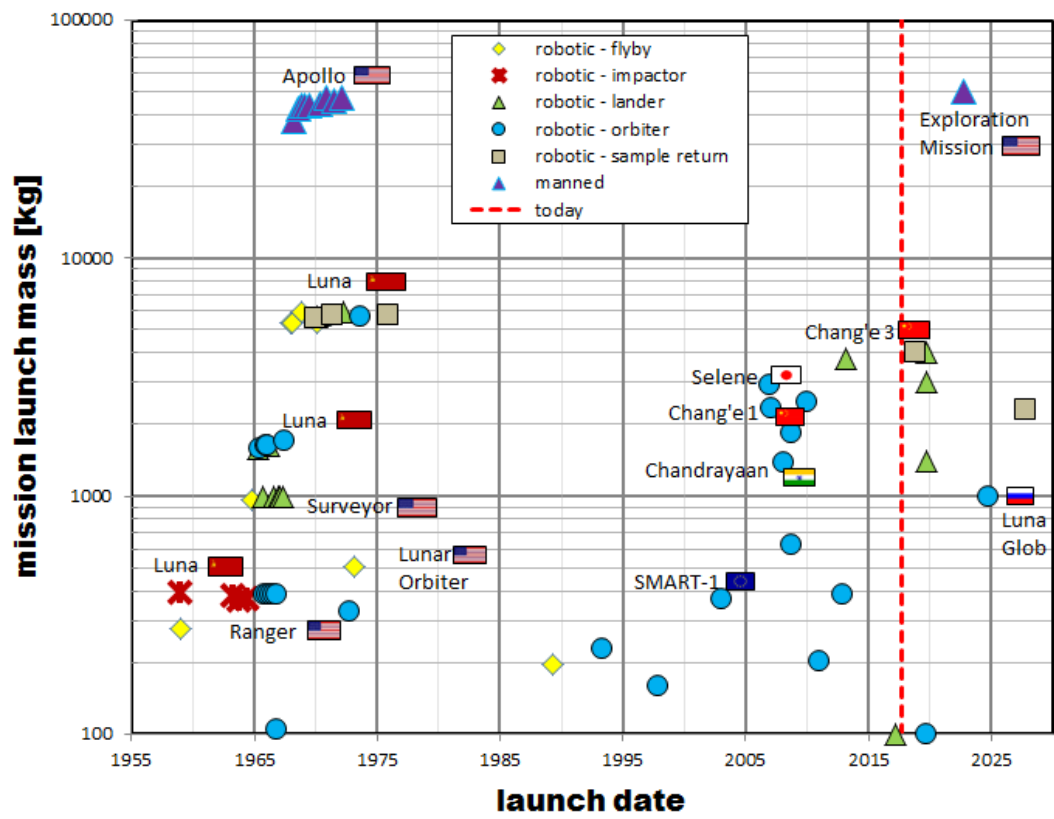
Figure A.3.: Overview of lunar missions in the past and future

1st stage S-IC		Time	0:00:00
Burn time	168 s	Max. acceleration	3.94 g
Thrust	33600 kN	Max. velocity	2.4 km/s
2nd stage S-II		Time	0:02:42
Burn time	384 s	Max. acceleration	1.82 g
Thrust	5140 kN	Max. velocity	6.5 km/s
3rd stage S-IVB – 1st burn	**Orbit insertion**	Time	0:09:09
Burn time	147 s	Max. acceleration	0.69 g
Thrust	900 kN	Max. velocity	7.4 km/s
Earth Orbit Data		Time	0:11:49
Perigee	183.2 km	Apogee	185.9 km
Descending Node	123.1°	Inclination	32.5°
3rd stage S-IVB – 2nd burn	**Translunar Injection**	Time	2:44:16
Burn time	347 s	Max. acceleration	1.45 g
Thrust	900 kN	Max. velocity	10.4 km/s
Transposition, docking and extraction		Time	3:15:23

The Command/Service Module separated from the S-IVB, turned by 180° and docked with the Lunar Module again. Afterwards the CSM and LM would together separate from S-IVB.

CSM	**Evasive maneuver**	Time	4:40:02
Burn time	2.93 s	ΔV	-6 m/s
Thrust	91 kN		
CSM	**Lunar orbit insertion**	Time	75:49:51
Burn time	357.5 s	ΔV	-889.254 m/s
Altitude cutoff	60.1 n mi		
CSM	**Orbit circularization**	Time	80:11:37
Burn time	16.9 s	ΔV	-48.4 m/s
Aposelen	66.1 n mi	Periselen	54.5 n mi
	CSM/LM undocking	Time	100:12:00
Burn time	9 s	ΔV	0.8 m/s
LM	**Descent orbit insertion**	Time	101:36:14
Burn time	30 s	ΔV	-23.3 m/s

Thrust	43.9 kN max (throttle 10%-60%)		
Aposelen	58.5 n mi	Periselen	7.8 n mi
LM	**Powered descent**	Time	102:33:05
Burn time	756.4 s		
LM	**Ascent**	Time	124:22:01
Burn time	434.9 s	ΔV	1850.2 m/s
Thrust	14.3 kN		
Aposelen	48 n mi	Periselen	9.4 n mi
LM	**Coelliptic sequence init.**	Time	125:19:35
Burn time	47 s	ΔV	51.5 m/s
Aposelen	49.3 n mi	Periselen	45.7 n mi
LM	**Const. differential height**	Time	126:17:50
Burn time	17.8 s	ΔV	6.1 m/s
Aposelen	47.4 n mi	Periselen	42.1 n mi
LM	**Terminal phase init.**	Time	127:03:52
Burn time	22.7 s	ΔV	7.7 m/s
Aposelen	61.7 n mi	Periselen	43.7 n mi
LM	**Midcourse corrections**		
ΔV #1	0.3 m/s	Time	127:18:31
ΔV #2	0.46 m/s	Time	127:33:31
LM	**Terminal phase finalize**	Time	127:46:10
Burn time	28.4 s	ΔV	9.6 m/s
Aposelen	63.0 n mi	Periselen	56.6 n mi
CSM/LM	**Docking**	Time	128:03:00
CSM/LM	**Ascent Stage Jettisoned**	Time	130:09:31
CSM/LM	**Separation**	Time	130:30:01
Burn time	7.2 s	ΔV	0.7 m/s
Aposelen	62.7 n mi	Periselen	54.0 n mi
CSM	**Transearth injection**	Time	135:23:42
Burn time	151.4 s	ΔV	999.4 m/s

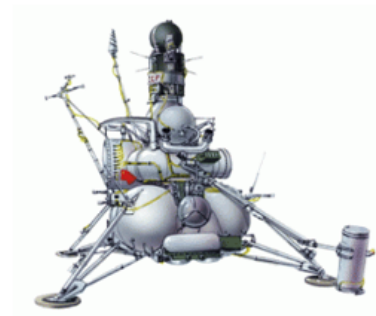| CSM	Midcourse corrections	Time	150:29:57.4
Burn time	10.0 s	ΔV	1.5 m/s
CM/SM	**Separation**	Time	194:49:12.7

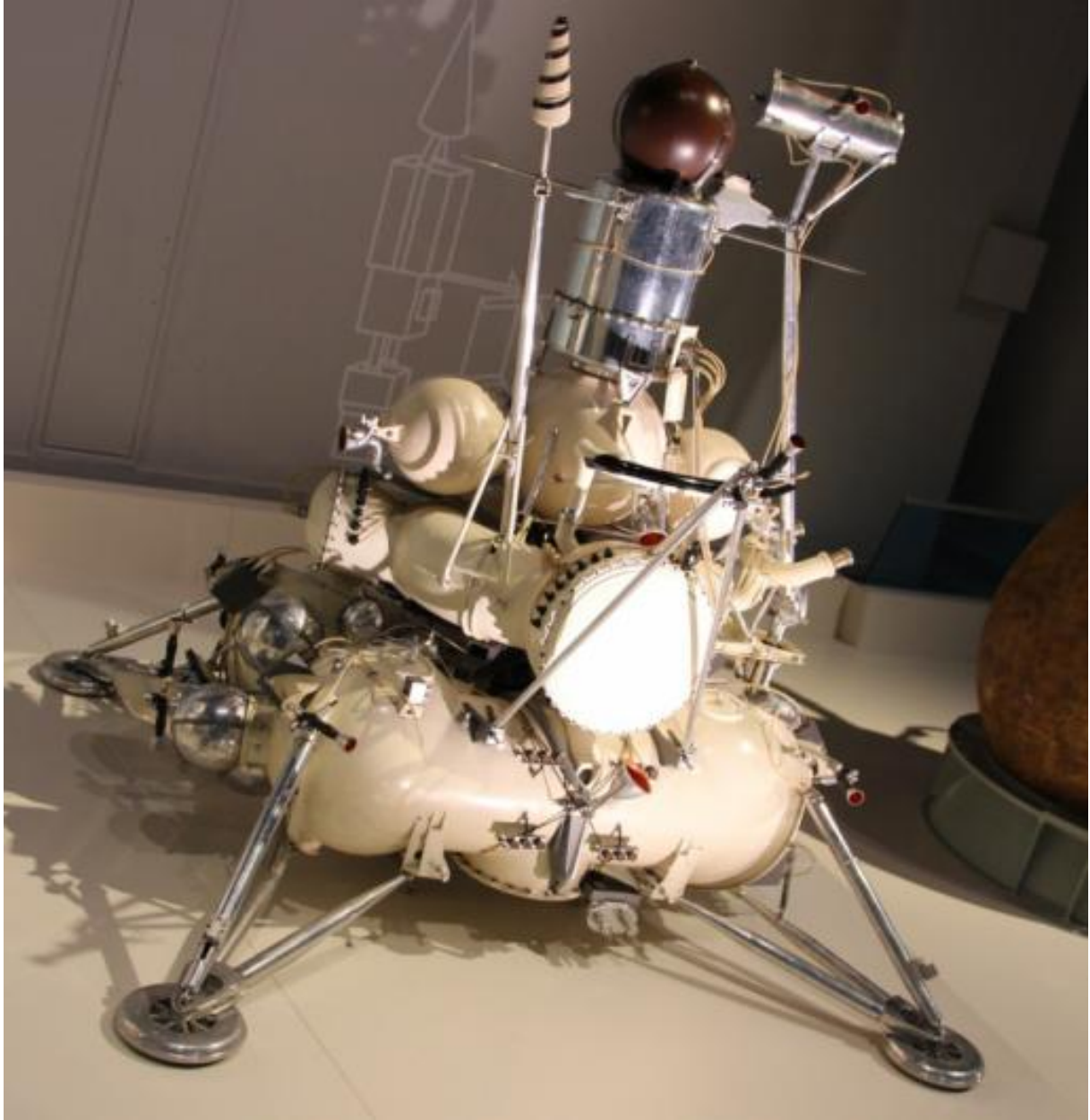Figure A.4.: Landers of Apollo and Luna Moon programs, [83, 84]

Figure A.5.: Luna 24 lander module replica, [85]

B. Hybrid Rocket Research Groups

Figure B.1.: Research on hybrid propulsion in Europe

Table B.1.: Hybrid rocket propulsion research groups

No.	Marker	Organisation	Type, Nation	Field of Work
Europe				
1	1	HyEnD University of Stuttgart	Student group, Germany	Hybrid sounding rockets (32 km altitude record), paraffin-based fuels
2	2	WARR University of Munich	Student group, Germany	Hybrid sounding rockets
3	3	ERIG University of Braunschweig	Student group, Germany	Hybrid sounding rockets
4	4	ZARM University of Bremen	Student group, Germany	Hybrid sounding rockets
5	5	Aquasonic City Uni. of Bremen	Student group, Germany	Hybrid sounding rockets
6	6	HyCOMET City Uni. of Augsburg	Student group, Germany	Hybrid sounding rockets
7	7	DLR Lampoldshausen	Research Institute, Germany	Advanced paraffin-based fuels, fundamental research, hybrid rocket engine tests
8	8	DLR Braunschweig	Research Institute, Germany	Simulation, advanced fuel geometries
9	9	DLR Trauen	Research Institute, Germany	Hybrid rocket engine tests
10	10	CISAS, University of Padova	University, Italy	Fundamental research, numerics, tests, HYPROGEO
11	11	Politecnico di Milano	University, Italy	Fundamental research, numerics, tests
12	12	Sapienza - University of Rome	University, Italy	Fundamental research, numerics, tests
13	13	Starthclyde University	University, UK	Fundamental research, HYPROGEO
14	14	Surrey University	University, UK	Fundamental research, alternative geometry
15	15	PERSEUS (in coop. with CNES, ONERA)	Student project, France	Hybrid sounding rocket, student education
16	16	DARE, University of Delft	Student group, Netherlands	Hybrid sounding rockets
17	17	Nammo Raufoss	Industry, Norway	Northstar Microlauncher Project, HYPROGEO

Table B.1.: Hybrid rocket propulsion research groups

No.	Marker	Organisation	Type, Nation	Field of Work
18	18	Space Forest Gdynia	Industry, Poland	Small scale hybrid rocket engines
19	19	Institute of Aviation Warsaw	Research Institute, Poland	Fundamental research, small scale tests
20	20	SPARTAN: (Coordinator: Thales Alenia)	Industry, EU	Hybrid propulsion lander demonstrator
21	21	HYPROGEO: (Coordinator: ASL)	Industry, EU	Hybrid propulsion system for orbit applications
22	22	HYPROGEO: MOOG	Industry, EU	
23	23	HYPROGEO: Von Karman Institute	Research Institute, EU	
24	24	Bloodhound SSC Project	Industry, UK	Speed Record Car
25	25	University of Naples	University, Italy	

World

No.	Marker	Organisation	Type, Nation	Field of Work
26	30	Pennsylvania State University	University, USA	
27	31	Stanford University	University, USA	
28	32	Purdue University Hybrid Propulsion	Student group, USA	
29	33	HYSOR University of Colorade, Boulder	Student group, USA	
30	34	NASA FSGC Hybrid Motor Rocket Competition	Student Project, USA	
31	35	Sierra Nevada Corporation	Industry, USA	
32	36	ORBITEC	Industry, USA	
33	37	Space Propulsion Group	Industry, USA	
34	38	Virgin Galactic / Scaled Composites	Industry, USA	
35	39	NASA Ames (Peregrine Rocket Project)	Research Institute, USA	
36	40	NASA JPL (Mars Ascent Vehicle)	Research Institute, USA	
37	41	NASA Glenn (Mars Ascent Vehicle)	Research Institute, USA	
38	42	NASA Marshall (Mars Ascent Vehicle)	Research Institute, USA	

Table B.1.: Hybrid rocket propulsion research groups

No.	Marker	Organisation	Type, Nation	Field of Work
39	50	Keldysh Research Center	Research Institute, Russia	
40	60	JAXA ISAS Sagamihara	Research Institute, Japan	
41	61	JAXA Tsukuba	Research Institute, Japan	
42	62	Tokyo Metropolitan University	University, Japan	
43	63	Tokai University	University, Japan	
44	64	Saitama Institute of Technology	University, Japan	
45	65	Hokkaido University of Science	University, Japan	
46	66	Gas Turbine Div. Kawasaki Heavy Industries	University, Japan	
47	67	Advanced Rocket Research Center	Research Institute, Taiwan	
48	70	ISRO VSSC	Research Institute, India	
49	71	ISRO LPSC	Research Institute, India	
50	80	Gilmour Space Tech Singapore	Industry, Singapore	
51	81	Gilmour Space Tech Australia	Industry, Australia	
52	82	HyPER, University of Adelaide	Student group, Australia	
53	90	INPE LCP Cachoeira Paulista	Research Institute, Brasil	
54	91	University of Brasilia	University, Brasil	
55	92	Hybrid Propulsion Team University of Brasil	Student group, Brasil	
56	93	University of Kwazulu-Natal	University, South Africa	

C. ESPSS: Enthalpy Balance at the Fuel Grain

In the ESPSS model (function "GasSol_exch") the heat of formation of the decomposed fuel is notated with dH. For clarity in this document the notation is $\Delta H^\theta_{f,dec}$. The heat of formation can be given in literature for solid, liquid or gaseous state. Usually for fuels that are solid at ambient conditions, the heat of formation is given for the solid state as $\Delta H^\theta_{f,sp}$. The heat of formation of atomic, gaseous carbon and hydrogen is unequal to zero. Only solid carbon and molecular hydrogen have a heat of formation of zero. The heat of formation of the solid fuel at room temperature is named LH_{sp} in ESPSS, which is confusing, since LH stands for latent heat. Latent heats however are the heats of phase changes like vaporization and melting, not decomposition. Therefore in this document the heat of formation is again renamed to $\Delta H^\theta_{f,sp}$.

In the model for the hybrid combustor the the decomposed fuel mass flow is calculated with one of the regression rate laws. The heat flow from the flame zone to the surface zone therefore is directly bound to the fuel mass flow. In the ESPSS 3.2 component the heat flow $\dot{Q}_{vs}$ is calculated as follows and its positive direction is from the surface zone to the flame zone:

$$\dot{Q}_{vs} = \dot{m}_f \Delta H^\theta_{f,dec} - \dot{Q}_{trans} = \dot{m}_f \Delta H^\theta_{f,dec} - A_f h_c \left(T_g - T_{vap} \right) \tag{C.1}$$

The first term incorporates the heat flow bound to the mass flow of decomposed fuel. The second term Q_{trans} is the heat flow by conduction and radiation from the flame to the surface zone. One condition that is mandatory to be fullfilled is, that this heat flow must be equal to the heat flows necessary to melt, vaporize and pyrolyse the fuel, as well as heating up the solid fuel grain. The heat flow to the solid fuel grain is:

$$\dot{Q}_{sp} = A_f h_{sp} \left(T_{vap} - T_g \right) \tag{C.2}$$

The following equation can be obtained:

$$\dot{Q}_{trans} + \dot{m}_f \Delta H^\theta_{f,sp} = \dot{m}_f \Delta H^\theta_{f,dec} + \dot{Q}_{sp} \tag{C.3}$$

On the left side the transfered heat due to conduction and convection is added to the heat of formation, which is set free for decomposition of the solid fuel. For most of the solid fuels, the heat of formation is negative, since the decomposition is endothermic. The right side represents the enthalpy that flows out of the zone: The heat bound to the mass flow in form of heat of formation and the heat flow to the solid fuel. If the heat of formation of the solid fuel is unknown, and only the gaseous or liquid heat of formation is known, it can be simply

rearranged:

$$\Delta H_{f,sp}^{\theta} = \Delta H_{f,liq}^{\theta} + h_{melt} = \Delta H_{f,gas}^{\theta} + h_{melt} + h_{vap} \tag{C.4}$$

In that case, additionally the latent heat for melting and vaporization is accounted for. This equations are not always fullfilled in the ESPSS model.

The following problems were identified with the ESPSS code:

- As Q_{trans} is calculated simply with heat conduction and $\dot{m}_f$ is calculated with the regression model, there is no link between both and therefore the enthalpy balance is not kept.

- The heat transfer coefficient h_c from the gas flow in the port to the vapor layer is calculated via a Nusselt correlation with the gas flow properties of the node:

$$h_c = \frac{k}{D} \left(Nu_l^{16} + Nu_t^{16} \right)^{\frac{1}{16}} \tag{C.5}$$

with the laminar Nusselt number $Nu_l = 4$, the turbulent Nusselt number Nu_t, heat conductivity k and the flow diameter D. The turbulent Nusselt number is calculated with the Reynolds number Re and the Prandtl number Pr:

$$Nu_t = 0.023 Re^{0.8} Pr^{0.4} \tag{C.6}$$

This simplified heat transfer coefficient which is calculated for a homogeneous tube flow cannot represent the inhomogeneous heat transfer situation in the hybrid combustion chamber with many different processes.

- The temperature T_{vap} was identified with a saturation temperature T_{sat}, which does not exist for all solid fuels. The name vaporization temperature T_{vap} is much clearer, and different to the saturation temperature, if it exists for the fuel. It can be assumed that the temperature close to the solid fuel is the vaporization temperature. For liquefying fuels also a melting temperature T_{melt} can be determined. Respectively the temperature close to the surface of a liquefying fuel is close to the melting temperature.

The correct way to calculate the enthalpy balance and heat flows depends on the regression rate law. For the "stdHybrid" regression law, the regression rate is based on experiments and can be assumed as correct approximation. In this case the heat flows are justified by experimental data. For the models of Marxman and Zilliac/Karabeyoglu the heat flow and enthalpy conservation was the starting point of deriving the equations. Therefore also here the heat flow is correct, when it is matched to the necessary heat of vaporization and decomposition. The heat flow from the vapor zone to the solid stays the same, and therefore the heat flow from the gas to the vapor zone can be modified:

$$\dot{Q}_{trans} = \dot{m}_f \left(\Delta H_{f,dec}^{\theta} - \Delta H_{f,sp}^{\theta} \right) + \dot{Q}_{sp} \tag{C.7}$$

The enthalpy flow $\dot{Q}_{vs}$ is then:

$$\dot{Q}_{vs} = -\dot{m}_f \Delta H^{\theta}_{f,sp} + \dot{Q}_{sp} \qquad (C.8)$$

If this equation is compared to Equation C.1, it is visible, that the wrong heat of formation is used in the original code. The heat of formation of the decomposed fuel $\Delta H^{\theta}_{f,dec}$ is not occuring in the heat flow, because this heat is first flowing from the hot gas to the fuel grain in order to decompose the fuel but then is going back to the gas flow bound to the fuel mass flow. In this context also the problems with the advanced regression rate model "vapModel" can be highlighted. This model actually accounts for energy balance and calculates the vaporization of fuel with the enthalpy flow into the boundary layer. The mistake is, that this model does only respect heat of formation of the solid fuel but not the heat of formation of the decomposition. However, that enthalpy must be provided too, if it is unequal to zero (like in H-atoms). Therefore it produces regression rates much higher than observed in experiments. Solved for the mass flow in the vaporization model "vapModel" this results in:

$$\dot{m}_f = \frac{\dot{Q}_{trans} - \dot{Q}_{sp}}{\Delta H^{\theta}_{f,dec} - \Delta H^{\theta}_{f,sp}} \qquad (C.9)$$

The regression model "vapModel" was improved:

$$\dot{m}_f = A_f \frac{h_c \left(T_g - T_{vap} \right) - h_{sp} \left(T_{vap} - T_s \right)}{\Delta H^{\theta}_{f,dec} - \Delta H^{\theta}_{f,sp}} \qquad (C.10)$$

Instead of the mean gas temperature T_g, the flame sheet temperature T_c is used to calculate the heat flow. The fuel mass flow is highly dependent on the heat transfer coefficient h_c, which increases with viscosity. So the regression rate is increasing with the chamber temperature. As mentioned before, the heat transfer coefficient of a tube flow with isothermic gas is not precise for a hybrid combustor. For the other regression laws, where the regression rate is not computed with the heat balance, the heat transfer from the gas to the vapor zone can be calculated directly with the needed heat for vaporization and decomposition of the fuel mass flow.
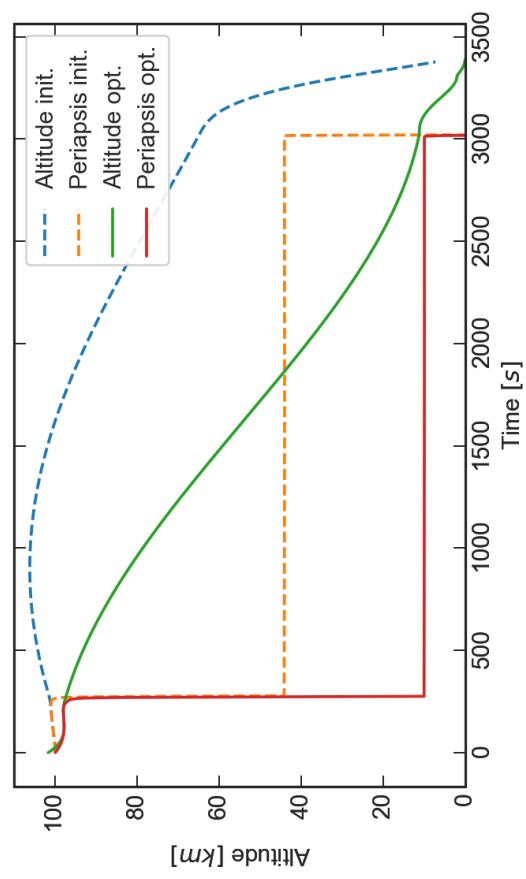
D. Lunar Lander Optimization

A hybrid propulsion lunar lander with a sample return rocket was introduced in a previous work [23]. The mission is designed to be launched with an Ariane 5 or comparable launcher to a direct Moon orbit transfer. The initial Moon orbit of the vehicle is a hyperbolic flyby with a low periselen of about 100 km. At the periselen the first of two hybrid rocket kick stages is ignited to lower the periselen to about 10 km altitude. Then the emtpy stage is ejected and after a coast the second kick stage is ignited at the new periselen of 10 km. The second stage is reducing the horizontal and vertical velocity close to zero, then it is ejected and the lunar lander starts its final vertical descent. The mass of the lander and the kick stages in total is 8300 kg with paraffin-based fuel and 95% hydrogen peroxide as oxidizer. Previously the simulation and optimization of the lander and its trajectory was done using only rough estimations of the propulsion systems' performance. A constant performance was assumed. Now the simulation and optimization has been renewed with the new ASTOS and ESPSS interface for hybrid propulsion systems. One change that has been done to the original model was the engine set-up. The four parallel engines on each kick stage were replaced by one larger hybrid rocket engine. This change was possible, since new regression rate results in experiments showed, that it can be feasible to have one large long burning hybrid rocket engine. The optimum in terms of structural mass to fuel ratio has to be found in the future. Table D.1 displays the lunar lander mass before and after optimization of the trajectory. In total 200 kg of H_2O_2 are included for RCS thrusters. The payload includes the return rocket as well as power supply and instrumenation of the lander. It can be seen that the payload and masses were not improved a lot by the optimizer. The reason for this is, that the inputs were already taken from the optimized trajectory of the previous work. However the trajectory itself was optimized, as well as the rocket engine's geometries which are listed in Table D.2. Figure D.1a shows the altitude and periapsis altitude of the lander. Both initial guess and optimized curves are printed. The initial guess is not very close to a realistic descent on the Moon's surface. The descent rate at the end is increasing, which can be also seen in Figure D.1b. Even though the initial guess was not very good, the optimization with ASTOS found an optimal trajectory which would meet the conditions of a soft touch down. Figure D.1c shows a detailed view of the final landing. It features the end of the second kick stage's burn until 3300 s, a short coast of 25 s and a nearly vertical descent until touch down with a flight path speed of about 1.5 m/s. A first impression of the possible landing module with a return rocket is pictured in Figure D.1d. The combustion chambers and nozzles as well as the H_2O_2 tanks are in true scale both for the landing craft and the return rocket. The diameter of the truss is about 2.5 m and the height is about 3.1 m.[69]

Table D.1.: Initial and optimized lunar lander masses[69]

Stage	Component	Optimizable	Initial mass		Optimized
1st	Propellant	Yes	2300 kg	→	2302 kg
	Tank structure	Fixed ratio	4 % of oxidizer mass		
	Engine structure	Yes	115 kg	→	115 kg
	Additional Structures	No	355 kg		
	Total Stage Mass		2852 kg	→	2851 kg
2nd	Propellant	Yes	2550 kg	→	2497 kg
	Tank structure	Fixed ratio	4 % of oxidizer mass		
	Engine structure	Yes	115 kg	→	115 kg
	Additional Structures	No	380 kg		
	Total Stage Mass		3135 kg	→	3079 kg
3rd	Propellant	Yes	290 kg	→	171 kg
	Tank structure	Fixed ratio	9.8 % of oxidizer mass		
	Engine structure	Yes	10 kg	→	10 kg
	Additional Structures	No	920 kg		
	Total Stage Mass		1230 kg	→	1167 kg
	Payload	Yes	1217 kg	→	1200 kg

Table D.2.: Lunar lander engine parameters[69]

| Stage	Component	Initial value		Optimized value
1st	Fuel length	850 mm	→	830 mm
	Fuel diameter	720 mm	→	720 mm
	Throat diameter	104 mm	→	104 mm
	Expansion ratio	180	→	182.5
2nd	Fuel length	850 mm	→	849 mm
	Fuel diameter	720 mm	→	740 mm
	Throat diameter	104 mm	→	100.6 mm
	Expansion ratio	180	→	190
3rd	Fuel length	155 mm	→	160 mm
	Fuel diameter	140 mm	→	144.5 mm
	Throat diameter	18 mm	→	15.1 mm
	Expansion ratio	190	→	200

(a) Altitude and periapsis of the lander before and after optimization[69]
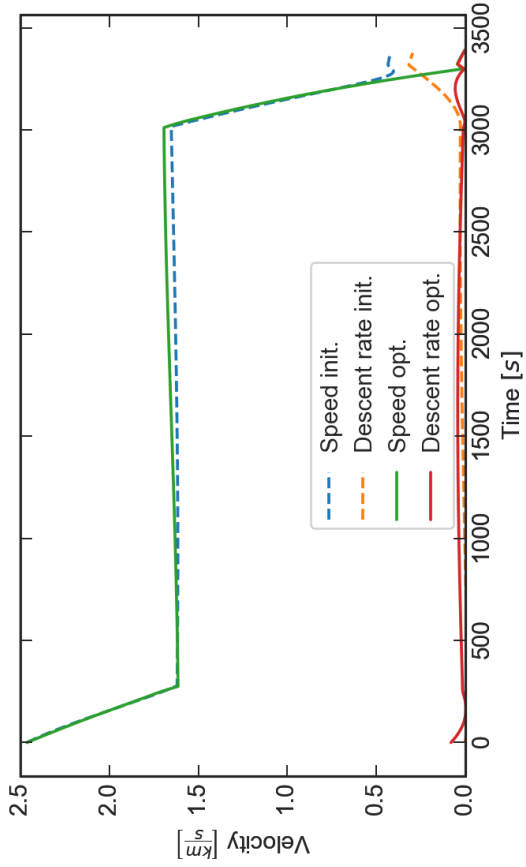
(b) Speed and descent rate of the lander before and after optimization[69]
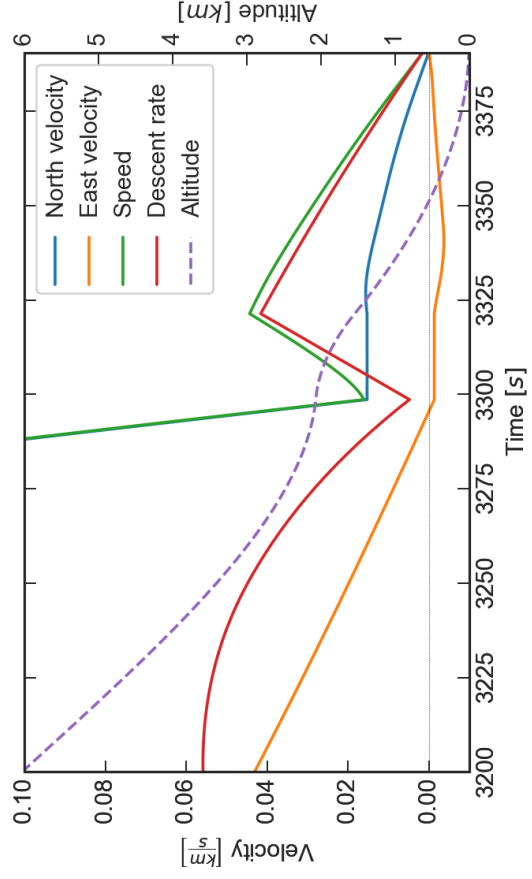
(c) Velocities and altitude of the lander in the final landing sequence[69]
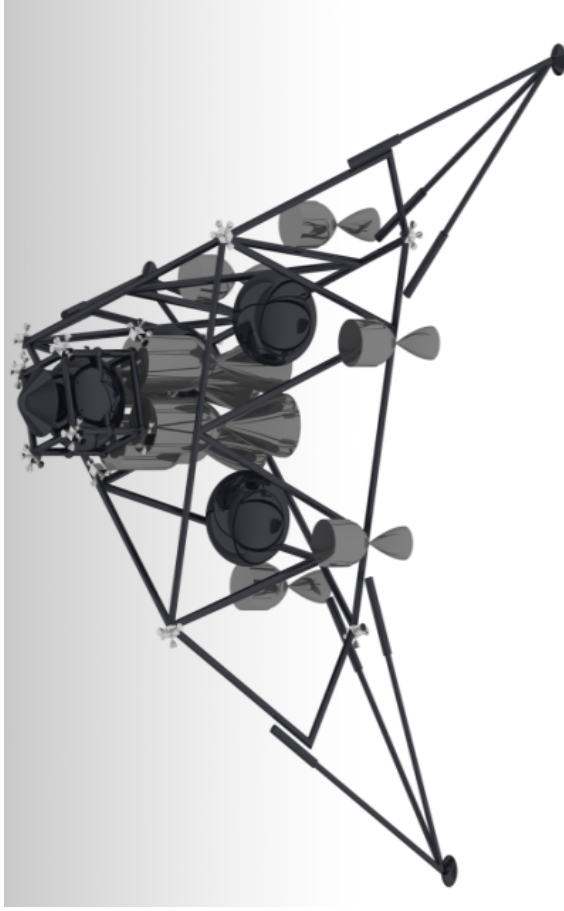
(d) Preliminary illustration of the lunar lander module with a return rocket[69]

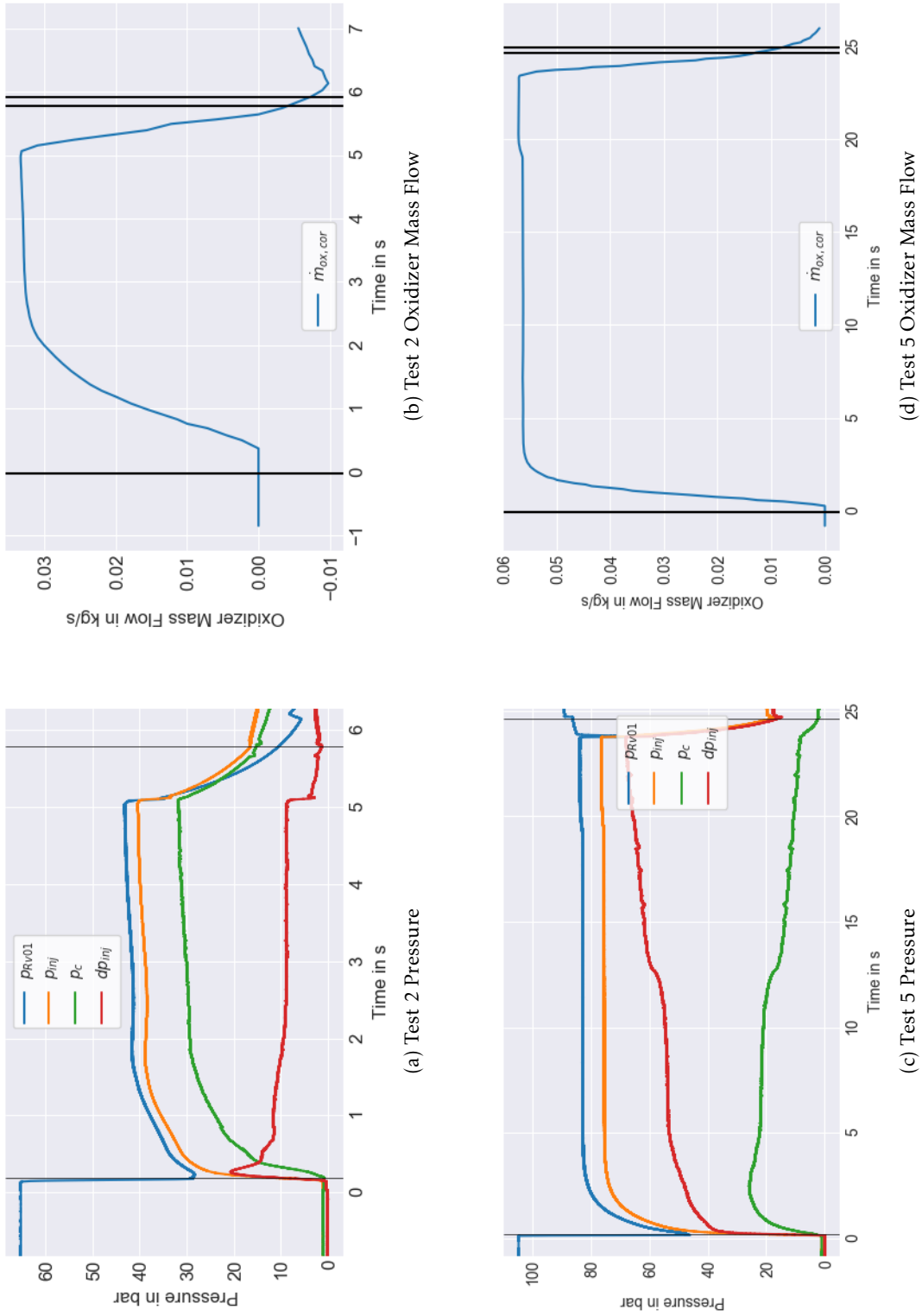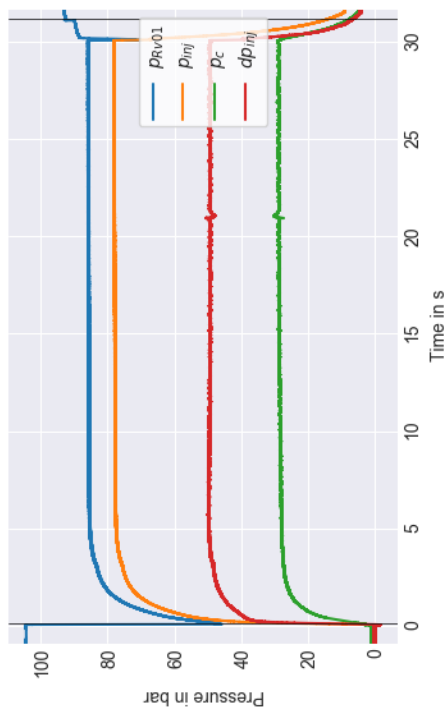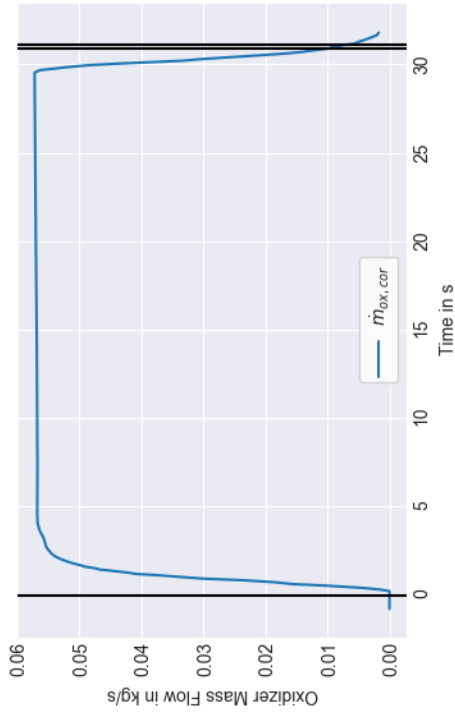Figure D.1.: Hybrid lunar lander data
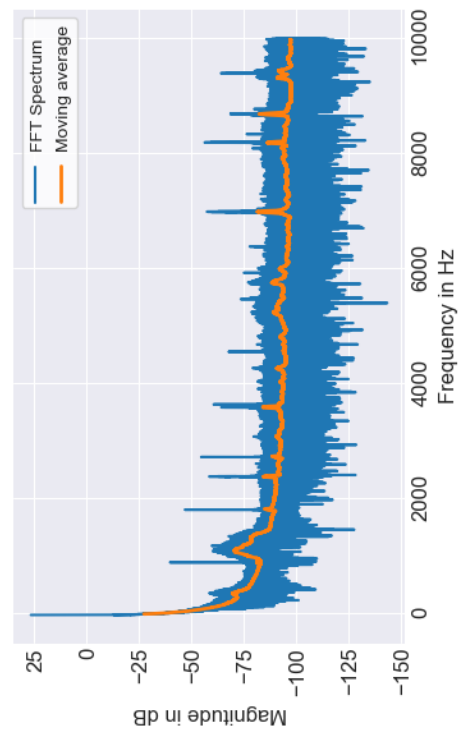
E. Test Results

(a) Test 2 Pressure

(b) Test 2 Oxidizer Mass Flow

(c) Test 5 Pressure

(d) Test 5 Oxidizer Mass Flow

Figure E.1.: Test 2 and 5 measurements

(a) Test 6 Pressure

(b) Test 6 Oxidizer Mass Flow

(c) Test 5 Pressure
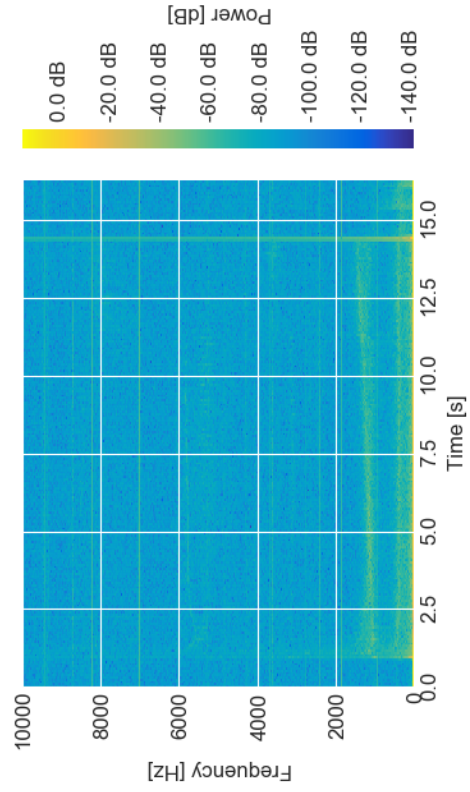
(d) Test 5 Oxidizer Mass Flow

Figure E.2.: Test 2 and 5 measurements

F. Hybrid Propulsion Lunar Lander

H_2O_2 was used as the oxidizer. Figure F.1 shows the thrust on the left with an exemplary thrust level of 13 kN. The engine is ignited in the simulation after 10 s. Before that the oxidizer tank is pressurized to the feed pressure which is illustrated on the right. The pressurization tank's pressure is 300 bar. Figure F.2 illustrates the propellant masses. On the left the liquid oxidizer in the tank is compared to the solid propellant in all four engines. On the right the pressurization gas is shown, which is reduced in the pressurization tank and flowing into the main oxidizer tank. The mass flows of the stage is shown in Figure F.3 on the left. The injector and nozzle mass flow are for a single engine with a mixture ratio of about 7.9. Figure F.4 depicts the regression rate and the fuel port diameter over time.
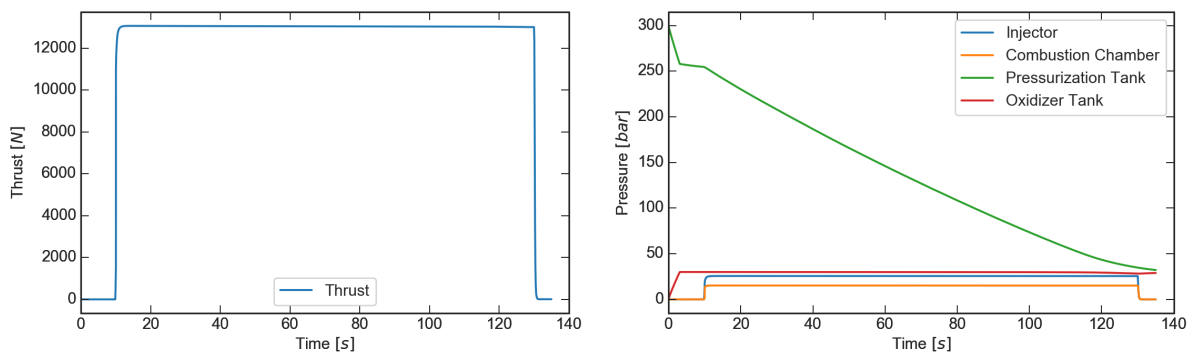

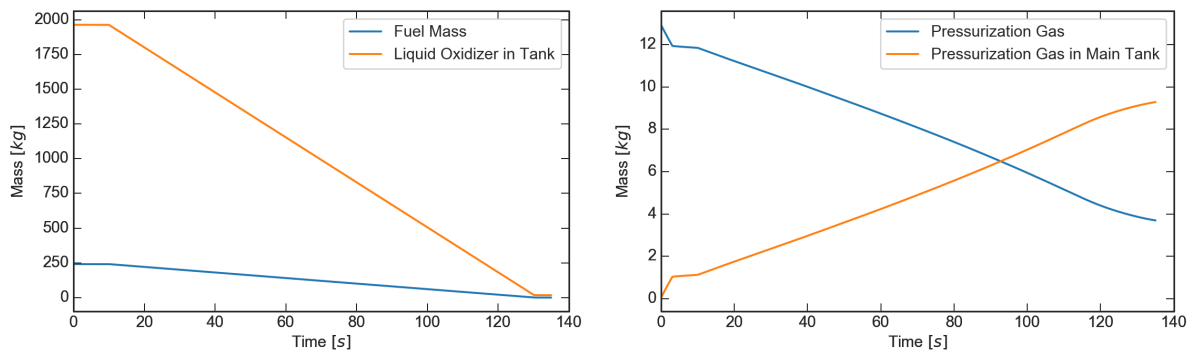Figure F.1.: Thrust and pressure simulation for hybrid propulsion kick stage

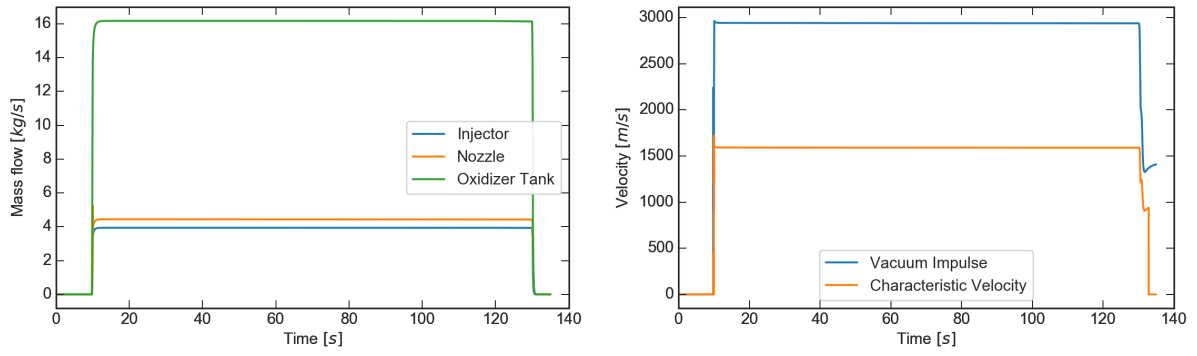Figure F.2.: Mass over time for hybrid propulsion kick stage

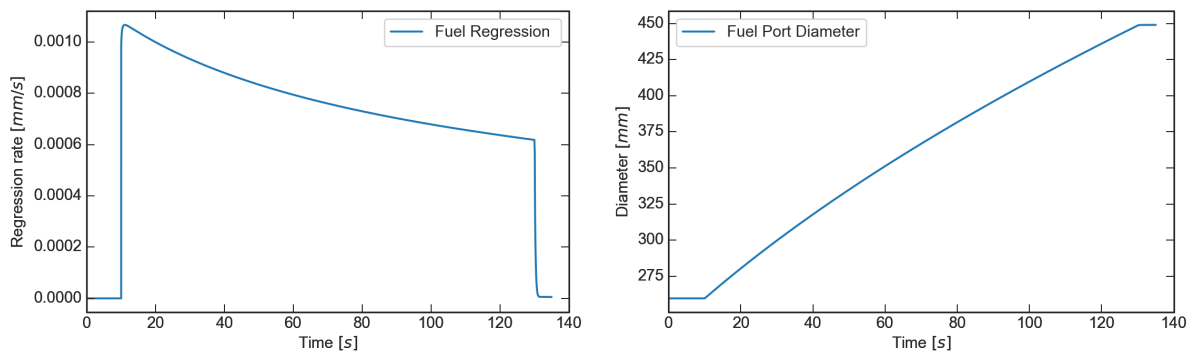Figure F.3.: Mass flow, I_{Vac} and c^* for hybrid propulsion kick stage

Figure F.4.: Regression rate and fuel port diameter for hybrid propulsion kick stage